A NEAR-INFRARED VIEW OF LUMINOUS QUASARS: BLACK HOLE MASSES, OUTFLOWS AND HOT DUST

LIAM COATMAN
Institute of Astronomy
& Robinson College

A dissertation submitted to the
University of Cambridge for the degree of
DOCTOR OF PHILOSOPHY

Under the supervision of
PROF. PAUL C. HEWETT
& DR. MANDA BANERJI

April 2017

ABSTRACT

Supermassive black holes (BHs) and their host-galaxies are thought to evolve in tandem, with the energy output from the rapidly-accreting BH regulating star formation and the growth of the BH itself. The goal of better understanding this process has led to much work focussing on the properties of quasars and active galactic nuclei (AGN) at relatively high redshifts, $z \gtrsim 2$, when cosmic star formation and BH accretion both peaked. At these redshifts, however, ground-based statistical studies of the quasar population generally have no access to the rest-frame optical spectral region, which is needed to measure Hβ-based BH masses and narrow line region outflow properties. The cornerstone of this thesis has been a new near-infrared spectroscopic catalogue providing rest-frame optical data on 434 luminous quasars at redshifts $1.5 \lesssim z \lesssim 4$.

At high redshift, $z \gtrsim 2$, quasar BH masses are derived using the velocity-width of the C IV broad emission-line, based on the assumption that the observed velocity-widths arise from virial-induced motions. However, C IV exhibits significant asymmetric structure which suggests that the associated gas is not tracing virial motions. By combining near-infrared spectroscopic data (covering the hydrogen Balmer lines) with optical spectroscopy from the Sloan Digital Sky Survey (covering C IV), we have quantified the bias in C IV BH masses as a function of the C IV blueshift. C IV BH masses are shown to be over-estimated by almost an order of magnitude at the most extreme blueshifts. Using the monotonically increasing relationship between the C IV blueshift and the mass ratio BH(C IV)/BH(Hα) we derive an empirical correction to all C IV BH-masses. The correction depends only on the C IV line properties and therefore enables the derivation of un-biased virial BH mass estimates for the majority of high-luminosity, high-redshift, spectroscopically confirmed quasars in the literature.

Quasars driving powerful outflows over galactic scales is a central tenet of galaxy evolution models involving 'quasar feedback' and significant resources have been devoted to searching for observational evidence of this phenomenon. We have used [O III] emission to probe ionised gas extended over kiloparsec scales in luminous $z \gtrsim 2$ quasars. Broad [O III] velocity-

widths and asymmetric structure indicate that strong outflows are prevalent in this population. We estimate the kinetic power of the outflows to be up to a few percent of the quasar bolometric luminosity, which is similar to the efficiencies required in recent quasar-feedback models. [O III] emission is very weak in quasars with large C IV blueshifts, suggesting that quasar-driven winds are capable of sweeping away gas extended over kilo-parsec scales in the host galaxies.

Using data from a number of recent wide-field photometric surveys, we have built a parametric spectral energy distribution model that is able to reproduce the median optical to infrared colours of tens of thousands of AGN at redshifts $1 < z < 3$. In individual objects, we find significant variation in the near-infrared spectral energy distribution, which is dominated by emission from hot dust. We find that the hot dust abundance is strongly correlated with the strength of outflows in the quasar broad line region, suggesting that the hot dust may be in a wind emerging from the outer edges of the accretion disc.

DECLARATION

I hereby declare that this dissertation is the result of my own work and includes nothing which is the outcome of work done in collaboration except as declared in the Preface and specified in the text. It is not substantially the same as any that I have submitted, or, is being concurrently submitted for a degree or diploma or other qualification at the University of Cambridge or any other University or similar institution except as declared in the Preface and specified in the text. I further state that no substantial part of my dissertation has already been submitted, or, is being concurrently submitted for any such degree, diploma or other qualification at the University of Cambridge or any other University or similar institution except as declared in the Preface and specified in the text. It does not exceed the prescribed limit for the Degree Committee of Physics and Chemistry of 60 000 words.

This thesis has used material from the following publications.

- Chapters 2 and 3 use material from Coatman et al. (2016) and Coatman et al. (2017).

Liam Coatman

ACKNOWLEDGMENTS

First and foremost, I would like to express my sincere gratitude to my supervisors Paul Hewett and Manda Banerji for their advice, encouragement and unwavering support. Paul and Manda have been endlessly patient and always approachable – thank you for investing in me not only as a scientist but as a person.

I am indebted to Gordon Richards, whose enthusiasm and ideas have contributed much to this work. Special thanks also to Joe Hennawi and Xavier Prochaska for providing me with some remarkable data. Finally, I am grateful to the Science and Technology Facilities Council for funding my work.

Liam Coatman
Cambridge, April 2017

CONTENTS

1 INTRODUCTION 1
- 1.1 The discovery of quasars 1
- 1.2 The AGN-host galaxy connection 1
- 1.3 AGN: the current paradigm 2
  - 1.3.1 Accretion disc 3
  - 1.3.2 Broad line region 4
  - 1.3.3 Dusty torus 5
  - 1.3.4 Narrow line region 6
- 1.4 Large surveys and the systematic study of AGN properties 6
- 1.5 Measuring black hole masses 7
  - 1.5.1 Reverberation mapping 7
  - 1.5.2 Single-epoch virial estimates 8
- 1.6 Winds and outflows in AGN 10
- 1.7 AGN SEDs 12
- 1.8 Thesis structure 13

2 A NEAR-INFRARED SPECTROSCOPIC DATABASE OF HIGH-REDSHIFT QUASARS 15
- 2.1 Spectroscopic surveys 15
- 2.2 Near-infrared spectroscopic data 16
  - 2.2.1 Coatman et al. (2016) sample 19
  - 2.2.2 Shen (2016) sample 21
  - 2.2.3 Quasars Probing Quasars sample 21
  - 2.2.4 VLT SINFONI 22
  - 2.2.5 NTT SOFI 22
  - 2.2.6 Hale TripleSpec 23
- 2.3 Redshift and luminosity distribution of catalogue 23
- 2.4 Supplementary data 24
  - 2.4.1 Observed-frame optical spectroscopic data 24
  - 2.4.2 Photometric data 25
  - 2.4.3 Radio/BAL quasar classification 26
- 2.5 Absolute flux calibration of near-infrared spectra 26
  - 2.5.1 SDSS spectrum as a fiducial baseline 27

2.5.2 BOSS spectrum as a fiducial baseline 28
2.5.3 Photometric data as a fiducial baseline 28
2.5.4 Reliability of luminosity measurements 30
2.6 Correcting for instrumental broadening 30

3 CORRECTING C IV-BASED VIRIAL BLACK HOLE MASSES 33
3.1 Single-epoch virial BH masses 33
3.2 Quasar sample 36
3.3 Spectral measurements 37
3.3.1 Modelling C IV 39
3.3.2 Modelling Hα 40
3.3.3 Modelling Hβ and [O III] 41
3.3.4 Fitting procedure 42
3.3.5 Spectra removed from sample 43
3.3.6 Emission-line parameter uncertainties 45
3.3.7 Contemporaneity of spectra 47
3.3.8 Quasar monochromatic luminosity 47
3.3.9 Characterising the emission-line widths 48
3.4 An empirical correction to C IV-based virial BH mass estimates 51
3.4.1 Hα/Hβ FWHM comparison 51
3.4.2 Measuring the quasar systemic redshift 55
3.4.3 Balmer/C IV line widths as a function of C IV-blueshift 56
3.4.4 C IV-based virial BH mass estimates 61
3.4.5 C IV-derived BH masses at low C IV blueshift 62
3.5 Practical application of the C IV-based BH mass correction 63
3.5.1 Recipe for unbiased C IV based BH masses 63
3.5.2 Systematic trends in residuals 69
3.5.3 Effectiveness of the C IV blueshift based correction to BH masses 72

3.5.4 Comparison to previous prescriptions 74
3.6 Population trends with C IV blueshift 77
3.7 Frequency of quasars with high accretion rates 81
3.8 Summary 82
3.9 Catalogue of derived properties 83

4 QUASAR-DRIVEN GALAXY-WIDE OUTFLOWS IN IONISED GAS 87
4.1 [O III] as a probe of quasar-driven outflows 87
4.2 Quasar sample 89
4.3 Spectral measurements 89
4.3.1 Transforming spectra to rest-frame wavelengths 90
4.3.2 Removing Fe II emission 90
4.3.3 Modelling Hβ and [O III] 93
4.3.4 Modelling Hα 94
4.3.5 Emission-line parameters 96
4.3.6 Uncertainties on parameters 99
4.3.7 Flagging low EQW [O III] 100
4.3.8 Reliability of systemic redshift estimates 100
4.4 [O III] properties in luminous quasars 102
4.4.1 Strength and kinematics of [O III] 102
4.4.2 Luminosity-dependence of [O III] properties 104
4.4.3 EV1 trends in high-redshift quasars 107
4.4.4 Connections with C IV emission properties 108
4.4.5 A link between BLR and NLR outflows 111
4.4.6 The BAL parent population 113
4.4.7 Extreme [O III] profiles 114
4.5 Mass outflow rate and kinetic power 117
4.6 Mean field independent component analysis 119
4.6.1 Generating MFICA components 120
4.6.2 MFICA reconstruction of luminous quasar spectra 120
4.6.3 Interpretation of MFICA components 121

4.6.4 MFICA component weight distributions 123
4.7 Summary 126

5 OUTFLOWS AND HOT DUST EMISSION 129
5.1 Introduction 129
5.2 Data 130
5.2.1 SDSS 130
5.2.2 UKIDSS Large Area Survey 130
5.2.3 WISE All-WISE Survey 131
5.2.4 Computing Vega-AB magnitude offsets 131
5.2.5 Galactic extinction correction 132
5.2.6 Cross-matching SDSS to UKIDSS and WISE 133
5.2.7 Quasar sample 133
5.3 Constructing an AGN SED model 133
5.3.1 Accretion disc 135
5.3.2 Balmer continuum 135
5.3.3 Hot dust 136
5.3.4 Emission-lines 136
5.3.5 Dust extinction 137
5.4 A parametric SED template for the quasar population 138
5.4.1 Fitting procedure 138
5.4.2 Quality of fit 139
5.5 Diversity of hot dust properties 141
5.5.1 Defining a sample with uniform UV/optical properties 142
5.5.2 Fitting procedure 144
5.5.3 Distribution of hot dust parameters 145
5.5.4 Relationship between hot dust and BLR outflows 145
5.5.5 Correlations with fundamental quasar properties 147
5.6 Summary 149

6 SUMMARY AND FUTURE PROSPECTS 151
6.1 Correcting C IV-Based Virial Black Hole Masses 151
6.2 Quasar-driven galaxy-wide outflows in ionised gas 152
6.3 Outflows and hot dust emission 152
6.4 Future prospects 152

6.4.1 Further improvements to BH mass estimates 152
6.4.2 Studying feedback with IFU spectroscopy 154

BIBLIOGRAPHY 157

LIST OF FIGURES

1.1 Cartoon picture of the inner regions on an AGN. 3
1.2 Median radio-loud AGN SED. 12
2.1 The redshift and luminosity distribution of quasar sample. 24
2.2 Demonstration of absolute flux calibration of near-infrared spectra. 29
3.1 Composite spectra of the C IV emission-line as a function of C IV blueshift. 35
3.2 Demonstration of the effectiveness of C IV line parameter estimation scheme. 40
3.3 Demonstration of the effectiveness of Hα line parameter estimation scheme. 42
3.4 Demonstration of the effectiveness of Hβ line parameter estimation scheme. 43
3.5 Model fits to Hα, Hβ, and C IV emission in four quasars. 44
3.6 The redshift and luminosity distributions of the spectra removed from sample. 46
3.7 FWHM, dispersion and shape of C IV as a function of the C IV blueshift. 49
3.8 Comparison of the C IV line profiles of J123611+112922 and J152529+292813. 51
3.9 The Hα and Hβ emission-line regions in the median composite spectrum. 52
3.10 Comparison of Hα and Hβ FWHM measurements for 99 quasars. 53
3.11 Projections of the MCMC sampling of the posterior distribution from the fit to FWHM(Hα) and FWHM(Hβ). 54

3.12 C IV FWHM relative to Hα FWHM and C IV based BH mass compared to Hα based mass, both as a function of the C IV blueshift. 57
3.13 C IV FWHM relative to Hβ FWHM and C IV based BH mass compared to Hβ based mass, both as a function of the C IV blueshift. 58
3.14 Projections of the MCMC sample of the posterior distribution for a linear fit to FWHM(C IV)/FWHM(Hα) as a function of the C IV blueshift. 59
3.15 The distribution of the orthogonal displacement of each data point from the best-fitting linear relationship in the fit to FWHM(C IV)/FWHM(Hα) as a function of the C IV blueshift. 61
3.16 Rest-frame EQW versus blueshift of the broad C IV emission-line for SDSS quasars using three different redshift estimation schemes. 65
3.17 Composite spectra from Lyα to C III] for quasars with different C IV blueshifts. 66
3.18 Same as Figure 3.12a, with the marker colour representing the Hα FWHM. 70
3.19 Rest-frame EQW versus blueshift of the broad C IV emission-line for our sample and for SDSS quasars. 71
3.20 Comparison of the C IV- and Hα-based BH masses before and after applying the C IV blueshift-based correction to the C IV FWHM. 73
3.21 Comparison of the C IV and Hα line dispersion 74
3.22 Comparison of BH mass estimates derived from C IV and Hα as a function of the C IV blueshift, using various corrections to the C IV-based masses proposed in the literature. 75

3.23 Comparison of corrected C IV-based BH masses and Hα-based masses as a function of the C IV blueshift. 76
3.24 The FWHM, dispersion and shape of Hα as a function of the C IV blueshift. 78
3.25 Hα-derived Eddington ratio versus C IV blueshift. 79
4.1 Spectra of the 24 objects for which significant Fe II emission is still present following our Fe II-subtraction procedure. 91
4.2 Example model fits to the Hβ/[O III] emission in eight quasars. 95
4.3 Non-parametric measures of the [O III] velocity-profile. 97
4.4 Uncertainty in v_{10} as a function of the EQW. 100
4.5 Comparison of systemic redshift estimates using [O III], Hβ and Hα. 101
4.6 Probability density distributions of the [O III] parameters EQW, w_{80} and asymmetry A. 103
4.7 The [O III] EQW as a function of the quasar bolometric luminosity. 105
4.8 [O III] velocity-width w_{80} as a function of quasar bolometric luminosity. 106
4.9 The distribution of objects in the EV1 parameter space. 107
4.10 Parameter space of C IV blueshift and EQW. 109
4.11 [O III] EQW as a function of the C IV blueshift. 110
4.12 Relationship between the C IV and [O III] blueshifts. 111
4.13 Objects excluded from Figure 4.12. 112
4.14 Comparison of the Hβ/[O III] region for BAL and non-BAL quasars. 114
4.15 Model fits to the Hβ/[O III] emission in 18 quasars with extreme [O III] emission profiles. 115

4.16 Velocity-widths and rest-frame 5 μm luminosities of the 18 quasars in sample with extreme [O III] emission profiles and the four dust-reddened quasars from Zakamska et al. (2016). 117
4.17 MFICA reconstruction of the Hβ/[O III] emission in quasar J002952+020607. 122
4.18 Distributions of each of the MFICA component weights in our sample of luminous quasars and in the $z \lesssim 1$ SDSS sample. 124
4.19 Median MFICA-reconstructed spectra as a function of the C IV blueshift. 125
5.1 Distribution of our sample in the redshift-luminosity plane. 134
5.2 Model quasar spectrum at $z = 1$. 135
5.3 Model quasar spectrum at three different redshifts. 138
5.4 Median colours of quasars and best-fitting SED model as a function of redshift. 140
5.5 Residuals from fitting a single SED model to the colours of $1 < z < 3$ quasars as a function of rest-frame wavelength. 141
5.6 $W1 - W2$ colours of quasars as a function of redshift. 143
5.7 $i - K$ colours of quasars as a function of redshift. 144
5.8 Histograms of the ratio of near-infrared to ultra-violet luminosity and blackbody temperature and the correlation between these two parameters. 146
5.9 Hot dust abundance as a function of rest-frame EQW and blueshift of the C IV line. 147
5.10 Best-fitting near-infrared to ultra-violet luminosity as a function of ultra-violet luminosity, BH mass and Eddington ratio. 148

For Figures 2.1, 3.16, 3.19, 4.8, 4.9, 4.10, 5.1, 5.8 and 5.10, in regions of high point-density, contours show equally-spaced

lines of constant probability density generated using a Gaussian kernel-density estimator.

LIST OF TABLES

2.1 Number of database objects observed with each near-infrared spectrograph/telescope. 16

2.2 Quasars in the near-infrared spectroscopic database. 18

2.3 Percentage of catalogue for which observed-frame optical spectroscopic data is available from the given sources. 25

2.4 Cross-matched surveys and the percentage of successful matches. 27

2.5 Methods used in absolute flux calibration of near-infrared spectra. 28

2.6 Spectral resolutions of the spectrographs used in this thesis. 31

3.1 The numbers of quasars with reliable Hα and Hβ line measurements, and the spectrographs and telescopes used to obtain the near-infrared spectra. 37

3.2 The number of spectra removed from our sample by different quality cuts. 45

3.3 The fractional error on the corrected BH mass as a function of C IV blueshift for different uncertainties in the quasar systemic redshift. 66

3.4 The format of the table containing the emission-line properties from our parametric model fits. 85

4.1 The numbers of quasars with [O III] line measurements and the spectrographs and telescopes used to obtain the near-infrared spectra. 89

4.2 Summary of models used to fit the Hβ emission, and the number of quasars to which each model is applied. 93
4.3 Summary of models used to fit the [O III] emission, and the number of quasars to which each model is applied. 94
4.4 Summary of models used to fit the Hα emission, and the number of quasars to which each model is applied. 96
4.5 The format of the table containing the emission-line properties from our parametric model fits. 98
4.6 Physical interpretation of the MFICA components. 123
5.1 Available photometric data, effective wavelengths of passbands, Vega to AB magnitude offsets and conversions from $E(B-V)$ to passband extinction. 131
5.2 Free parameters in SED model and best-fitting values from fit to the median colours of quasars at redshifts $1 < z < 3$. 139

ACRONYMS

2MASS	Two Micron All Sky Survey
AGN	Active Galactic Nuclei
ARC	Astrophysics Research Consortium
BAL	Broad Absorption Line
BH	Black Hole
BLR	Broad Line Region
BOSS	Baryon Oscillation Spectroscopic Survey
BSS	Blind Source Separation
DR	Data Release
EQW	Equivalent Width
ESO	European Southern Observatory
EV1	Eigenvector 1
FIRE	Folded-port InfraRed Echellette
FWHM	Full-Width at Half-Maximum
GH	Gauss-Hermite
GNIRS	Gemini Near-Infrared Spectrograph
HiBAL	High-ionization Broad Absorption Line
HIRES	High Resolution Echelle Spectrometer
ISAAC	Infrared Spectrometer And Array Camera
LIRIS	Long-slit Intermediate Resolution Infrared Spectrograph
MCMC	Markov Chain Monte Carlo
MFICA	Mean Field Independent Component Analysis
NAL	Narrow Absorption Line
NIRI	Near InfraRed Imager and Spectrometer

NLR	Narrow Line Region
NTT	New Technology Telescope
P200	Palomar 200-inch Hale telescope
PCA	Principal Component Analysis
PI	Principal Investigator
S/N	Signal-to-noise ratio
SDSS	Sloan Digital Sky Survey
SED	Spectral Energy Distribution
SINFONI	SINgle Faint Object Near-IR Investigation
SOFI	Son of ISAAC
UKIDSS	UKIRT Infrared Deep Sky Survey
UKIRT	United Kingdom Infra-Red Telescope
UVES	UV-Visual Echelle Spectrograph
VHS	VISTA Hemisphere Survey
VIKING	VISTA Kilo-Degree Infrared Galaxy Survey
VISTA	Visible and Infrared Survey Telescope for Astronomy
VLT	Very Large Telescope
WHT	William Herschel Telescope
WISE	Wide-field Infrared Explorer

1 INTRODUCTION

1.1 THE DISCOVERY OF QUASARS

In 1963, the powerful radio source 3C 273 was identified as a star-like, thirteenth magnitude object with a strongly red-shifted[1] optical spectrum (Schmidt, 1963). This finding implied 3C 273 was at an enormous distance (at least by the standards of the time). For an object this distant to appear so bright it must be extremely luminous: 10 times more luminous, in fact, than the largest galaxies known. At the same time, its rapid variability meant that it could be no bigger than a light-week across. 3C 273 was therefore a new kind of exotic object, at the edge of the known Universe. Understandably, its discovery caused a lot of excitement, both for astronomers and the wider public. It was quickly realised that 'quasars'[2], and other lower-luminosity classes of active galactic nuclei (AGN)[3], are powered by the release of gravitational potential energy as mass is accreted onto a super-massive[4] black hole (BH) at the centre of a galaxy (e.g. Hoyle and Fowler, 1963; Salpeter, 1964; Lynden-Bell, 1969; Lynden-Bell and Rees, 1971).

1.2 THE AGN-HOST GALAXY CONNECTION

Beginning in the early 1990s, inactive super-massive BHs were found in the centres of many nearby massive galaxies (e.g. Kormendy and Richstone, 1995; Ferrarese and Ford, 2005; Kormendy and Ho, 2013). This proved that, rather than being rare and exceptional objects, quasar activity was in fact a stage in the life of all massive galaxies (e.g. Lynden-Bell, 1969). Shortly after, it was discovered that the BH mass was tightly correlated with properties of the host-galaxy bulge (e.g. the stellar veloc-

1 Redshift $z = c(\Delta\lambda/\lambda) = 0.158$, where c is the speed of light.

2 The term 'quasar' originated as a contraction of 'quasi-stellar radio source', although 90 per cent of quasars are now known to be radio-quiet.

3 Throughout this thesis we use the terms 'quasar' and 'Active Galactic Nucleus (AGN)' interchangeably to describe active super-massive black holes, although the term quasar is generally reserved for the luminous ($L_{Bol} > 10^{12}\,L_\odot$) subset of AGN.

4 Super-massive: $10^{6-9}\,M_\odot$.

ity dispersion, σ, which is proportional to the bulge mass; e.g. Magorrian et al., 1998; Ferrarese and Merritt, 2000; Gebhardt et al., 2000; Graham et al., 2001; Tremaine et al., 2002; Marconi and Hunt, 2003; Aller and Richstone, 2007; Gültekin et al., 2009). This was an unexpected finding, given that the sphere-of-influence[5] of a BH ($\lesssim$ 100 parsecs; e.g. Kormendy and Ho, 2013), is many orders of magnitude smaller than the dimensions of a typical galactic bulge. The tight correlation between their masses suggested that the BH and the host-galaxy bulge grow synchronously. Both the density of quasars and the cosmic star formation history evolve strongly with redshift and peak at $2 \lesssim z \lesssim 3$ (e.g. Boyle and Terlevich, 1998; Brandt and Hasinger, 2005; Richards et al., 2006b). The similarity of their cosmic evolution was taken as further evidence for the existence of an intimate connection between quasars and their host galaxies.

In a currently favoured model, rapid BH fuelling and star-formation are triggered by a gas-rich galaxy merger (e.g. Hopkins et al., 2006), satellite accretion or secular processes (e.g. Fanidakis et al., 2012). The energetic output of the rapidly-accreting BH couples with the gas in the host-galaxy and regulates star formation and the growth of the BH itself (e.g. Silk and Rees, 1998; King, 2003; Di Matteo, Springel, and Hernquist, 2005; King and Pounds, 2015). This process, which is referred to as 'quasar feedback', is also commonly invoked to reproduce the high-mass end of the galaxy luminosity function in cosmological simulations (e.g. Kauffmann and Haehnelt, 2000). The insight that quasars may play a crucial role in the evolution of galaxies has led to an explosion of interest in their properties in recent years.

1.3 AGN: THE CURRENT PARADIGM

The basic features of the current AGN paradigm are widely accepted, although many of the details are unknown. The basic features are: a hot accretion disc surrounding a super-massive BH, rapidly orbiting clouds of ionised gas, and a dusty, obscuring structure (generally referred to as the 'torus'). Collimated jets of relativistic plasma and/or associated lobes are also seen in the 10 per cent of quasars that are radio-loud (e.g. Peterson,

5 Sphere-of-influence: where the gravity of the BH dominates over the other mass components.

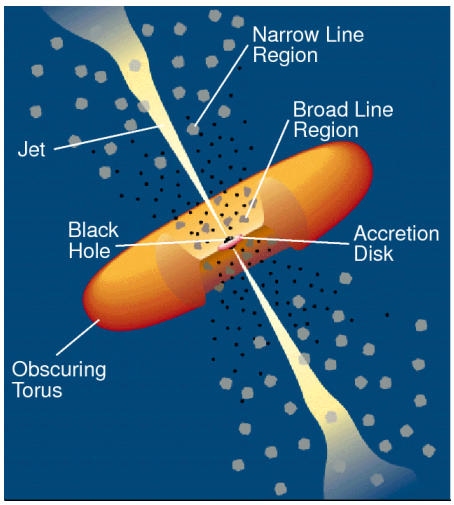

Figure 1.1: Cartoon picture of the inner regions on an AGN. Credit: Urry and Padovani (1995).

1997). A cartoon picture illustrating the basic structure of an AGN is shown in Figure 1.1.

1.3.1 *Accretion disc*

Material is pulled towards a super-massive BH and sheds angular momentum through viscous and turbulent processes in a hot accretion disc (e.g. Begelman, 1985). The basic physics of accretion discs is described by Pringle (1981). For an optically thick steady thin disc the temperature T depends on the radius R within the disc, and behaves as

$$T = \left\{ \frac{3GM\dot{M}}{8\pi R^3 \sigma} \left[1 - (R_*/R)^{\frac{1}{2}} \right] \right\}^{\frac{1}{4}} \tag{1.1}$$

where σ is the Stefan-Boltzmann constant, M the mass of the BH, $\dot{M}$ the accretion rate and R_* the inner radius of the disc. This results in a spectral energy distribution (SED) which is exponential at high frequencies ν, Rayleigh-Jeans at low frequencies, and is proportional to $\nu^{\frac{1}{3}}$ in between. The inner radius of the accretion disc is usually taken as that of the innermost stable orbit, i.e. three times the Schwarzschild radius, so the energy radiated is $\sim \frac{1}{12}\dot{M}c^2$. In quasars, accretion discs reach temperatures of $\sim 10^6$ K and radiate primarily at ultra-violet to soft X-ray wavelengths.

The Eddington luminosity (L_{Edd}) is the luminosity for which the outward force due to radiation pressure on electrons balances the inward gravitational force, so

$$\frac{L_{Edd}\sigma_T}{4\pi R^2 c} = \frac{G m_p M_{BH}}{R^2} \tag{1.2}$$

where σ_T is the Thompson cross-section and m_p is the proton mass. Rearranging the above equation, we find

$$L_{Edd} = \frac{4\pi G M_{BH} m_p c}{\sigma_T} \tag{1.3}$$

$$\simeq 3.2 \times 10^4 \left(\frac{M_{BH}}{M_\odot}\right) L_\odot. \tag{1.4}$$

Because radiation pressure drives a net outflow of material at higher luminosities, the Eddington luminosity is the maximum luminosity an AGN can reach (assuming spherical accretion and neglecting other radiation processes such as bound-free and free-free interactions). The Eddington ratio, λ_{Edd}, relates the AGN bolometric luminosity, L_{Bol}, to the Eddington luminosity:

$$\lambda_{Edd} = \frac{L_{Bol}}{L_{Edd}}. \tag{1.5}$$

Thus, for a quasar accreting at its Eddington limit, $\lambda_{Edd} = 1$.

1.3.2 *Broad line region*

One of the pre-eminent features of many AGN spectra are broad optical and ultra-violet emission-lines produced in the broad line region (BLR). The BLR, which is between several light-days and several light-months from the central BH, is photo-ionised by the ultra-violet continuum emission emanating from the accretion disc.

The overall geometry of the BLR is as shown in Figure 1.1. It is generally thought to consist of individual clouds, although direct evidence for this is not strong. If BLR were completely uniform then one might expect, e.g., C IV absorption to be a ubiquitous spectral feature. The absence of this absorption in the majority of objects points to a more clumpy structure for the BLR.

The very broad velocity-widths of emission lines produced in the BLR are assumed to be Doppler-broadened, and imply line-of-sight velocities of many thousands of $\mathrm{km\,s^{-1}}$. The line widths are much too great to be explained by thermal broadening, and so bulk motion must be involved. Because of the close proximity to the central super-massive BH, bulk motions are likely dominated by gravity and radiation pressure from the accretion disc.

It has long been known that redshifts derived from different broad emission lines can differ by significantly more than typical measurement errors (e.g. Gaskell, 1982). Higher ionisation lines (including C IV) are often found to be blueshifted relative to lower-ionisation lines (including Mg II and Hβ), which are approximately at the AGN systemic redshift. This suggests that the structure of the BLR is stratified, with higher-ionisation lines emitted in regions of the BLR where an outflow component is significant.

1.3.3 *Dusty torus*

Further out from the central engine on parsec-scales are dusty, molecular clouds which are co-planar with the accretion disc. These dusty clouds are generally referred to as the 'torus'. The torus is a central feature of orientation-based unification schemes (e.g. Antonucci, 1993) in which different observational properties are explained as the effect of observing anisotropic objects in different orientations. In a Type II AGN, the system is observed in an edge-on configuration and, as a result, emission from the accretion disc and BLR is obscured by the dusty torus. The orientation of a Type I AGN is such that the observer has direct sight-lines to the accretion disc and BLR. Although this simple picture (shown in Figure 1.1 as well as in countless other publications) is a useful starting point, the idea of a torus as a static, doughnut-like structure is almost certainly a gross over-simplification. For example, the problem of maintaining the large scale height required to explain the observed fraction of Type I/II AGN has long been recognized (e.g. Krolik and Begelman, 1988). In one set of more realistic models, the torus is a dusty wind blown from the outer edge of the accretion disc (e.g. Konigl and Kartje, 1994; Everett, Gallagher, and Keating, 2009; Gallagher et al., 2012; Everett, 2005; Keating et al., 2012; Elitzur and Shlosman, 2006).

1.3.4 *Narrow line region*

At even greater distances from the central BH is the spatially-extended narrow emission-line region (NLR). Like the BLR, the NLR is ionised by radiation from the accretion disc. Unlike the BLR, densities in the NLR are low enough that forbidden transitions are not collisionally suppressed. Because of its high equivalent width (EQW), [O III]λ5008 is the most studied of the narrow quasar emission-lines. Emission-line widths are typically hundreds of $\mathrm{km\,s^{-1}}$ in the NLR. The size of the NLR grows with the AGN luminosity, and can reach kilo-parsec scales in luminous quasars (e.g. Hainline et al., 2013).

1.4 LARGE SURVEYS AND THE SYSTEMATIC STUDY OF AGN PROPERTIES

The Palomar-Green bright quasar survey (Schmidt and Green, 1983), the first large-area quasar survey, identified 114 quasars via their ultra-violet excess relative to stars. Boroson and Green (1992) were among the first to use the Palomar-Green quasar sample to analyse quasar spectroscopic properties in a systematic way. In their landmark study, they used a principal component analysis (PCA) to identify the features responsible for the largest variance in quasar spectra. The first eigenvector of their PCA decomposition – generally referred to as 'eigenvector 1' (EV1) – is correlated with the full-width at half-maximum (FWHM) of the broad Hβ emission-line and the relative strengths of optical Fe II and Hβ. The underlying driver behind EV1 is thought to be the Eddington ratio.

With the advent of CCD[6] technology came a new generation of optical spectroscopic surveys, most notably the Sloan Digital Sky Survey (SDSS; York et al., 2000) and the 2QZ survey (Croom et al., 2004). SDSS, and the next-generation SDSS-III: Baryon Oscillation Spectroscopic Survey (BOSS; Dawson et al., 2013), now contain spectra of ~ 400 000 AGN and quasars. These large, uniform data sets have revolutionised the study of AGN and quasars by facilitating statistical studies of their properties covering wide ranges in redshift and luminosity.

Emission-lines provide a wealth of information about the properties of AGN and their environments. The rest-frame optical region in particular includes a number of strong emission

6 CCD: Charge coupled device.

features, including the Balmer lines and the [O III] doublet that are used to measure BH masses, accretion rates, systemic redshifts and outflow properties. However, at $z \sim 2$, rest-frame optical lines are redshifted to near-infrared wavelengths. Near-infrared spectroscopy is therefore essential for a complete understanding of quasars during the peak epoch of galaxy formation. However, spectroscopic observations are challenging at infrared wavelengths. As a result, the number of high-redshift quasars with near-infrared spectra is limited and previous investigations of the rest-frame optical spectra of quasars at redshifts $z \sim 2$ have typically used samples containing just a few dozen objects (e.g. Netzer et al., 2004; Marziani et al., 2009; Shen and Liu, 2012; Shen, 2016).

1.5 MEASURING BLACK HOLE MASSES

The BH mass is one of the most important physical parameters of a quasar and considerable resources have been devoted to measuring the masses of BHs in active galaxies. Large-scale studies of AGN and quasar demographics have become possible through the calibration of single-epoch virial-mass estimators using results from reverberation-mapping campaigns (e.g. Peterson, 2010; Vestergaard et al., 2011; Marziani and Sulentic, 2012; Shen, 2013).

1.5.1 *Reverberation mapping*

Under the assumptions that the BLR dynamics are virialised[7] and the gravitational potential is dominated by the BH, the BH mass is given by:

$$M_{BH} \simeq \frac{V_{Virial}^2 R_{BLR}}{G} \tag{1.6}$$

where V_{virial} is the virial velocity in the BLR and R_{BLR} the characteristic BLR radius. The problem of measuring the mass therefore reduces to the problem of measuring the velocity and orbital radius of the line-emitting clouds in the BLR.

Continuum variability is a common characteristic of quasars, owing to the stochastic nature of the accretion process. Because

7 The virial theorem states that the average kinetic energy of a system is equal to half of the average negative potential energy.

the BLR is photo-ionized by the continuum, the broad emission-lines also vary with some characteristic lag, which is related to the light travel time across the BLR. The reverberation mapping method, first proposed by Blandford and McKee (1982), uses the time lag between variations in the continuum emission and correlated variations in the broad line emission to measure the typical size of the BLR (e.g. Peterson, 1993; Netzer and Peterson, 1997; Peterson, 2014).

The typical velocity in the BLR is measured from the Doppler-broadened width of an emission-line produced in the BLR. Since the structure and geometry of the BLR is unknown, a virial coefficient, f, is introduced to transform the observed line-of-sight velocity inferred from the line width into a virial velocity. Unfortunately, f is unknown and likely varies from object to object. In practice, the value of f is empirically determined by requiring that the reverberation-mapping masses are consistent with those predicted from the M_{BH}-σ relation for local inactive galaxies.

Because reverberation mapping depends on temporal resolution rather than spatial resolution, this technique can be applied out to much greater distances than direct dynamical modelling (e.g. Kormendy and Ho, 2013). However, because reverberation mapping relies on dense spectrophotometric monitoring campaigns which span many years, the number of AGN with measured lags is limited to ~ 50 AGN (e.g. Kaspi et al., 2000; Peterson et al., 2004; Kaspi et al., 2007; Bentz et al., 2009; Denney et al., 2010; Barth et al., 2011; Grier et al., 2012). This sample is strongly biased to low luminosity Seyfert 1 galaxies[8], and the maximum redshift is just $z \sim 0.3$. Comprehensive statistical studies of active BHs, particularly during the epoch of peak galaxy formation ($z \gtrsim 2$), therefore require a different approach to measuring BH masses.

1.5.2 *Single-epoch virial estimates*

Reverberation mapping campaigns have also revealed a tight relationship between the radius of the BLR and the quasar optical (or ultra-violet) luminosity (the $R_{BLR} - L$ relation; e.g. Kaspi et al., 2000; Kaspi et al., 2007). This relation provides a much less expensive method of measuring the BLR radius, and large-scale studies of AGN and quasar demographics (e.g. Greene and Ho,

8 Seyfert 1: A low-luminosity ($L_{Bol} < 10^{12} L_{\odot}$) class of AGN with broad emission-lines and clearly detectable host-galaxies.

2005b; Vestergaard and Peterson, 2006; Vestergaard and Osmer, 2009; Shen et al., 2011; Shen and Liu, 2012; Trakhtenbrot and Netzer, 2012) have thus become possible through the calibration of single-epoch virial-mass estimators using the reverberation-mapping measurements (e.g. Vestergaard, 2002; McLure and Jarvis, 2002; Vestergaard and Peterson, 2006; McGill et al., 2008; Wang et al., 2009; Rafiee and Hall, 2011; Park et al., 2013).

With single-epoch virial masses, the growth rate of massive BHs can be measured across cosmic time. This conveys important information about the accretion processes occurring in active BHs (e.g. Kollmeier et al., 2006) and is crucial in order to understand the processes responsible for establishing the M_{BH}-σ relation (e.g. Bennert et al., 2011). Single-epoch virial estimates have been used to calculate BH masses in the highest redshift quasars (e.g. a $10^9\,M_\odot$ BH in a redshift $z = 7.1$ quasar; Mortlock et al., 2011). Recent claims of a BH with mass $10^{10}\,M_\odot$ in a redshift $z = 6.3$ quasar (when the Universe is less than 1 Gyr old; Wu et al., 2015) challenges our understanding of the accretion histories of supermassive BHs (e.g. Willott, McLure, and Jarvis, 2003).

The uncertainties in reverberation mapped BH masses are estimated to be ~ 0.4 dex (e.g. Peterson, 2010), and the uncertainties in virial masses are similar (e.g. Vestergaard and Peterson, 2006). However, the main concern and biggest unknown is the extension of the method to high redshifts. This requires that the relations calibrated for sub-Eddington BHs with $M_{BH} \sim 10^7\,M_\odot$ are valid for BHs with masses up to $10^{10}\,M_\odot$ that are radiating near the Eddington luminosity. Furthermore, the vast majority of reverberation mapping measurements are for Hβ and so the $R_{BLR} - L$ relation that underpins the virial method has only been established using this line. Hβ is redshifted beyond the reach of optical spectrographs at redshifts $z \gtrsim 0.7$, and extending the method to higher redshifts requires the secondary-calibration of other low-ionization emission-lines such as Hα and Mg II (e.g. Vestergaard, 2002; McLure and Jarvis, 2002; Wu et al., 2004; Kollmeier et al., 2006; Onken and Kollmeier, 2008; Wang et al., 2009; Rafiee and Hall, 2011).

At redshifts of $z \gtrsim 2$ the low-ionization hydrogen and Mg II emission-lines are no longer present in the optical spectra of quasars and it is necessary to employ an emission-line in the rest-frame ultra-violet. The strong C IV emission doublet is visible in the optical spectra of quasars to redshifts of $z \sim 5$ and

C IV-derived BH masses have become the standard (e.g. Vestergaard and Peterson, 2006; Park et al., 2013). However, C IV has long been known to exhibit significant displacements to the blue and these 'blueshifts' almost certainly signal the presence of strong outflows. As a consequence, single-epoch virial BH mass estimates derived from C IV velocity-widths are known to be systematically biased compared to masses from the hydrogen Balmer lines (e.g. Baskin and Laor, 2005a; Trakhtenbrot and Netzer, 2012; Shen and Liu, 2012).

1.6 WINDS AND OUTFLOWS IN AGN

Quasars are very powerful sources of radiation, and are embedded in matter-rich environments at the centres of galaxies. Strong winds, driven by some combination of gas pressure, radiation pressure, and magnetic forces, are to be expected under these conditions (e.g. Blandford and Payne, 1982; Proga, Stone, and Kallman, 2000; Everett, 2005). Radiation pressure can act through continuum absorption by neutral hydrogen and by dust, as with electron scattering. In both cases the cross-sections are considerably larger than the Thompson cross-section, and the effectiveness then depends on how much neutral Hydrogen or dust is present. There is evidence that line absorption also plays a role (e.g. Bowler et al., 2014). In line with expectations, evidence for outflowing gas is common in the spectra of quasars.

Perhaps the most dramatic evidence for outflows is seen in broad absorption-line quasars (BAL quasars; Weymann et al., 1991). BAL quasars are characterised by broad absorption features in the ultra-violet resonance lines of highly ionised N V, C IV and Si IV. The absorption troughs are thousands of $\mathrm{km\,s^{-1}}$ wide and significantly blueshifted relative to the quasar rest-frame[9]. The absorption is thought to occur in outflows reaching $60\,000\,\mathrm{km\,s^{-1}}$ (e.g. Turnshek, 1988). The near-universal blueshifting of the observed absorption features can be understood if the far-side of the outflow is obscured by the accretion disc, and so only the near-side, which is moving towards the observer, is detected. The observed C IV BAL fraction in radio-quiet quasars is ~ 15 per cent (e.g. Hewett and Foltz, 2003; Reichard et al., 2003). Outflows can also explain narrow ultra-violet and X-ray absorption-lines (NALs) which are seen

9 Much rarer cases of redshifted BAL troughs do also exist (e.g. Hall et al., 2013).

in ~ 60 per cent of Seyfert 1 galaxies (Crenshaw et al., 1999) and some quasars (e.g. Hamann et al., 1997). The blueshifting of high-ionisation lines in the BLR (including C IV) can also be understood if the lines are produced in outflowing clouds (although see, e.g., Gaskell and Goosmann 2016, for an alternative explanation). The blueshifting of C IV appears to be nearly ubiquitous in the quasar population (e.g. Richards et al., 2002; Richards et al., 2011).

Together, these results suggest that outflows are very common and the energy released by quasars can have a dramatic effect on their immediate surroundings. Accretion-disc wind models have been developed to explain the wide range of emission and absorption-line phenomena which are observed (e.g. Murray et al., 1995; Elvis, 2000; Proga, Stone, and Kallman, 2000; Everett, 2005).

In models for the co-evolution of quasars and galaxies, the energy released by quasars impacts galaxies on much larger scales than is probed by the emission and absorption diagnostics described above. In recent years, a huge amount of resources have been devoted to searching for observational evidence of galaxy-wide, quasar-driven outflows (for recent reviews, see Alexander and Hickox, 2012; Fabian, 2012; Heckman and Best, 2014). This has resulted in recent detections of outflows in AGN host-galaxies using tracers of atomic, molecular, and ionised gas with enough power to sweep their host-galaxies clear of gas (e.g. Nesvadba et al., 2006; Arav et al., 2008; Nesvadba et al., 2008; Moe et al., 2009; Dunn et al., 2010; Alexander et al., 2010; Harrison et al., 2012; Harrison et al., 2014; Nesvadba et al., 2010; Rupke and Veilleux, 2013; Veilleux et al., 2013; Nardini et al., 2015; Feruglio et al., 2010; Alatalo et al., 2011; Cimatti et al., 2013; Cicone et al., 2014).

The advent of large optical spectroscopic surveys (e.g. SDSS) has facilitated studies of the NLR in tens of thousands of AGN at redshifts $z \lesssim 0.4$ which has provided constraints on the prevalence and drivers of ionised outflows (e.g. Mullaney et al., 2013; Zakamska and Greene, 2014). Because of its high EQW, [O III] is the most studied of the narrow AGN emission-lines. By following [O III] to near-infrared wavelengths, these investigations can be extend to quasars at redshifts $z \gtrsim 2$, when cosmic star formation and BH accretion both peaked. It is likely that correlations between BHs and their host galaxies (e.g. the M_{BH}-σ relation) were established during this epoch, since mas-

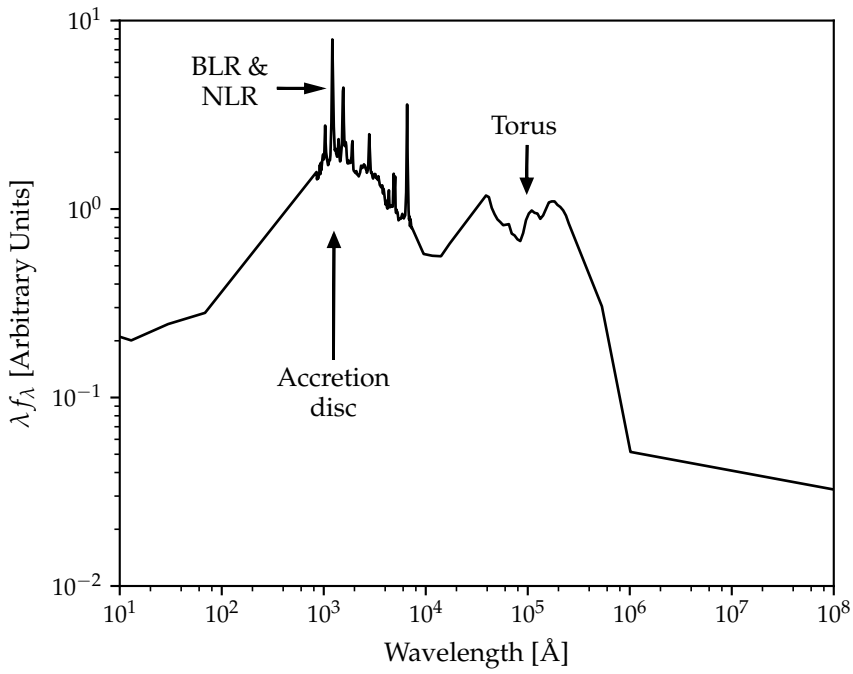

Figure 1.2: Median radio-loud AGN SED from Shang et al. (2011).

sive galaxies and BHs grew most of their mass at this time. Therefore, this is the key epoch for studies of quasar feedback.

1.7 AGN SEDS

AGN emit strongly over many decades of the electromagnetic spectrum (Figure 1.2). Different physical processes dominate AGN SEDs at different frequencies. Hard X-ray emission is dominated by Compton up-scattering of accretion disk photons by electrons in a hot corona (e.g. Sunyaev and Titarchuk, 1980), ultra-violet/optical by thermal accretion disc emission, IR by dust at a wide range of temperatures, and radio by synchrotron emission in relativistic jets. A complete understanding of AGN properties therefore critically depends on the availability of multi-wavelength data that spans the full SED. Progress has been made in recent years using data from new sensitive, wide-field photometric surveys (e.g. Roseboom et al., 2013). These surveys include the ultra-violet/optical SDSS, the near-infrared UKIRT Infrared Deep Sky Survey (UKIDSS; Lawrence et al., 2007) and the mid-infrared Wide-field Infrared Explorer (WISE; Wright et al., 2010).

To first order, AGN have remarkably similar SEDs that show very little dependence on luminosity, redshift, BH mass or accretion rate (e.g. Elvis et al., 2012; Hao et al., 2013). On the other hand, the SED properties of individual quasars do show significant variation. Relating variations in SED properties to underlying physical processes is a key aim for AGN-related science.

1.8 THESIS STRUCTURE

The structure of this thesis is as follows.

In Chapter 2, we describe the construction of a near-infrared spectroscopic catalogue containing 434 high-luminosity ($L_{Bol} = 10^{45.5} - 10^{48.5}$ erg s^{-1}), redshift $1.5 < z < 4.0$ quasars. This is the largest sample of its kind, and has facilitated the investigations of quasar BH masses and outflow properties which are described in Chapters 3 and 4.

In Chapter 3, we use a sample of 230 quasars with both C IV and Balmer line spectra to quantify the bias in C IV BH masses as a function of the C IV blueshift. Using the monotonically increasing relationship between the C IV blueshift and the mass ratio BH(C IV)/BH(Hα), we derive an empirical correction to all C IV-based BH masses.

In Chapter 4, we analyse the [O III] emission properties in a sample of 354 quasars. Broad velocity-widths and asymmetric structure in [O III] imply galaxy-wide, high-velocity outflows are common in these objects. We study the effect BLR outflows (traced by C IV) have on gas extended over kilo-parsec scales (traced by [O III]) in the quasar host galaxies.

In Chapter 5, we build a simple parametric SED model that is able to reproduce the median optical to infrared colours of tens of thousands of SDSS AGN at redshifts $1 < z < 3$. We use this model to study the relationship between the hot dust emission that dominates the near-infrared SED and outflows in the quasar BLR.

Throughout this thesis, we adopt a ΛCDM cosmology with $h_0 = 0.71$, $\Omega_M = 0.27$, and $\Omega_\Lambda = 0.73$. All wavelengths and EQW measurements are given in the quasar rest-frame, and all emission-line wavelengths are given as measured in vacuum. Unless otherwise stated, optical (i.e. SDSS) magnitudes are given in the AB system and infrared magnitudes in the Vega system, following the conventions of the original surveys.

2

A NEAR-INFRARED SPECTROSCOPIC DATABASE OF HIGH-REDSHIFT QUASARS

2.1 SPECTROSCOPIC SURVEYS

Emission-lines provide a wealth of information about the properties of AGN and their environments. They provide diagnostics of dynamics, temperatures, densities, dust content, elemental abundances and the shape of the ionising spectrum which are often unattainable through any other technique. The rest-frame optical region includes a number of strong emission features, including the broad Balmer lines Hα (6565 Å) and Hβ (4863 Å) and the narrow [O III]$\lambda\lambda$4960,5008 doublet. As we will see in Chapter 3, the Balmer lines are routinely used to derive BH masses and AGN accretion rates. As the strongest narrow emission-line in the rest-frame optical spectrum, [O III] is used to measure systemic redshifts, and to probe AGN-driven outflows in the NLR (see Chapter 4).

Large optical surveys have provided spectra for hundreds of thousands of AGN and quasars. With it's twelfth data release in 2016, the number of AGN and quasars in the SDSS spectroscopic catalogue alone reached almost 400 000. However, the rest-frame optical region is redshifted beyond the reach of optical spectrographs at redshifts $z \gtrsim 0.4$. Accessing the rest-frame optical lines at redshifts $2 \lesssim z \lesssim 4$, during the peak epoch of galaxy evolution, requires near-infrared spectroscopy.

Spectroscopic observations are more challenging at near-infrared wavelengths than in the optical because the Earth's atmosphere is both bright and highly variable at infrared wavelengths. As a result, the number of high-redshift quasars with near-infrared spectra is limited and previous investigations of the rest-frame optical spectra of quasars at redshifts $z \sim 2$ have typically used samples containing a few dozen objects (e.g. Marziani et al., 2009; Shen and Liu, 2012; Shen, 2016).

In this chapter, we will describe the construction of a database containing 434 high-redshift quasars with near-infrared spectra. In later chapters, we will describe how this data has been used to significantly reduce large systematic biases afflicting BH mass estimates for quasars at redshifts $z \gtrsim 2$

Instrument	Number
FIRE/Magellan	36
GNIRS/Gemini	29
ISAAC/VLT	13
LIRIS/WHT	21
NIRI/Gemini	31
NIRSPEC/Keck	3
SINFONI/VLT	84
SofI/NTT	111
TRIPLESPEC/ARC	38
TRIPLESPEC/Hale	60
XSHOOTER/VLT	36
Total	462

Table 2.1: Number of database objects observed with each near-infrared spectrograph/telescope.

(Chapter 3) and to study the prevalence and drivers of quasar-driven galaxy-wide outflows (Chapter 4). The unprecedented size and quality of this dataset make a number of other investigations possible, some of which are described in Chapter 6.

2.2 NEAR-INFRARED SPECTROSCOPIC DATA

The near-infrared spectra in our database are taken from published catalogues, by downloading and reducing archival spectra, and by reducing previously un-published spectra acquired in programmes led by Prof. J. Hennawi (UCSB) and Prof. X. Prochaska (UCO/LICK). We undertook two further observing programmes (Principal Investigator (PI): L. Coatman) to increase the number of objects in under-sampled regions of the C IV EQW and blueshift parameter space (see Section 3.1 for a detailed discussion of C IV emission properties in high-redshift quasars). The telescopes and instruments used to observe the spectra are summarised in Table 2.1 and information on individual spectra is provided in Table 2.2. There are 434 unique quasars in our catalogue. Multiple spectra exists for a number of quasars, and the total number of spectra in our catalogue is 462. The columns in Table 2.2 are as follows:

1 ID: Jhhmmss+ddmmss. ID is repeated when multiple spectra exist for the same object.

2 Unique catalogue name.

3 Date spectrum acquired.

4-5 RA and DEC (J2000; truncated coordinates).

6 Instrument and telescope used to acquire spectrum.

7 Wavelength range covered by spectrum.

8 Velocity per pixel in spectrum.

9 Signal-to-noise ratio (S/N) per pixel in spectrum.

10 Redshift.

Table 2.2: Quasars in the near-infrared spectroscopic database. Only the first 15 entries are shown. The full table (including 462 objects) is available online at http://dx.doi.org/10.5281/zenodo.557069.

ID	Cat. Name	Date	Ra	Dec	Instr.	$\Delta\lambda$ [μm]	Δv [km s^{-1}]	S/N	z
(1)	(2)	(3)	(4)	(5)	(6)	(7)	(8)	(9)	(10)
J000039-001804	QSO460	2015-09-02	+00h00m39.00s	-00d18m03.90s	SofI/NTT	1.50-2.54	154.0	4.9	2.14
J000345-232353	QSO552	2009-07-07	+00h03m45.00s	-23d23m53.40s	SINFONI/VLT	1.44-1.87	36.0	12.7	2.27
J000345-232353	QSO330	2011-09-18	+00h03m45.00s	-23d23m53.40s	SofI/NTT	1.48-1.83	63.0	36.0	2.26
J000451-084450	QSO290	2013-07-12	+00h04m50.66s	-08d44m49.63s	XSHOOTER/VLT	0.31-2.28	15.0	10.3	3.00
J000451-084452	QSO289	2013-08-08	+00h04m50.91s	-08d44m51.98s	XSHOOTER/VLT	0.31-2.28	15.0	5.4	3.00
J000500-003348	QSO454	2015-09-01	+00h05m00.42s	-00d33m48.20s	SofI/NTT	1.50-2.54	154.0	8.2	2.18
J000501+010221	QSO459	2015-09-02	+00h05m00.53s	+01d02m20.80s	SofI/NTT	1.50-2.54	154.0	6.8	2.13
J001016+001228	QSO475	2015-09-04	+00h10m16.49s	+00d12m27.60s	SofI/NTT	1.50-2.54	154.0	8.9	2.28
J001247+001239	QSO082	2013-06-06	+00h12m47.12s	+00d12m39.49s	ISAAC/VLT	1.52-1.60	15.0	19.1	2.16
J001708+813508	QSO107	2012-08-04	+00h17m08.48s	+81d35m08.10s	TRIPLESPEC/Hale	0.94-2.80	39.0	36.5	3.40
J001919+010152	QSO476	2015-09-04	+00h19m19.31s	+01d01m52.20s	SofI/NTT	1.50-2.54	154.0	6.5	2.32
J001955-091316	QSO001	2004-11-26	+00h19m54.67s	-09d13m16.45s	GNIRS/Gemini	0.60-2.61	88.0	9.9	2.12
J002018-233654	QSO553	2009-07-07	+00h20m18.41s	-23d36m53.80s	SINFONI/VLT	1.44-1.87	36.0	16.9	2.30
J002023-414639	QSO554	2009-07-08	+00h20m23.38s	-41d46m38.90s	SINFONI/VLT	1.09-1.41	35.0	33.4	1.57
J002111-242247	QSO555	2009-07-16	+00h21m10.90s	-24d22m47.20s	SINFONI/VLT	1.44-1.86	36.0	11.1	2.26

2.2.1 *Coatman et al. (2016) sample*

2.2.1.1 *Target selection*

We selected quasars from the Seventh Data Release (DR7; Schneider et al., 2010) of the SDSS spectroscopic quasar catalogue. The sample was restricted to objects with redshifts $2.14 < z < 2.51$ ($7,258$ quasars), to ensure that the Hβ and Hα emission-lines fall within the H- and K-passbands respectively, allowing us to observe both simultaneously with the appropriate grism configuration. Given the limited number of quasars for which near-infrared spectra could be obtained, the quasar sample was further restricted to objects that are radio-quiet ($5,980$ quasars), show no evidence of BALs in their spectra ($5,299$ quasars), and are free from significant dust extinction. We removed radio-loud objects and BAL quasars using the classification flags described in Section 2.4.3. The removal of quasars with significant dust extinction was achieved by identifying quasars with $i - K$ colours redder than a parametric SED model combined with an extinction curve with $E(B - V) = 0.05$ (a very similar procedure is described in greater detail in Section 5.5.1).

The K-magnitude (used to compute the $i - K$ colour) was taken from the UKIDSS Large Area Survey (ULAS). The requirement to be in the ULAS footprint and have reliable K passband photometry reduced our sample of possible targets to $1,683$, and the $E(B - V)$ cut left $1,204$ in our sample. Finally, a flux-limit of $K < 18.5$ (AB) was applied to ensure that spectra of sufficient S/N could be obtained (leaving 412 quasars).

We were able to obtain new infrared spectra for 19 quasars from this sample of 412 possible targets. The quasars included in this sub-sample were selected to have C IV-emission blueshifts which span the full range observed in the population (e.g. Richards et al., 2011). Reliably quantifying the distribution of C IV-emission blueshifts has been made possible thanks to recent improvements in the estimation of systemic redshifts from ultra-violet spectra (see Section 3.5.1 for details).

2.2.1.2 *Observations*

Near-infrared spectra were obtained with the Long-slit Intermediate Resolution Infrared Spectrograph (LIRIS; Manchado et al., 1998) mounted on the 4.2 m William Herschel Telescope (WHT) at the Observatorio del Roque de los Muchachos (La Palma,

Spain). Observations took place over four non-contiguous nights from 2015 March 31 to April 4. Approximately one night was lost due to poor weather and a further half-night was affected by poor transparency due to cloud. A one arcsecond slit-width was employed and the LIRIS $H+K$ low-resolution grism was selected, which covers the spectral ranges $1.53-1.79\,\mu m$ and $2.07-2.44\,\mu m$ with a dispersion of 9.7 Å/pixel. The spatial scale of the instrument is 0.25 arcsecond/pixel. Observations were divided into 60 second sub-exposures and performed in an ABBA nodding pattern, with the object placed at two positions along the slit 12 arcsecond apart. Bright $A0-5V$ stars were observed at similar air-masses to the targets in order to provide both telluric absorption corrections and a flux calibration of the quasar spectra.

2.2.1.3 *Data reduction*

The raw LIRIS data frames incorporate a known 'pixel shift' which was first removed from all frames using the LIRIS data reduction package `LIRISDR`. Subsequent data reduction was undertaken with standard `IRAF`[1] procedures. The flat-field images, which were taken at the beginning of each night via illumination of the dome, were averaged and normalised to remove any wavelength-dependent signature. Each individual two-dimensional spectrum was then flat-field corrected. Consecutive AB and BA pairs of two-dimensional spectra were subtracted to remove the sky background. All the subtracted AB/BA-pairs for a given target were then averaged to give the final two-dimensional spectrum.

The size of the one-dimensional spectrum extraction windows, in the slit direction, varied from $6-10$ pixels. To increase the S/N, optimal variance-weighted extraction with sigma clipping was employed. For the fainter objects in our sample we were unable to trace the spectrum across the dispersion axis reliably and the trace from a telluric standard-star observation, observed at a similar air-mass and time, was used instead. The wavelength calibration, using argon and xenon lamp exposures, resulted in root mean square errors in the range $1.01-1.71$ Å, with a mean of 1.47 Å. The telluric standard star observations were reduced using the same steps described above. The stel-

1 `IRAF` is distributed by the National Optical Astronomy Observatory, which is operated by the Association of Universities for Research in Astronomy (AURA) under a cooperative agreement with the National Science Foundation.

lar continuum was divided out of the standard star spectrum, which was then divided into the quasar spectrum to remove telluric absorption features. The spectral type and magnitude of the standard star were used to flux calibrate the quasar spectrum both in a relative and absolute sense[2].

2.2.2 *Shen (2016) sample*

Shen (2016) and Shen and Liu (2012) obtained near-infrared spectroscopy for a sample of 74 luminous, $1.5 < z < 3.5$ quasars selected from the SDSS DR7 quasar catalogue. Targets were required to possess good observed-frame optical spectra covering the C IV line and have redshifts $z \sim 1.5$, 2.1, and 3.3 to ensure that the Hβ-[O III] region was covered in one of the near-infrared JHK passbands. Thirty-eight of the quasars were observed with TripleSpec (Wilson et al., 2004) on the Astrophysics Research Consortium (ARC) 3.5 m telescope, and 36 with the Folded-port InfraRed Echellette (FIRE; Simcoe et al., 2010) on the 6.5 m Magellan-Baade telescope. The reduction of the spectra is described in Shen (2016) and Shen and Liu (2012).

2.2.3 *Quasars Probing Quasars sample*

A large part of our catalogue was observed as part of an ongoing effort to identify quasar pairs at very close projected separations (Quasars Probing Quasars[3]; Hennawi et al., 2006a; Hennawi et al., 2010). The primary science driver of this work is to study the circum-galactic medium of the foreground quasars in absorption (Hennawi et al., 2006b). Very accurate systemic redshift measurements are a requirement and a large amount of resources have been devoted to obtaining near-infrared spectra which cover low-ionisation broad lines or features from the quasar NLR (Prochaska and Hennawi, 2009; Lau, Prochaska, and Hennawi, 2016; Hennawi et al., 2015).

Twenty-nine quasars were observed with the Gemini Near-Infrared Spectrograph (GNIRS; Elias et al., 2006) on the 8.1 m Gemini North telescope, thirteen using the Infrared Spectrometer And Array Camera (ISAAC; Moorwood et al., 1998) on the European Southern Observatory (ESO) Very Large Telescope (VLT), thirty-one with the Near InfraRed Imager and Spectrom-

2 The data reduction pipeline is available at https://github.com/liamcoatman/SpectraTools.

3 www.ucolick.org/~xavier/QPQ/Quasars_Probing_Quasars

eter (NIRI; Hodapp et al., 2003) also on Gemini North and thirty-six with XSHOOTER (Vernet et al., 2011), again, on the VLT.

The XSHOOTER spectra were reduced with a custom software package developed by Prof. G. Becker (for details, see Lau, Prochaska, and Hennawi, 2016). The remaining data was processed with algorithms in the LowRedux[4] package (see Prochaska and Hennawi, 2009)[5].

2.2.4 *VLT SINFONI*

We performed a search of the ESO archive for high-redshift quasars observed with the SINFONI integral field spectrograph (Eisenhauer et al., 2003; Bonnet et al., 2004) at VLT/UT4. We found 79 quasars with redshifts $1.5 < z < 3.7$ which have H and/or K SINFONI spectroscopy, covering the Hβ and Hα lines respectively. Seventy-two of the quasars are from a large programme (083.B-0456; PI: L. Wisotzki) to study the mass function and Eddington ratios of active BHs drawn from the Hamburg-ESO survey (Wisotzki et al., 2000). A further seven SINFONI spectra are from a programme (090.B-0674; PI: J. Kurk) to obtain reliable BH mass estimates from Hα/Hβ for a sample of radio-loud/radio-quiet SDSS quasars.

The SINFONI spectra were reduced using the package EASYSINF[6]. The package, which is based on the ESO-SINFONI pipeline, is described in Williams et al. (2016).

2.2.5 *NTT SOFI*

One quarter of the quasar catalogue derives from a large programme (187.A-0645; PI: J. Hennawi) to combine near-infrared spectra from SOFI (Moorwood, Cuby, and Lidman, 1998) on the 3.6 m New Technology Telescope (NTT) with archival high-resolution optical spectra from the UV-Visual Echelle Spectrograph (UVES; Dekker et al., 2000) at VLT/UT2 and the High Resolution Echelle Spectrometer (HIRES; Vogt et al., 1994) at Keck to construct a legacy database of bright, high-redshift ($2 < z < 4$) quasars with both rest-frame optical spectra, covering the Hβ-[O III] complex, and high-resolution rest-frame

4 www.ucolick.org/~xavier/LowRedux
5 Spectra in this sample were reduced by Prof. J Hennawi, Prof. X. Prochaska and collaborators.
6 www.mrao.cam.ac.uk/~rw480/easysinf

ultra-violet spectra. The main science goal is to obtain precise systemic redshifts which are crucial for the study of absorption-line systems. Observations were undertaken over 16 nights from 2011 September to 2013 March. Both the 'red' ($R \simeq 1000$) and the H and K ($R \simeq 1500$) grisms were employed. The spectra were reduced using a custom pipeline built from algorithms in the LowRedux package.

Over five nights from 2015 August 31 to September 4 we obtained near-infrared SOFI spectra for a further 26 quasars (095.B-0644; PI: L. Coatman). These quasars were selected from the SDSS DR7 quasar catalogue using criteria very similar to those described above for the WHT/LIRIS sample. In particular, we selected quasars for which C IV was significantly blueshifted relative to the quasar rest-frame to improve the statistics in this region of the C IV emission-line parameter space. The 'red' grism was employed with a one arcsecond slit-width. The spectra were reduced using the same LowRedux pipeline described above.

2.2.6 *Hale TripleSpec*

A further 60 quasars in our catalogue are bright SDSS quasars which were observed with the TRIPLESPEC spectrograph (Herter et al., 2008) on the Palomar 200-inch Hale telescope (P200). The objects were observed with the same science goals as the SOFI NTT large programme. The spectra were reduced using a custom pipeline, again using algorithms in the LowRedux package[7].

2.3 REDSHIFT AND LUMINOSITY DISTRIBUTION OF CATALOGUE

In Figure 2.1 we show the luminosities and redshifts of the quasar sample relative to the redshift-luminosity distribution of the SDSS DR7 spectroscopic quasar catalogue. Our sample spans a redshift range $1.5 < z < 4.0$ and a bolometric luminosity range $10^{45.5} - 10^{48}$ erg s^{-1}. Spectra were obtained within one or more of the JHK passbands and the gaps in our sample coverage at $z \sim 1.8$ and $z \sim 3$ are due to the presence of atmospheric absorption. Obtaining near-infrared spectra of adequate resolution and S/N of even moderately bright quasars

7 Spectra in this sample were reduced by Prof. X. Prochaska and collaborators.

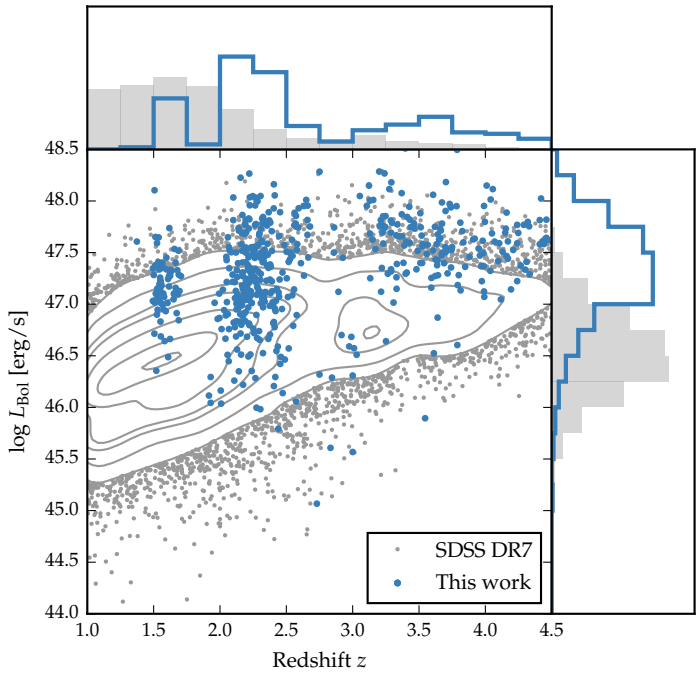

Figure 2.1: The ranges in redshift and luminosity covered by our sample, relative to the redshift-luminosity distribution of the SDSS DR7 quasar catalogue. For the SDSS sample we use Hewett and Wild (2010) redshifts and bolometric luminosities computed by Shen et al. (2011) from L_{3000} ($z < 1.9$) and L_{1350} ($z > 1.9$) using bolometric corrections $L_{Bol} = 5.15L_{3000}$ and $L_{Bol} = 3.81L_{1350}$ (Richards et al., 2006a). For the quasars in this work the redshift is defined using the peak of the Hα/Hβ emission and the bolometric luminosity is computed from L(5100 Å) using BC(5100 Å) = 9.26 (Richards et al., 2006a).

remains resource intensive. As a consequence, at fixed redshift, the luminosities of the quasars are brighter than the average luminosity of the SDSS sample, although the dynamic range in luminosity is a full 1.5 decades.

2.4 SUPPLEMENTARY DATA

2.4.1 *Observed-frame optical spectroscopic data*

Observed-frame optical spectra are available for 79 per cent of the catalogue. The sources of the optical spectra (summarised in Table 2.3) are as follows:

	Source	%
(1)	SDSS	60
(2)	BOSS	45
(3)	HAMBURG-ESO	7
(4)	VLT/UVES	4
(5)	VLT/XSHOOTER	8

Table 2.3: Percentage of catalogue for which observed-frame optical spectroscopic data is available from the given sources.

1. SDSS DR7 spectroscopic quasar catalogue. Spectra are moderate resolution ($R \simeq 2000$) and S/N ($S/N \simeq 20$) and cover the observed-frame wavelength interval $\sim 3800 - 9180$ Å.

2. BOSS DR12 (Pâris et al., 2017) spectroscopic quasar catalogue. Compared to SDSS spectra, BOSS spectra cover a slightly broader wavelength range and are typically higher S/N.

3. The Hamburg-ESO survey (Wisotzki et al., 2000). The spectra have a typical $R \simeq 700$ spectral resolution and $S/N \gtrsim 10$ per pixel.

4. Spectra taken with VLT/UVES. The reduced and fluxed UVES spectra were made available to us by Dr. A. Dall'Aglio (a description of the reduction procedure is contained in Dall'Aglio, Wisotzki, and Worseck 2008). The spectral resolution of the UVES observations is very high ($R \simeq 40\,000$) and the S/N of the spectra, re-binned to a resolution of $R \simeq 2000$, is $S/N \simeq 300$.

5. Spectra taken with VLT/XSHOOTER. The XSHOOTER spectra are moderate resolution ($R \simeq 6000$) and cover the full observed-frame optical to near-infrared spectral region ($0.30 - 2.50\,\mu$m).

2.4.2 *Photometric data*

We cross-matched our catalogue with photometric data from a number of wide-field surveys. The matching was done using a three arcsecond matching radius, with only the closest neighbour retained in the case of multiple matches. The cross-matched surveys and the percentage of successful matches is

summarised in Table 2.4. The cross-matched surveys are as follows:

1. SDSS DR9 (Ahn et al., 2012) photometric source catalogue. Point spread function magnitudes.
2. Two Micron All Sky Survey (2MASS; Skrutskie et al., 2006) Point Source Catalogue. Default magnitudes.
3. ULAS DR10. One arcsecond radius aperture corrected magnitudes ('apermag3').
4. Visible and Infrared Survey Telescope for Astronomy (VISTA) Hemisphere Survey (VHS; McMahon et al., 2013). One arcsecond radius aperture corrected magnitudes ('apermag3').
5. VISTA Kilo-Degree Infrared Galaxy (VIKING; Edge et al., 2013) Survey (DR4). One arcsecond radius aperture corrected magnitudes ('apermag3').
6. WISE AllWISE Data Release (Mainzer et al., 2011). Profile-fitting magnitudes ('mpro').

2.4.3 *Radio/BAL quasar classification*

Using the catalogues provided by Shen et al. (2011), Allen et al. (2011) and Pâris et al. (2017) and visual inspection, 19 quasars in the catalogue are identified as being C IV BAL quasars.

We cross-match our catalogue to the FIRST radio catalogue (White et al., 1997). We classify quasars with matches within five arcsecond as core-dominated, while, if multiple matches are found within 30 arcsecond, quasars are classified as lobe-dominated (e.g. Shen et al., 2011). 128 objects are outside of the FIRST footprint, 269 are not detected in FIRST, 29 are detected and are core-dominated, and 8 are detected and are lobe-dominated.

2.5 ABSOLUTE FLUX CALIBRATION OF NEAR-INFRARED SPECTRA

Relative flux-calibration of the infrared spectra as a function of wavelength has been achieved through observations of appropriate flux standards. The absolute flux levels, however, can be in error by large factors due to variable atmospheric conditions

	SDSS (1)	2MASS (2)	UKIDSS (3)	VHS (4)	VIKING (5)	WISE (6)
u	73	-	-	-	-	-
g	73	-	-	-	-	-
r	73	-	-	-	-	-
i	73	-	-	-	-	-
z	73	-	-	-	9	-
Y	-	-	41	10	9	-
J	-	57	41	34	9	-
H	-	57	41	20	9	-
K	-	57	41	33	9	-
W1	-	-	-	-	-	97
W2	-	-	-	-	-	97
W3	-	-	-	-	-	97
W4	-	-	-	-	-	97

Table 2.4: Cross-matched surveys and the percentage of successful matches.

combined with the narrow slit widths. For the majority of the quasars we have, therefore, established the absolute flux scale for each near-infrared spectrum using either SDSS/BOSS spectroscopy or the available photometric data as a fiducial baseline. The methods are attempted in the order given below, and the method we adopt is dependent on the availability of the required data. We are unable to verify the absolute flux calibration of the near-infrared spectra for four objects because neither SDSS/BOSS spectra nor optical/near-infrared data is available. The methods used to flux calibrate the near-infrared spectra are summarised in Table 2.5.

2.5.1 *SDSS spectrum as a fiducial baseline*

The flux calibration of the SDSS spectra is excellent, and so these spectra can be used as a fiducial baseline to calibrate the near-infrared spectra. The quasar SED model described in Chapter 5 is used to bridge the gap between the wavelength coverage of the near-infrared and optical SDSS spectrum. This model provides a very good fit to the SDSS and UKIDSS magnitudes of SDSS DR7 quasars, reproducing the individual magnitudes to < 0.1 mag. The first step is to normalise the SED model to the SDSS spectrum. This is done using a variance-weighted χ^2 minimisation procedure in several emission-line-free inter-

Method	%
SDSS	60
BOSS	9
NIR photometry	25
NIR+OPT photometry	6
None	1

Table 2.5: Methods used in absolute flux calibration of near-infrared spectra and the percentage of spectra to which each method is applied.

vals of the spectrum. The second step is to normalise the near-infrared spectrum to the SED model. Again, this is done using a variance-weighted χ^2 minimisation procedure, with regions of the spectrum falling between the near-infrared passbands masked-out in the minimisation. The flux calibration procedure is demonstrated in Figure 2.2a.

2.5.2 *BOSS spectrum as a fiducial baseline*

This procedure is identical to one described in the previous section, the only difference being that the SDSS spectrum is substituted for a BOSS spectrum. To avoid the known issues in the flux calibration of the BOSS DR12 quasar spectra at blue wavelengths (Lee et al., 2013), our fitting was confined to rest-frame wavelengths long-ward of 1275 Å.

2.5.3 *Photometric data as a fiducial baseline*

In the first step, the quasar SED model is normalised to the available optical (SDSS) and near-infrared (VHS, Viking, UKIDSS or 2MASS) photometric data. The SED model is integrated through the appropriate passband transmission functions to give model magnitudes (Equations 5.1 and 5.2), and a variance weighted χ^2 minimisation procedure is performed with the observed magnitudes. The second step in the procedure is then identical to the previous two sections. This procedure is illustrated in Figure 2.2b.

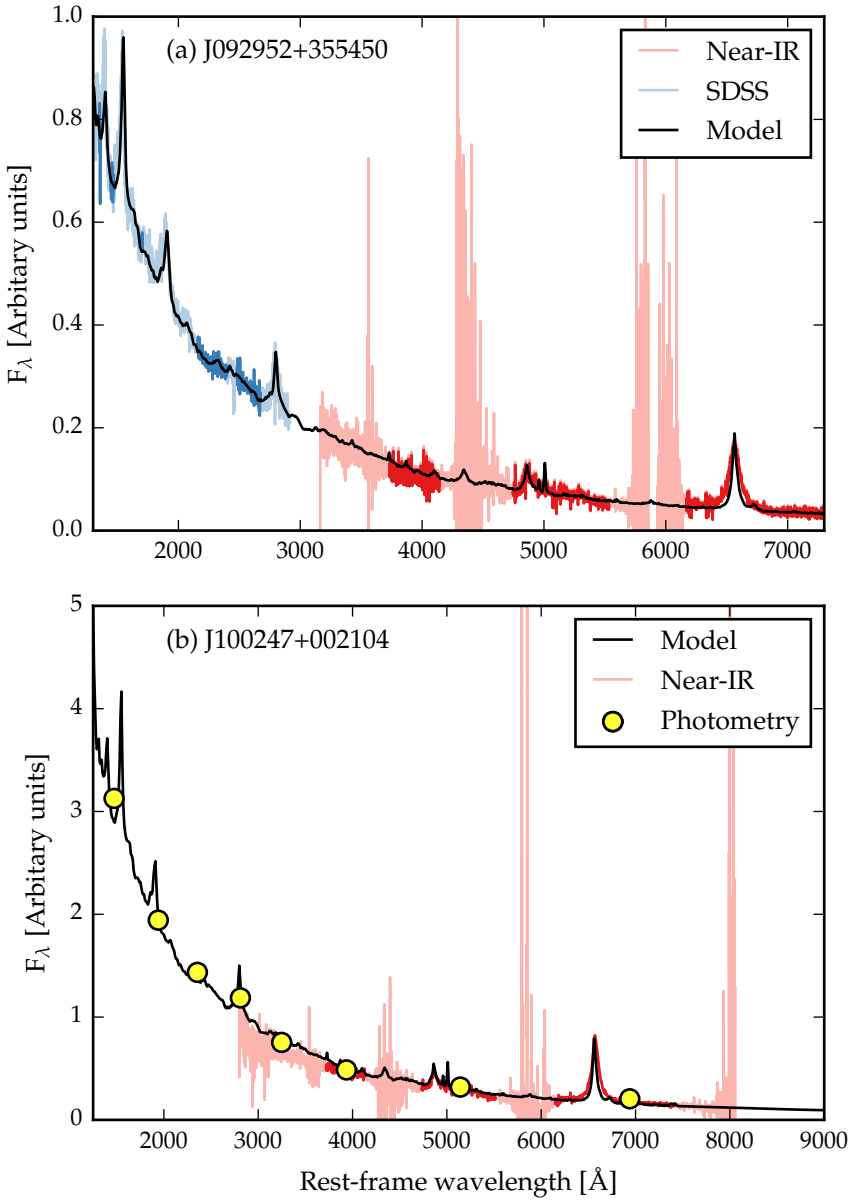

Figure 2.2: Demonstration of how the absolute flux calibration of a near-infrared spectrum is established using the SDSS spectrum (a) or photometric data (b) as fiducial baselines. An empirical quasar SED model is used to bridge the discontinuity in the wavelength coverage between the optical and near-infrared data. The darker regions of the spectra are used in the fitting procedures.

2.5.4 *Reliability of luminosity measurements*

The fluxes at 1350 and 5100 Å were read off directly from the normalised SED model. These were converted into monochromatic continuum luminosities, which are used to compute BH masses and bolometric luminosities in Chapters 3, 4 and 5. Comparison of the 5100 Å luminosity, computed using the photometry- and spectrum-based methods for 296 quasars, showed a scatter (mean absolute deviation) of just ~ 0.1 dex. We therefore assume 0.1 dex to be the measurement uncertainty on the 5100 Å luminosities. We expect the uncertainties on the 1350 Å luminosities to be at similar level. For all the catalogue quasars, the optical and near-infrared spectra as well as the near-infrared photometry were obtained at different epochs, with rest-frame time differences of up to ~ 5 years. Intrinsic quasar photometric variability in the rest-frame ultra-violet and optical will therefore add additional scatter of ~ 0.2 mag (e.g. MacLeod et al., 2010) to the derived 1350 and 5100 Å luminosities.

The monochromatic continuum luminosity at 5 μm was also computed by linearly interpolating through the WISE photometric data points. 5 μm luminosities were derived in this way for quasars up to redshift $z = 3.4$. At higher redshifts, the longest wavelength WISE passband ($W4$) is at < 5 μm in the quasar rest-frame and so 5 μm luminosities could not be computed using this method.

2.6 CORRECTING FOR INSTRUMENTAL BROADENING

Throughout this thesis, reported line-width measures are corrected for instrumental broadening by subtracting the resolution of the spectrograph in quadrature. Because the quasar emission-line profiles are typically non-Gaussian, this deconvolution procedure is only approximate. The spectrograph resolutions, which we estimate from the line widths in the observed sky spectra, are given in Table 2.6. The resolutions are generally small relative to the widths of quasar broad emission-lines (FWHM $\sim 4000\,\mathrm{km\,s^{-1}}$).

Spectrograph	FWHM [$\mathrm{km\,s^{-1}}$]
FIRE	59
GNIRS	136
ISAAC	46
LIRIS	477
NIRI	465
NIRSPEC	122
SINFONI	124
SOFI (MR)	323
SOFI (LR)	535
P200 TRIPLESPEC	88
ARC TRIPLESPEC	97
XSHOOTER	25
SDSS/BOSS	152
UVES	3
HAMBURG-ESO	400

Table 2.6: Spectral resolutions of the spectrographs used in this thesis.

3

CORRECTING C IV-BASED VIRIAL BLACK HOLE MASSES

3.1 SINGLE-EPOCH VIRIAL BH MASSES

The goal of better understanding the origin of the correlation between the masses of super-massive BHs and the masses of host-galaxy spheroids has led to much work focussing on the properties of quasars and AGN at relatively high redshifts, $z \gtrsim 2$. Extensive reverberation-mapping campaigns have been used to calibrate single-epoch virial-mass estimates which use the velocity widths of the hydrogen Balmer emission-lines and the nuclear continuum luminosity to provide reliable BH masses. Single-epoch virial BH mass estimates using Hβ are possible up to redshifts $z \sim 0.7$, and the technique has been extended to redshifts $z \sim 1.9$ via the calibration of the broad Mg II$\lambda\lambda$2796,2803 emission-line (McLure and Jarvis, 2002; Onken and Kollmeier, 2008; Wang et al., 2009; Rafiee and Hall, 2011). At redshifts $z \gtrsim 2$, however, ground-based statistical studies of the quasar population generally have no access to the rest-frame optical and near-ultra-violet spectral regions.

The C IV$\lambda\lambda$1548,1550 emission doublet is both relatively strong in the majority of quasars and visible in modern optical spectra, such as those provided by SDSS, to redshifts exceeding $z \sim 5$. C IV-derived BH masses have therefore become the standard (e.g. Vestergaard and Peterson, 2006; Park et al., 2013) for both individual quasars and in studies of quasar population demographics.

Currently, the number of reverberation mapped quasars is small ($\sim$ 50 quasars; Park et al., 2013) and restricted to low redshifts and luminosities. The luminosities of quasars at redshifts $z \gtrsim 2$ are much greater than in the reverberation mapped sample, and the reliability of the existing calibration involving C IV FWHM velocity measurements and ultra-violet luminosity is not established definitively when extrapolating to high-redshifts and luminosities. While some authors have found good agreement between BH mass-estimates based on C IV and Hβ (e.g. Vestergaard and Peterson, 2006; Assef et al., 2011; Tilton and Shull, 2013), others have questioned the consistency

(e.g. Baskin and Laor, 2005a; Trakhtenbrot and Netzer, 2012; Shen and Liu, 2012).

In contrast to a number of low-ionisation emission-lines, such as Mg II, the C IV emission has long been known to exhibit significant asymmetric structure, with an excess of flux to the blue of the predicted rest-frame transition wavelength (Gaskell, 1982). More recent work (e.g. Sulentic, Marziani, and Dultzin-Hacyan, 2000; Richards et al., 2011) has established that the extent of 'blueshifts' in the C IV emission correlates with a number of properties of quasar SEDs. A fundamental assumption on which single-epoch virial BH mass estimates are based is that the widths of the broad emission-lines are directly related to the virial motions of the emitting clouds moving in the gravitational potential of the central BH. While the physical origin of the blueshifted emission has not been established there is a consensus that the associated gas is not tracing virial-induced velocities. A favoured interpretation associates the blueshifted emission with out-flowing material (see Netzer, 2015, for a recent review), reaching velocities significantly larger than virial-induced velocities associated with the BH (e.g. Sulentic et al., 2007; Richards et al., 2011). These outflows, most likely, result from the presence of a radiation line-driven accretion-disc wind (e.g. Konigl and Kartje, 1994; Murray et al., 1995; Proga, Stone, and Kallman, 2000; Everett, 2005; Gallagher et al., 2015; Higginbottom and Proga, 2015).

Figure 3.1 shows the shape of the C IV-emission in composite spectra constructed from SDSS DR7 quasars as a function of C IV blueshift. The profiles show how, at large values of blueshift ($\gtrsim 2000\,\mathrm{km\,s^{-1}}$) the C IV-profile is displaced to the blue by amounts comparable to the FWHM of the profile. At fixed emission-line EQW, virtually the entire C IV-profile appears to shift blueward and the change in line shape is not simply an enhancement of flux in the blue wing of a still identifiable symmetric component. While gravity almost certainly plays a key role, determining the escape velocity for out-flowing material for example, it is clear that the virial assumption, on which single-epoch BH mass measurements are predicated, is not straightforwardly applicable for the C IV emission-line in quasars exhibiting large blueshifts. In general, researchers studying quasar demographics at high-redshift adopt estimates of BH masses based on the width of C IV-emission, without reference to the blueshift of the C IV-emission (e.g. Vestergaard, 2004; Kollmeier et al., 2006; Gav-

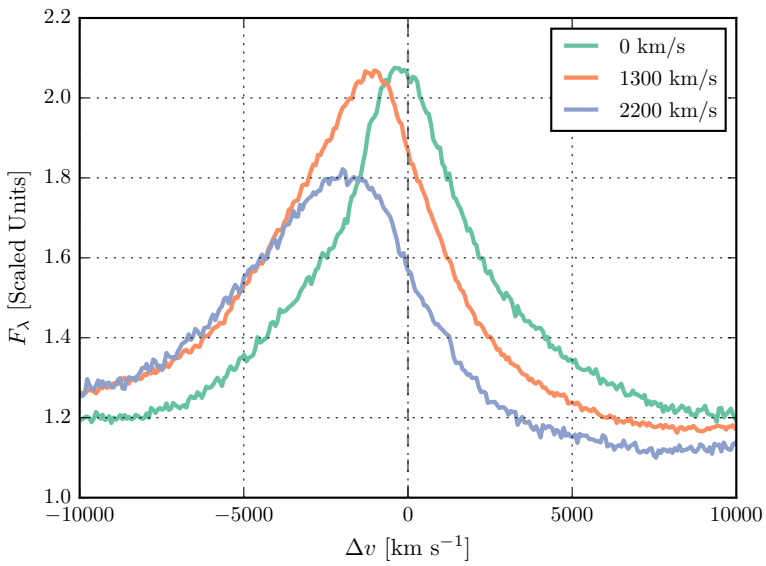

Figure 3.1: Composite spectra of the C IV emission-line as a function of C IV blueshift for SDSS DR7 quasars. Quasars classified as BALs, or possessing strong associated absorbers have been excluded, and the composite spectra shown are derived using an arithmetic mean of a minimum of 200 spectra at each blueshift. Virtually the entire C IV-profile appears to shift blueward and the change in line shape is not simply an enhancement of flux in the blue wing of a still identifiable symmetric component. In order of increasing C IV blueshift, the composite spectra have FWHM 4870, 5610, and 6770 km s^{-1} and EQW 33.1, 31.6, and 28.8 Å.

ignaud et al., 2008; Vestergaard et al., 2008; Vestergaard and Osmer, 2009; Kelly et al., 2010; Kelly and Shen, 2013). As a consequence, BH masses derived from C IV emission-line velocity-widths are systematically biased compared to masses from the Balmer lines (e.g. Shen et al., 2008; Shen and Liu, 2012).

As highlighted by Richards et al. (2011), the sample of reverberation mapped quasars includes a restricted range of the C IV emission-line shapes seen in the quasar population. In particular, the reverberation mapped objects generally possess high C IV EQWs and low C IV-blueshifts. Nevertheless, the derived scaling relations based on the reverberation-mapped sample are regularly applied to the quasar population with low C IV EQWs and/or large C IV-blueshifts, where any non-virial outflow-related contribution to the dynamics is significant.

In recent literature, attempts have been made to minimise the influence of the systematic non-virial contribution to the

C IV emission on estimates of the BH mass. Strategies include (i) significantly reducing the dependence of the derived masses on the emission-line velocity width (e.g. from the ΔV^2 dependence predicted assuming a virialized BLR to just $\Delta V^{0.56}$ in Park et al. 2013; see also Shen and Liu 2012), (ii) adopting a measure of emission-line velocity-width that is relatively insensitive to changes in the core of the emission-line profile (e.g. Denney et al., 2013) and (iii) estimating the amplitude of the non-virial contribution to the C IV emission-line via comparison with other ultra-violet emission-lines (e.g. Si IV+O IVλ1400 in Runnoe et al. 2013 and Brotherton et al. 2015). The increased number of quasars with high-quality spectra that cover both the observed-frame optical (where the redshifted C IV appears) and near-infrared (where Hβ and Hα lie) enables us to take a rather different approach in this chapter. We will use properties of the C IV emission-line itself to reduce, or even remove, the systematic bias in the BH mass estimates. Specifically, using the low-ionisation Balmer lines Hα and Hβ as reliable proxies for the virial velocity, we will measure empirically the systematic bias in C IV-based virial BH mass estimates as a function of the C IV emission-line blueshift.

3.2 QUASAR SAMPLE

We have compiled a sample of 307 non-BAL quasars at redshifts $1.5 < z < 4$ with both optical and near-infrared spectra. Reliable emission-line properties were measured for 230 quasars (Section 3.3.5), with 164 possessing Hα line measurements and 144 Hβ line measurements. This will allow us to directly compare virial BH mass estimates based on the C IV line-width with estimates based on the line-widths of the low-ionisation Balmer lines Hα and Hβ. The sample is considerably larger than previous studies of the rest-frame optical spectra of high-z quasars (e.g. Shen and Liu, 2012). As we demonstrate in Section 3.5.3, the quasars have C IV blueshifts of up to $\sim 5000\,\mathrm{km\,s^{-1}}$, and span virtually the full range of blueshifts observed in the population.

The near-infrared data has been described in Chapter 2 and the telescopes/spectrographs used are summarised in Table 3.1. Corresponding optical spectroscopy was obtained from the SDSS (70 quasars), BOSS (126 quasars) and Hamburg-ESO surveys (15 quasars), and with VLT/UVES (11 quasars) and VLT/XSHOOTER (8 quasars). Many of the quasars in the SDSS

Spectrograph	Telescope	Hα Sample	Hβ Sample
FIRE	MAGELLAN	18	19
GNIRS	GEMINI-N	22	17
ISAAC	VLT	0	4
LIRIS	WHT	15	0
NIRI	GEMINI-N	0	12
SINFONI	VLT	2	25
SOFI	NTT	47	23
TRIPLESPEC	ARC-3.5m	33	20
TRIPLESPEC	P200	23	19
XSHOOTER	VLT	4	7
Total		164	144

Table 3.1: The numbers of quasars with reliable Hα and Hβ line measurements, and the spectrographs and telescopes used to obtain the near-infrared spectra.

DR7 catalogue have been re-observed as part of BOSS. As the BOSS spectra typically have higher S/N than the SDSS DR7 spectra, we have used the BOSS spectra when available. Once more, further details are provided in Chapter 2. We have subdivided our sample into two overlapping groups: quasars with reliable Hα line measurements (the 'Hα sample') and quasars with reliable Hβ measurements (the 'Hβ sample').

3.3 SPECTRAL MEASUREMENTS

Conventionally, single-epoch virial estimates of the BH mass are a function of the line-of-sight velocity width of a broad emission-line and the quasar luminosity. The velocity width is a proxy for the virial velocity in the BLR and, as revealed in reverberation-mapping studies, the luminosity is a proxy for the typical size of the BLR (the $R_{BLR} - L$ relation; e.g. Kaspi et al., 2000; Kaspi et al., 2007). Most reverberation mapping campaigns have employed Hβ time-lags and velocity widths, but the line-widths of Hα and Mg II have been shown to yield consistent BH masses (e.g. McLure and Jarvis, 2002; Greene and Ho, 2005b; Onken and Kollmeier, 2008; Shen et al., 2008; Wang et al., 2009; Rafiee and Hall, 2011; Mejía-Restrepo et al., 2016). In Section 3.4.1, we verify that the Hα and Hβ line-widths yield consistent BH masses for the 99 quasars in our sample with measurements of both.

In our work, a robust measure of the C IV emission-line 'blueshift' provides the basis for the corrected C IV velocity-width measurements, and hence BH masses. The effectiveness of the scheme is validated via a direct comparison of the C IV velocity-widths to the Balmer emission velocity-widths in the same quasars. Our process is as follows. First, an accurate measure of the quasar's systemic redshift is required, for which we adopt the centre of the Balmer emission, where the centre, $\lambda_{\rm half}$, is the wavelength that bisects the cumulative total flux. Balmer emission centroids are available for all quasars in the catalogue but we verify that the measure is relatively unbiased through a comparison of the centroids to the wavelength of the peak of the narrow [O III]λ5008 emission-line for the subset of spectra where both are available (Section 3.4.2). Second, the blueshift of the C IV emission-line is determined. Again, we adopt the line centroid to provide a robust measure of the C IV emission blueshift. The blueshift (in $\mathrm{km\,s^{-1}}$) is defined as

$$c \times \frac{1549.48\,\text{Å} - \lambda_{\rm half}}{1549.48\,\text{Å}} \tag{3.1}$$

where c is the velocity of light and 1549.48 Å is the rest-frame wavelength for the C IV doublet[1]. Positive blueshift values indicate an excess of emitting material moving towards the observer and hence out-flowing from the quasar.

Emission-line velocity widths are derived from the FWHM of the lines but we also compute the line dispersion as some authors have claimed this provides a better estimate of the virial velocity (Denney et al., 2013). The line dispersion, σ, is calculated from the flux-weighted second moment of the velocity distribution, and is defined by

$$\sigma^2 = \langle\lambda^2\rangle - \langle\lambda\rangle^2 \tag{3.2}$$

$$= \left[\frac{\int \lambda^2 P(\lambda)\,d\lambda}{\int P(\lambda)\,d\lambda}\right] \tag{3.3}$$

$$- \left[\frac{\int \lambda P(\lambda)\,d\lambda}{\int P(\lambda)\,d\lambda}\right]^2 . \tag{3.4}$$

where $P(\lambda)$ is the emission-line profile.

1 The adopted C IV rest-frame wavelength assumes an optically thick BLR, in which case the contribution from each component is equal. Adopting a 2 : 1 ratio (appropriate for an optically thin BLR) changes the blueshifts by $\sim 80\,\mathrm{km\,s^{-1}}$.

To minimise the impact of the finite S/N of the quasar spectra and the presence of absorption features superposed on the broad emission-lines we first fit a parametric model to the continuum and the emission-lines. The particular form of the model parametrisations is not important and the fits are used only to provide robust line parameters, such as the centroid $\lambda_{\rm half}$, and FWHM, which are measured non-parametrically from the best-fitting model. The models used and the fitting procedure are described below. The issues involved in deriving parameters for broad emission-lines from spectra of modest S/N – for example, subtraction of narrow line emission, subtraction of Fe II emission – have been covered comprehensively by other authors (e.g. Shen et al., 2011; Shen and Liu, 2012; Denney et al., 2013; Shen, 2016) and, as far as possible, we follow standard procedures described in the literature.

3.3.1 *Modelling C IV*

We first define a power-law continuum, $f(\lambda) \propto \lambda^{-\alpha}$, with the slope, α, determined using the median[2] values of the flux in two continuum windows at 1445-1465 and 1700-1705 Å (the same wavelengths as adopted by Shen et al. 2011). The continuum emission is subtracted from the spectra, which is then transformed from wavelength units into units of velocity relative to the rest-frame line-transition wavelength for the C IV doublet. The parametric model is ordinarily fit within the wavelength interval 1500-1600 Å (corresponding to approximately $\pm 10\,000\,\mathrm{km\,s^{-1}}$ from the rest-frame transition wavelength), a recipe that is commonly adopted (e.g. Shen et al., 2011; Denney et al., 2013). The line-window was extended if more than 5 per cent of the total flux in the profile was present blueward of the short wavelength limit. Narrow absorption features, which are frequently found superimposed on C IV emission, were masked out during the fit.

The C IV emission was fit with sixth-order Gauss-Hermite (GH) polynomials, using the normalisation of van der Marel and Franx (1993) and the functional forms of Cappellari et al. (2002). We allowed up to six components, but in many cases a lower order was sufficient (40 and 45 per cent were fit with second- and fourth-order GH polynomials respectively). GH polynomials were chosen because they are flexible enough to

2 The median is used to improve the robustness of the continuum estimate from the relatively small wavelength intervals.

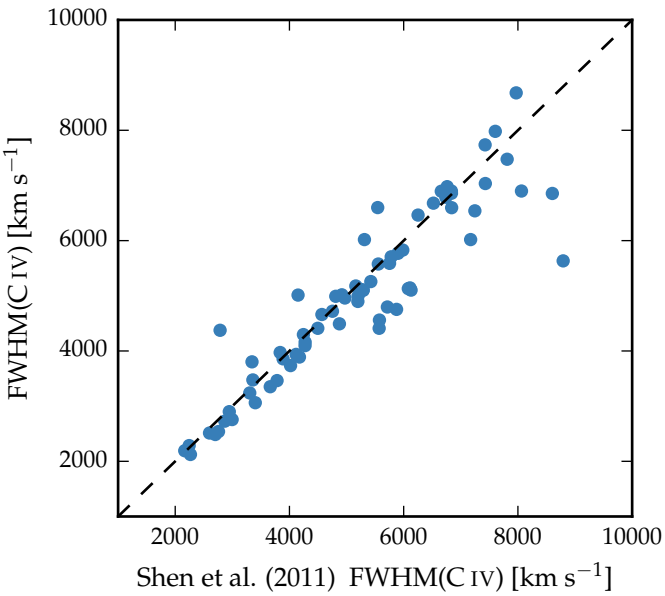

Figure 3.2: Demonstration of the effectiveness of our line parameter estimation scheme via a comparison of the C IV FWHM with Shen et al. (2011).

model the often very asymmetric C IV line profile. The flip-side of this flexibility, however, is that the model has a tendency to over-fit when spectra possess low S/N. The fits were therefore carefully checked visually and the number of components reduced if over-fitting was evident.

We find that using the commonly employed three-Gaussian component model, rather than the GH polynomials, resulted in only marginal differences in the line parameters. Our best-fit parameters are also in good agreement with Shen et al. (2011), who employ a multi-Gaussian parametrisation. In Figure 3.2 we compare our measurements of the C IV FWHM from the 71 SDSS DR7 spectra in our sample with the measurements published in Shen et al. (2011). There is a very strong agreement between our measurements, with a scatter (median absolute deviation) of 190 km s^{-1}.

3.3.2 *Modelling Hα*

A power-law continuum is fit using two continuum windows at 6000-6250 and 6800-7000 Å. The continuum-subtracted flux is then fit in the wavelength interval 6400 – 6800 Å. We adopt a rest-frame transition wavelength of 6564.89 Å to transform

wavelengths into equivalent Doppler velocities. The broad component of Hα is fit using one or two Gaussians, constrained to have a minimum FWHM of 1200 km s^{-1}. When two Gaussians are used, the velocity centroids are constrained to be the same.

The emission-line profiles of both Hβ and Hα frequently include a significant narrow component from the physically more extended NLR. Additional Gaussian components were included in our parametric model to fit the narrow component of Hα as well as [N II]λλ6548,6584 and [S II]λλ6717,6731. This resulted in a better fit to the observed flux in 50 per cent of cases. We impose a 1200 km s^{-1} upper limit on the FWHM of all narrow lines and the amplitudes of all components must be non-negative. The relative flux ratio of the two [N II] components is also fixed at the expected value of 2.96. In 70 per cent of the spectra the [O III]λλ4960,5008 doublet is detected at moderate S/N in the Hβ region. In these cases the peak of the [O III] is used to fix the velocity offsets and the FWHMs of the narrow line components in the Hα region. For spectra where the [O III] doublet does not constrain the velocity and FWHM accurately, the narrow emission in the Hα and Hβ regions are fitted independently but, for each region, the individual narrow-line velocity offsets and the FWHMs are constrained to be identical. In these objects the narrow line contribution is generally weak, and so does not have a large effect on the line parameters we measure for the broad component.

The model described above is very similar to the one described in Shen and Liu (2012) and Shen et al. (2011), the only major differences being that we do not fit the Hα and Hβ emission regions simultaneously and we fix the centroids of the Gaussian components used to fit the broad emission. In Figure 3.3 we plot our Hα FWHM measurements against the measurements published in Shen and Liu (2012), for 51 quasars in common to both samples. There is a strong correlation and a scatter of 300 km s^{-1}.

3.3.3 *Modelling Hβ and [O III]*

Emission from optical Fe II is generally strong in the vicinity of Hβ. We therefore fit a combination of a power-law continuum and an optical Fe II template – taken from Boroson and Green (1992) – to two windows at 4435-4700 and 5100-5535 Å. The Fe II template is convolved with a Gaussian, and the width of this Gaussian, along with the normalisation and velocity offset of

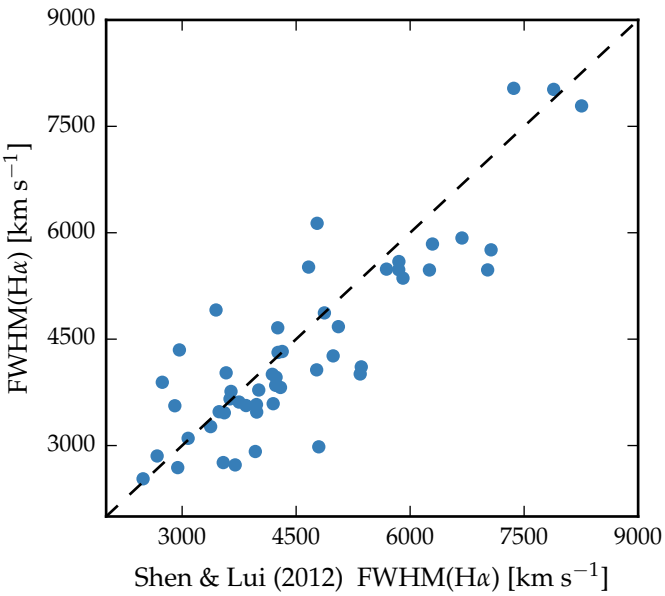

Figure 3.3: Demonstration of the effectiveness of our line parameter estimation scheme via a comparison of the Hα FWHM with Shen and Liu (2012).

the Fe II template, are free variables in the pseudo-continuum fit. We use the same model to fit the broad and narrow components of Hβ as was used with Hα. Each line in the [O III] doublet is fit with two Gaussians, to model both the systemic and any outflow contributions. The peak flux ratio of the [O III] 4960 Å and 5008 Å lines is fixed at 1:3. As for the fit to the narrow lines in the spectral region around Hα, the width and velocity offsets of all the narrow components are set to be equal, and an upper limit of 1200 km s^{-1} is placed on the FWHM.

The parametric model we fit to the Hβ/[O III] emission region was very similar to the model employed by Shen (2016). In Figure 3.4 we plot our Hβ FWHM measurements against the measurements published in Shen (2016), for 39 quasars in common to both samples. As expected, we observe a very tight correlation, with a scatter of 270 km s^{-1}.

3.3.4 *Fitting procedure*

Model parameters were derived using a standard variance-weighted least-squares minimisation procedure employing the Nelder-Mead algorithm. Prior to the fit, the spectra were in-

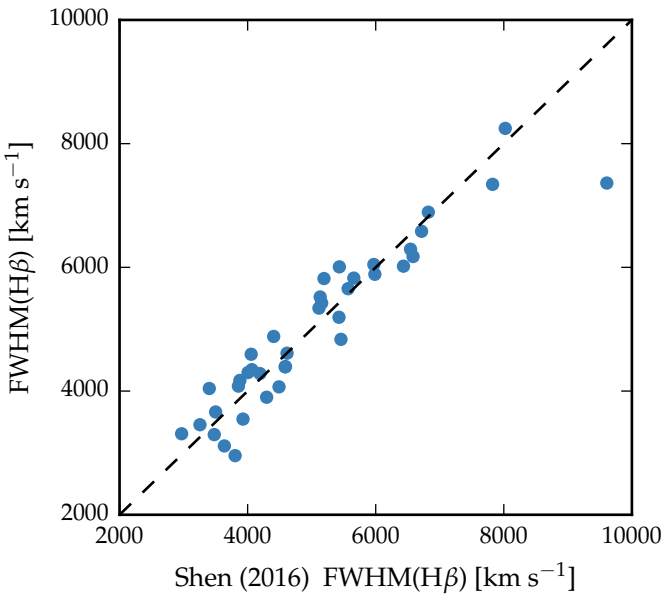

Figure 3.4: Demonstration of the effectiveness of our line parameter estimation scheme via a comparison of the Hβ FWHM with Shen (2016).

spected visually and regions significantly affected by absorption or of low S/N were masked out.

In Figure 3.5 we present our parametric fits to the C IV, Hα and Hβ emission-lines in a handful of quasars, which have been chosen to illustrate the range of spectrum S/N and line shapes in the sample. The Doppler velocities have been shifted so that the Hα emission-line centroid is at $0\,\mathrm{km\,s^{-1}}$. The y-axes of the data-minus-model residual plots have been scaled by the spectrum flux errors. The median reduced-χ^2 values in our Hα, Hβ and C IV fits are 0.96, 1.58, and 0.91 respectively and, in general, there are no strong features observable in the model residuals. The only significant features seen in the residual C IV spectra correspond to the location of narrow absorption-lines which were excluded in the fitting procedure.

Table 3.4 includes the line parameters of our best-fitting model for each line.

3.3.5 *Spectra removed from sample*

Through visual inspection we flagged and discarded the spectra of quasars for which reliable emission-line parameters could not be obtained.

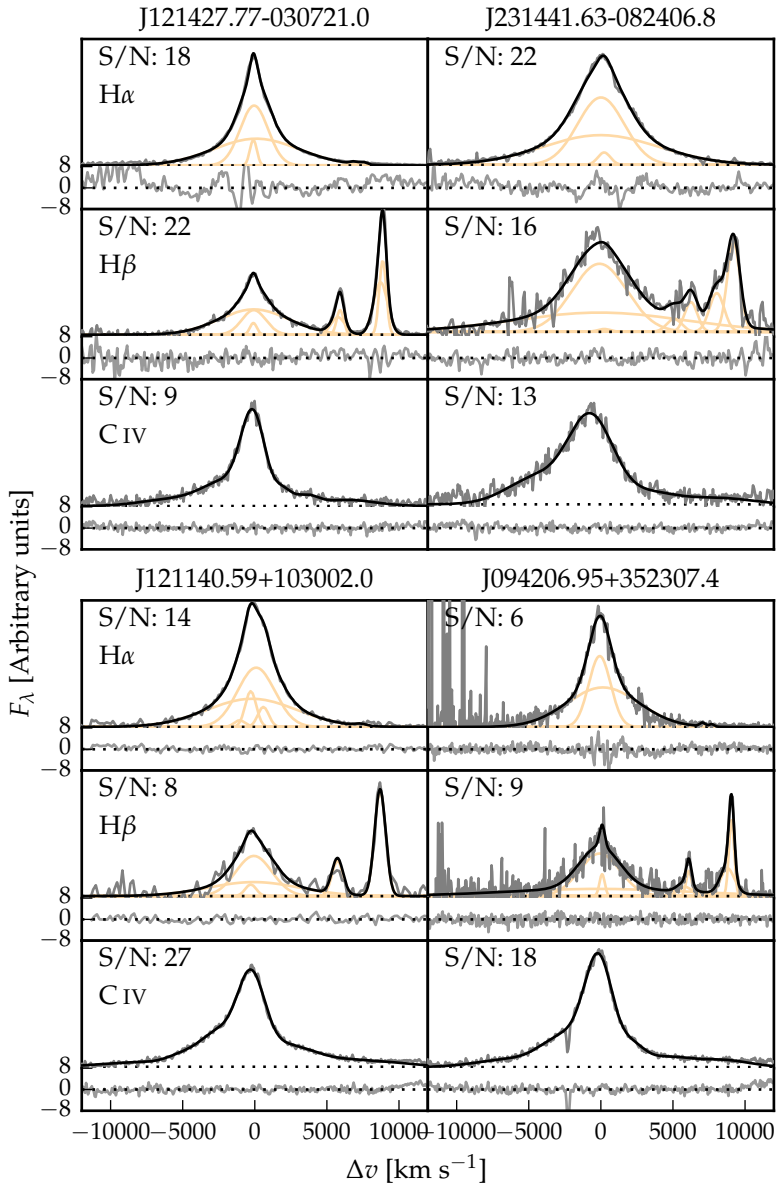

Figure 3.5: Model fits to continuum-subtracted Hα, Hβ, and C IV emission in four quasars. The data is shown in grey, the best-fitting parametric model in black, and the individual model components in orange. The centroid of the broad Hα emission is used to set the redshift, and Δv is the velocity shift from the line rest-frame transition wavelength. The S/N is indicated and is measured in a region of the continuum and quoted per 150 km s^{-1} pixel. Below each line we plot the data minus model residuals, scaled by the errors on the fluxes.

		Hα sample	Hβ sample
Total		194	279
Hα/Hβ	Wavelength	6	27
	S/N	8	83
C IV	Wavelength	6	5
	S/N	4	12
	Absorption	6	8
Total remaining		164	144

Table 3.2: The number of spectra removed from our sample by the cuts described in Section 3.3.5.

First, we flagged emission-lines in spectra that possessed insufficient S/N. A single minimum S/N threshold was not entirely effective and, instead, spectra were flagged when it was judged conservatively that no meaningful constraints could be placed on the velocity centroid and/or width of the emission-line.

Second, we flagged emission-lines where significant regions of the continuum and/or emission-line fell outside of the wavelength coverage of the spectra. Reliable continuum definition and subtraction is not straightforward for emission-lines so affected.

Third, we flagged C IV emission-lines because of strong, narrow absorption close to the peak of the line where reliable interpolation across the absorption, using our parametric model, was not possible.

The number of spectra that are removed by each cut is given in Table 3.2 and the distribution in redshift and luminosity is shown in Figure 3.6. Unsurprisingly, there is a preferential removal of intrinsically faint quasars, whose spectra can be of poorer S/N, and a loss of quasars at redshifts $z \sim 2.6$ where the Hα emission falls at the edge of the K-passband. Hβ is much weaker than Hα, and the Hβ spectra are generally of lower S/N. As a result, the fraction of Hβ spectra that are flagged – 39 per cent – is particularly high.

3.3.6 *Emission-line parameter uncertainties*

To calculate realistic uncertainties on our fitted variables, accounting for potential sources of systematic error such as the continuum subtraction, we employed a Monte Carlo approach. One thousand artificial spectra were synthesised, with the flux

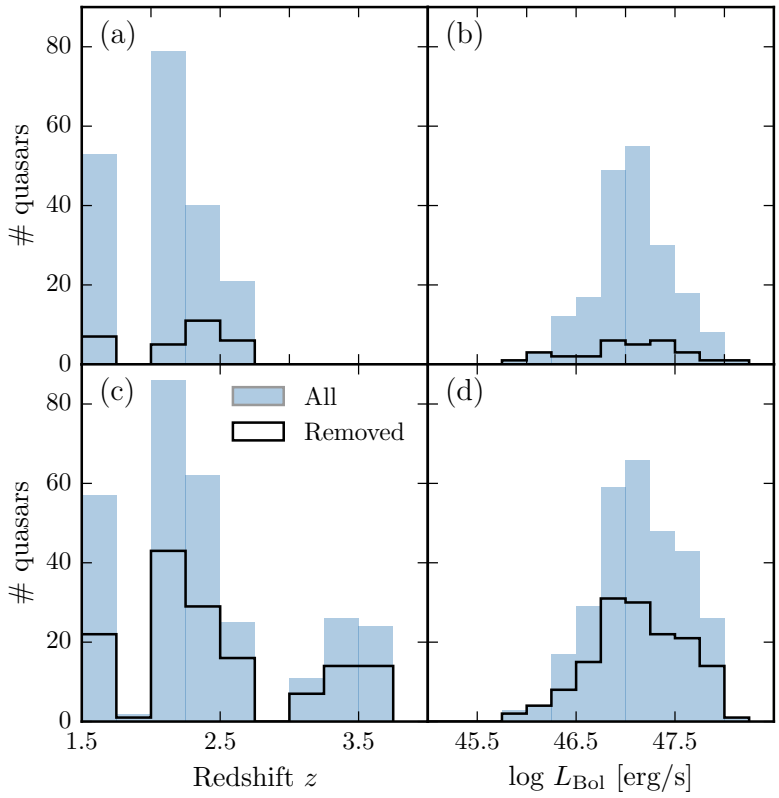

Figure 3.6: The redshift and luminosity distributions of the spectra removed from our Hα/C IV (a, b) and Hβ/C IV (c, d) samples.

at each wavelength drawn from a Normal distribution (mean equal to the measured flux and standard deviation equal to the known error). Our emission-line fitting recipe was then implemented on each of these mock spectra. The uncertainty in each parameter is given by the spread in the best-fitting values from the one thousand realisations of the fitting routine. In some cases the standard deviation of the parameter distribution was biased by extreme values caused by bad fits[3]. We therefore chose to measure the spread in the parameter distribution by fitting a composite model with two Gaussian components – one to model uncertainty in the parameter and the other any possible outlier component. The uncertainty in each line parameter

3 In the analysis of the real spectra such fits are identified via visual inspection.

was then taken to be the width of the narrower Gaussian. The uncertainties on all derived quantities, such as the BH mass, are propagated through by assuming that the uncertainties are uncorrelated and independent.

3.3.7 *Contemporaneity of spectra*

The epochs of the near-infrared and optical spectra can differ by many years. For example, the NTT SOFI spectra were taken ~ 14 years after the SDSS spectra, and the VLT SINFONI spectra 20 years or more after the Hamburg-ESO observations[4]. If the broad emission-line profiles varied significantly on these time-scales the relation between the C IV and Balmer line-width measurements could be blurred.

Cases do exist of dramatic changes in quasar spectra over short time-scales, but this phenomenon is rare (MacLeod et al., 2016). In our spectroscopic catalogue there are 112 SDSS DR7 quasars which are re-observed in BOSS and included in the DR12 quasar catalogue. The mean time elapsed between the two sets of observations is ~ 8 years. The root-mean-square difference in the C IV FWHM measured from the BOSS and SDSS spectra is a modest $\simeq 500\,\mathrm{km\,s^{-1}}$. Differences in the S/N of the spectra will make a substantial contribution and the scatter due to true variations in the C IV velocity-width will be significantly smaller than $500\,\mathrm{km\,s^{-1}}$. We conclude therefore that any intrinsic changes with time do not materially affect the emission-line measurements.

3.3.8 *Quasar monochromatic luminosity*

Computing virial BH masses also requires the quasar luminosity in an emission-line free region of the continuum adjacent to the broad line being used. The luminosity is used as a proxy for the size of the BLR. The monochromatic continuum flux is generally measured at 1350 Å for C IV and 5100 Å for Hα and Hβ. The calculation of these luminosities is described in Chapter 2.

As described in Chapter 2, we estimate the uncertainties on the monochromatic luminosities to be ~ 0.3 dex. Given that the luminosity enters into the calculation of BH mass only as the square-root, the uncertainty on the luminosities does not make

4 Time differences in the quasar rest-frame are reduced by a factor of $(1+z)$.

a large contribution to the uncertainties in the BH mass estimates.

3.3.9 *Characterising the emission-line widths*

There has been a considerable degree of attention paid to the effectiveness of different velocity-width measures of the C IV-emission; specifically, the line FWHM and the dispersion, σ, derived from the second-moment velocity (e.g. Assef et al., 2011; Denney et al., 2013). The FWHM and line dispersion trace different parts of the broad line velocity field, with the FWHM relatively more sensitive to any low-velocity core present and the line dispersion relatively more sensitive to the high velocity wings. In practice, the line dispersion is almost certainly a more robust velocity indicator when the assumptions underlying the virial-origin of the emission-line velocity width are true and the spectral S/N and resolution are adequate. This was demonstrated by Denney et al. (2013) for a sample of quasars possessing a significantly smaller range in C IV-blueshift than investigated here.

In reality, however, as highlighted by Denney (2012), contributions to the C IV emission-line profile from gas where virial motions do not dominate can be significant. Looking to the future, the results of the new reverberation-mapping projects (Shen et al., 2015; King et al., 2015) will show what fraction of the C IV emission-line, as a function of velocity, does reverberate for quasars with an extended range of C IV emission shapes. The derivation of quantitative corrections to transform velocity-width measures from single-epoch to reverberation-only line profiles should then be possible.

As such information is not yet available, there is a strong rationale for investigating whether the systematic changes in the C IV emission-line profile can be used to improve the single-epoch BH mass estimates derived using the C IV line. In Figure 3.7 we show how the C IV FWHM, line dispersion, σ, and line shape, FWHM/σ, vary as a function of the blueshift. The C IV FWHM is correlated with the blueshift, with the median FWHM of quasars with the largest blueshifts a factor of $2-3$ higher than quasars with only moderate blueshifts. The dispersion, however, does not show a similarly strong systematic variation.

Without knowledge of the C IV-blueshifts, the dynamic range present in the FWHM and line dispersion measurements ac-

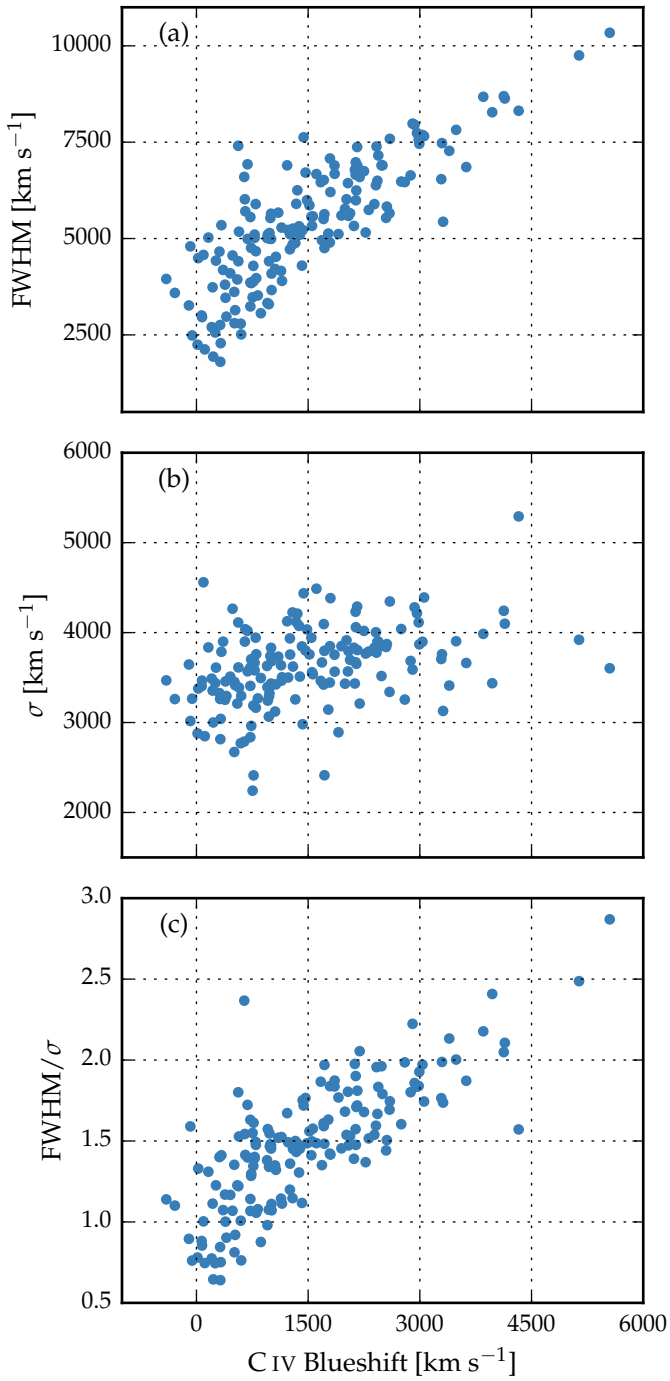

Figure 3.7: FWHM, dispersion (σ) and shape (FWHM/σ) of C IV as a function of the C IV blueshift.

cords with the expectations from the study of Denney et al. (2013); the factor of $\simeq 4$ spread in the FWHM measurements indicating greater sensitivity to the emission-line profile shape than is the case for the dispersion, which varies by a factor of only $\lesssim 2$. Adopting a value of $1200\,\mathrm{km\,s^{-1}}$ to define 'low' and 'high' blueshift, the median C IV-emission dispersion for the low and high-blueshift samples differ by only 10 per cent. It follows, therefore, that while the dispersion provides a relatively line-profile independent measure of the velocity width for quasars where the underlying assumption regarding the virial-origin of the velocity width applies, quasars where the assumption is not true can be assigned apparently normal velocity-widths and hence potentially incorrect BH masses.

To emphasise this point, in Figure 3.8 we overlay the C IV line profiles of J123611+112922 and J152529+292813, whose dispersions are indistinguishable (4168 ± 271 and $4303 \pm 128\,\mathrm{km\,s^{-1}}$ respectively). Notwithstanding the very similar dispersion values, the emission-line velocity fields differ dramatically and, therefore, the dispersion values cannot be measuring accurately the virial-induced velocity spread of the C IV emission in both quasars.

The analysis here, building on earlier work (including Sulentic et al., 2007; Shen and Liu, 2012), confirms a link between C IV emission-line shape and blueshift, raising the prospect of developing a blueshift-dependent correction to single-epoch BH mass estimates based on the C IV line. Expressed in another way, we are interested in testing if the significant systematic change in line shape as a function of C IV blueshift can be used to provide improved single-epoch BH masses from the C IV emission-line. The tightness of the correlation we observe between the C IV FWHM and blueshift implies that such an approach may be more effective than using the C IV emission-line velocity dispersion without reference to blueshifts. A further practical advantage is that, given the typical S/N of current survey-quality spectra, virial BH mass estimates for high-redshift quasars are usually based on the FWHM rather than the dispersion (e.g. Shen et al., 2011), which, being strongly affected by the continuum placement, is often found to be difficult to measure robustly (e.g. Mejía-Restrepo et al., 2016).

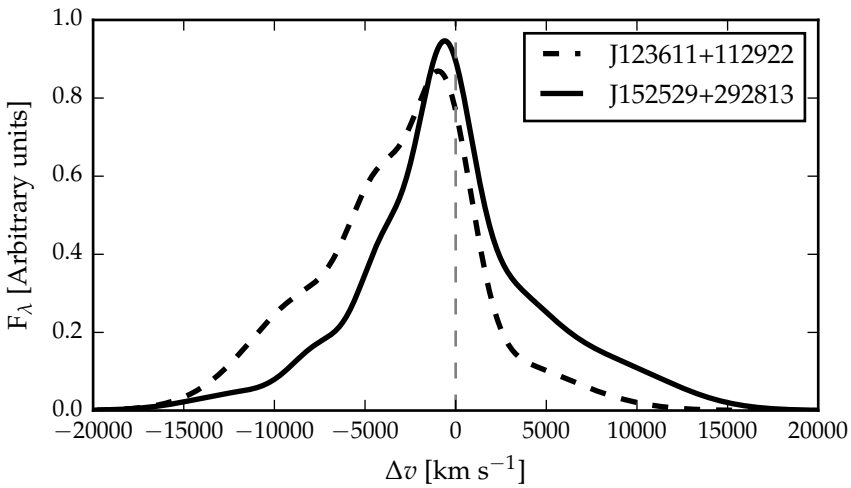

Figure 3.8: Comparison of the C IV line profiles of J123611+112922 and J152529+292813. Notwithstanding the essentially identical dispersion values, the emission-line velocity fields differ dramatically and, therefore, the dispersion values cannot be measuring accurately the virial-induced velocity spread of the C IV emission in both quasars.

3.4 AN EMPIRICAL CORRECTION TO C IV-BASED VIRIAL BH MASS ESTIMATES

3.4.1 *Hα/Hβ FWHM comparison*

BH mass calibrations which use the width of the broad Hβ emission-line as a proxy for the virial velocity are widely regarded as the most reliable, since most reverberation mapping employs the Hβ line and the $R_{BLR} - L$ relation has been established using Hβ. When Hβ is not available, Hα has been shown to be a reliable substitute (e.g. Greene and Ho, 2005b; Shen et al., 2011; Shen and Liu, 2012).

We first compared the typical Hα and Hβ profiles by constructing composite spectra. Individual continuum- and Fe II- (Hβ only) subtracted spectra were first de-redshifted to the quasar rest-frame, and then interpolated on to a common wavelength grid with a 1 Å resolution. The spectra were scaled by the mean flux in the interval 4700-5100 Å (Hβ) and 6400-6800 Å (Hα). The Hα and Hβ lines in the median composite spectra are shown in Figure 3.9. Hβ has a significantly broader profile than Hα in the composite spectra. This is to be expected if

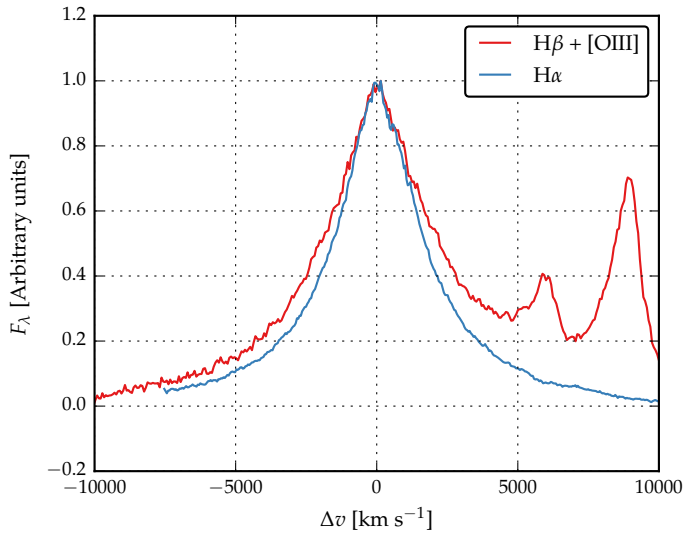

Figure 3.9: The Hα and Hβ emission-line regions in the median composite spectrum, shown as function of the velocity shift from the respective predicted line peak wavelengths. The background continuum and optical Fe II emission (Hβ only) has been modelled and subtracted. The line fluxes have been scaled in order for the profile shapes to be readily compared.

the density and/or ionisation parameter[5] in the BLR decreases with increasing radii, because Hβ is emitted preferentially over Hα when the density and/or ionisation parameter is higher (e.g. Osterbrock, 1989).

In our sample, we have 99 quasars with reliable measurements of both Hα and Hβ lines. The line widths in individual objects are compared in Figure 3.10 and, as expected, a tight correlation is observed. Greene and Ho (2005b), using a sample of 162 quasars with high S/N SDSS spectra at $z < 0.35$, established the following relation between the Hα and Hβ FWHMs:

$$\mathrm{FWHM(H\beta)} = (1.07 \pm 0.07) \times 10^3 \left(\frac{\mathrm{FWHM(H\alpha)}}{10^3\ \mathrm{km\ s^{-1}}} \right)^{(1.03 \pm 0.03)} . \quad (3.5)$$

The relation is shown as the dashed line in Figure 3.10. The root-mean-square scatter about this relation is 0.07 dex, compared to the ~ 0.1 dex reported by Greene and Ho (2005b). However, we find a systematic offset, in the sense that the Hβ line-widths

5 Ionisation parameter: the ratio of the ionising photon number density to the particle density (e.g. Peterson, 1997).

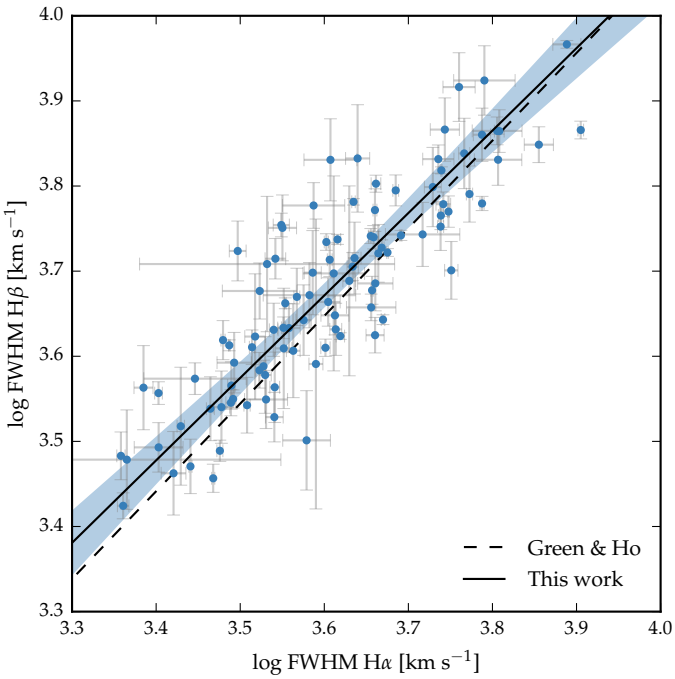

Figure 3.10: Comparison of Hα and Hβ FWHM measurements for 99 quasars. The solid line is our best-fitting power-law model, and the blue-shaded region shows the 2-σ uncertainties on the model parameters. The dashed line is the relation found by Greene and Ho (2005b) using a sample of $z < 0.35$ SDSS AGN.

we measure are on average larger by 270 km s^{-1} than predicted by the Greene and Ho (2005b) relation. As our sample covers higher redshifts and luminosities than the sample in Greene and Ho (2005b), we derive a new relation between the Hα and Hβ FWHMs.

We assume a relation of the same form used by Greene and Ho (2005b), i.e. a simple power-law, and infer the model parameters by fitting a linear model (with slope α and intercept β) in log-log space. The fit is performed within a Bayesian framework described by Hogg, Bovy, and Lang (2010). Each data point is treated as being drawn from a distribution function that is a convolution of the projection of the point's covariance tensor, Σ_i^2, with a Gaussian of variance V representing the intrinsic variance in the data. The log-likelihood is then given by

$$\ln\mathcal{L} = -\sum_{i=1}^{N} \frac{1}{2}\ln\left[2\pi\left(\Sigma_i^2 + V\right)\right] - \sum_{i=1}^{N} \frac{\Delta_i^2}{2[\Sigma_i^2 + V]} \tag{3.6}$$

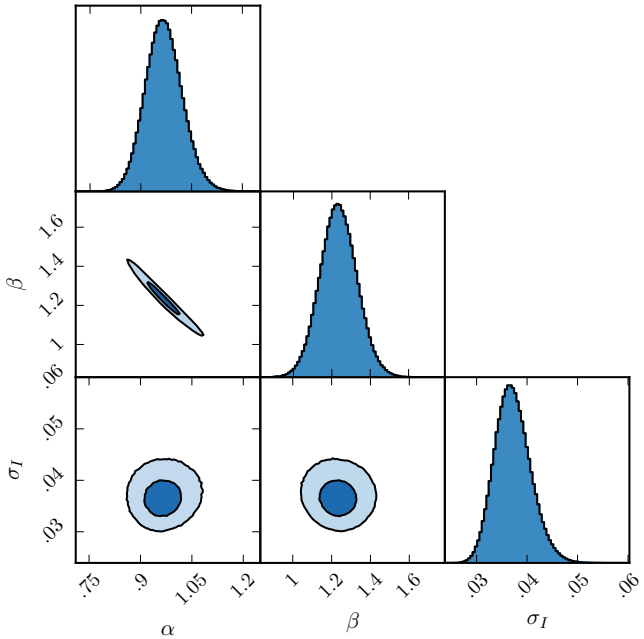

Figure 3.11: One- and two-dimensional projections of the MCMC sampling of the posterior distribution from the fit to FWHM(Hα) and FWHM(Hβ) (Figure 3.10). α is the power-law index, 10^{β} is the normalisation, and σ_I is the intrinsic scatter. In the two-dimensional projections, 1- and 2-σ contours are shown.

where Δ_i is the orthogonal displacement of each data point from the linear relationship. An advantage of this approach is that it allows a proper treatment of the measurement errors on both variables, which in this case are comparably large. The model also makes the reasonable assumption that there is an intrinsic scatter in the relationship between the variables that is independent of the measurement errors. Following the suggestion by Hogg, Bovy, and Lang (2010), the linear model was parametrized in terms of $(\theta, b_\perp)$, where θ is the angle the line makes with the horizontal axis and $b_\perp$ is the perpendicular distance from the line to the origin. Uniform priors were placed on these parameters, and the Jeffreys prior (the inverse variance) was placed on the intrinsic variance. The posterior distribution was sampled using a Markov Chain Monte Carlo (MCMC) method using the Python package `emcee` (Foreman-Mackey et al., 2013).

The one- and two-dimensional posterior distributions are shown in Figure 3.11. The solid line in Figure 3.10 is the maximum likelihood solution

$$\mathrm{FWHM}(\mathrm{H}\beta) = (1.23 \pm 0.10) \times 10^3 \left(\frac{\mathrm{FWHM}(\mathrm{H}\alpha)}{10^3 \mathrm{km\,s^{-1}}}\right)^{0.97\pm0.05} \tag{3.7}$$

and the shaded region shows the 2-σ uncertainties on the model parameters.

As discussed above, our relation is displaced to slightly higher Hβ FWHM than the Greene and Ho (2005b) relation – the offset is 210 km s^{-1} for a quasar with Hα FWHM 4500 km s^{-1}. We infer a power-law index that, although slightly shallower, is consistent with the Greene and Ho (2005b) index within the quoted uncertainties. The intrinsic scatter in the data, σ_I, we infer from the fit is 0.04 dex. This is smaller than the total scatter seen in Figure 3.10 (0.06 dex), which suggests that measurement errors make a significant contribution to the total scatter in the relation.

For 19 of the 99 quasars with Hβ and Hα emission profiles, one of the two Gaussians used to reproduce the Hβ profiles has a FWHM greater than 20 000 km s^{-1} and a fractional contribution to the total Hβ broad line flux greater than 30 per cent (Marziani et al., 2009; Marziani et al., 2013). The very broad Hβ-component, which is not seen in the Hα profiles, may be an artefact of the fitting scheme. A particular issue for Hβ is the presence of Fe II emission, often at a significant level. Furthermore, additional lines could be contributing to the underlying continuum (e.g. the He I$\lambda\lambda$4922,5017 doublet; Véron, Gonçalves, and Véron-Cetty, 2002; Zamfir et al., 2010). If the Hβ FWHM is calculated only from the narrower of the two Gaussian components, then the Hβ FWHM decreases by 630 km s^{-1} on average, and the new relationship between the Hα and Hβ FWHM is much closer to one-to-one. The C IV FWHM relative to the Hα/Hβ FHWM will be enhanced by $\sim$ 15 per cent, and so the C IV-based BH masses relative to the Balmer-based masses will increase by $\sim$ 30 per cent.

3.4.2 *Measuring the quasar systemic redshift*

An accurate measure of the quasar's systemic redshift is required in order for the blueshift of the C IV emission-line to be determined. Balmer emission centroids are available for all

quasars in the catalogue and so we use this to define the systemic redshift.

For 62 and 86 quasars in the Hα and Hβ samples respectively narrow [O III] emission is also detected with sufficient S/N to measure the line centroid. In the model fit to the Hβ region the velocity centroids of the broad Hβ-line and the core component of the [O III] emission were deliberately determined separately. We find the intrinsic difference in the velocity centroids of the Hα and Hβ emission and the narrow [O III] emission to have a dispersion of 300 and 400 $\mathrm{km\,s^{-1}}$, which is very similar to the value found by Shen et al. (2016). However, the velocity centroid of the narrow component of the [O III] emission is blueshifted by on average 250 $\mathrm{km\,s^{-1}}$ relative to the centroid of the broad Balmer line. Applying our parametric model fitting routine to the composite spectrum from Hewett and Wild (2010), which is constructed using relatively low redshift SDSS quasars with $L_{\mathrm{Bol}} \sim 10^{44}\,\mathrm{erg\,s^{-1}}$, the centroids of the broad component of Hβ and the narrow component of [O III] are found to be at essentially identical velocities, suggesting that the blueshifting of narrow [O III] could be luminosity dependent.

As described in Section 3.3, the broad components of Hα and Hβ were modelled with up to two Gaussians, with identical velocity centroids. We also tested models with no constraints on the centroids of the two broad Gaussians, and measured the systemic redshift from the peak of the composite profile. With this set of models, the median difference between the [O III]- and Hα(Hβ) based redshift estimates is reduced to $-100(-120)\,\mathrm{km\,s^{-1}}$, with a $290(320)\,\mathrm{km\,s^{-1}}$ scatter. This suggests that there is a $\sim 100\,\mathrm{km\,s^{-1}}$ systematic error in our Balmer-based redshift estimates. Regardless, since both the systematic offset and the scatter are small in comparison to the dynamic range in C IV blueshifts ($\sim 5000\,\mathrm{km\,s^{-1}}$), the blueshift-based empirical correction we will derive does not depend on whether the broad Balmer emission or the [O III] centroid is used to define the systemic redshift, or how the broad Balmer emission is parametrised.

3.4.3 *Balmer/C IV line widths as a function of C IV-blueshift*

In this section, we directly compare the C IV and Hα/Hβ line widths as a function of the C IV blueshift. Because virial BH mass estimates are generally based on the Hβ FWHM, we first convert our Hα FWHM measurements into equivalent

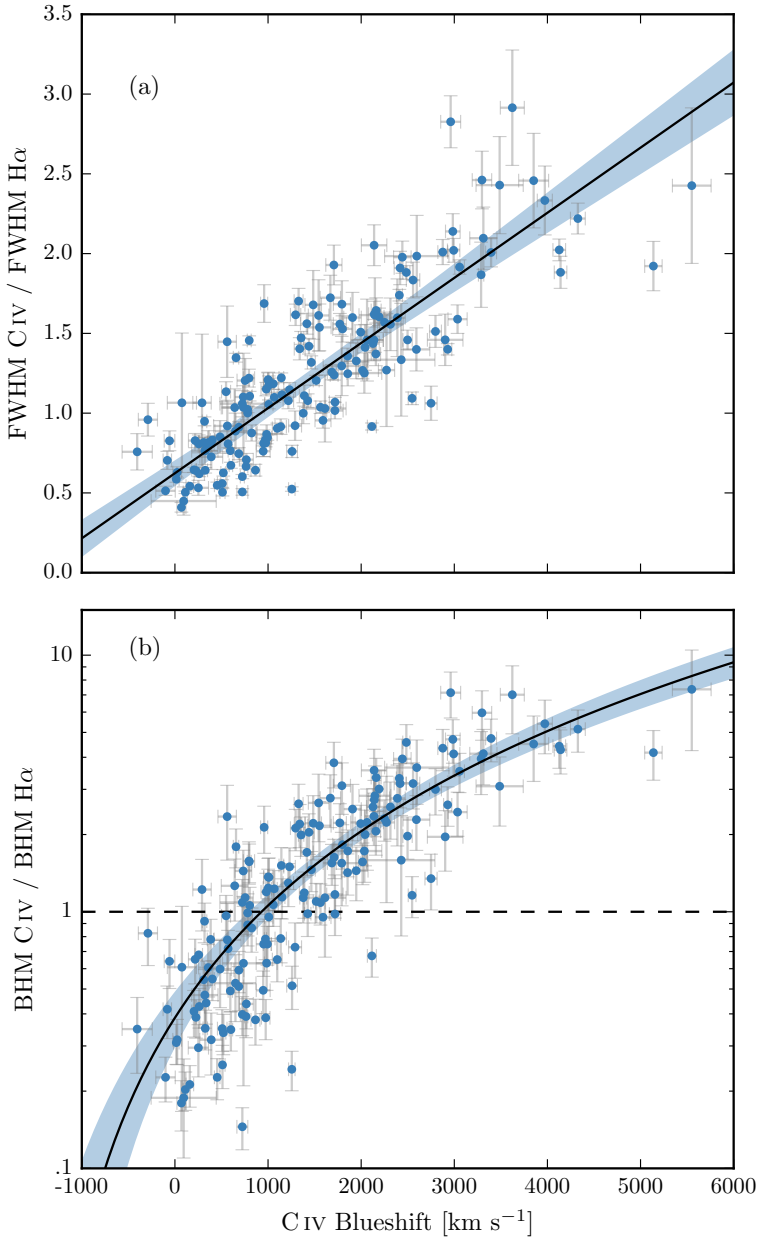

Figure 3.12: C IV FWHM relative to Hα FWHM (a), and C IV based BH mass (BHM) compared to Hα based mass (b), both as a function of the C IV blueshift. The black line is our best-fit linear model, and the shaded region shows the 2-σ uncertainties on the slope and intercept. The Hα FWHM have been scaled to match the Hβ FWHM using Equation 3.7.

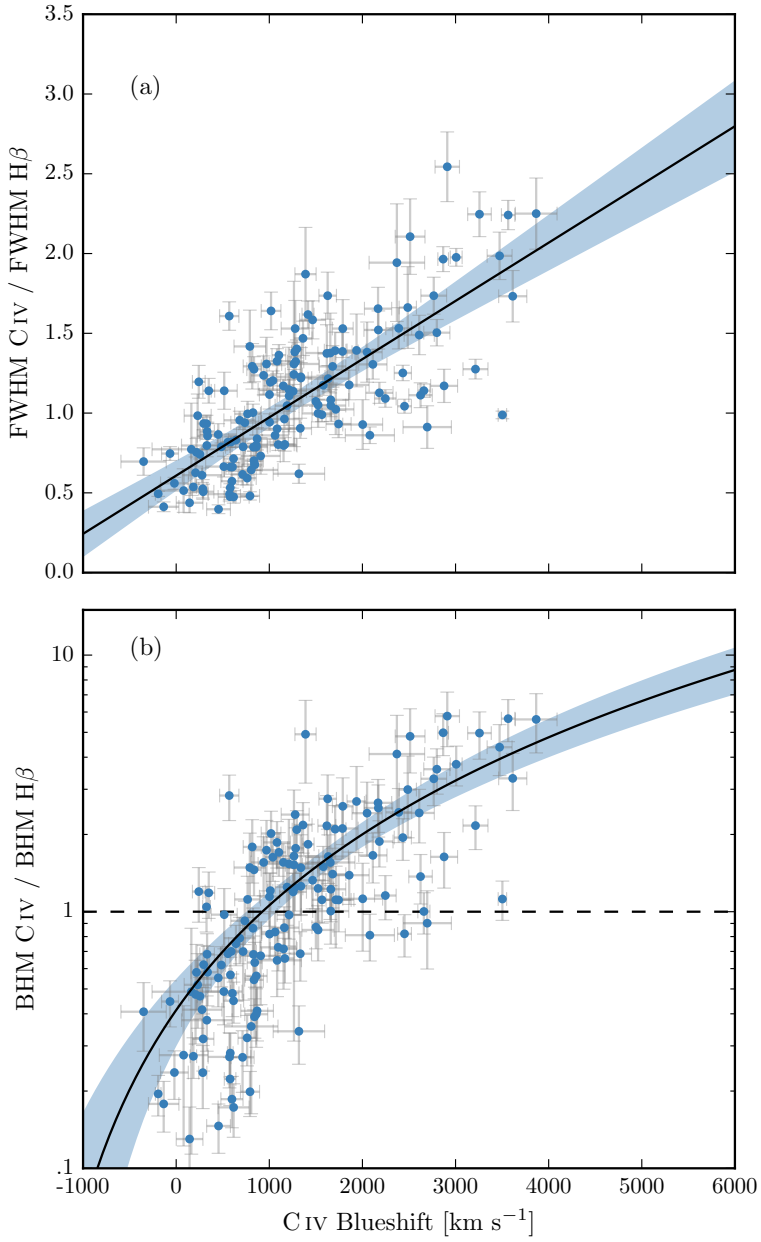

Figure 3.13: C IV FWHM relative to Hβ FWHM (a), and C IV based BH mass (BHM) compared to Hβ based mass (b), both as a function of the C IV blueshift.

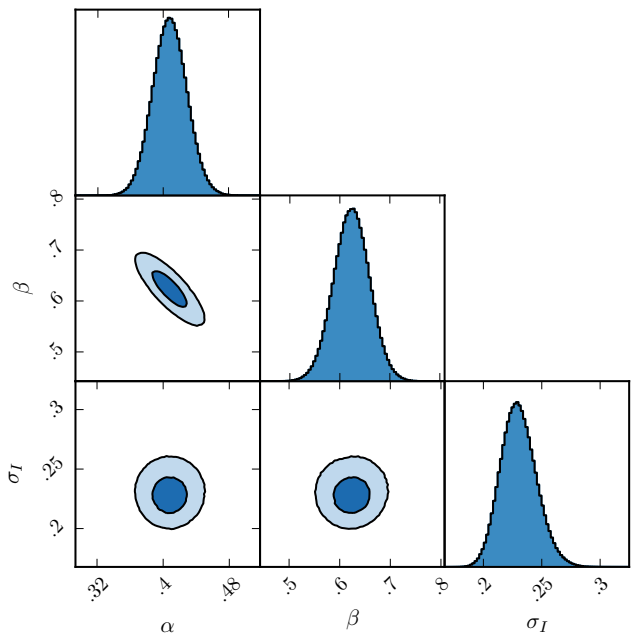

Figure 3.14: One- and two-dimensional projections of the MCMC sample of the posterior distribution from the linear fit to FWHM(C IV)/FWHM(Hα) as a function of the C IV blueshift. α is the gradient, β the y-intercept, and σ_I the intrinsic scatter. In the two-dimensional projections we show 1- and 2-σ contours. The posterior distribution for the linear fit to FWHM(C IV)/FWHM(Hβ), which we do not show, has a very similar appearance.

Hβ FWHM using Equation 3.7. In Figures 3.12a and 3.13a we show the C IV FWHM relative to both the (Hβ-scaled) Hα FWHM and the Hβ FWHM, as a function of the C IV blueshift.

Employing the same Bayesian fitting framework described in Section 3.4.1, we fit independent linear models to the C IV FWHM relative to the Hα and Hβ FWHM as a function of the C IV blueshift. As before, our model has an additional parameter representing any intrinsic scatter in the relationship between the variables which is independent of measurement errors. We also tested a model where some fraction of the data points (which is free to vary) is drawn from an outlier distribution, represented by a broad Gaussian centred on the mean of the data. We found, however, that the inferred outlier fraction was very low (0.004, corresponding to ~ 0.7 data points) and so did not include such a component in our model.

In Figure 3.14 we show the one- and two-dimensional projections of the posterior distribution from the linear fit to FWHM(C IV)/FWHM(Hα) as a function of the C IV blueshift. The projections from the FWHM(C IV)/FWHM(Hβ) fit, which we do not show, have very similar appearances. In Figure 3.12a we plot the maximum likelihood model and the 2-σ uncertainties on the model parameters. The maximum likelihood line is given by

$$\mathrm{FWHM(C\,IV, Corr.)} = \frac{\mathrm{FWHM(C\,IV, Meas.)}}{(0.41 \pm 0.02)\left(\frac{\mathrm{C\,IV\,Blueshift}}{10^3\,\mathrm{km\,s^{-1}}}\right) + (0.62 \pm 0.04)} \tag{3.8}$$

for the C IV/Hα fit and

$$\mathrm{FWHM(C\,IV, Corr.)} = \frac{\mathrm{FWHM(C\,IV, Meas.)}}{(0.36 \pm 0.03)\left(\frac{\mathrm{C\,IV\,Blueshift}}{10^3\,\mathrm{km\,s^{-1}}}\right) + (0.61 \pm 0.04)} \tag{3.9}$$

for the C IV/Hβ fit. In the above relations, FWHM(C IV, Corr.) is the FWHM of Hα or Hβ obtained from the C IV FWHM and blueshift, using the fitted relation. The intercepts of the Hα- and Hβ-based relations are statistically consistent, while the difference between the slopes is only marginally inconsistent given the quoted uncertainties.

The intrinsic scatter in the data about the linear relation we infer is 0.23 ± 0.02 and 0.25 ± 0.02 for the Hα and Hβ fits respectively. The intrinsic scatter for the Hα fit is represented by the Normal probability density distribution shown in Figure 3.15. In the same Figure, we show the distribution of the orthogonal displacement of each data point from the best-fitting linear relationship. The two distributions are well-matched, which demonstrates that our model is a good representation of the data and the measurement errors on the data points are small relative to the intrinsic scatter.

The overall (intrinsic and measurement) scatter about the best-fitting model is slightly higher when the C IV line-widths are compared to Hβ (0.12 dex) than when compared to Hα (0.10 dex). This is likely due, at least in part, to the generally higher S/N of the Hα emission. In addition, contributions from the strong [O III] doublet and from Fe II in the vicinity of Hβ make de-blending the Hβ emission more uncertain. As a consequence, for quasars where Hα and Hβ are both measured, the mean uncertainty on the Hα FWHM is $130\,\mathrm{km\,s^{-1}}$, compared to $340\,\mathrm{km\,s^{-1}}$ for Hβ.

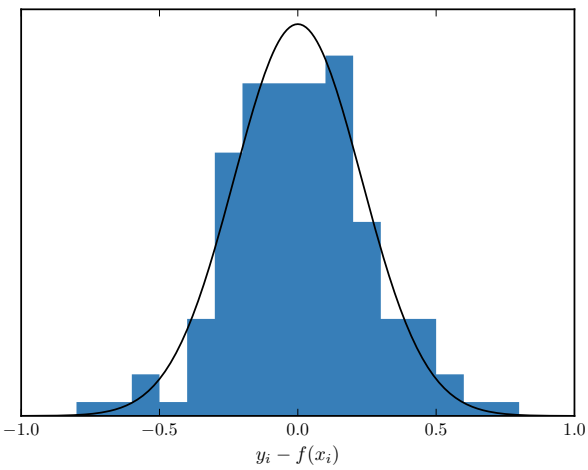

Figure 3.15: The distribution of the orthogonal displacement of each data point from the best-fitting linear relationship in the fit to FWHM(C IV)/FWHM(Hα) as a function of the C IV blueshift (blue histogram). The black curve is a Normal distribution with a width equal to the intrinsic scatter in the population inferred from the fit. The two distributions are well-matched, which demonstrates that our model is a good representation of the data and the measurement errors on the data points are small relative to the intrinsic scatter.

In the next section, we use both the Hα and Hβ lines to calculate unbiased BH masses. However, we use the Hα measurements to derive an empirical C IV blueshift based correction to the C IV masses (Equation 3.10) because of the issues related to the accurate modelling of the Hβ-profile just described. An extra advantage, which is evident in Figures 3.12a and 3.13a, is that the Hα sample has a better C IV blueshift coverage. However, as can be seen from the similarity of Equations 3.8 and 3.9, our results would not change significantly were we instead to use the Hβ sample.

3.4.4 *C IV-based virial BH mass estimates*

Virial BH masses were calculated using the widely adopted Vestergaard and Peterson (2006) calibrations. BH masses are computed using the line and continuum properties given in Table 3.4, and we convert our Hα emission-line velocity-width measures to predicted Hβ widths using Equation 3.7.

In Figures 3.12b and 3.13b the C IV-based estimates are compared to the Hα/Hβ estimates as a function of the C IV blueshift. There is a strong systematic error in the C IV-based masses as a function of blueshift, which is a direct consequence of the FWHM trend described in the previous section. The C IV emission-based BH masses are in error by a factor of more than five at 3000 km s^{-1} in C IV emission blueshift and the overestimate of the BH masses reaches a factor of 10 for quasars exhibiting the most extreme blueshifts, $\gtrsim$ 5000 km s^{-1}.

The virial product is the product of the virial velocity squared and the BLR radius (e.g. Shen, 2013), and is proportional to the BH mass. We use the corrected C IV FWHM given by Equation 3.8 as an indicator of the virial velocity, and adopt the same $R_{BLR} - L$ relation for the 1350 Å continuum luminosity as Vestergaard and Peterson (2006) (i.e. $R_{BLR} \propto L^{0.53}$). To find the constant scaling factor necessary to transform the virial product into a BH mass we compute the inverse-variance weighted mean difference between the virial products and the Hα-based masses. The virial BH mass can then be expressed in terms of the corrected C IV FWHM and monochromatic continuum luminosity at 1350 Å:

$$\mathrm{MBH(C\,IV, Corr.)} = 10^{6.71} \left(\frac{\mathrm{FWHM(C\,IV, Corr.)}}{10^3\ \mathrm{km\,s^{-1}}} \right)^2 \left(\frac{\lambda L_\lambda(1350\text{Å})}{10^{44}\ \mathrm{erg\,s^{-1}}} \right)^{0.53} \tag{3.10}$$

Given measured C IV emission-line FWHM and blueshift, Equations 3.8 and 3.10 can then be used to provide an unbiased estimate of the quasar BH mass.

3.4.5 *C IV-derived BH masses at low C IV blueshift*

Reverberation mapping measurements of nearby AGN have revealed the BLR to be stratified, with high-ionisation lines, including C IV, emitted closer to the BH than low-ionisation lines, including Hα and Hβ (e.g. Onken and Peterson, 2002). Vestergaard and Peterson (2006) found that the C IV-emitting region is at approximately half the radius of the Hβ/Hα emitting region. Given the $\Delta V \propto R_{BLR}^{-0.5}$ virial relation, this leads to the prediction that the C IV line widths should be $\simeq$ 1.4 times broader than Hα/Hβ for a given BH mass, and this expectation is reflected in the relative normalisations of the Vestergaard and Peterson (2006) C IV- and Hβ-based BH mass calibrations.

In our sample, the median C IV/Hα FWHM ratio is 0.97 ± 0.31 for the 77 quasars with C IV blueshifts $< 1200\,\mathrm{km\,s^{-1}}$. This is significantly smaller than the predicted value of 1.4. As a direct consequence of the empirically small C IV/Hα FWHM ratio, the C IV-derived BH mass estimates are systematically lower than the corresponding Hα-derived masses when the blueshift is small. This can be seen in Figure 3.12b, where for almost every quasar with a C IV blueshift $<1200\,\mathrm{km\,s^{-1}}$, the C IV-derived BH mass is smaller than the corresponding Hα-derived mass.

Denney (2012) used multiple-epoch spectra from reverberation mapping campaigns to isolate the part of the C IV profile which is varying. In some profiles they identified a non-varying core component, possibly originating from gas at larger radii than the BLR. In single-epoch spectra, both parts of the line – varying and non-varying – contribute to the measured FWHM. The gas at larger radii will enhance the profile at lower-velocity and lead to smaller FWHM values. This could explain the low C IV/Hα FWHM ratio observed in quasars with small C IV blueshifts.

3.5 PRACTICAL APPLICATION OF THE C IV-BASED BH MASS CORRECTION

3.5.1 *Recipe for unbiased C IV based BH masses*

3.5.1.1 *Measuring the systemic redshift*

Equations 3.8 and 3.10 together provide an un-biased estimate of the virial BH mass given the FWHM and blueshift of C IV, together with the continuum luminosity at 1350 Å. The FWHM is readily obtained, either directly from the data, or, via the fitting of a parametric model to the C IV emission-line. The blueshift – defined as the bisector of the cumulative line flux – is also straightforward to measure and our preferred procedure is described in Section 3.5.1.2. The only potential complication arises in establishing the quasar systemic redshift and hence defining the zero-point for the C IV-blueshift measurement, since both the blueshift and the systemic redshift cannot be determined from C IV alone. In practice, when rest-frame optical lines are accessible, as is the case for the quasar sample here, an accurate systemic redshift can be obtained. The [O III] doublet and the Balmer lines all have velocity centroids very close to systemic, and the same is true for the broad Mg II doublet. For quasars at

very high redshifts, $z \sim 6$, systemic redshifts can also be derived using the [C II] 158 μm emission in the sub-millimetre band (e.g. Venemans et al., 2016). However, in general, for example in determining the BH masses of quasars at redshifts $z > 2$, if only the rest-frame ultra-violet region is available determining a reliable systemic redshift is non-trivial.

The SDSS DR7 pipeline redshifts are not sufficiently reliable to measure the C IV blueshift accurately because, in part, the C IV emission-line itself contributes to the determination of the quasar redshifts. This is demonstrated in Figure 3.16a, in which we plot the C IV-blueshift versus C IV-emission EQW using the SDSS pipeline redshifts and the blueshifts calculated by Shen et al. (2011). A strong trend in the blueshift values as a function of line EQW is not evident in Figure 3.16a; structure in the parameter space is being masked because the C IV emission-line is itself being used in the determination of the quasar redshifts.

The redshift-determination scheme of Hewett and Wild (2010) provided much improved redshifts, not least because the redshift estimates for the majority of quasars were derived using emission-lines other than the C IV-line itself. Figure 3.16b shows SDSS DR7 quasars in the same C IV parameter space as Figure 3.16a, but now using Hewett and Wild (2010) redshifts. The improved redshift estimates are predominantly responsible for the differences seen in Figures 3.16a and 3.16b; the appearance in Figure 3.16b of the extension to high blueshift for quasars with low C IV EQW is particularly evident.

Shen et al. (2016) and our own work shows that there is an intrinsic variation of $\sigma \simeq 220\,\mathrm{km\,s^{-1}}$ in the velocity centroids of the BLR emission-lines relative to a systemic-frame defined by emission-lines in the quasar NLR. The redshifts for quasars in the SDSS DR10 and DR12 catalogues (Pâris et al., 2014; Pâris et al., 2017) possess errors of $\simeq 500 - 750\,\mathrm{km\,s^{-1}}$ (Pâris et al., 2012; Font-Ribera et al., 2013). The impact of low spectrum S/N for fainter quasars in all the SDSS data releases increases the uncertainty further. Table 3.3 includes the values for the fractional error in the corrected BH mass that result from a given error in the determination of the systemic rest-frame. For example, the fractional error in the corrected BH mass is 0.39 for a quasar with a $1000\,\mathrm{km\,s^{-1}}$ C IV blueshift when there is a $500\,\mathrm{km\,s^{-1}}$ uncertainty in the quasar systemic redshift.

Of potentially more significance for studies of BH masses as a function of quasar and host-galaxy properties are redshift errors that depend on the form of the quasar ultra-violet

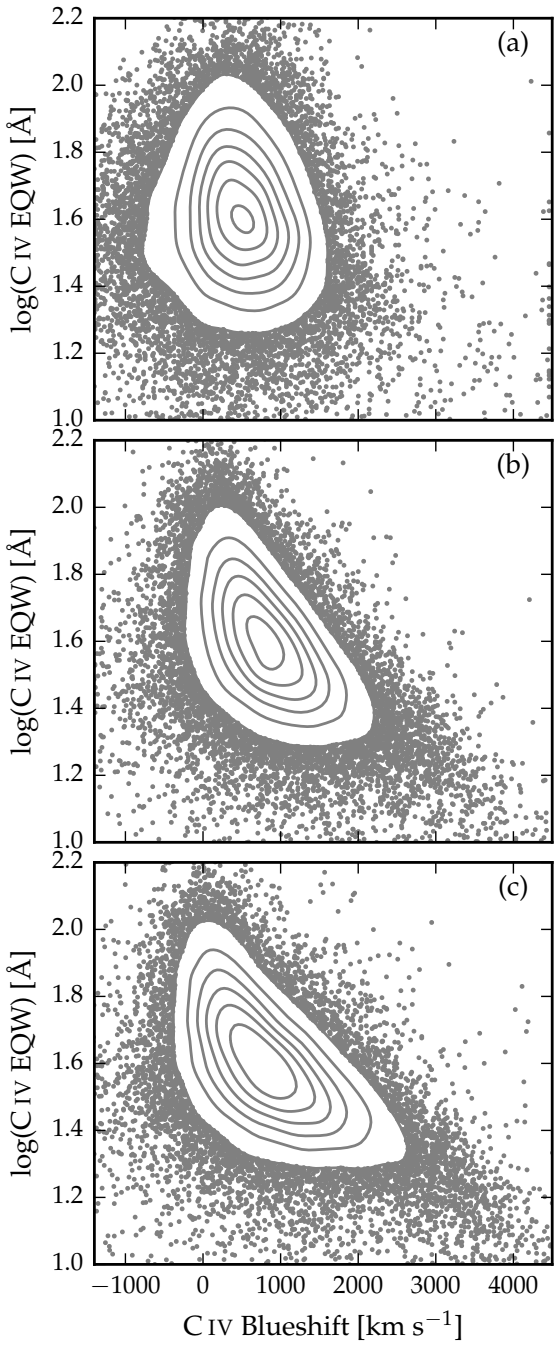

Figure 3.16: Rest-frame EQW versus blueshift of the broad C IV emission-line for 32,157 SDSS DR7 quasars at $1.6 < z < 3.0$. Panel (a) uses C IV line parameters from Shen et al. (2011) and SDSS pipeline systemic redshifts. Panels (b) and (c) use systemic redshifts from Hewett and Wild (2010) and Allen & Hewett (2017, in preparation) respectively, and C IV line measurements described in Section 3.5.1.2.

	C IV blueshift [km s^{-1}]			
δv [km s^{-1}]	0	1000	2000	4000
250	0.33	0.20	0.14	0.09
500	0.65	0.39	0.28	0.18
1000	1.30	0.79	0.57	0.36

Table 3.3: The fractional error on the corrected BH mass as a function of C IV blueshift for different uncertainties in the quasar systemic redshift.

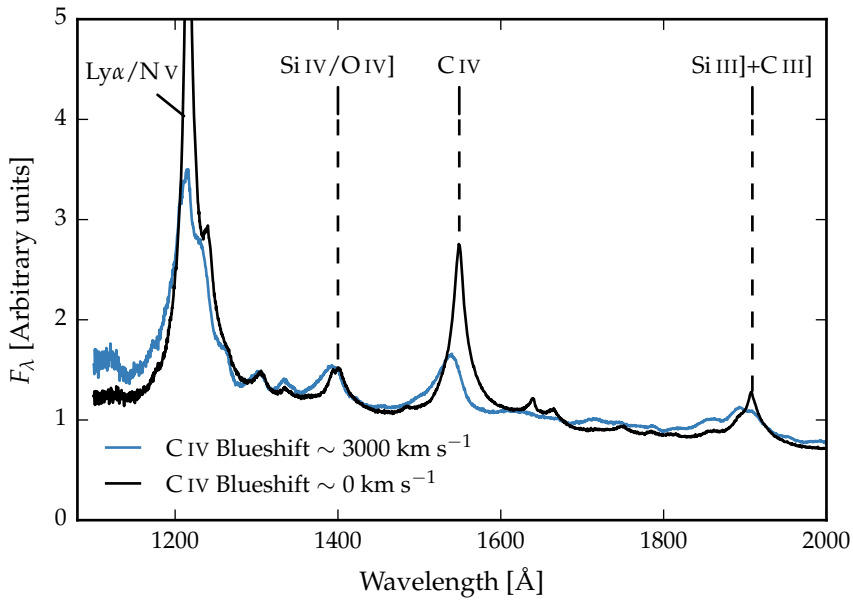

Figure 3.17: Composite spectra from Lyα to C III] for quasars with different C IV blueshifts. The systematic variation in the C IV shape is correlated with changes in the quasar SEDs, including the strengths of the Si III]λ1892 and C III]λ1908 emission-lines.

SED. The systematic variation in the C IV shape is correlated with changes in the quasar SEDs, including the strengths of the Si III]λ1892 and C III]λ1908 emission-lines in the rest-frame ultra-violet (Figure 3.17). As a consequence, the redshifts from Hewett and Wild (2010) still suffer from systematic errors that are correlated with the shape, and particularly the blueshift, of the C IV emission-line. For the Hewett and Wild (2010) redshifts, and ultra-violet emission-line based redshifts in general, quasars with large C IV EQW and modest blueshifts have rela-

tively small ($\simeq 300\,\mathrm{km\,s^{-1}}$) SED-dependent redshift errors. Redshift uncertainties as large as $\simeq 1000\,\mathrm{km\,s^{-1}}$ for such quasars are unusual and the large relative error in the corrected C IV BH mass given in Table 3.3 is pessimistic.

Conversely, systematic redshift errors are greatest for quasars with large blueshifts, reaching $\sim 750\,\mathrm{km\,s^{-1}}$ in the extreme for the Hewett and Wild (2010) values. The associated error in the corrected C IV BH masses is, however, mitigated somewhat due to the smaller gradient of the MBH(C IV)/MBH(Balmer) relation at large C IV blueshift (see Figures 3.12b and 3.13b). A definitive quantification of any systematic SED-dependent errors present in the quasar redshifts contained in the SDSS DR12 catalogue is not yet available but the principal component analysis (PCA) based redshift estimates are expected to be largely free of SED-dependent systematics.

Using published redshift estimates, notably those from Hewett and Wild (2010) for the SDSS DR7 quasars and the PCA-based redshifts from Pâris et al. (2017) for SDSS DR12, the correction formula given in Section 3.4.3 produces significant improvements to C IV-based BH mass estimates. In a forthcoming work, Allen & Hewett (2017, in preparation) will present a new redshift-estimation algorithm that produces redshifts independent of the C IV blueshift and other variations in the ultra-violet SEDs of luminous quasars. The low-ionization emission-lines visible in the rest-frame ultra-violet (over wavelengths from Mg II$\lambda\lambda$2796,2803 down to the O Iλ1304+Si IIλ1307 blend) using the new redshift-algorithm are located at rest-frame wavelengths in excellent agreement with the systemic redshift defined using the rest-frame narrow-line optical [O III] doublet and broad-line Hβ and Hα. SED-dependent systematic errors are below the apparent inherent dispersion of $\simeq 220\,\mathrm{km\,s^{-1}}$ associated with broad emission-line redshifts (Shen et al., 2016).

Figure 3.16c shows the C IV emission-line parameters calculated using the Allen & Hewett redshift-estimation algorithm. The systematic trends seen in Figure 3.16b, in particular the extension to high blueshift at low C IV EQW, become more apparent in Figure 3.16c, as expected from consideration of the known SED-related errors in the redshifts from Hewett and Wild (2010). A population of quasars with only modest blueshifts and low EQW is also apparently still present.

3.5.1.2 C IV *emission-line blueshift measurements*

The differences in the distribution of C IV emission-line properties seen in the three panels of Figure 3.16 are due primarily to the change in the systemic redshift estimates. It is also necessary, however, to obtain a measure of the C IV emission-line 'location' in order to calculate the blueshifts. When working with moderately-sized samples, parametric fits to the emission-line profile may be undertaken using careful mask-definition to minimise the effect of absorption features on the profiles used for the parametrisation, and this is the approach we followed in Section 3.3.

Effective analysis of the tens of thousands of spectra from SDSS DR7, and now DR12, however, requires a more robust scheme to determine a C IV-blueshift estimate that is not very sensitive to the range of S/N among the spectra or the presence of narrow absorption systems within the C IV-emission profile. Shen et al. (2011) provide a discussion (their section 3) of the factors that effect the measurement of broad emission-lines in quasar spectra of modest S/N. Their careful analysis of the C IV emission properties employed the results of parametric fits of three Gaussians to the spectra.

We take a different approach by adopting a non-parametric scheme to measure the blueshift of the C IV line. The continuum is first modelled and subtracted using the procedure described in Section 3.3.1. The C IV emission-line is taken to lie within the wavelength interval 1500-1600 Å. To reduce the impact of narrow absorption systems on the emission-line profile a 'pseudo continuum' is defined by applying a 41-pixel (~2800 km s^{-1}) median filter to the quasar spectrum. Pixels within the C IV profile that lie more than 2-σ below the pseudo-continuum are deemed to be affected by absorption and added to an 'absorber'-mask. Two pixels on either side of each such pixel are also included in the mask. For each masked pixel, the flux values in the spectrum are replaced by values from the pseudo-continuum[6]. The wavelength that bisects the cumulative total line flux is recorded and the blueshift computed using Equation 3.1.

Our experiments in quantifying the C IV emission properties of SDSS spectra show that this simple non-parametric measure of the C IV emission location reduces the number of outliers sig-

6 While the absorption identification and interpolation scheme is not effective for spectra that possess associated absorption spread over more than ~ 1200 km s^{-1}, objects containing C IV lines with such extensive absorption have been removed from the sample.

nificantly relative to the Gaussian-fitting scheme employed by Shen et al. (2011). Visual inspection of spectra demonstrate that the improvement is due primarily to the identification of, and interpolation over, associated and outflow absorption systems.

3.5.2 *Systematic trends in residuals*

The scatter about the best-fitting line in the FWHM(C IV)/FWHM(Hα) versus C IV-blueshift relation is $\sim$ 0.1 dex. With a view to reducing the scatter further, we searched for parameters which correlate with the scatter at fixed C IV blueshift, including the luminosity, redshift, [O III] EQW, and Fe II EQW. The only significant correlation we find is with the Hα FWHM (Figure 3.18). Quasars with broad Hα lines tend to lie below the relation while quasars with narrow Hα tend to lie above it. One possibility is that this correlation is simply due to random scatter (either intrinsic or measurement error) in the Hα FWHM which, with the other quasar properties fixed, would naturally produce a correlation between FWHM(C IV)/FWHM(Hα) and FWHM(Hα). However, the fact that we see no such correlation between the model residuals and the C IV FWHM suggests that the Hα FWHM correlation could be revealing something more fundamental. The Hα FWHM is part of the Boroson and Green (1992) EV1. Figure 3.18 suggests that part of the scatter between the Balmer and C IV velocity widths might be attributed to differences in the spectral properties which are correlated with EV1 (Marziani et al., 2013).

The shape of an emission-line can be characterised by the ratio FWHM/σ. FWHM/$\sigma \simeq 2.35$ for a Gaussian profile, while FWHM/$\sigma \simeq 1$ for a peakier Lorentzian profile[7]. In our sample, we find the model residuals and the Hα FWHM correlate with the shape of the line. The narrow lines are, on average, 'peakier' (with FWHM/$\sigma \simeq 1$) than the broader lines (with FWHM/$\sigma \simeq 2$). This suggests that the BLR structure (e.g. the balance between rotation, turbulence and radial motions) is changing with the emission-line FWHM (e.g. Collin et al., 2006; Kollatschny and Zetzl, 2011; Kollatschny and Zetzl, 2013). This raises the question of whether the Balmer-line FWHM is a reli-

7 Strictly FWHM/$\sigma \to 0$ for a Lorentzian profile, but values close to unity are typical when the dispersion is calculated over a velocity range, $\simeq \pm 10\,000\,\mathrm{km\,s^{-1}}$, used to parametrize broad emission-lines in quasar spectra.

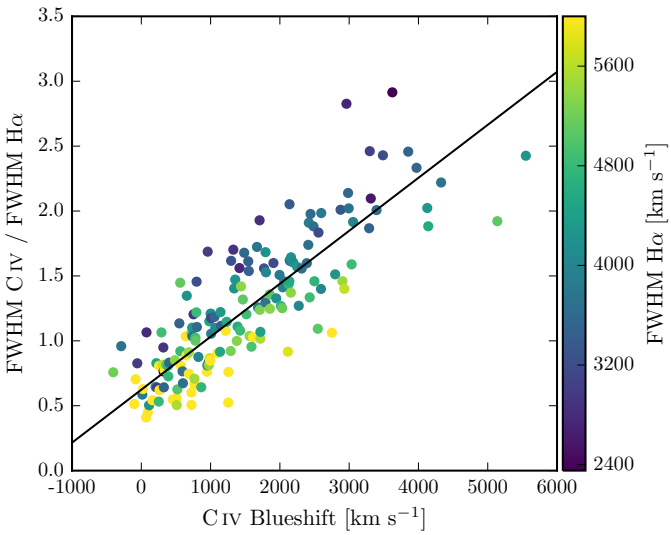

Figure 3.18: Same as Figure 3.12a, with the marker colour representing the Hα FWHM. At fixed C IV blueshift, there is a clear Hα FWHM dependent systematic in the model residuals.

able proxy for the virial-induced velocity dispersion for the full range of Balmer line shapes we have in our sample.

When calibrating the virial-product to masses derived independently using the $M_{BH} - \sigma$ relation, Collin et al. (2006) find that the scaling factor, f, is a factor ~ 2 larger for their Population '1' sources (with $FWHM/\sigma < 2.35$ and essentially equivalent to population A of Sulentic et al. 2000) than for their Population 2 (with $FWHM/\sigma > 2.35$ and equivalent to population B of Sulentic et al. 2000). For single-epoch BH mass estimates, assuming a constant value of the virial coefficient, f, as is normally done (e.g. Vestergaard and Peterson, 2006), means that Population 1 masses will be underestimated and Population 2 will be overestimated. This could account for some of the remaining scatter between the C IV- and Balmer-based BH masses (Figure 3.18).

Shen and Ho (2014) argue that a large part of the scatter observed in the Hβ FWHM relates not to a spread in BH masses, but rather to the orientation of the BLR relative to the line-of-sight of the observer. This would be the case if the BLR had a flattened disc-like geometry. In this case, the observed line width would increase with the inclination of the disc relative to the line of sight. At radio wavelengths, the morphology of the radio structure, parametrized in terms of 'core dominance', is believed, at least in a statistical sense, to be a proxy for

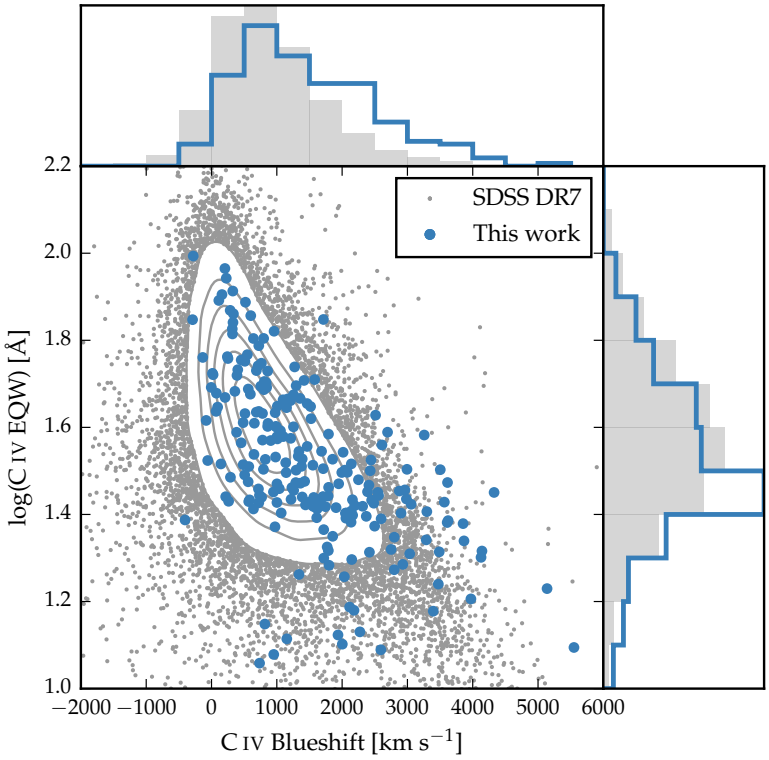

Figure 3.19: Rest-frame EQW versus blueshift of the broad C IV emission-line for SDSS DR7 quasars and our sample (see Figure 3.16b for details). Our sample has very good coverage of the parameter space; the shift to high blueshifts is a result of the high luminosity of our sample in relation to the SDSS sample and the correlation between luminosity and C IV blueshift.

the orientation of the accretion disc (e.g. Jackson and Browne, 1991). Twenty core-dominated quasars and six lobe-dominated quasars were identified in our sample, but no statistically significant differences in the Hα line-widths of the two samples were found. It should be noted that the sub-sample of radio-detected quasars is small and the effectiveness of the test is further compromised by the lack of radio-detected quasars at large blueshifts (see figure 14 of Richards et al., 2011, for example).

3.5.3 *Effectiveness of the C IV blueshift based correction to BH masses*

Figure 3.19 demonstrates that our sample has an excellent coverage of the C IV EQW-blueshift parameter space in relation to SDSS DR7 quasars at redshifts $1.6 < z < 3.0$. The systematic offset to higher C IV blueshifts for our catalogue relative to the SDSS quasars as a whole is a result of the higher mean luminosity relative to the SDSS sample (Figure 2.1). Our sample includes 21 quasars with C IV blueshifts $> 3000\,\mathrm{km\,s^{-1}}$, and extends to $\sim 5000\,\mathrm{km\,s^{-1}}$, i.e. at the very extreme of what is observed in this redshift and luminosity range. This demonstrates that the C IV-blueshift based correction derived in this chapter is applicable to very high blueshifts. Conversely, there are no quasars in our catalogue with C IV blueshifts $\lesssim 0\,\mathrm{km\,s^{-1}}$ and we caution against extrapolating the correction formula to negative blueshifts. In particular, quasars with negative blueshifts as large as $\sim 1000\,\mathrm{km\,s^{-1}}$ appear in the SDSS DR7 catalogue and applying our correction in this regime boosts the derived masses by un-physical factors.

Figure 3.20 compares the C IV- and Hα-based BH masses before and after applying the blueshift-based correction to the C IV FWHM. Before the correction, the correlation between the C IV- and Hα-based BH masses is very weak, and the scatter between the masses is 0.4 dex. After correcting the C IV FWHM for the non-virial contribution, the correlation improves dramatically. The scatter between the corrected C IV-based masses and the Hα-based masses is reduced to 0.2 dex. The scatter is 0.24 dex at low C IV blueshifts ($\sim 0\,\mathrm{km\,s^{-1}}$) and 0.10 dex at high blueshifts ($\sim 3000\,\mathrm{km\,s^{-1}}$).

There has been a considerable amount of attention regarding the relative merits of using the FWHM or dispersion to characterise the velocity width (e.g. Denney et al., 2013). The existence of a trend in the C IV-dispersion values with C IV blueshift is evident from inspection of Figure 3.7b but the systematic trend relative to the spread at fixed blueshift is significantly smaller than when using C IV FWHM. Therefore, without the blueshift information, using the line dispersion would yield a more accurate BH mass than the FWHM (Figure 3.21).

The correlation between the Hα and C IV line dispersion is, however, weak. The Pearson coefficient for the correlation is 0.36 (and just 0.15 when the Hβ measurements are used in place of Hα). Furthermore, there is little dynamic range in

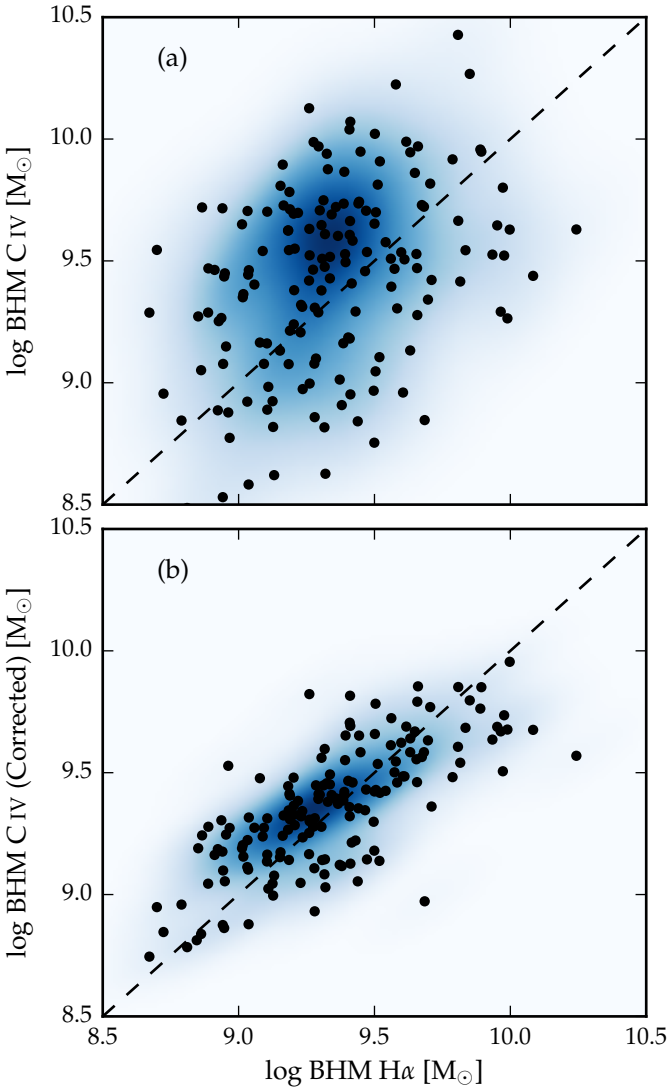

Figure 3.20: Comparison of the C IV- and Hα-based BH masses before (a) and after (b) applying the C IV blueshift-based correction to the C IV FWHM. The density of the plotted points (estimated using a Gaussian kernel density estimator) is represented by the colour. The correction to the C IV BH masses decreases the scatter from 0.4 to 0.2 dex.

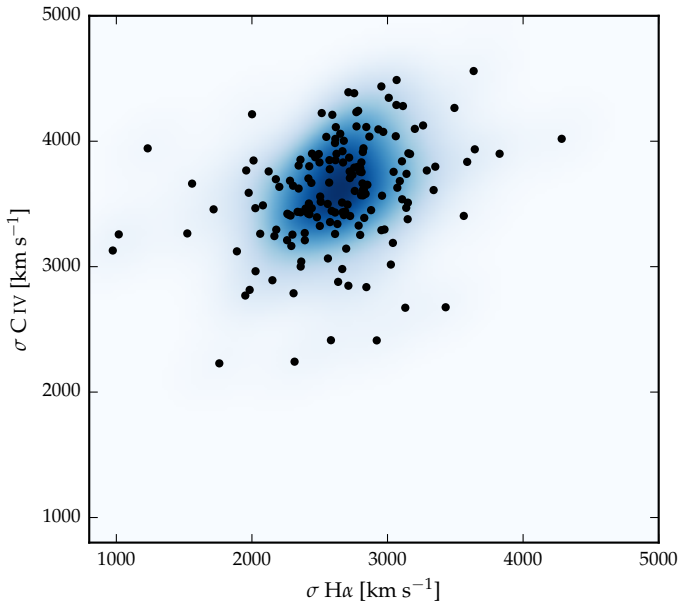

Figure 3.21: Comparison of the C IV and Hα line dispersion, σ. The density of the plotted points (estimated using a Gaussian kernel density estimator) is represented by the colour. Estimating a reliable BH mass from the C IV FWHM and blueshift is substantially more effective than using the C IV line dispersion with, or without, the line blueshift. The C IV dispersion values are larger than the corresponding Hα measurements by a factor of 1.4 on average, which is consistent with reverberation mapping measurements (Vestergaard and Peterson, 2006).

the line dispersion: the scatter is just 480 and 460 km s^{-1} for Hα and C IV respectively. This observation suggests that the line dispersion does not fully trace the dynamic range in BH mass present in the quasar population. At least part of the reason is that the line dispersion is difficult to measure reliably in current survey-quality data, particularly because of the sensitivity to flux ascribed to the wings of the emission-line (e.g. Mejía-Restrepo et al., 2016). Figures 3.20 and 3.21 demonstrate that estimating a reliable BH mass from the C IV FWHM and blueshift is substantially more effective than using the C IV line dispersion with, or without, the line blueshift.

3.5.4 *Comparison to previous prescriptions*

In Figure 3.22 we compare various prescriptions which have been proposed in the literature to derive BH masses from the

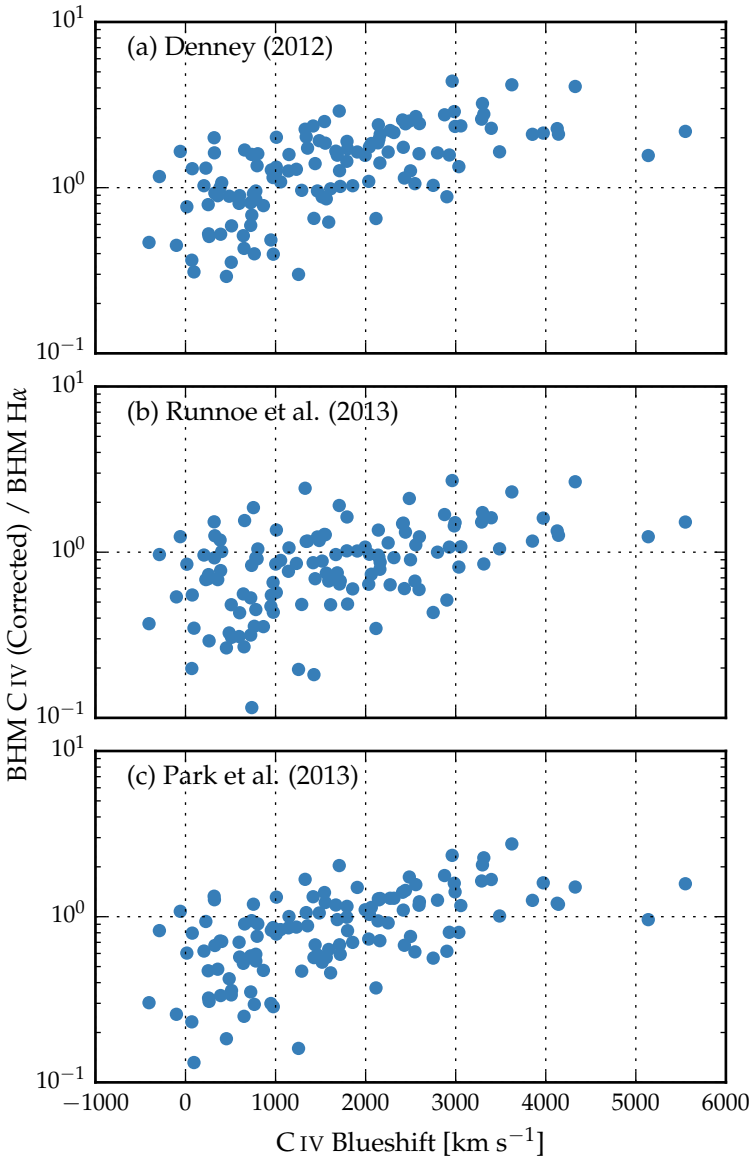

Figure 3.22: Comparison of BH mass estimates derived from C IV and Hα as a function of the C IV blueshift. Corrections to the C IV-based masses have been applied based on the shape (FWHM/σ) of the C IV emission-line (a; Denney, 2012), the peak flux ratio of the Si IV+O IV blend relative to C IV (b; Runnoe et al., 2013), and by significantly reducing the dependence of the derived BH mass on the C IV velocity-width (c; Park et al., 2013).

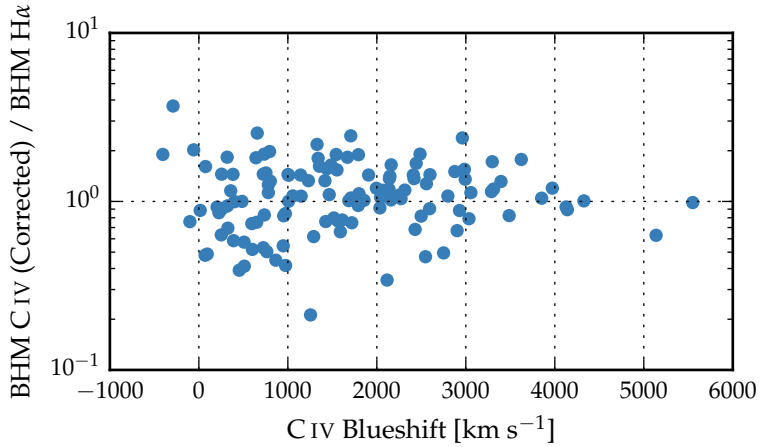

Figure 3.23: Comparison of BH mass estimates derived from C IV and Hα as a function of the C IV blueshift. C IV-based masses have been corrected using the C IV blueshift-based prescription presented in this chapter.

C IV line which are consistent with the masses derived from the Balmer lines. In each case, we compare the corrected C IV-based masses to the Hα-based masses as a function of the C IV blueshift. The C IV blueshift-based correction presented in this chapter is also tested in Figure 3.23. The correction proposed by Runnoe et al. (2013) is based on the spectral region at rest-frame wavelengths of ~1400 Å (see below). Therefore, our analysis is based on the 123 quasars with spectra covering this region.

In Figure 3.22a the C IV BH masses have been corrected using the C IV shape (FWHM/σ) based correction proposed by Denney (2012). Denney (2012) found the level of contamination in single-epoch spectra from non-reverberating gas to be correlated with the shape (FWHM/σ) of the C IV profile. In our sample, we observe a strong correlation between the shape of the C IV line and its blueshift (Figure 3.7c); between the two extremes in the C IV blueshift distribution the line shape changes from FWHM/σ ~ 1 − 2.5. The investigation of Denney (2012) was based on a sample of reverberation mapped quasars, which have a narrow range of C IV emission-line shapes, including the absence of any objects with large C IV blueshifts. As a result, the correction is not applicable at large C IV blueshifts. Therefore, while the consistency between the Hα- and C IV-based masses at low C IV blueshifts is improved, at high C IV blueshifts the C IV-based masses remain severely overestimated.

As explained above, reliably measuring the quasar systemic redshift from the ultra-violet region of the spectrum has proved difficult. However, the situation is improved dramatically by the new scheme developed by Allen & Hewett (2017, in preparation). Given the difficulty of measuring reliable C IV blueshifts without the Allen & Hewett scheme, Runnoe et al. (2013) opted instead to use the continuum-subtracted peak flux ratio of the ultra-violet emission-line blend of Si IV+O IV (at 1400 Å) to that of C IV to correct for non-virial contributions to the C IV velocity width. This parameter was chosen because it showed the strongest correlation with the FWHM C IV/Hβ residuals, as well as with the strengths of optical [O III] and Fe II.

Following Runnoe et al. (2013), we measure the peak flux by fitting a model with four Gaussian components (two for each emission-line) to the continuum-subtracted flux. As is evident from Figure 3.19, a correlation exists between the blueshift and EQW of C IV: C IV emission which is strongly blueshifted is typically weak. The Si IV+O IV emission-line blend, however, shows significantly less systematic variation (see Figure 3.17). Therefore, the Si IV+O IV-based correction is quite effective in practice: the systematic bias in the C IV BH masses at large C IV blueshifts is reduced to a factor of ~ 2 (Figure 3.22b). However, the C IV based masses are still systematically overestimated at large C IV blueshifts.

In contrast to the widely-used Vestergaard and Peterson (2006) C IV-based virial BH mass calibration, the more recent Park et al. (2013) calibration significantly reduces the dependence of the derived masses on the emission-line velocity width (from the ΔV^2 dependence predicted assuming a virialized BLR to just $\Delta V^{0.56}$). As a consequence, the C IV based masses of the quasars with large C IV blueshifts are much reduced (Figure 3.22c). However, the systematic error in the C IV-based BH masses as a function of C IV blueshift remains.

For comparison, the C IV-based masses shown in Figure 3.23 have been corrected using the C IV blueshift-based procedure presented in this chapter. No systematic in the BH masses as a function of the C IV blueshift is evident.

3.6 POPULATION TRENDS WITH C IV BLUESHIFT

As shown in Figure 3.24, there are systematic variations in the Hα line profile as a function of the C IV blueshift. At C IV-blueshift $< 1200\,\mathrm{km\,s^{-1}}$, the H$\alpha$ FWHM range is $\simeq 2000 -$

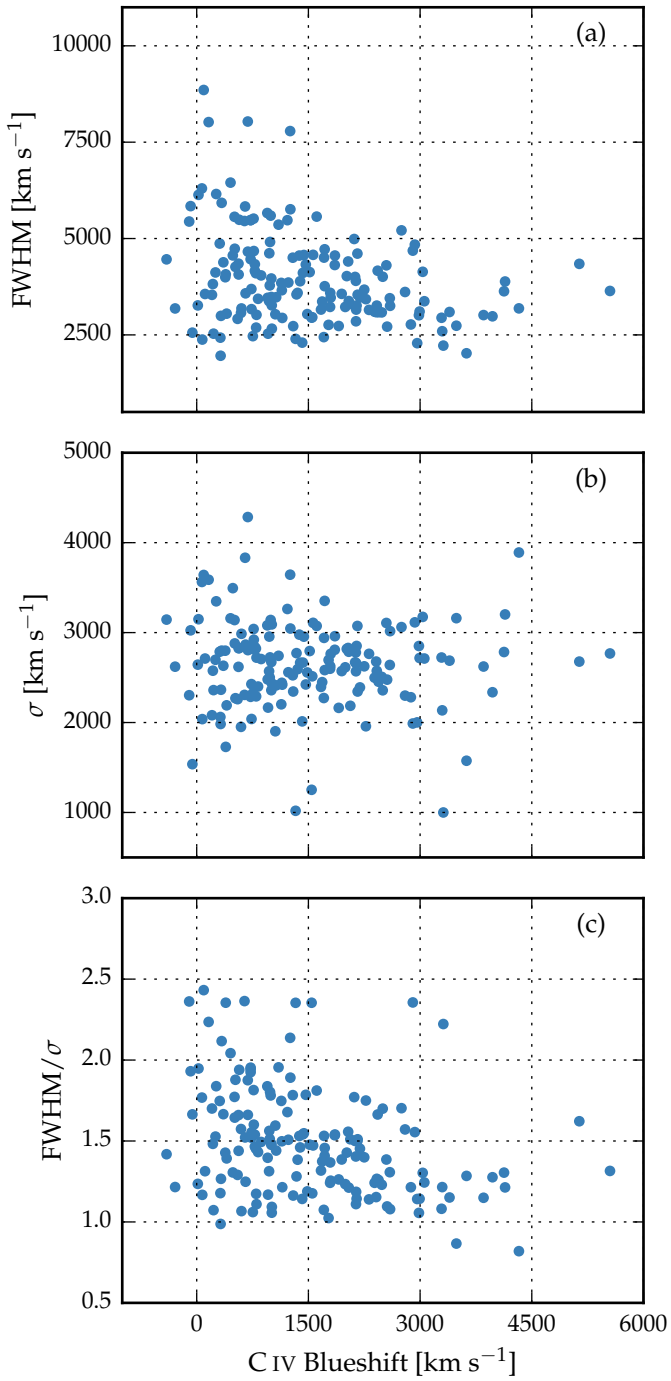

Figure 3.24: The FWHM, dispersion (σ) and shape (FWHM/σ) of Hα as a function of the C IV blueshift.

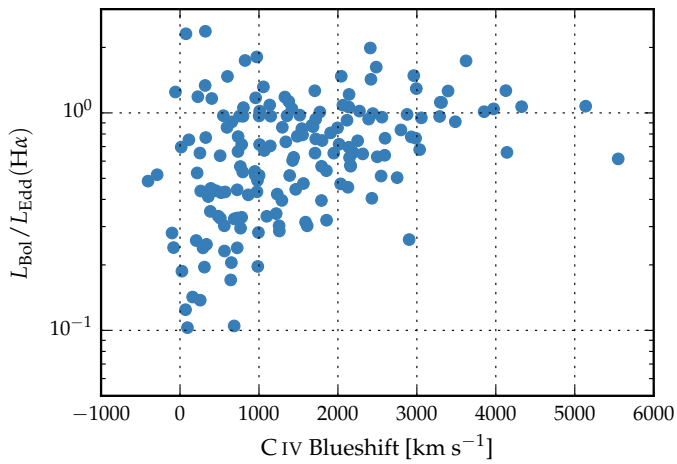

Figure 3.25: Hα-derived Eddington ratio versus C IV blueshift. At blueshift $\gtrsim 2000\,\mathrm{km\,s^{-1}}$ all quasars have high accretion rates ($L/L_{\rm Edd} \simeq 1$). This is in agreement with Kratzer and Richards (2015), but in contrast to what one would derive from naive use of C IV-based BH mass scaling relations.

$8900\,\mathrm{km\,s^{-1}}$, with mean $\simeq 4300\,\mathrm{km\,s^{-1}}$ (Figure 3.24a). However, amongst the quasars with C IV-blueshift $> 2000\,\mathrm{km\,s^{-1}}$, the mean Hα FWHM $= 3500\,\mathrm{km\,s^{-1}}$, with a scatter of just $700\,\mathrm{km\,s^{-1}}$. There is also an apparent trend of peakier Hα-emission, with FWHM/σ close to unity, at large C IV-blueshift (Figure 3.24c). Amongst the low-C IV-blueshift population there are in addition quasars with broader and more Gaussian-like Hα line profiles, with FWHM/$\sigma \simeq 2$.

The change in the Hα emission-line profiles as a function of C IV-blueshift means that the Hα-FWHM derived BH masses at high-blueshift are smaller than the sample mean. We transformed the observed luminosity into a mass-normalised accretion rate (Eddington ratio). To convert the monochromatic luminosity, which is observed, into a bolometric luminosity we use the bolometric correction factor given by Richards et al. (2006a) ($L_{\rm Bol} = 9.26 L_{5100}$). Although there is evidence that the bolometric correction factor is a function of the luminosity, as well as of other parameters including the C IV blueshift (Krawczyk et al., 2013), the differences are small over the parameter range covered by our sample, and for simplicity we adopt a constant factor.

The results, shown in Figure 3.25, demonstrate that at large blueshifts quasars are accreting at around their Eddington limits. This finding is in accord with our interpretation that

the blueshifting of C IV is evidence for strong outflows resulting from the presence of a radiation-driven accretion-disc wind. Richards et al. (2002) found that quasars with large C IV blueshifts have weak He II. This is evidence for weak soft X-ray continuum emission (Leighly, 2004), which would allow a strong line-driven wind to form. The strength of such a wind is predicted to be related to the quasar far-ultra-violet SED, which, in turn, could be related to the mass-accretion rate.

All of the objects in our sample which exhibit large C IV blueshifts would be classified as population A in the Sulentic et al. (2000) scheme based on the Hα FWHM. Our results therefore support the idea of the Sulentic et al. (2000) A/B division being driven by the Eddington ratio, with population A sources possessing higher accretion rates. However, we also observe a number of quasars which have high Eddington ratios but do not have line profiles suggestive of strong outflows in the C IV BLR. This suggests that a high accretion rate is a necessary but not sufficient condition for the existence of outflows (Baskin and Laor, 2005a).

The two-dimensional nature of the C IV emission-line parametrisation and the apparent anti-correlation between C IV EQW and C IV blueshift suggests that the quasar population exhibits a continuum of properties. As such, more accurate C IV blueshift measurements for SDSS-quasars should allow an improved mapping between the C IV-emission properties and key physical parameters of the quasars. This includes improving our understanding of the origin of quasars with exceptionally weak, blueshifted C IV emission (weak emission-line quasars; Luo et al., 2015) which could be exotic versions of wind-dominated quasars (Plotkin et al., 2015).

As we described in Section 3.5.2, the shape of the Balmer lines (FWHM/σ) depends strongly on the FWHM. This suggests that the BLR structure is changing with the emission-line FWHM. One possibility we discussed is that the Balmer line-width is orientation-dependent (e.g. Shen and Ho, 2014). This raises the question of whether the narrow Hα emission-lines observed in the quasars with the largest C IV blueshifts could be an orientation effect. However, there is no evidence that the C IV blueshift is dependent on the orientation (inferred from the radio core-dominance; Richards et al., 2011; Runnoe et al., 2014). Furthermore, Leighly (2004) showed that the He IIλ1640 emission-line properties of quasars with large C IV blueshifts are more consistent with differences in the SED rather than dif-

ferences in the orientation. Overall, therefore, orientation does not appear to be the dominant effect in determining the C IV blueshift and correlated changes in the Hα line profile.

As mentioned in Section 3.1 and discussed in Richards et al. (2011), quasars with current reverberation mapping measurements have a restricted range of C IV-line shapes. In particular, there are currently very few reverberation-mapping measurements of quasars with large C IV blueshifts. Looking to the future, the results of the large on-going statistical reverberation mapping projects (e.g. Shen et al., 2015; King et al., 2015) for luminous quasars at high-redshift will shed new light on the Balmer line emitting region of the BLR for quasars with a range of C IV blueshifts and lead to a greater understanding of the relation between the Balmer line profile and the BH mass.

3.7 FREQUENCY OF QUASARS WITH HIGH ACCRETION RATES

Quantifying the frequency of quasars producing outflows as a function of key parameters, e.g. quasar luminosity, BH mass, redshift, etc. will be important to constrain models of quasar-galaxy evolution. At fixed BH mass, the intrinsic and the observed fraction of quasars exhibiting properties that depend on the Eddington ratio can differ significantly. As an illustration, we consider the implications for the intrinsic fraction of quasars possessing large C IV blueshifts given the observed numbers in the $i < 19.1$ flux-limited sub-sample of the SDSS DR7 quasar catalogue. In order to estimate the size of the selection effect, we considered the detection probability for a much-simplified quasar population. We assume that all quasars with C IV blueshifts $> 1200\,\mathrm{km\,s^{-1}}$ have enhanced accretion rates relative to the 'normal' population (with C IV blueshifts $< 1200\,\mathrm{km\,s^{-1}}$). If the accretion rate of the high-blueshift population is double the rate of the low-blueshift population (which is true in an average sense – see Figure 3.25), then the high-blueshift population will be brighter by $\simeq 0.75$ magnitude. Under the assumption that the BH mass distribution is independent of the C IV blueshift, the high-blueshift population will then be over-represented in a flux-limited sample. To estimate the size of the bias, we need to know how many more quasars, at redshifts $2 < z < 2.5$, there are with $i < 19.1 + 0.75 = 19.85$ relative to $i < 19.1$. This is the fraction of the population which, as a consequence of having enhanced accretion rates, are

boosted above the survey flux limit. The main colour-selected SDSS DR7 quasar catalogue extends only to $i = 19.1$ and, assuming the luminosity function is continuous[8] we thus use the number counts at $i < 19.1$ and $i < 18.35$, which differ by a factor of $\simeq 4$.

At redshifts $2 < z < 2.5$, there are 3,834 quasars with C IV blueshifts $< 1200\,\mathrm{km\,s^{-1}}$ and 2,484 with blueshifts $> 1200\,\mathrm{km\,s^{-1}}$ in the SDSS DR7 $i < 19.1$ quasar sample, a ratio of $\sim$ 2:1. The above calculation, although much idealised, suggests that the intrinsic fraction of high-blueshift quasars is a factor of four smaller than in the flux-limited sample (i.e. $\sim$ 15 per cent of the ultra-violet-selected non-BAL quasar population).

3.8 SUMMARY

The main results of this chapter are as follows:

- We have analysed the spectra of 230 high-luminosity ($10^{45.5} - 10^{48}\,\mathrm{erg\,s^{-1}}$), redshift $1.5 < z < 4.0$ quasars for which spectra of the Balmer emission-lines and the C IV emission-line exist. The large number of quasars in our spectroscopic catalogue and the wide range in C IV blueshifts the quasars possess has allowed us to directly investigate biases in C IV-based BH mass estimates which stem from non-virial contributions to the C IV emission as a function of the C IV blueshift, which, in turn, depends directly on the form of the quasar ultra-violet SEDs (Richards et al., 2011).

- The C IV emission-based BH masses are systematically in error by a factor of more than five at $3000\,\mathrm{km\,s^{-1}}$ in C IV emission blueshift and the overestimate of the BH masses reaches a factor of 10 for quasars exhibiting the most extreme blueshifts, $\gtrsim 5000\,\mathrm{km\,s^{-1}}$.

- We have derived an empirical correction formula for BH mass estimates based on the C IV emission-line FWHM and blueshift. The correction may be applied using Equations 3.8 and 3.10 in Section 3.4.3. The large SED-dependent systematic error in C IV-based BH masses is removed using the correction formulae. The remaining scatter between the corrected C IV-based masses and the Hα-

8 The luminosity function and number-counts vary only smoothly (e.g. Ross et al., 2013) for the magnitude and redshift range used here.

based masses is 0.24 dex at low C IV blueshifts ($\sim 0\,\mathrm{km\,s^{-1}}$) and 0.10 dex at high blueshifts ($\sim 3000\,\mathrm{km\,s^{-1}}$). This is a significant improvement on the 0.40 dex scatter observed between the un-corrected C IV and Hα BH masses. The correction depends only on the C IV line properties – i.e. the FWHM and blueshift – and allows un-biased single-epoch virial BH mass estimates to be made from optical spectra, such as those provided by the SDSS, out to redshifts exceeding $z \sim 5$.

3.9 CATALOGUE OF DERIVED PROPERTIES

Table 3.4 includes the line parameters from our emission-line fits, and other derived properties used in this chapter. The columns in Table 3.4 are as follows:

1 Catalogue name.

2-3 Broad Hα FWHM, and its error, in $\mathrm{km\,s^{-1}}$.

4-5 Broad Hα line dispersion, and its error, in $\mathrm{km\,s^{-1}}$.

6-7 Broad Hα redshift, and its error.

8-9 Hα-FWHM-based BH mass using Vestergaard and Peterson (2006) calibration, and its error, in $\mathrm{M_{\odot}}$. Hα FWHM is first converted into equivalent Hβ FWHM using Equation 3.7.

10-11 Broad Hβ FWHM, and its error, in $\mathrm{km\,s^{-1}}$.

12-13 Broad Hβ line dispersion, and its error, in $\mathrm{km\,s^{-1}}$.

14-15 Broad Hβ redshift, and its error.

16-17 Hβ-FWHM-based BH mass using Vestergaard and Peterson (2006) calibration, and its error, in $\mathrm{M_{\odot}}$.

18-19 Broad C IV FWHM, and its error, in $\mathrm{km\,s^{-1}}$.

20-1 Broad C IV line dispersion, and its error, in $\mathrm{km\,s^{-1}}$.

22-23 Broad C IV EQW, and its error, in Å.

24 Si IV+O IV/C IV peak flux ratio.

25-27 C IV blueshift, relative to Hα, and its error, in $\mathrm{km\,s^{-1}}$.

27-28 C IV blueshift, relative to Hβ, and its error, in $\mathrm{km\,s^{-1}}$.

29-30 Uncorrected C IV-FWHM-based BH mass using Vestergaard and Peterson (2006) calibration, and its error.

31 Corrected C IV-FWHM-based BH mass.

Column	Name	Units	Description
1	UID		Catalogue name
2	FWHM_BROAD_HA	$\mathrm{km\,s^{-1}}$	Broad Hα FWHM
3	FWHM_BROAD_HA_ERR	$\mathrm{km\,s^{-1}}$	
4	SIGMA_BROAD_HA	$\mathrm{km\,s^{-1}}$	Broad Hα σ
5	SIGMA_BROAD_HA_ERR	$\mathrm{km\,s^{-1}}$	
6	Z_BROAD_HA		Hα redshift
7	Z_BROAD_HA_ERR		
8	LOGMBH_HA	$\mathrm{M_\odot}$	Hα BH mass
9	LOGMBH_HA_ERR	$\mathrm{M_\odot}$	
10	FWHM_BROAD_HB	$\mathrm{km\,s^{-1}}$	Broad Hβ FWHM
11	FWHM_BROAD_HB_ERR	$\mathrm{km\,s^{-1}}$	
12	SIGMA_BROAD_HB	$\mathrm{km\,s^{-1}}$	Broad Hβ σ
13	SIGMA_BROAD_HB_ERR	$\mathrm{km\,s^{-1}}$	
14	Z_BROAD_HB		Hβ redshift
15	Z_BROAD_HB_ERR		
16	LOGMBH_HB	$\mathrm{M_\odot}$	Hβ BH mass
17	LOGMBH_HB_ERR	$\mathrm{M_\odot}$	
18	FWHM_CIV	$\mathrm{km\,s^{-1}}$	Broad C IV FWHM
19	FWHM_CIV_ERR	$\mathrm{km\,s^{-1}}$	
20	SIGMA_CIV	$\mathrm{km\,s^{-1}}$	Broad C IV σ
21	SIGMA_CIV_ERR	$\mathrm{km\,s^{-1}}$	
22	EQW_CIV	Å	Broad C IV EQW
23	EQW_CIV_ERR	Å	
24	1400_CIV		Si IV+O IV/C IV peak flux ratio
25	BLUESHIFT_CIV_HA	$\mathrm{km\,s^{-1}}$	C IV blueshift, relative to Hα
26	BLUESHIFT_CIV_HA_ERR	$\mathrm{km\,s^{-1}}$	
27	BLUESHIFT_CIV_HB	$\mathrm{km\,s^{-1}}$	C IV blueshift, relative to Hβ
28	BLUESHIFT_CIV_HB_ERR	$\mathrm{km\,s^{-1}}$	
29	LOGMBH_CIV_VP06	$\mathrm{M_\odot}$	Uncorrected C IV BH mass
30	LOGMBH_CIV_VP06_ERR	$\mathrm{M_\odot}$	
31	LOGMBH_CIV_C17	$\mathrm{M_\odot}$	Corrected C IV BH mass

Table 3.4: The format of the table containing the emission-line properties from our parametric model fits and other derived parameters used in this chapter. The full table is available online at http://dx.doi.org/10.5281/zenodo.557069.

4

QUASAR-DRIVEN GALAXY-WIDE OUTFLOWS IN IONISED GAS

4.1 [O III] AS A PROBE OF QUASAR-DRIVEN OUTFLOWS

X-ray and ultra-violet spectroscopy has revealed high-velocity outflows to be nearly ubiquitous in high accretion rate quasars. Strong evidence for high-velocity outflows in the vicinity of quasars include BALs, NALs and blueshifted emission-lines. These observations suggest that the energy released by quasars can have a dramatic effect on their immediate environments.

Quasars driving powerful outflows over galactic scales is a central tenet of galaxy evolution models involving 'quasar feedback' (e.g. Silk and Rees, 1998; Springel et al., 2005; Bower et al., 2006). In recent years, a huge amount of resources have been devoted to searching for observational evidence of this phenomenon. This has resulted in recent detections of outflows in quasar-host galaxies using tracers of atomic, molecular, and ionised gas (e.g. Nesvadba et al., 2006; Arav et al., 2008; Nesvadba et al., 2008; Moe et al., 2009; Alexander et al., 2010; Dunn et al., 2010; Feruglio et al., 2010; Nesvadba et al., 2010; Alatalo et al., 2011; Cano-Díaz et al., 2012; Harrison et al., 2012; Harrison et al., 2014; Cimatti et al., 2013; Rupke and Veilleux, 2013; Veilleux et al., 2013; Cicone et al., 2014; Nardini et al., 2015).

One particularly successful technique has been to use forbidden quasar emission-lines to probe the dynamical state of the ionised gas extended over kilo-parsec scales in quasar host-galaxies. Because of its high equivalent width, [O III]λ5008 is the most studied of the narrow quasar emission-lines. The [O III] emission is found to consist of two distinct components: a narrow 'core' component, with a velocity close to the systemic redshift of the host-galaxy, and a broader 'wing' component, which is normally blueshifted. The core component is dominated by the gravitational potential of the host-galaxy. However, the velocity-width of the wing is much too broad for the gas to be in dynamical equilibrium with the host-galaxy (e.g. Liu et al., 2013) and the general consensus is that it is tracing high-velocity outflowing gas. The receding side of the outflow may be obscured due to the presence of dust, either in the out-

flow or elsewhere, and so only the near-side of the outflow, which is blueshifted, is observed. The relative balance between the core and wing components varies significantly from object to object, and governs the width and asymmetry of the overall [O III] emission profile (e.g. Shen and Ho, 2014).

Observations of broad velocity-widths and blueshifts in narrow emission-lines stretch back several decades (e.g. Weedman, 1970; Stockton, 1976; Heckman et al., 1981; Veron, 1981; Feldman et al., 1982; Heckman, Miley, and Green, 1984; Vrtilek, 1985; Whittle, 1985; Boroson and Green, 1992). However, these studies rely on small samples, which are often unrepresentative of the properties of the quasar population. More recently, the advent of large optical spectroscopic surveys (e.g. SDSS) have facilitated studies of the NLR in tens of thousands of quasars (e.g. Boroson, 2005; Greene and Ho, 2005a; Zhang et al., 2011; Mullaney et al., 2013; Zakamska and Greene, 2014; Shen and Ho, 2014). This has provided constraints on the prevalence and drivers of ionised outflows. At the same time, spatially resolved spectroscopy has revealed that these outflows are extended over galaxy scales (e.g. Greene et al., 2009; Greene et al., 2011; Harrison et al., 2012; Hainline et al., 2013; Harrison et al., 2014).

However, these studies do not cover the redshift range when star formation and BH accretion peaked ($2 \lesssim z \lesssim 4$), which is when the $M_{BH} - \sigma$ relation is thought to have been established. At these redshifts bright optical emission-lines including the [O III] doublet are redshifted to near-infrared wavelengths, where observations are far more challenging. As a consequence, studies at high redshifts have typically relied on relatively small numbers of objects. These studies find [O III] to be broader in more luminous quasars, with velocity-widths $\gtrsim 1000\,\mathrm{km\,s^{-1}}$ common (e.g. Netzer et al., 2004; Kim et al., 2013; Brusa et al., 2015; Shen, 2016). These findings suggest that quasar efficiency in driving galaxy-wide outflows increases with luminosity (e.g. Netzer et al., 2004; Nesvadba et al., 2008; Kim et al., 2013; Brusa et al., 2015; Carniani et al., 2015; Perna et al., 2015; Bischetti et al., 2016). The fraction of objects with very weak [O III] emission also appears to increase with redshift and/or luminosity (e.g. Netzer et al., 2004).

In this chapter, we analyse the [O III] properties of a sample of 354 high-luminosity, redshift $1.5 < z < 4$ quasars selected from our near-infrared spectroscopic catalogue. To date, this is the largest study of the NLR properties of high redshift quasars.

Spectrograph	Telescope	Number
FIRE	MAGELLAN	31
GNIRS	GEMINI-N	28
ISAAC	VLT	7
LIRIS	WHT	7
NIRI	GEMINI-N	29
NIRSPEC	Keck II	3
SINFONI	VLT	80
SOFI	NTT	76
TRIPLESPEC	ARC-3.5m	27
TRIPLESPEC	P200	45
XSHOOTER	VLT	21
Total		354

Table 4.1: The numbers of quasars with [O III] line measurements and the spectrographs and telescopes used to obtain the near-infrared spectra.

4.2 QUASAR SAMPLE

From our near-infrared spectroscopic catalogue (Chapter 2), we have selected 354 quasars which have spectra covering the [O III] doublet. The broad Balmer Hβ line has also been observed for all but two of the sample. For 165 quasars, the spectra extend to the broad Hα emission-line at 6565 Å, and in 260 objects optical spectra, including C IV, are also available (mostly from SDSS/BOSS). The sample covers a wide range in redshifts ($1.5 \lesssim z \lesssim 4$) and luminosities ($45.5 \lesssim \log L_{Bol} \lesssim 49$ erg s^{-1}). The spectrographs and telescopes used to obtain the near-infrared spectra are summarised in Table 4.1.

4.3 SPECTRAL MEASUREMENTS

In this section, the procedure we use to measure emission-line properties is described. Our approach is to model the Hβ/[O III] complex using a power-law continuum, an empirical Fe II template (taken from Boroson and Green 1992) and multiple Gaussian components. Non-parametric properties are then derived from the best-fitting model. This approach, which is commonly adopted in the literature (e.g. Shen et al., 2011; Shen and Liu, 2012; Shen, 2016), is more robust when analysing spectra with limited S/N (in comparison to measuring line

properties directly from the data) and allows adjacent emission-lines to be de-blended.

The modelling of Hα (used in this chapter to estimate the quasar systemic redshift) is also described. C IV emission-line properties (used to infer the strength of BLR outflows) are taken directly from Chapter 3.

4.3.1 *Transforming spectra to rest-frame wavelengths*

Before a spectrum can be modelled, it must first be transformed to the rest-frame of the quasar. The redshift used in this transformation is either derived from the peak of the broad Hα emission ($\sim$ 40 per cent of our sample), from the peak of the broad Hβ emission ($\sim$ 40 per cent) or from the peak of the narrow [O III] emission (20 per cent). The rest-frame transformation is only required to be accurate to within $\sim 1000\,\mathrm{km\,s^{-1}}$ of the true systemic redshift for our fitting procedure to function. In later sections, more precise estimates of the systemic redshift will be calculated using our parametric model fits.

4.3.2 *Removing Fe II emission*

Before Hβ/[O III] is modelled, we first model and subtract the nearby continuum and Fe II emission using the procedure described in Chapter 3. We encountered 24 objects for which the procedure failed to adequately remove the Fe II emission from the spectra (Figure 4.1). In these objects the relative strengths of the Fe II lines differ significantly from those of I Zw 1, on which the Boroson and Green (1992) Fe II template we use is based. The residual Fe II emission is at rest-frame wavelengths very close to the laboratory wavelengths of the [O III] doublet, which is generally very weak in these objects. As a result, the [O III] line parameters we derive for these objects are unreliable. These objects are therefore flagged and excluded from our analysis in the remainder of this chapter (leaving 330 objects in our sample).

To illustrate the importance of the Fe II subtraction procedure in reliably measuring [O III] emission properties, we consider the object J223819-092106 (shown bottom row, centre in Figure 4.1). This object was also analysed by Shen (2016), who reported the [O III] emission to have an extreme redshift ($\sim 7500\,\mathrm{km\,s^{-1}}$) relative to the Hewett and Wild (2010) systemic redshift. However, our analysis suggests that the emis-

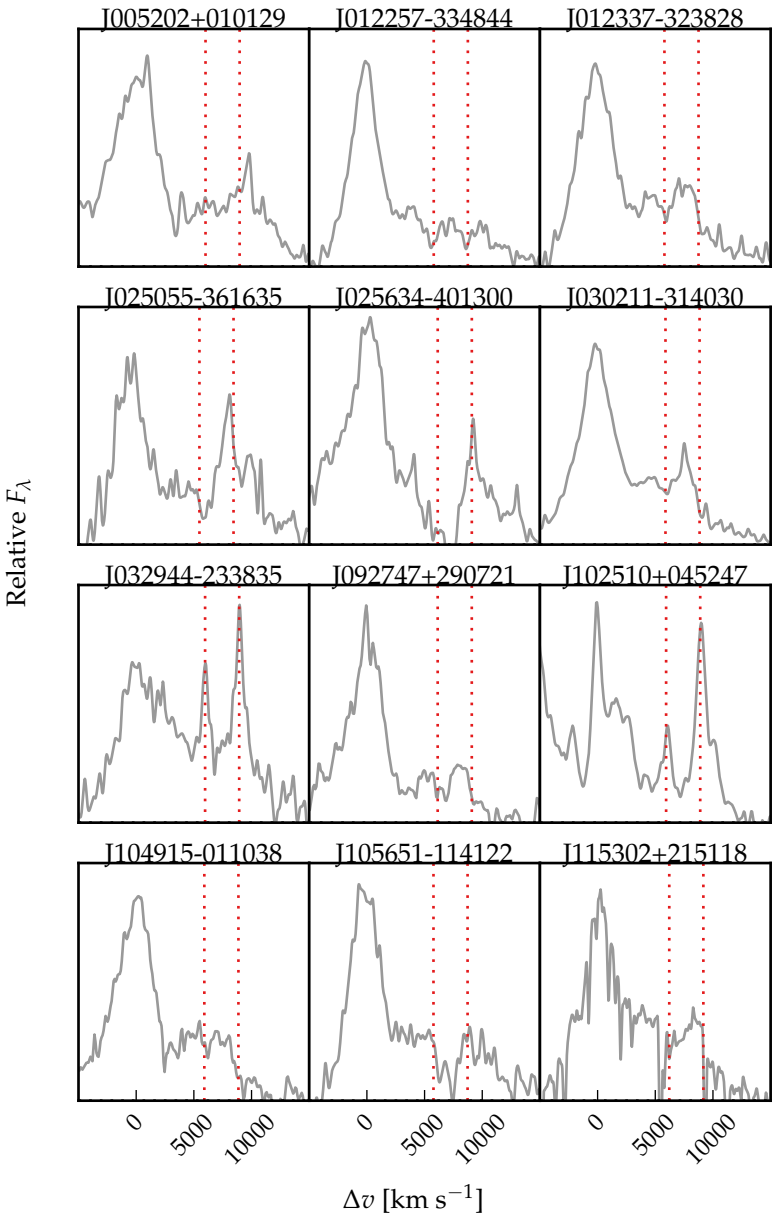

Figure 4.1: Spectra of the 24 objects for which significant Fe II emission is still present following our Fe II-subtraction procedure. Spectra have been smoothed via convolution with a 100 km s^{-1} Gaussian kernel. The vertical lines indicate the expected positions of the [O III] doublet (which is generally very weak in these objects) with the systemic redshift defined using the peak of the broad Hβ emission.

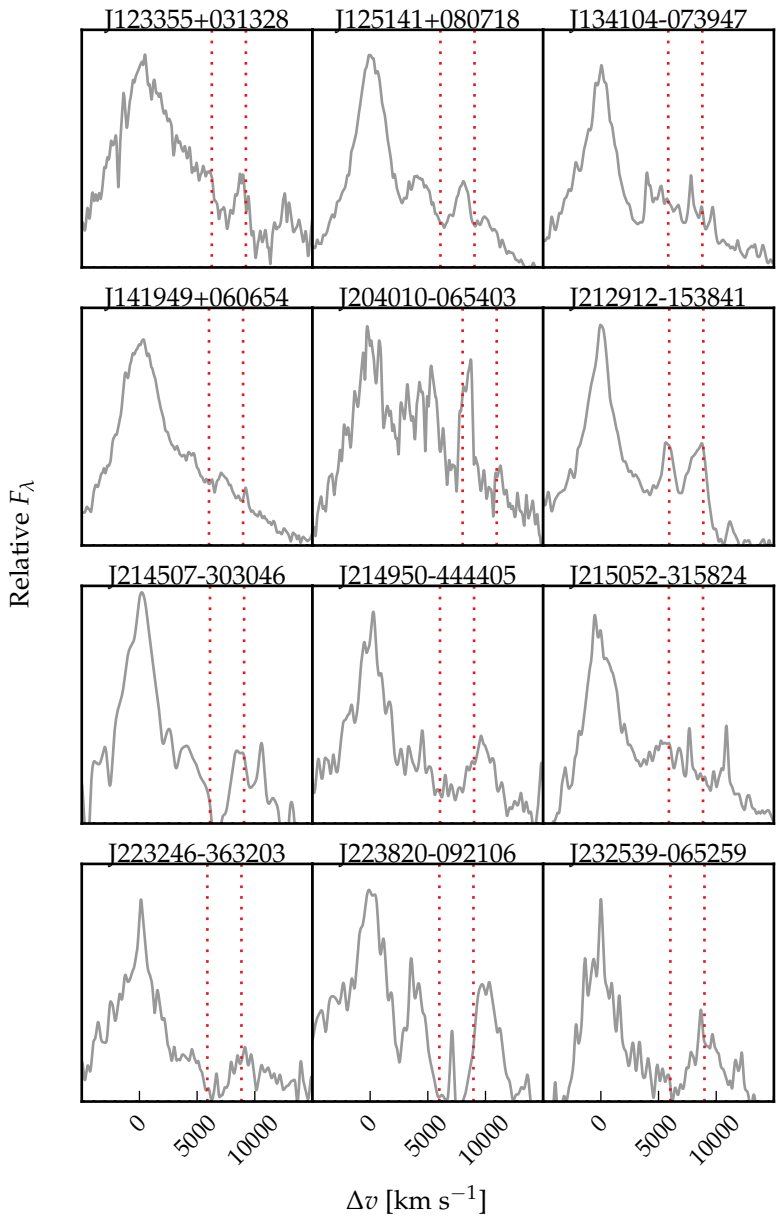

Figure 4.1: Continued.

Model	Fix centroids?	Number
2 broad Gaussians + 1 narrow Gaussian	No	9
2 broad Gaussians	No	295
2 broad Gaussians	Yes	39
1 broad Gaussian	N/A	9

Table 4.2: Summary of models used to fit the Hβ emission, and the number of quasars to which each model is applied.

sion which was modelled by Shen (2016) as [O III] is more likely to be poorly-subtracted Fe II.

4.3.3 *Modelling Hβ and [O III]*

In general, Hβ is modelled with two Gaussians with non-negative amplitudes and FWHM greater than 1200 km s^{-1}. In nine objects Hβ is modelled with a single Gaussian and in 39 objects Hβ is modelled with two Gaussians, but the velocity centroids of the two Gaussians are constrained to be equal. These spectra generally have low S/N, and adding extra freedom to the model does not significantly decrease the reduced-χ^2. In addition there are cases where the blue wing of the Hβ emission is below the lower wavelength limit of the spectra; in these cases models with more freedom are insufficiently constrained by the data.

Contributions to the Hβ emission from the NLR is generally weak in our sample, and an additional Gaussian component to model this emission is not required for the vast majority of objects. In nine objects features in the model - data residuals suggest that a narrow emission component is significant, and an additional narrow Gaussian is included in the model for these quasars. If the NLR contribution to the Hβ emission is significant in more of our sample, then measures of the Hβ velocity-width will be biased to lower values. However, our systemic redshift estimates that use the peak of the Hβ emission (Section 4.3.8) will not be affected. The Hβ models, and the numbers of quasars to which each model is applied, are summarised in Table 4.2.

Each component of the [O III] doublet is fit with one or two Gaussians, depending on the fractional reduced-χ^2 difference between the one- and two-component models. Concretely, if the addition of the second Gaussian decreases the reduced-χ^2 by more than 5 per cent then the double-Gaussian model is

Model	Number
2 Gaussians	140
1 Gaussian	128
Template	62

Table 4.3: Summary of models used to fit the [O III] emission, and the number of quasars to which each model is applied.

accepted. One hundred and twenty-eight spectra are fit with a single Gaussian and 140 with two Gaussians. The peak flux ratio of the [O III] 4960 Å and 5008 Å components are fixed at the expected 1:3 ratio and the width and velocity offsets are set to be equal[1].

In 62 objects with very weak [O III] (mean EQW $\sim$ 2 Å) we find that the Gaussian model has a tendency to fit features to the noise. This can lead to large errors on the [O III] line properties. To avoid this problem, we instead fit a fixed [O III] template (FWHM $\simeq$ 900 km s^{-1}) to the spectra, with the normalisation of this template the only free-parameter in the fit. This template is generated by running our line-fitting routine on a median composite spectrum that we have constructed from the 268 quasars with reliable [O III] line measurements. The spectra used to construct the composite were first de-redshifted and continuum- and Fe II-subtracted.

The models we use to fit [O III], and the numbers of quasars to which each model is applied, are summarised in Table 4.3.

In Figure 4.2 we show example fits to eight objects. The median reduced-χ^2 value in the whole sample is 1.31 and, in general, there are no strong features observable in the spectrum-minus-model residuals.

4.3.4 *Modelling Hα*

There are 165 quasars in our sample with spectra covering the Hα emission-line. In Section 4.3.8, we use the peak of the Hα emission as one estimate of the quasar systemic redshift. In this section, we describe how the Hα emission was modelled.

The continuum emission is first modeled and subtracted using the procedure described in Section 3.3.2. We then test five different models with increasing degrees of freedom to model

1 For J003136+003421, a significantly better fit ($\Delta\chi^2_\nu \sim 25\%$) is obtained when the peak flux ratio constraint is relaxed; the peak ratio of the best-fitting model is 1:2.13.

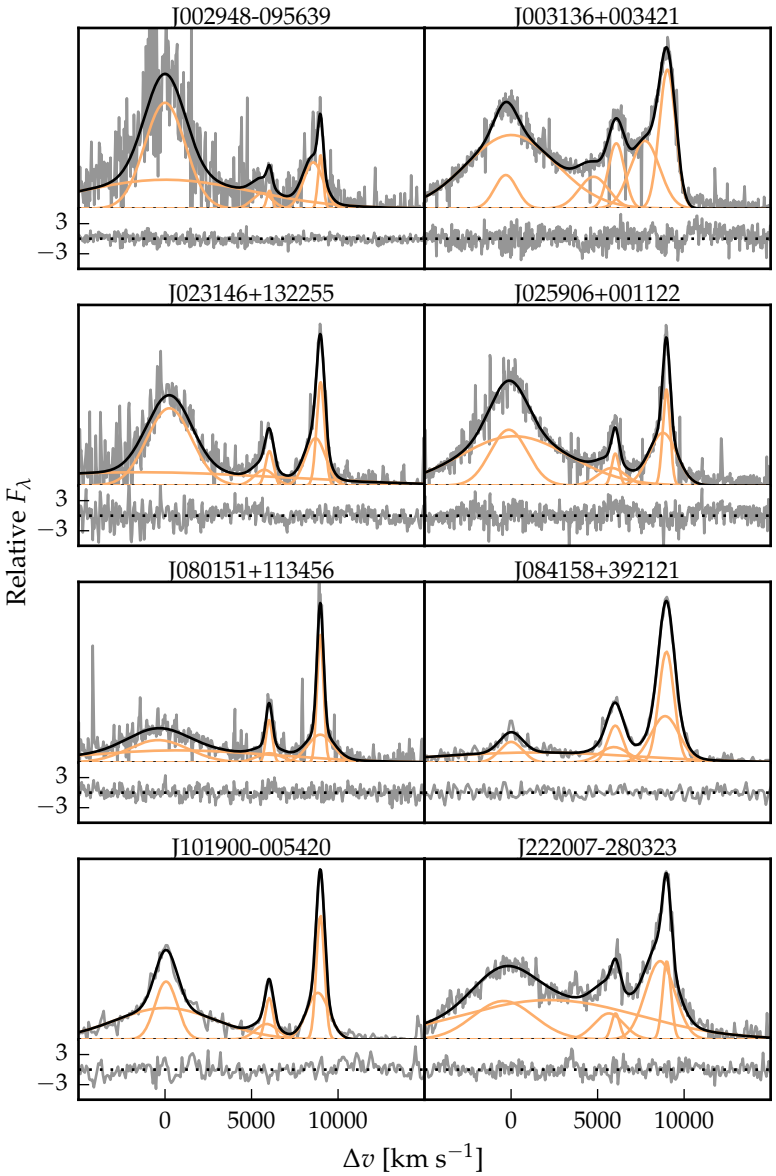

Figure 4.2: Example model fits to the continuum- and Fe II-subtracted Hβ/[O III] emission in eight quasars. The data is shown in grey, the best-fitting model in black, and the individual model components in orange. The peak of the [O III] emission is used to set the redshift, and Δv is the velocity shift from the rest-frame transition wavelength of Hβ. Below each spectrum we plot the data-minus-model residuals, scaled by the errors on the fluxes.

Model	Components	Fix centroids?	Number
1	1 broad Gaussian	N/A	8
2	2 broad Gaussians	Yes	47
3	2 broad Gaussians	No	20
4	2 broad Gaussians + narrow Gaussians	Yes	42
5	2 broad Gaussians + narrow Gaussians	No	48

Table 4.4: Summary of models used to fit the Hα emission, and the number of quasars to which each model is applied.

the Hα emission. The models are summarised in Table 4.4. They are (1) a single broad Gaussian; (2) two broad Gaussians with identical velocity centroids; (3) two broad Gaussians with different velocity centroids; (4) two broad Gaussians with identical velocity centroids, and additional narrower Gaussians to model narrow Hα emission, and the narrow components of [N II]$\lambda\lambda 6548, 6584$ and [S II]$\lambda\lambda 6717, 6731$; (5) two broad Gaussians with different velocity centroids, and additional narrower Gaussians. If used, the width and velocity of all narrow components are set to be equal in the fit, and the relative flux ratio of the two [N II] components is fixed at the expected value of 2.96.

In order to determine which model is selected for each spectrum we use the following procedure. Each of the five models are fit to every spectrum and the reduced-χ^2 recorded. Initially, the model with the smallest reduced-χ^2 is selected. We then measure how the reduced-χ^2 changes as the complexity of the model is decreased (i.e. considering the models in Table 4.4 in descending order). If using the simpler model results in an increase in the reduced-χ^2 which is less than 10 per cent relative to the best fitting model, then the simpler model is selected.

4.3.5 *Emission-line parameters*

All [O III] line properties are derived from the [O III]λ5008 peak, but, as described above, the kinematics of [O III]λ4960 are constrained to be identical in our fitting routine.

We do not attach any physical meaning to the individual Gaussian components used in the model. Decomposing the [O III] emission into a narrow component at the systemic redshift and a lower-amplitude, blueshifted broad component is often highly degenerate and dependent on the spectral S/N and resolution. Furthermore, there is no theoretical justification that the broad component should have a Gaussian profile.

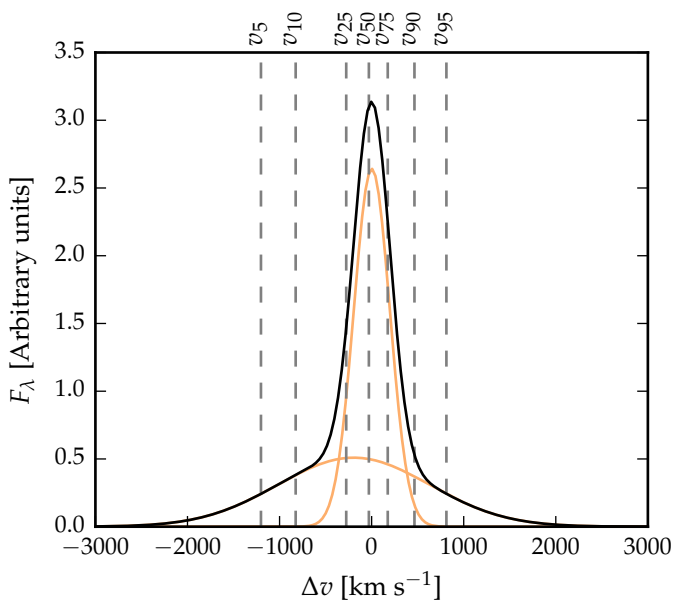

Figure 4.3: Non-parametric measures of the [O III] velocity-profile, as described in the text.

We therefore choose to characterize the [O III] line profile using a number of non-parametric measures, which are commonly used in the literature (e.g. Whittle, 1985; Zakamska and Greene, 2014; Zakamska et al., 2016). A normalised cumulative velocity distribution is constructed from the best-fitting model, from which the velocities below which 5, 10, 25, 50, 75, 90, and 95 per cent of the total flux accumulates can be calculated. These velocities are then adjusted so that the peak of the [O III] emission is at $0\,\mathrm{km\,s^{-1}}$. The [O III] velocities for an example model are shown in Figure 4.3.

We calculate the velocity-width containing 90 per cent of the flux w_{90} by rejecting 5 per cent of the flux in the blue and red wings of the profile ($w_{90} \equiv v_{95} - v_5$). We also calculate w_{80} ($\equiv v_{90} - v_{10}$) and w_{50} ($\equiv v_{75} - v_{25}$). w_{90} is relatively most sensitive to the flux in the wings of the line, whereas w_{50} is relatively most sensitive to the flux in the core. In terms of the FWHM, $w_{50} \simeq$ FWHM/1.746, $w_{80} \simeq$ FWHM/0.919, $w_{90} \simeq$ FWHM/0.716, assuming a Gaussian line profile.

All of the derived parameters we have calculated are summarised in Table 4.5. The columns are as follows:

1 Catalogue name.

2-15 v_5, v_{10}, v_{25}, v_{50}, v_{75}, v_{90} and v_{95} velocity of [O III], relative to [O III] peak, v_{peak}, and their errors, in $\mathrm{km\,s^{-1}}$.

Column	Name	Units	Description
1	UID		Catalogue name
2	OIII_V5	$\mathrm{km\,s^{-1}}$	[O III] v_5
3	OIII_V5_ERR	$\mathrm{km\,s^{-1}}$	
4	OIII_V10	$\mathrm{km\,s^{-1}}$	[O III] v_{10}
5	OIII_V10_ERR	$\mathrm{km\,s^{-1}}$	
6	OIII_V25	$\mathrm{km\,s^{-1}}$	[O III] v_{25}
7	OIII_V25_ERR	$\mathrm{km\,s^{-1}}$	
8	OIII_V50	$\mathrm{km\,s^{-1}}$	[O III] v_{50}
9	OIII_V50_ERR	$\mathrm{km\,s^{-1}}$	
10	OIII_V75	$\mathrm{km\,s^{-1}}$	[O III] v_{75}
11	OIII_V75_ERR	$\mathrm{km\,s^{-1}}$	
12	OIII_V90	$\mathrm{km\,s^{-1}}$	[O III] v_{90}
13	OIII_V90_ERR	$\mathrm{km\,s^{-1}}$	
14	OIII_V95	$\mathrm{km\,s^{-1}}$	[O III] v_{95}
15	OIII_V95_ERR	$\mathrm{km\,s^{-1}}$	
16	OIII_Z		[O III] redshift
17	OIII_Z_ERR		
18	OIII_W50	$\mathrm{km\,s^{-1}}$	[O III] w_{50}
19	OIII_W50_ERR	$\mathrm{km\,s^{-1}}$	
20	OIII_W80	$\mathrm{km\,s^{-1}}$	[O III] w_{80}
21	OIII_W80_ERR	$\mathrm{km\,s^{-1}}$	
22	OIII_W90	$\mathrm{km\,s^{-1}}$	[O III] w_{90}
23	OIII_W90_ERR	$\mathrm{km\,s^{-1}}$	
24	OIII_A		[O III] asymmetry
25	OIII_A_ERR		
26	OIII_EQW	Å	[O III] EQW
27	OIII_EQW_ERR	Å	
28	OIII_LUM	$\mathrm{erg\,s^{-1}}$	[O III] luminosity
29	OIII_LUM_ERR	$\mathrm{erg\,s^{-1}}$	
30	EQW_FE_4434_4684	Å	Fe II EQW
31	EQW_FE_4434_4684_ERR	Å	
32	HB_VPEAK	$\mathrm{km\,s^{-1}}$	Hβ peak velocity
33	HB_VPEAK_ERR	$\mathrm{km\,s^{-1}}$	
34	HA_VPEAK	$\mathrm{km\,s^{-1}}$	Hα peak velocity
35	HA_VPEAK_ERR	$\mathrm{km\,s^{-1}}$	
36	HB_Z		Hβ redshift
37	HB_Z_ERR		
38	HA_Z		Hα redshift
39	HA_Z_ERR		
40	OIII_FE_FLAG		Bad Fe II subtraction
41	OIII_EXTREM_FLAG		Extreme [O III] emission

Table 4.5: The format of the table containing the emission-line properties from our parametric model fits. The full table is available online at http://dx.doi.org/10.5281/zenodo.557069.

16-17 Systemic redshift measured at [O III] peak wavelength, and its error.

18-23 w_{50} ($\equiv v_{75} - v_{25}$), w_{80} ($\equiv v_{90} - v_{10}$) and w_{90} ($\equiv v_{95} - v_5$) velocity-width of [O III], and their errors, in $\mathrm{km\,s^{-1}}$.

24-25 Dimensionless [O III] asymmetry A, and its error. The asymmetry is define as

$$A = \frac{(v_{90} - v_{\rm peak}) - (v_{\rm peak} - v_{10})}{(v_{90} - v_{10})}.$$

26-27 Rest-frame [O III] EQW, and its error, in Å.

28-29 [O III] luminosity, and its error, in $\mathrm{erg\,s^{-1}}$.

30-31 4434-4684 Å rest-frame Fe II EQW, and its error, in Å.

32-33 Velocity of Hβ peak, relative to [O III] peak, and its error, in $\mathrm{km\,s^{-1}}$.

34-35 Velocity of Hα peak, relative to [O III] peak, and its error, in $\mathrm{km\,s^{-1}}$.

36-37 Redshift of Hβ peak, and its error.

38-39 Redshift of Hα peak, and its error.

40 Fe II flag. When flag is 1 Fe II-subtraction procedure has been unsuccessful (Section 4.3.2).

41 Extreme [O III] flag. When flag is 1 [O III] emission is extremely broad and blueshifted (Section 4.4.7).

4.3.6 *Uncertainties on parameters*

To estimate realistic uncertainties on emission-line parameters derived from the best-fitting model we use the same Monte Carlo approach described in Section 3.3.6. Very briefly, random simulations of each spectrum are generated. Our fitting-procedure is run on each simulated spectrum, and the errors on the line parameters are estimated by measuring the spread of the parameter distribution from the ensemble of simulations. In a slight modification of the procedure in Section 3.3.6, the error is defined as half the 68 (84 - 16) percentile spread in the parameter values.

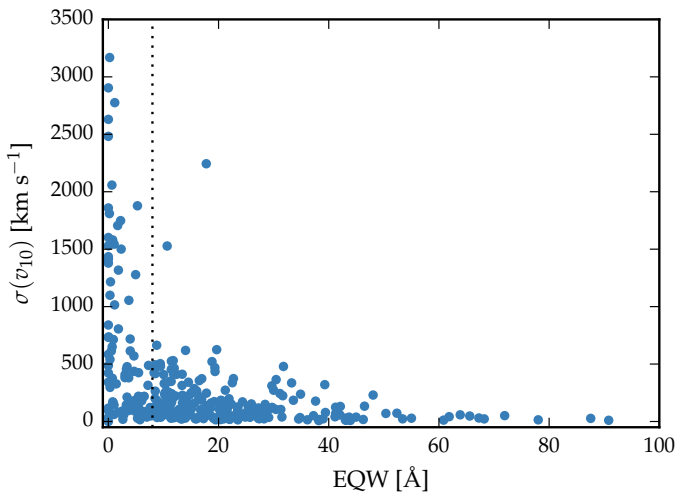

Figure 4.4: Uncertainty in v_{10} as a function of the EQW, for [O III]. Uncertainties in v_{10} are large to the left of the vertical line, at 8 Å. These objects are ignored in our subsequent analysis of the [O III] line shape.

4.3.7 *Flagging low EQW [O III]*

In Figure 4.4 we show how the uncertainty in [O III] v_{10} depends on the EQW. As the strength of [O III] decreases, the average uncertainty in v_{10} increases. When the [O III] EQW $>$ 80 Å, the mean uncertainty in v_{10} is 50 km s^{-1}; this increases to 450 km s^{-1} when $10 <$ EQW < 20 Å. As the EQW drops below 8 Å, uncertainties in v_{10} become very large (exceeding 1000 km s^{-1} in many objects). Clearly, the emission-line is too weak for its shape to be reliably measured in many of these objects. Therefore, when the [O III] line properties (e.g. velocity-width, centroid) are analysed in later sections, objects with EQW $<$ 8 Å will be excluded. This leaves 226 quasars in the sample.

4.3.8 *Reliability of systemic redshift estimates*

In this section, we compare systemic redshift estimates based on [O III], Hβ and Hα. The wavelength of each of these lines is measured at the peak of the emission and this measurement is made using the best-fitting parametric model. In the case of the Balmer lines, this model includes both broad and (if present) narrow emission features.

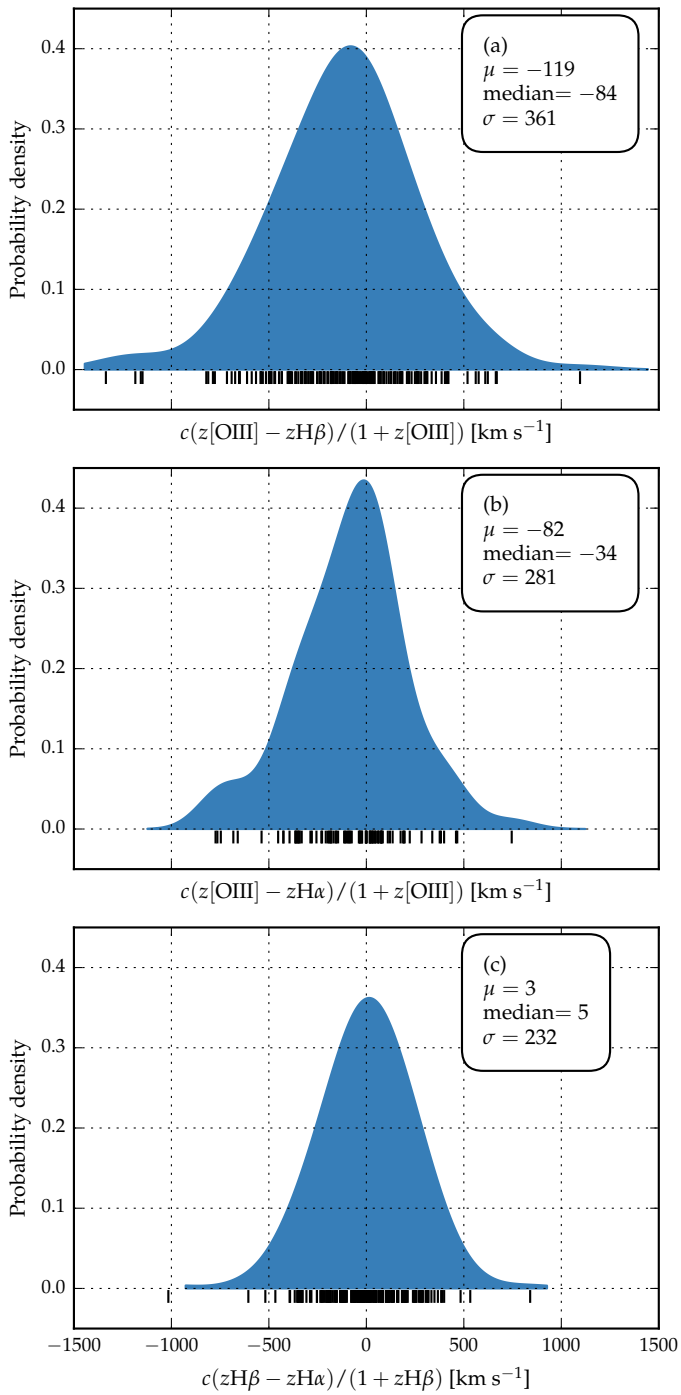

Figure 4.5: Comparison of systemic redshift estimates using [O III], Hβ and Hα. The probability density distributions are generated using a Gaussian kernel density estimator with 170, 120 and 140 km s^{-1} kernel widths for (a), (b) and (c) respectively. The short black lines show the locations of the individual points.

We compare systemic redshift estimates based on [O III] and Hβ (Figure 4.5a), [O III] and Hα (Figure 4.5b) and Hβ and Hα (Figure 4.5c). We generate probability density distributions using a Gaussian kernel density estimator. The kernel width, which is optimised using leave-one-out cross-validation, is 170, 120 and 140 $\mathrm{km\,s^{-1}}$ in Figures 4.5a, 4.5b and 4.5c respectively.

There are 182, 85 and 162 objects being compared in Figures 4.5a, 4.5b and 4.5c respectively. We have excluded [O III], Hβ and Hα measurements when the uncertainties on the peak velocities exceed 200, 300 and 200 $\mathrm{km\,s^{-1}}$ respectively. We also exclude [O III] measurements from 16 objects with very broad, blueshifted [O III] emission that is strongly blended with the red wing of Hβ (these objects are discussed in Section 4.4.7).

The scatter between the different redshift estimates (360, 280, and 230 $\mathrm{km\,s^{-1}}$ in Figures 4.5a, 4.5b and 4.5c respectively) is consistent with previous studies of redshift uncertainties from broad emission-lines (e.g. Shen et al., 2016). The systematic offset between the Hα and Hβ estimates is effectively zero. However, the [O III] redshifts appear to be systematically offset in comparison to both Hα and Hβ, in the sense that [O III] is blueshifted in the rest-frame of the Balmer lines. This effect is strongest when [O III] is compared to Hβ, in which case [O III] is shifted by $\sim 100\,\mathrm{km\,s^{-1}}$ to the blue.

Hewett and Wild (2010) found that [O III] was blueshifted by $\sim 45\,\mathrm{km\,s^{-1}}$ relative to a rest-frame defined using photospheric Ca IIλλ3935,3970 absorption in the host galaxies of $z < 0.4$ SDSS AGN and that [O III] is increasingly blue-asymmetric at higher luminosities. Therefore, the 100 $\mathrm{km\,s^{-1}}$offset we measure is consistent with Hewett and Wild (2010) once the very different luminosities of the two samples are accounted for.

4.4 [O III] PROPERTIES IN LUMINOUS QUASARS

4.4.1 *Strength and kinematics of [O III]*

In our sample of 330 quasars we observe a significant diversity in [O III] emission properties.

The probability density distribution of the [O III] EQW is shown in Figure 4.6a. The median of the distribution is 14 Å and the 68 percentile range is 3 to 30 Å. The maximum EQW is 391 Å. In 10 per cent of the sample [O III] is very weak, with EQW < 1 Å.

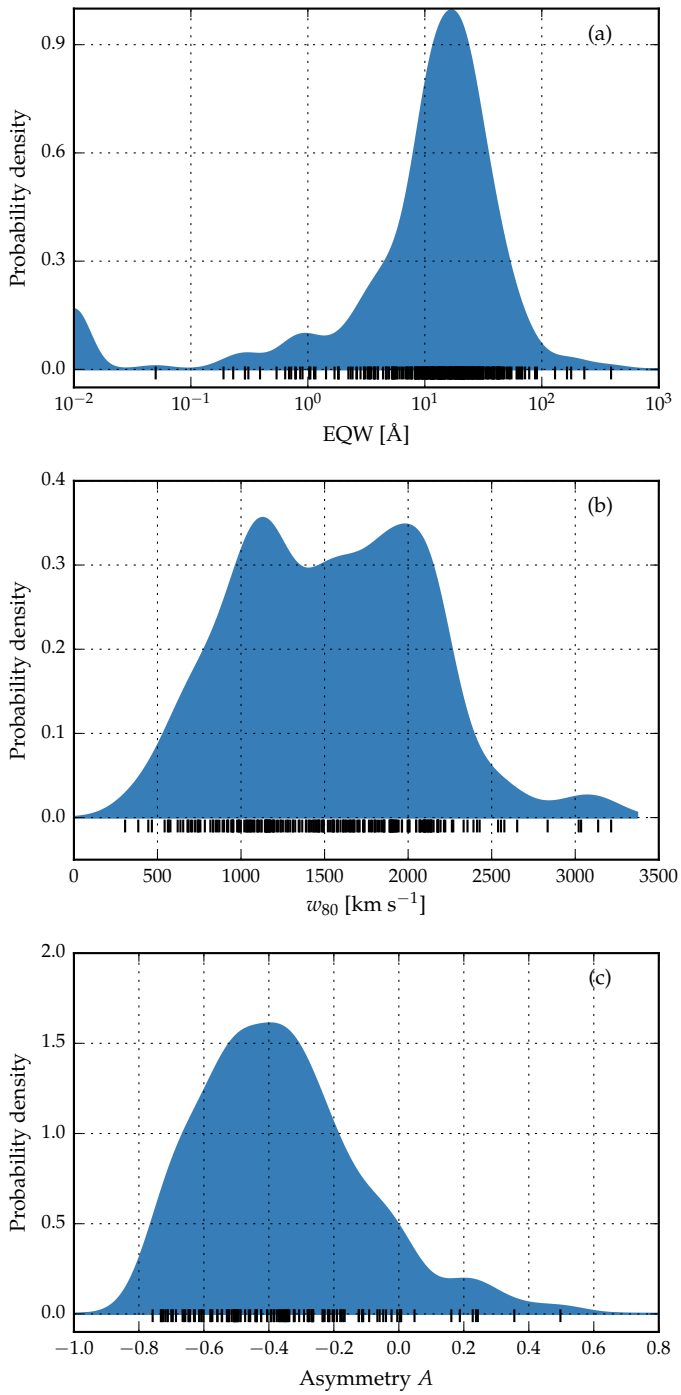

Figure 4.6: Probability density distributions of the [O III] parameters EQW (a), w_{80} (b) and asymmetry A (c), generated using Gaussian kernel density estimation. The 1200 km s^{-1} upper limit on the velocity-width of the Gaussian functions used to model [O III] is responsible for the peak at 1200 km s^{-1} in (b).

The median of the line-width (characterized by w_{80} and shown in Figure 4.6b) is 1540 km s^{-1} and the 68 percentile range is 950 to 2100 km s^{-1}, with a minimum of 300 km s^{-1} and a maximum of 3200 km s^{-1}.

The [O III] asymmetry is shown in Figure 4.6c. In 40 per cent of the sample [O III] is fit with a single Gaussian. The asymmetry is zero in this model and so these objects are excluded. For the [O III] emission-lines modelled with two Gaussians, [O III] is blue-asymmetric in 90 per cent. The median asymmetry is −0.37 and the 68 percentile range is −0.61 to −0.12.

Blue-asymmetric structure and high-velocity gas is generally associated with outflows. Our results suggests that NLR outflows are prevalent in this sample of luminous quasars.

We also find weak correlations between these three [O III] parameters. The EQW is anti-correlated with both the line-width and asymmetry: as the [O III] emission gets weaker it gets broader and more blue-asymmetric (e.g. Shen and Ho, 2014).

4.4.2 *Luminosity-dependence of [O III] properties*

In this section, we compare our sample of luminous $2 \lesssim z \lesssim 4$ quasars to a sample of $z \lesssim 1$ SDSS quasars in order to investigate the luminosity and redshift dependence of key [O III] parameters. We use 20 663 quasars with [O III] measurements from the Shen et al. (2011) catalogue. The median redshift of these objects is 0.55 and the median bolometric luminosity is $10^{45.5}$ erg s^{-1}.

In Figure 4.7 we show the [O III] EQW as a function of the quasar bolometric luminosity. Bolometric luminosities are estimated from monochromatic continuum luminosities at 5100 Å, using the correction factor given by Richards et al. (2006a). Considering only the objects for which [O III] is detected with EQW $>$ 1 Å, we observe a decrease in the [O III] EQW as the luminosity increases (from 17 Å at $L_{Bol} = 10^{45.25}$ erg s^{-1} to 12 Å at $L_{Bol} = 10^{47.75}$ erg s^{-1}). Given the luminosity spans a full 2.5 dex, the decrease in the [O III] EQW (30 per cent) is very modest. However, [O III] EQW $<$ 1 Å in 10 per cent of the luminous quasars, compared to just one per cent of the $z \lesssim 1$ SDSS sample. This is explored further in Section 4.4.4.

Many authors have reported the [O III] EQW to decrease with quasar luminosity (e.g. Brotherton, 1996; Sulentic et al., 2004; Baskin and Laor, 2005b; Zhang et al., 2011; Stern and Laor, 2012). The origin of this correlation – known as the [O III] Bald-

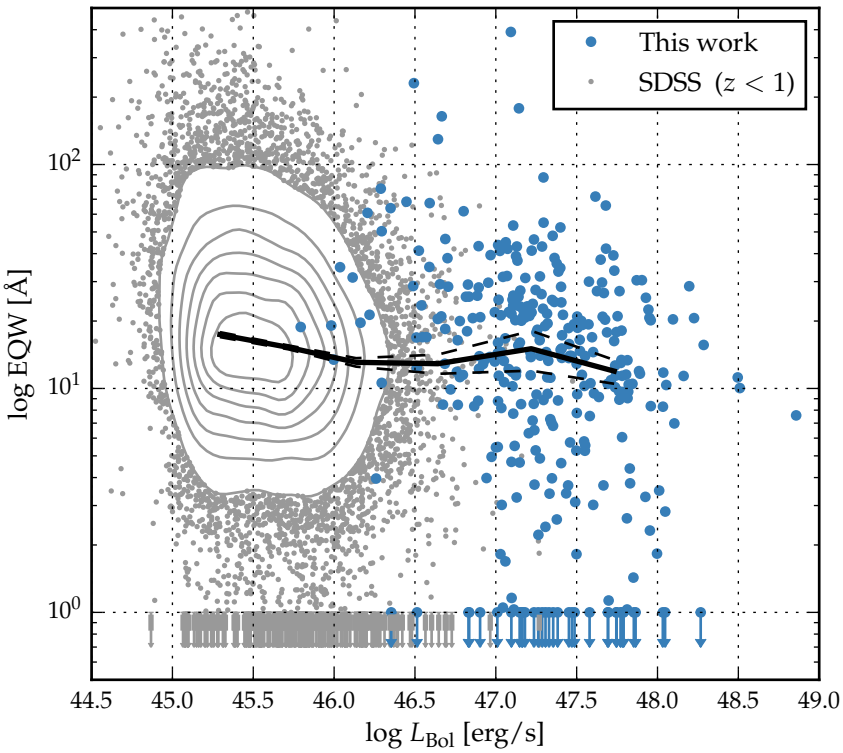

Figure 4.7: The [O III] EQW as a function of the quasar bolometric luminosity for the sample of luminous quasars presented in this chapter and the $z \lesssim 1$ SDSS sample. An upper limit at EQW = 1 Å indicates points with EQW < 1 Å. The solid line shows the median [O III] EQW as a function of luminosity and the dashed lines show the 1-σ standard error on the median. The average EQW decreases from 17 to 12 Å over the luminosity range considered. At the same time, the fraction of quasars with very weak [O III] (EQW < 1 Å) is ten times higher in the luminous quasar sample.

win effect (e.g. Baldwin, 1977) – has not been demonstrated conclusively. The size of the NLR (and hence the [O III] luminosity) is predicted to scale with the square root of the luminosity of the source of ionising photons (e.g. Netzer, 1990) and low-luminosity Seyfert galaxies appear to obey this relationship (e.g. Bennert et al., 2002). Extrapolating this relationship to high luminosity quasars leads to the prediction of NLRs with galactic dimensions. Under these conditions, the size of the NLR will be limited by the density and ionisation state in the NLR. In other words, the NLR can't continue to grow beyond the radius at which there is no longer gas available to be ionised

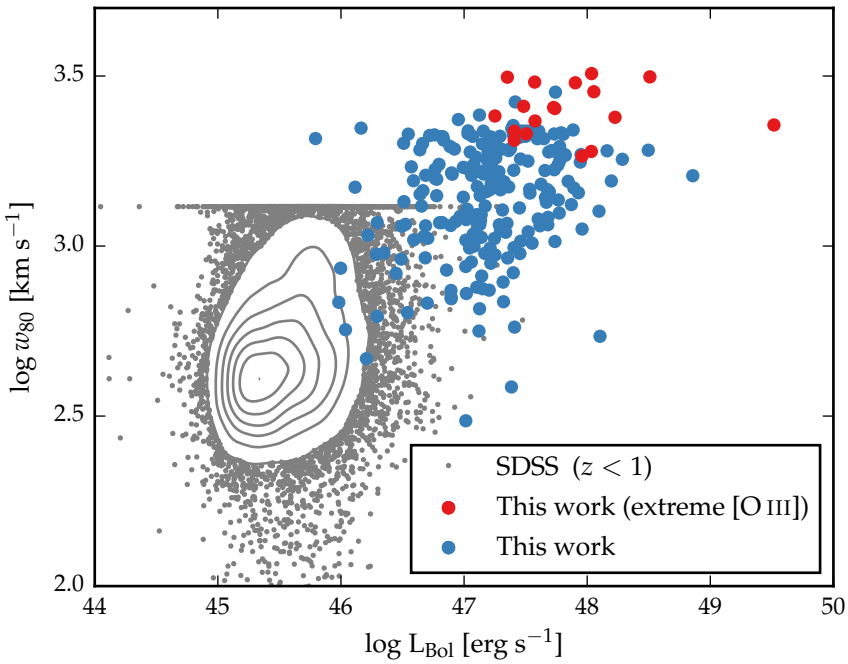

Figure 4.8: [O III] velocity-width w_{80} as a function of quasar bolometric luminosity. Objects with extreme [O III] profiles (Section 4.4.7) are shown in red. The grey contours and dots show $z \lesssim 1$ SDSS quasars. The FWHM measurements given by Shen et al. (2011) have been converted into equivalent w_{80} values by assuming $w_{80} \simeq$ FWHM/0.919. The build-up of points at $w_{80} = 1300\,\mathrm{km\,s^{-1}}$ is caused by the upper-limit $1200\,\mathrm{km\,s^{-1}}$ imposed by Shen et al. (2011) on the [O III] FWHM. The typical [O III] velocity-width increases from $440\,\mathrm{km\,s^{-1}}$ at $\log L_{Bol} = 45.5\ \mathrm{erg\,s^{-1}}$ to $1850\,\mathrm{km\,s^{-1}}$ at $\log L_{Bol} = 48\ \mathrm{erg\,s^{-1}}$.

and the luminosity of the NLR will saturate (e.g. Hainline et al., 2013; Hainline et al., 2014).

In Figure 4.8 we show that the [O III] velocity-width is strongly correlated with the quasar bolometric luminosity. The typical [O III] velocity-width increases from $440\,\mathrm{km\,s^{-1}}$ at $\log L_{Bol} = 45.5\ \mathrm{erg\,s^{-1}}$ to $1850\,\mathrm{km\,s^{-1}}$ at $\log L_{Bol} = 48\ \mathrm{erg\,s^{-1}}$. This demonstrates that the highest velocity outflows are associated with the most luminous AGN which suggests that the outflows are driven by radiative forces.

Considering only objects in a narrow luminosity range ($47 < \log L_{Bol} < 47.5\ \mathrm{erg\,s^{-1}}$) we observe no correlations between the redshift and either the [O III] velocity-width or EQW. The lack of any evolution in typical [O III] properties between $z = 0$

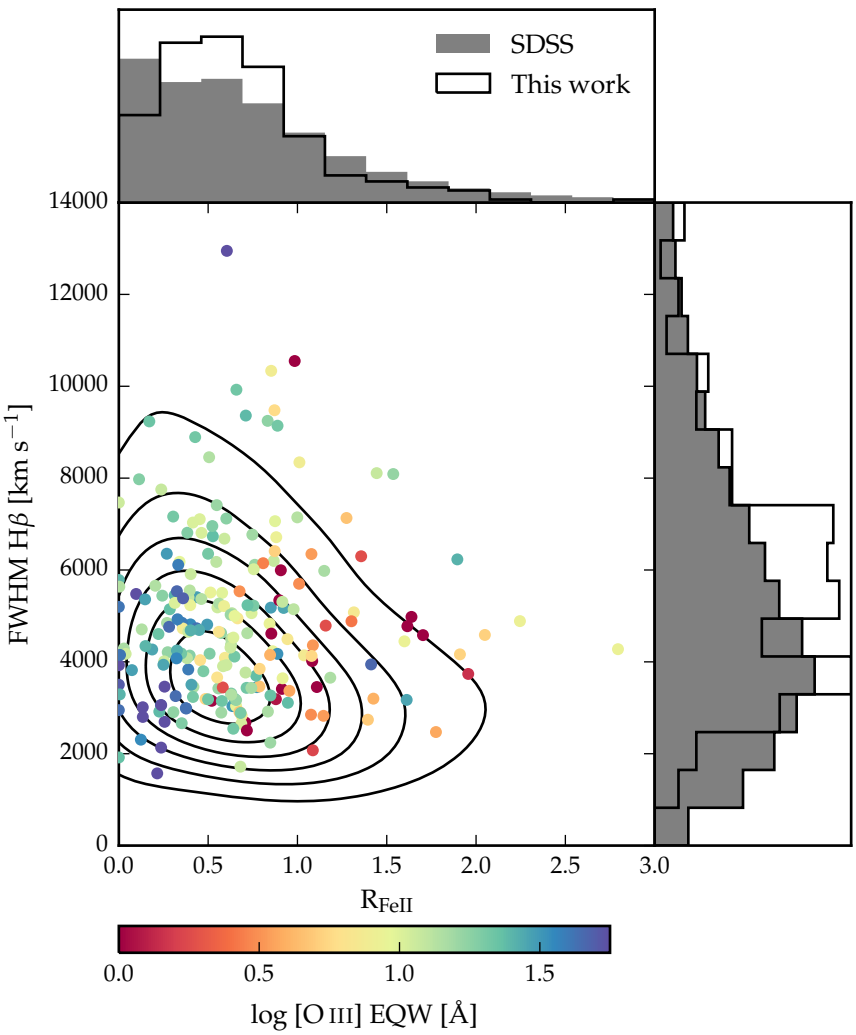

Figure 4.9: The distribution of objects in the EV1 parameter space. The distribution of luminous quasars (shown using circles) is similar to the distribution of $z \lesssim 1$ SDSS quasars (shown using contours), with the displacement to higher Hβ FWHM indicative of higher BH masses in the luminous sample.

and $z = 1.5$ has previously been reported (e.g. Harrison et al., 2016); our sample demonstrates that the [O III] properties do not evolve from $z = 1.5$ all the way to $z = 4$.

4.4.3 *EV1 trends in high-redshift quasars*

The FWHM of the broad Hβ emission-line, the strength of [O III] and the relative strengths of optical Fe II and Hβ have been identified as the features responsible for the largest vari-

ance in the spectra of AGN and form part of EV1 (Boroson and Green, 1992). In Figure 4.9 we show the [O III] EQW as a function of the Hβ FWHM and the optical Fe II strength. The optical Fe II strength is defined as the ratio of the Fe II and Hβ EQW, where the Fe II EQW is measured between 4434 and 4684 Å. There are 231 objects in our sample with spectra that include Hβ, [O III], and at least 150 Å of the 4434-4684 Å Fe II region. For comparison, $z \lesssim 1$ SDSS quasars are also shown in Figure 4.9.

In our sample, the EV1 parameters follow similar correlations to what is observed at low-redshift. In particular, we observe a strong anti-correlation between the [O III] EQW and Fe II strength. The Hβ FWHM are displaced to higher values, which is consistent with the high-redshift, high-luminosity sample having larger BH masses. Thus, with a much bigger sample, we confirm earlier results suggesting that the EV1 correlations exist in high-redshift quasars (e.g. Netzer et al., 2004; Sulentic et al., 2004; Sulentic et al., 2006; Runnoe et al., 2013; Shen, 2016). This suggests that similar underlying physical processes govern the spectral properties of AGN and quasars over a wide range of redshifts and luminosities.

4.4.4 *Connections with C IV emission properties*

Like the EV1 parameter space, the C IV blueshift and EQW are diagnostics that similarly span the diversity of broad emission-line properties in high redshift quasars (Sulentic et al., 2007; Richards et al., 2011). In Figure 4.10 we show the [O III] EQW as a function of the C IV blueshift and EQW. When [O III] is strong, the C IV blueshift is measured relative to the [O III] peak. Otherwise, the C IV blueshift is measured relative to Hβ or Hα. In Section 4.3.8 we found that redshifts measured from [O III], Hβ and Hα are consistent to within $\sim 300\,\mathrm{km\,s^{-1}}$, which is small in comparison to the dynamic range in C IV blueshifts we see in Figure 4.10. Also shown are the C IV line parameters of 32 157 SDSS DR7 quasars at redshifts $1.6 < z < 3.0$. For this sample, systemic redshifts are taken from Allen & Hewett (2017, in preparation).

The [O III] EQW decreases systematically from the small C IV blueshift, large EQW region of the parameter space to the large C IV blueshift, small EQW region. In the top left of the distribution (C IV blueshift $< 1000\,\mathrm{km\,s^{-1}}$, EQW > 60 Å) the mean

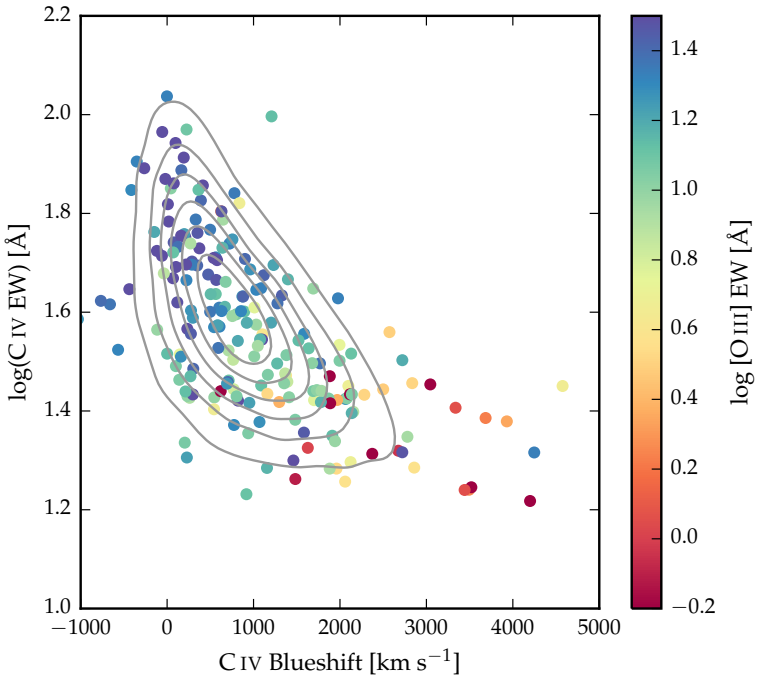

Figure 4.10: Parameter space of C IV blueshift and EQW. Our sample is shown with the coloured circles, and quasars from the full SDSS catalogue are shown with grey contours. The [O III] EQW varies systematically across the C IV blueshift-EQW parameter space. In the small C IV blueshift, high EQW region the mean [O III] EQW is 47 Å; this drops dramatically to 6Å in the large C IV blueshift, low EQW region.

[O III] EQW is 47 Å; this drops dramatically to 6Å in the bottom right (C IV blueshift $> 2000\,\mathrm{km\,s^{-1}}$, EQW < 30 Å).

Qualitatively, the distribution of objects in the Hβ FWHM - Fe II strength EV1 parameter space (Figure 4.9) is very similar to the distribution of objects in the C IV blueshift-EQW parameter space (Figure 4.10). In Figure 3.24 we showed that objects with large C IV blueshifts also have narrow Hα emission-lines. However, the converse is not true: many of the objects with narrow Hα emission-lines also have small C IV blueshifts. In contrast, Figure 4.10 demonstrates that the [O III] EQW provides a less degenerate mapping between the EV1 and C IV parameter spaces.

A different projection of the same data is shown in Figure 4.11, which shows the [O III] EQW as a function of the C IV blueshift. The luminosity of the quasars is indicated by the colour of the points. Both the [O III] EQW and the C IV blueshift

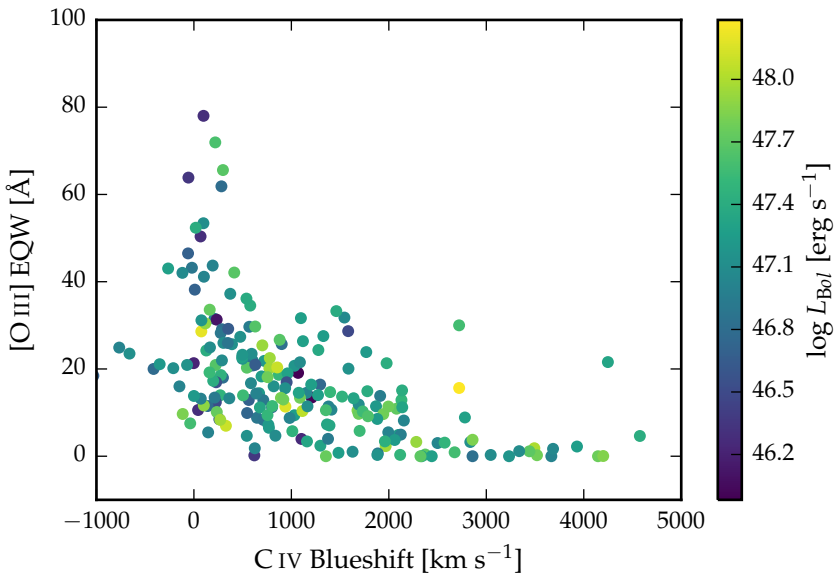

Figure 4.11: [O III] EQW as a function of the C IV blueshift. The [O III] EQW is strongly anti-correlated with the C IV blueshift. On the other hand, no strong luminosity-dependent trends (indicated by the colours of the points) are evident.

are known to depend on the quasar luminosity. However, Figure 4.11 demonstrates that the strong correlation between the C IV blueshift and [O III] EQW is clearly not being driven by the mutual dependence of these parameters on the luminosity.

Blueshifted C IV emission is thought to arise in a high-velocity accretion disc wind. The strong anti-correlation between the C IV blueshift and the [O III] EQW suggests that these outflows are having a dramatic impact on gas extended over kilo-parsec scales in the NLR. Dynamical time-scales for the impact of fast moving outflows even on large NLRs are very short: it would take 10^6 years for an outflow travelling at 3000 km s^{-1} to reach 3 kilo-parsec. Lifetimes of luminous quasars at these redshifts may be 10^7 years (e.g. Martini and Weinberg, 2001). Therefore, if the BLR outflows can break out into the interstellar medium of the host-galaxy, the NLR can be cleared on a relatively short time-scale. One possibility is that the BLR winds collide with the interstellar medium and shock and accelerate it to produce a galaxy-wide wind (e.g. King, Zubovas, and Power, 2011; Faucher-Giguère and Quataert, 2012). C IV blueshifts are generally weaker in lower-luminosity quasars. Therefore, this picture also explains our finding that objects with very weak

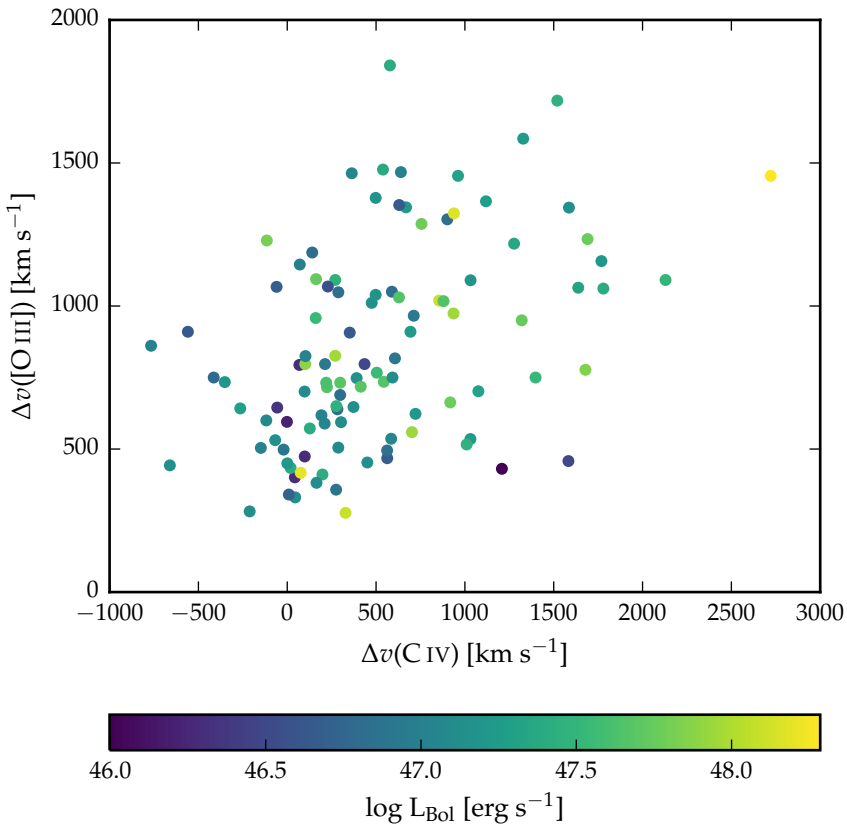

Figure 4.12: Relationship between the C IV (v_{50}(C IV) - v_{peak}([O III])) and [O III] (v_{10}([O III]) - v_{peak}([O III])) blueshift. The C IV and [O III] blueshifts are correlated with $\rho_S = 0.46$. This correlation is independent of the luminosity (indicated by the colour of the points).

[O III] (EQW < 1 Å) are ten times rarer in $z \lesssim 1$ SDSS quasars than in our sample of luminous quasars.

4.4.5 *A link between BLR and NLR outflows*

In Figure 4.12 we show that the [O III] blueshift is correlated with the C IV blueshift. The Spearman correlation coefficient, ρ_S, is 0.46, with p-value $= 6 \times 10^{-7}$. This shows that high-velocity winds in the NLR are preferentially seen when strong winds are being driven in the vicinity of the central engine. As we demonstrate in Figure 4.12, this correlation is not driven by the luminosity. Although we currently lack direct spatial information, this correlation suggests a connection between gas kinematics on sub-parsec and kilo-parsec scales.

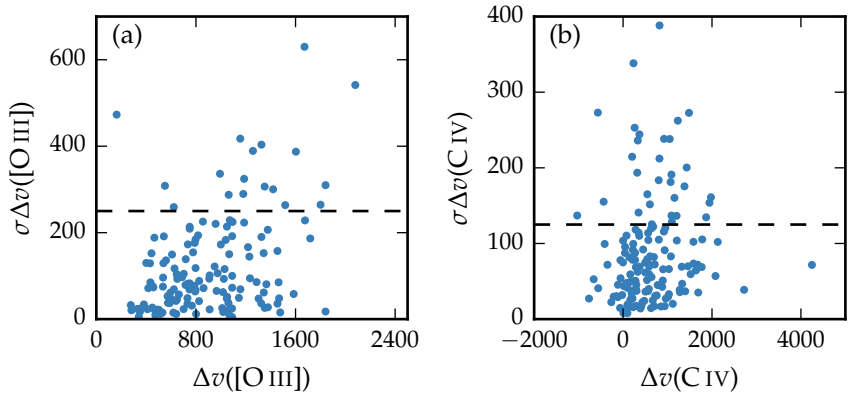

Figure 4.13: [O III] blueshift error as a function of the [O III] blueshift (a), and C IV blueshift error as a function of the C IV blueshift (b). Objects with errors on the [O III] and C IV blueshifts exceeding 250 or 125 km s^{-1} respectively are excluded from Figure 4.12. The [O III] and C IV blueshifts of these objects, which lie above the dashed lines in (a) and (b), are similar to the main sample, meaning our results should not be biased by their exclusion.

The [O III] blueshift is defined as v_{10}([O III]) - $v_{\rm peak}$([O III]) and the C IV blueshift is defined as v_{50}(C IV) - $v_{\rm peak}$([O III]). We considered a number of alternative approaches to parametrising both the [O III] line shape and the systemic redshift. Very similar trends are observed when the [O III] line shape is parametrised using $v_{25} - v_{\rm peak}$, $v_{50} - v_{\rm peak}$, $w_{80} = v_{90} - v_{10}$, or the asymmetry A. The same trend is also observed when the systemic redshift is defined using the peak of the Hβ emission.

In the previous section, we saw how [O III] is very weak in quasars with C IV blueshifts exceeding $\sim$ 2000 km s^{-1}. The [O III] blueshift cannot be reliably measured if the emission-line EQW $\lesssim$ 8 (Section 4.3.7) and so this limits the dynamic range of C IV blueshifts probed in Figure 4.12.

We do not show objects for which the errors on the [O III] and C IV blueshifts exceed 250 or 125 km s^{-1} respectively. The [O III] and C IV blueshifts of these objects, shown in Figures 4.13a and 4.13b, are similar to the main sample, meaning our results should not be biased by their exclusion. We also remove the objects with extreme [O III] emission (Section 4.4.7), because the systemic redshift determined from the peak of the [O III] emission is strongly biased in these objects.

Shen and Ho (2014) showed how the [O III] EQW decreases as the optical Fe II strength (which is related to the Eddington ratio) or luminosity increase. However, the amplitude of the systemic, core [O III] emission decreases faster than the wing component. A by-product of this effect is that overall the [O III] profile becomes broader and more blueshifted, as the broad wing becomes relatively more prominent. If the anti-correlation between the [O III] EQW and C IV blueshift is primarily being driven by a reduction in the flux of the core component (as a stable NLR is removed by the outflowing material), this would lead to a correlation between the [O III] blueshift and C IV blueshift similar to the one seen in Figure 4.12. This effect could also explain the anti-correlation between the [O III] EQW and blue-asymmetry / velocity-width we reported in Section 4.4.1.

4.4.6 *The BAL parent population*

Classical high-ionization BAL (HiBAL) quasars are likely to be radiating with relatively high L/L_{Edd} (e.g. Zhang et al., 2014). We therefore propose that the subset of the quasar population that exhibits large C IV-emission blueshifts may be directly related to the HiBAL quasar population – perhaps even the 'parent' population (Richards, 2006).

To test this hypothesis, we selected 18 C IV BAL quasars from our catalogue which have near-infrared spectra including the Hβ/[O III] region. Using the same method described in Section 3.4.1, we constructed a median composite spectrum from this sample. For comparison, we also constructed composite spectra for quasars with modest and large C IV blueshifts. The results are shown in Figure 4.14. We find that [O III] is very weak in the BAL quasars and that the median [O III] emission profiles in the BAL quasars and non-BAL quasars with large C IV blueshifts are very similar (e.g. Yuan and Wills, 2003). This suggests that the impact outflows have on the NLR gas in BAL quasars and non-BAL quasars with large C IV blueshifts is similar. On the other hand, Hβ is narrower in BAL quasars than in non-BAL quasars (with or without large C IV blueshifts). One possibility is that, while the [O III] emission is relatively isotropic, the Hβ FWHM has some dependence on the orientation of the BLR (e.g. Shen and Ho, 2014). In this scenario, the narrower Hβ emission suggests that BAL quasars are preferentially observed in relatively face-on orientations.

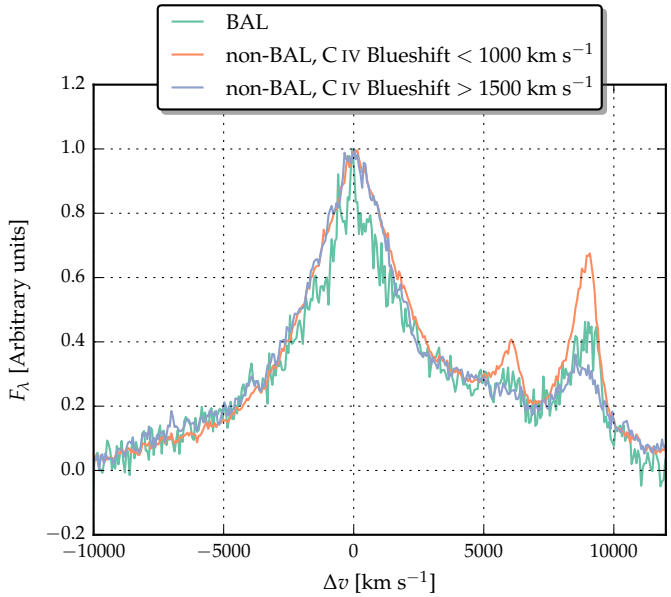

Figure 4.14: Composite spectra of the Hβ/[O III] region made of BAL quasars, non-BAL quasars with C IV blueshifts below 1000 km s^{-1}, and non-BAL quasars with C IV blueshifts above 1500 km s^{-1}. [O III] is similar in BAL quasars and non-BAL quasars with large C IV blueshifts, whereas Hβ is narrower in the BAL quasars.

4.4.7 *Extreme [O III] profiles*

Figure 4.15 shows the spectra of 18 objects which we visually identified as having [O III] emission profiles with similar characteristics to four extremely dust-reddened quasars at $z \sim 2$ recently identified by Zakamska et al. (2016). The extreme nature of the [O III] emission in their sample of red quasars led Zakamska et al. (2016) to propose that these objects are being observed in the process of expelling the gas in their host-galaxies and transitioning from a dust-obscured, star-burst phase to a luminous, blue quasar (e.g. Sanders et al., 1988).

The [O III] emission in the 18 objects in our sample is very broad ($1800 \lesssim w_{80} \lesssim 3200\,\mathrm{km\,s^{-1}}$; Figure 4.8). In many of these objects the systemic, core component of [O III] is not detected. The [O III] doublet is blended together, and is also heavily blended with the red wing of the Hβ emission. The Fe II emission may also be significant in this region of the spectrum.

In Figure 4.16 we compare the velocity-widths and rest-frame 5 μm luminosities of the 18 quasars in our sample with the four quasars from Zakamska et al. (2016). On average, the Zakam-

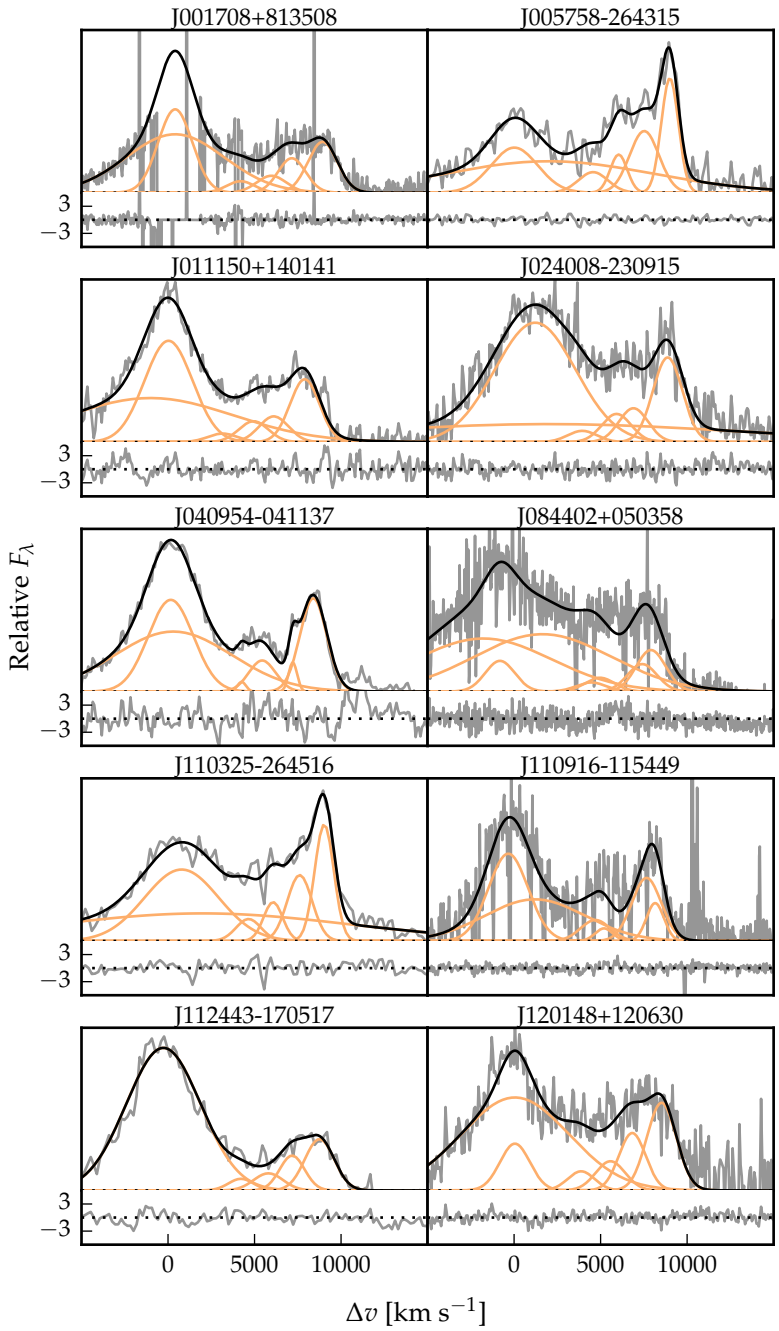

Figure 4.15: Model fits to the continuum- and Fe II-subtracted Hβ/[O III] emission in 18 quasars with extreme [O III] emission profiles. The data is shown in grey, the best-fitting model in black, and the individual model components in orange. The peak of the [O III] emission is used to set the redshift, and Δv is the velocity shift from the rest-frame transition wavelength of Hβ. Below each spectrum we plot the data- minus-model residuals, scaled by the errors on the fluxes.

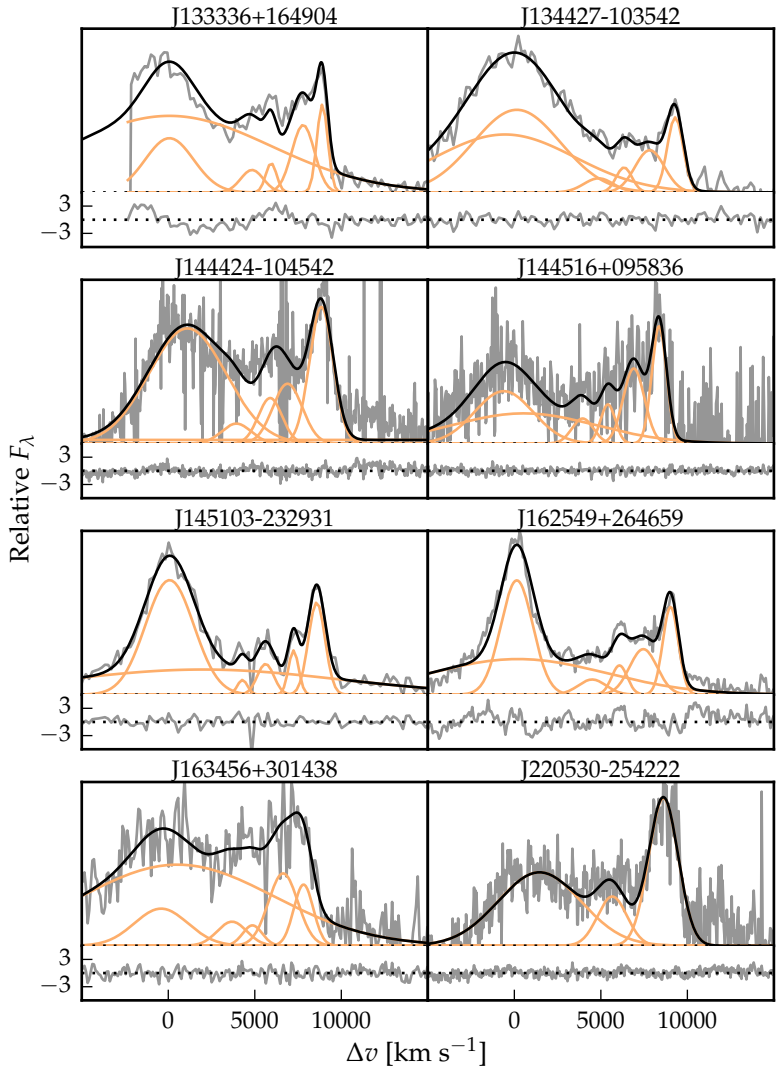

Figure 4.15: Continued.

ska et al. (2016) quasars have higher luminosities ($10^{46.7}$ versus $10^{46.3}$ erg s^{-1}) and the [O III] emission is broader ($w_{90} = 5740$ versus 3120 km s^{-1}). However, the [O III] velocity-width and luminosity of the least extreme Zakamska et al. (2016) quasar has properties very similar to our sample, and our objects lie on top of the velocity-luminosity relation derived by Zakamska et al. (2016) (Figure 4.16).

The [O III] velocity-widths and luminosities of the 18 quasars in Figure 4.15 are very large, but are comparable to many other objects in our sample. However, we find that of the six objects

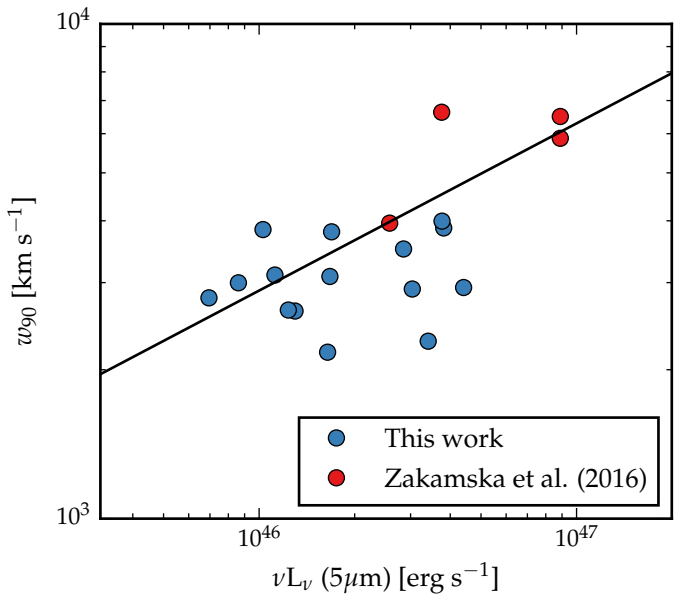

Figure 4.16: Velocity-widths, w_{90}, and rest-frame 5 μm luminosities of the 18 quasars in our sample with extreme [O III] emission profiles and the four dust-reddened quasars from Zakamska et al. (2016). Our sample falls on the width-luminosity relation derived by Zakamska et al. (2016).

which fall within the footprint of the FIRST radio survey, four are radio-loud (three core-dominated and one lobe-dominated). Given the fraction of radio-loud objects in our sample is 11 per cent, the binomial probability of finding four radio-loud objects in a sample of six is 0.1 per cent. Relativistic jets are known to accelerate gas to velocities of up to a few thousand km s^{-1} (e.g. Nesvadba et al., 2006; Nesvadba et al., 2008), and this could be inducing the disturbed [O III] gas kinematics of these objects.

4.5 MASS OUTFLOW RATE AND KINETIC POWER

The mass outflow rate and kinetic power of galaxy-wide outflows are important in order to understand the role played by quasars in the evolution of galaxies. In this section, we calculate the mass outflow rate ($\dot{M}$) and kinetic power (P_K) of the ionised outflows in our sample of luminous quasars, using the [O III] emission as a gas tracer (e.g. Harrison et al., 2012; Cano-Díaz et al., 2012; Liu et al., 2013; Brusa et al., 2015; Carniani et al., 2015; Bischetti et al., 2016; Kakkad et al., 2016). By making reasonable assumptions for unknown quantities (including the geometry,

spatial scale and density of the gas in the outflow) we can calculate order of magnitude estimates of the outflow properties. Our calculations are based on the model of Cano-Díaz et al. (2012), and a comprehensive description of the assumptions in the model and their impact on the inferred outflow properties can be found in Cano-Díaz et al. (2012) and Kakkad et al. (2016).

Following Cano-Díaz et al. (2012), the mass in the ionised outflow is given by

$$M \simeq 5.33 \times 10^{7} \left(\frac{C}{10^{[O/H]-[O/H]_\odot}}\right) \left(\frac{L([OIII])}{10^{44}\,\mathrm{erg\,s^{-1}}}\right) \times \left\langle \frac{n_e}{10^{3}\,\mathrm{cm^{-3}}} \right\rangle^{-1} M_\odot \tag{4.1}$$

where $L([OIII])$ is the luminosity of [O III] emitted in the outflow (in units of 10^{44} erg s^{-1}), $\langle n_e \rangle$ is the electron density in the outflowing gas (in units of 10^3 cm^{-3}), $10^{[O/H]}$ is the metallicity (in units of Solar metallicity), C ($= \langle n_e \rangle^2 / \langle n_e^2 \rangle$) is the condensation factor (assumed to be $\simeq 1$). Assuming a conical outflow with uniformly distributed clouds out to a radius R with a constant outflow velocity, the mass outflow rate of the gas is given by

$$\dot{M} = 164 \left(\frac{R}{1\,\mathrm{kpc}}\right)^{-1} \left(\frac{C}{10^{[O/H]-[O/H]_\odot}}\right) \left(\frac{L([OIII])}{10^{44}\,\mathrm{erg\,s^{-1}}}\right) \times \left(\frac{v}{1000\,\mathrm{km\,s^{-1}}}\right) \times \left\langle \frac{n_e}{10^{3}\,\mathrm{cm^{-3}}} \right\rangle^{-1} M_\odot\,\mathrm{yr^{-1}} \tag{4.2}$$

where v is the outflow velocity (in units of 1000 km s^{-1}). The kinetic power of the outflow ($1/2\dot{M}v^2$) is given by:

$$P_K = 5.17 \times 10^{43} \left(\frac{R}{1\,\mathrm{kpc}}\right)^{-1} \left(\frac{C}{10^{[O/H]-[O/H]_\odot}}\right) \left(\frac{L([OIII])}{10^{44}\,\mathrm{erg\,s^{-1}}}\right) \times \left(\frac{v}{1000\,\mathrm{km\,s^{-1}}}\right)^{3} \times \left\langle \frac{n_e}{10^{3}\,\mathrm{cm^{-3}}} \right\rangle^{-1} \mathrm{erg\,s^{-1}} \tag{4.3}$$

We assume that the maximum outflow velocity ($\simeq v_5$) is representative of the average outflow velocity, with the lower velocities due to projection effects (Cano-Díaz et al., 2012). We assume the outflowing gas is represented by the broader of the two Gaussian components in our [O III] model, and use the luminosity of this component to estimate the luminosity of the outflowing gas. This is not possible when [O III] is modelled with a single Gaussian, and so these objects are not considered.

For the outflow radius we use 4 kilo-parsec. This is broadly consistent with spatially resolved observations of quasars at similar redshifts and luminosities (e.g. Cano-Díaz et al., 2012; Carniani et al., 2015; Brusa et al., 2016) and photo-ionisation estimates (e.g. Zakamska et al., 2016).

With these values, we calculate outflow rates which range from a few to $4000\,M_\odot\,yr^{-1}$. The mean for our sample is $560\,M_\odot\,yr^{-1}$. In terms of the kinetic power of the outflows, this corresponds to values from about $10^{41.8}$ to $10^{45.7}$ $erg\,s^{-1}$, with mean $10^{44.7}$ $erg\,s^{-1}$. The mean kinetic power corresponds to ~ 0.15 per cent of the bolometric luminosity, and this reaches almost 1 per cent in the most powerful outflows. However, if the ionised outflow is accompanied by a neutral/molecular outflow an order of magnitude more massive then the kinetic power is also likely to be an order of magnitude higher (Cano-Díaz et al., 2012), i.e. about 1.5 per cent of the bolometric luminosity for the mean kinetic power and 10 per cent for the most powerful outflows. These outflow efficiencies are in same ballpark as recent AGN feedback models (e.g. Zubovas and King, 2012), which predict a coupling efficiency between AGN-driven outflows and AGN power of ~ 5 per cent.

4.6 MEAN FIELD INDEPENDENT COMPONENT ANALYSIS

Blind source separation (BSS) techniques can be used to find a set of basis vectors from a set of spectra. An individual spectrum can then be represented as a linear combination of the basis vectors with a corresponding set of weights. Principal component analysis (PCA) is one example of a BSS technique that has been applied extensively to analyse astronomical spectra (e.g. Mittaz, Penston, and Snijders, 1990; Francis et al., 1992; Yip et al., 2004). However, in general it is not possible to physically interpret the individual PCA components. Mean field independent component analysis (MFICA) is a more powerful class of BSS technique that works by finding a basis of independent components to represent the data. Allen et al. (2013) used this technique to analyse the SDSS spectra of emission-line galaxies and demonstrated its effectiveness in identifying distinct emission sources in the spectra.

In this section, we use a set of ten MFICA-derived spectral components to reconstruct the rest-frame optical spectra of luminous quasars. The MFICA components have been derived from a large sample of $z \lesssim 1$ SDSS spectra. The set of weights

measured for each quasar provide a compact representation of its spectral properties. By equating components with physical properties of interest we can use the component weights in place of more commonly used emission-line parameters. We show below how the distribution of weights in the sample as a whole reveals many of the results previously brought to light using the more traditional approach adopted in the first part of this chapter (i.e. fitting multiple Gaussian components). At the same time, with the MFICA-derived components we are able to extend our analysis to a lower S/N regime.

As we will show later in this section, initial results from the MFICA analysis are very promising. Nevertheless, we face two outstanding issues. The first is the limited spectral diversity of the objects used to derive the components, which limits the diversity of the spectra the components are able to reconstruct. The second is cross-talk between the components, which blurs the mapping of component weights to physical properties. These are discussed below, together with our proposed solutions.

4.6.1 *Generating MFICA components*

We use a set of ten spectral components that have been generated using the MFICA algorithm on a sample of 2154 redshift $0.6 < z < 0.8$ BOSS quasars[2]. The sample was restricted to the highest luminosity quasars in this redshift interval (in order to reduce the host galaxy contribution) and a minimum threshold to the spectrum S/N (measured between 4600 and 5200 Å in the quasar rest-frame) was set at 10 per pixel. The MFICA components were generated in the rest-frame interval 4000-5600 Å. Six positive independent components and four lower-amplitude 'correction' components that can have negative weights were found to be sufficient to reconstruct the spectra.

4.6.2 *MFICA reconstruction of luminous quasar spectra*

Each spectrum in our sample of luminous quasars can be reconstructed as a linear combination of the 10 MFICA components. The optimum set of component weights, $\mathbf{w}$, for each input spectrum is determined using a variance-weighted χ^2 minimisation

2 Generation of the MFICA components was done by Prof. Paul Hewett.

procedure. The MFICA components and the input spectra are first pre-processed to remove any large-scale slope. The first six component weights are constrained to be non-negative, and a single velocity offset parameter (applied to all components) is an additional free parameter in the optimisation procedure.

The median reduced-χ^2 is 1.4 for quasars with $w_{80} < 2000\,\mathrm{km\,s^{-1}}$, which demonstrates that the MFICA components are able to accurately reproduce the spectra of objects with relatively narrow [O III] emission. The MFICA components are also able to accurately reproduce the Fe II emission in many of the quasars for which the Boroson and Green (1992) template was a poor model (Section 4.3.2).

However, the reduced-χ^2 increases as w_{80} increases, and visual inspection of the spectra confirm that the MFICA components are struggling to reproduce the very broad [O III] emission-lines present in our sample of luminous quasars. As we showed in Section 4.4.2, the typical [O III] emission properties in luminous quasars at $z \gtrsim 2$ are significantly different from the properties of $z \lesssim 1$ SDSS quasars. Specifically, [O III] is broader, weaker and more asymmetric in more luminous quasars. [O III] emission-lines with these characteristics are rare in the sample of $z \lesssim 1$ SDSS quasars used to derive the MFICA components, and so very broad [O III] emission-lines are not well represented in the components. This issue may be straightforwardly addressed by increasing the spectral diversity of the training set. Specifically, we can identify objects in the SDSS catalogue with broad [O III] emission-lines similar to the ones seen in luminous quasars, and add these to the set of spectra used to generate the MFICA components.

4.6.3 *Interpretation of MFICA components*

An example MFICA reconstruction of the Hβ/[O III] emission region is shown in Figure 4.17. The shape of the individual MFICA components are highly suggestive of a relation to the underlying physical processes contributing to the quasar spectrum. This correspondence is summarised in Table 4.6. The component w_1 corresponds to Fe II emission, the components w_2 and w_3 to broad Hβ emission, the components w_4 and w_5 to narrow [O III] and Hβ emission at the systemic redshift, and the component w_6 to broad, blueshifted [O III] emission.

As we show in the next section, the component weights can be used directly as a compact representation of the spectral

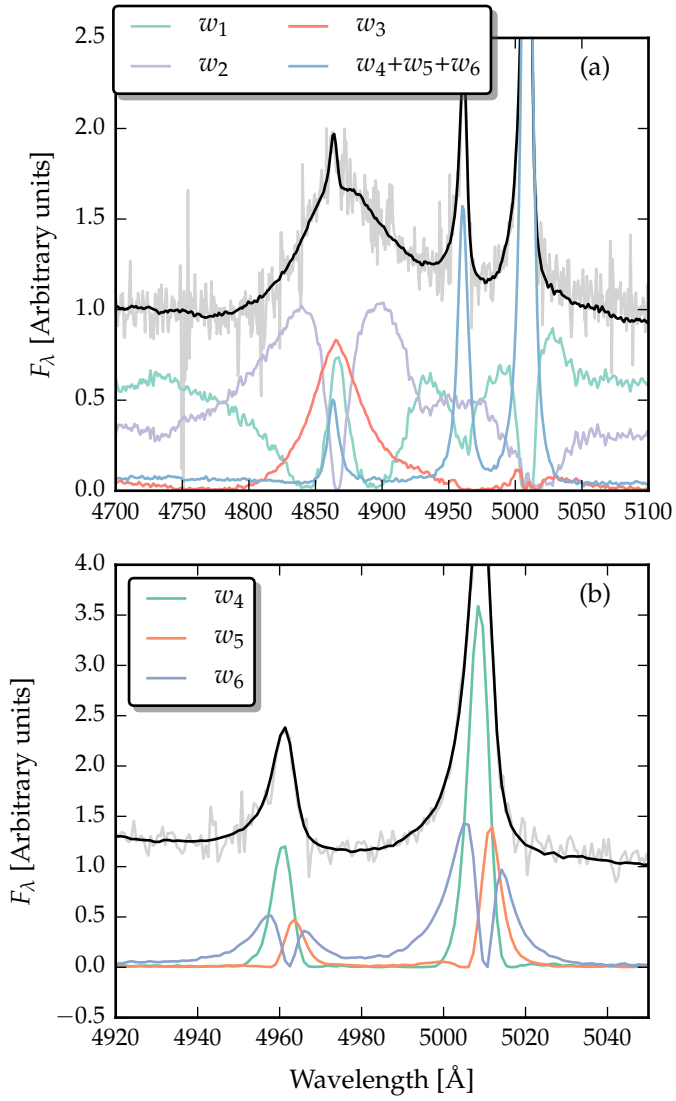

Figure 4.17: MFICA reconstruction of the Hβ/[O III] emission in quasar J002952+020607. The MFICA reconstruction is shown in black, and the spectrum in grey. The first three components (w_1, w_2, w_3), and the sum of components w_4, w_5 and w_6 are shown individually in (a). Components w_4, w_5, w_6 are shown individually in (b).

properties. However, we would also like to be able to measure non-parametric emission-line properties from the high-S/N MFICA reconstruction. These non-parametric properties can then be readily compared to the literature. If MFICA components w_4, w_5 and w_6 (the '[O III] components') comprised 100

Component	Origin
w_1	Fe II
w_2	Hβ
w_3	Hβ
w_4	[O III] core
w_5	[O III] core
w_6	[O III] wing

Table 4.6: Physical interpretation of the MFICA components.

per cent of the [O III] emission, then the [O III] emission could be reconstructed by setting the 'non-[O III] components' (w_1, w_2 and w_3) to zero. Standard non-parametric emission properties could then be computed from the [O III] reconstruction.

In practice, a very small fraction of the [O III] emission may be present in the non-[O III] components because of cross-talk between the signals in the components. However, we can ensure that close to 100 per cent of the [O III] emission is in the [O III] components by making a small adjustment to the MFICA component generation algorithm. The non-[O III] components will be generated first, with the [O III] emission region interpolated across. With these components fixed, the [O III] components, which will now include all of the [O III] signal, can then be generated.

4.6.4 *MFICA component weight distributions*

In this section, we consider how the distribution of quasars in the six-dimensional MFICA component weight parameter space changes as a function of luminosity and other quasar properties.

Figure 4.18 shows the one-dimensional distributions of each of the MFICA component weights in our sample of luminous quasars and in the $z \lesssim 1$ SDSS sample. The core [O III] emission (represented by components w_4 and w_5) is weaker in the more luminous quasar sample, but the strength of the [O III] wing (w_6) is similar. The relative weights of the core and wing components determine the overall [O III] width and asymmetry, and so this demonstrates that [O III] is broader and more blueshifted in the high-luminosity sample. The same conclusions were reached in Section 4.4.2. The distributions of MFICA component weights suggest that the varying strength of the core component, rather than the strength of the wing, is the

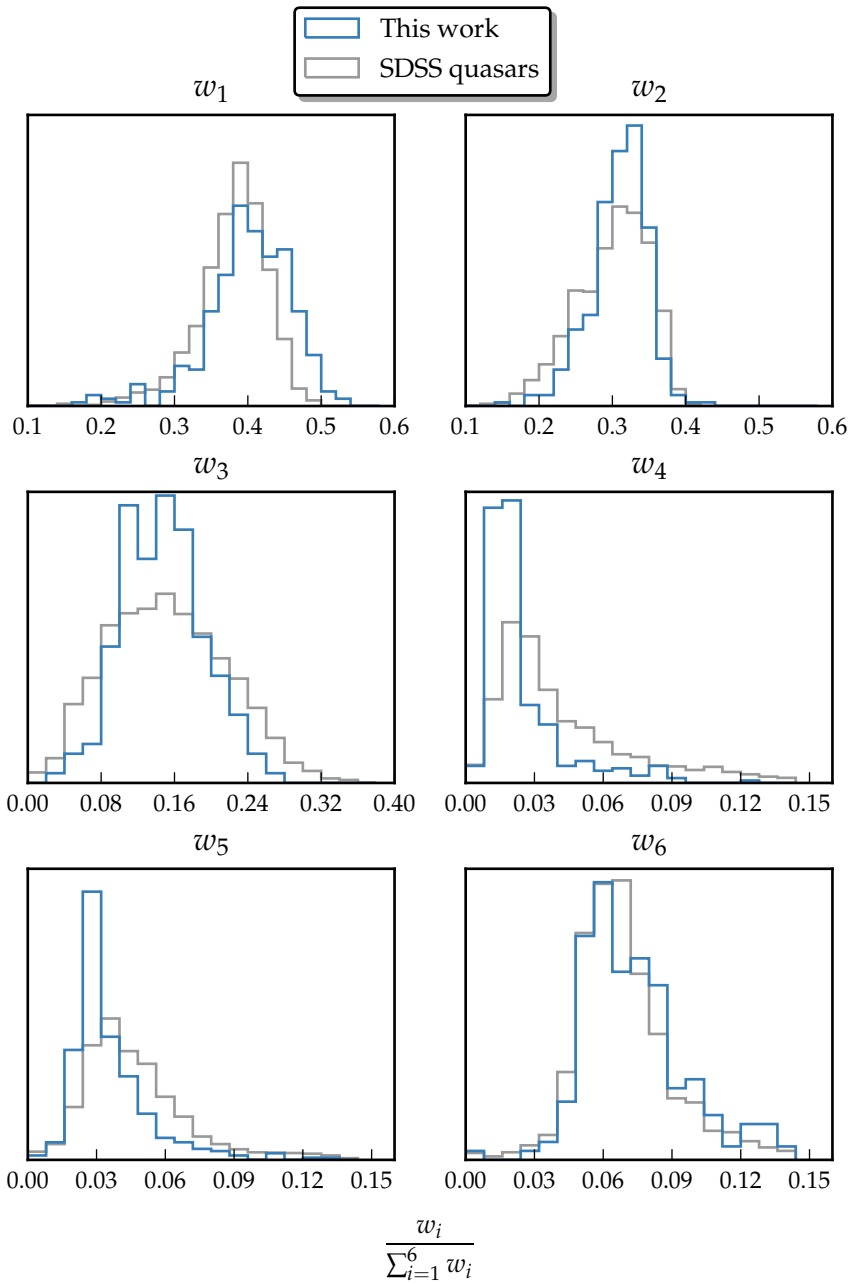

Figure 4.18: Distributions of each of the MFICA component weights in our sample of luminous quasars and in the $z \lesssim 1$ SDSS sample. The core [O III] emission (represented by components w_4 and w_5) is weaker in the more luminous quasar sample, but the strength of the [O III] wing (w_6) is similar.

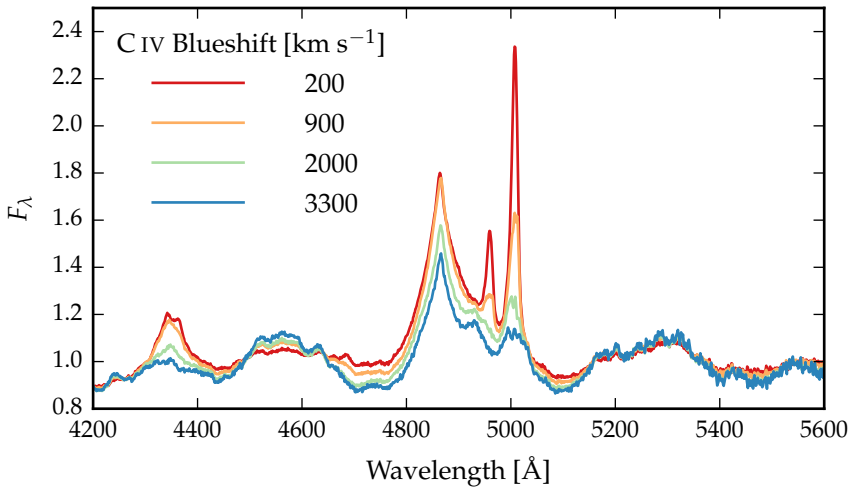

Figure 4.19: Median MFICA-reconstructed spectra as a function of the C IV blueshift.

dominant factor in determining the overall shape of the [O III] emission (e.g. Shen and Ho, 2014).

In Figure 4.19 we have taken the median MFICA component weights as a function of the C IV blueshift and used these to generate high S/N representations of such spectra. There are strong systematic differences in the spectra as a function of the C IV blueshift. [O III] becomes progressively weaker and more blueshifted as the C IV blueshift increases and in the highest C IV blueshift spectrum [O III] is undetected. The anti-correlation with the strength of Fe II in the 4434-4684 Å region is also apparent. The same trends were previously identified in Section 4.4.4. These results demonstrate that MFICA offers a promising route forward in terms of generating high-S/N reconstructions of the observed spectra which can then be studied in detail.

The systematic difference in the spectra presented in Figure 4.19 (e.g. the anti-correlated strengths of [O III] and Fe II) are the same trends identified in the first eigenvector of the Boroson and Green (1992) PCA analysis (EV1). Over the years, EV1 has been used in attempts to explain the diversity of AGN spectra and ultimately classify AGN in a similar way that the Hertzsprung–Russell diagram is used to classify stars. Unlike the PCA eigenvectors, the MFICA components are physically interpretable and, looking to the future, may prove to be a more effective means of classifying and understanding the diversity of AGN spectra.

4.7 SUMMARY

The main results of this chapter are as follows:

- We have analysed the [O III] emission properties of 330 quasars at redshifts ($1.5 \lesssim z \lesssim 4$) and luminosities ($45.5 \lesssim \log L_{Bol} \lesssim 49$ erg s^{-1}). In many of these objects [O III] is very broad and has a strong blueshifted component, suggesting that kilo-parsec-scale outflows in ionised gas are very common in this population.

- There is a strong anti-correlation between the [O III] EQW and the C IV blueshift. This suggests that quasar-driven winds are capable of sweeping away gas extended over kilo-parsec scales in the host galaxies. We suggest this as the cause of a factor of ten higher rate of occurrence of quasars with very weak [O III] in the luminous quasar sample relative to in $z \lesssim 1$ SDSS quasars.

- The [O III] blueshift is correlated with the C IV blueshift, which could indicate a connection between gas kinematics on sub-parsec and kilo-parsec scales. On the other hand, this correlation could be induced by the core component of the [O III] emission decreasing faster than the wing component, as the stable NLR gas is removed by the quasar-driven winds.

- We identify 18 objects with very broad [O III] emission profiles with similar characteristics to four extremely dust-reddened quasars recently identified by Zakamska et al. (2016). The high fraction of these objects which are radio-loud suggests that the disturbed [O III] gas kinematics could be induced by relativistic jets.

- The mean kinetic power of the ionised outflows is $10^{44.7}$ erg s^{-1}, corresponding to ~ 0.15 per cent of the bolometric luminosity. However, if the ionised outflows are accompanied by molecular outflows an order of magnitude more massive then the kinetic power may also be an order of magnitude higher, i.e. 1 per cent of the bolometric for a typical outflow, or up to 10 per cent for the most powerful outflows. These outflow efficiencies are in same ballpark as recent AGN feedback models.

- We use a set of ten MFICA-derived spectral components to reconstruct the rest-frame optical spectra. The corresponding set of component weights provide a compact representation of the quasar spectral properties. We show that the components correspond to physical properties, and that the distribution of component weights in the sample as a whole reveals many of the results previously brought to light using a more traditional analysis. At the same time, the MFICA-derived components provide a high S/N representation of the observed spectra and can also extend our analysis to a lower S/N regime.

5 OUTFLOWS AND HOT DUST EMISSION

5.1 INTRODUCTION

Many quasars and AGN show an excess in their rest-frame near-infrared continuum emission. This feature is generally attributed to thermal emission from dust heated by optical/ultraviolet radiation from the accretion disc. The wavelength of the feature ($\sim 2\,\mu$m) corresponds to the spectral peak for graphite dust at its sublimation temperature ($T \sim 1500\,$K; Barvainis, 1987). This suggests that the hot dust is very close to the central source, at a radius set by the sublimation temperature of the dust grains. In nearby AGN, reverberation measurements suggest that this radius is a few tens of light days (e.g. Minezaki et al., 2004; Suganuma et al., 2006), placing the hot dust at the innermost edge of the putative torus-like structure.

Studies have fitted the near-infrared SEDs of AGN using a blackbody spectrum to represent emission from hot dust (e.g. Edelson and Malkan, 1986; Barvainis, 1987; Kishimoto et al., 2007; Mor, Netzer, and Elitzur, 2009; Riffel, Storchi-Bergmann, and McGregor, 2009; Deo et al., 2011; Landt et al., 2011; Mor and Trakhtenbrot, 2011; Roseboom et al., 2013). A hot dust component is present in the vast majority of AGN, although populations of 'dust-free' objects have also been uncovered (Hao et al., 2010; Hao et al., 2011; Jiang et al., 2010; Mor and Trakhtenbrot, 2011). It is not yet clear how hot dust properties including the temperature and covering factor relate to other AGN properties such as BH mass, luminosity and accretion rate.

In recent years, the picture of the dusty torus has evolved away from a static 'doughnut' towards a more general circumnuclear, geometrically and optically thick dust distribution. As we have previously discussed (Section 1.6), winds and outflows launched from the accretion disc are very common in AGN. In the dusty wind model – first proposed by Konigl and Kartje (1994) and later developed by, amongst others, Everett (2005), Elitzur and Shlosman (2006), Keating et al. (2012) – the torus is the dusty part of an accretion disc wind that extends beyond the dust sublimation radius. The dusty clouds are uplifted above the disc where they are directly exposed to radi-

ation from the central engine. The dust is heated, and radiates in the near-infrared band. At the same time, radiation pressure on dust can efficiently accelerate the wind (e.g. Fabian, 2012). The wind is roughly polar, and so naturally provides circum-nuclear obscuration around the accretion disc and dust-free BLR. This model is supported by recent interferometric observations of nearby Seyfert galaxies which find that the mid-infrared emission is dominated by dust in the polar regions (e.g. Raban et al., 2009; Hönig et al., 2012; Hönig et al., 2013; Tristram et al., 2014; López-Gonzaga et al., 2016).

Studying the relationship between emission from hot dust and outflow diagnostics in the BLR can help place constraints on this dusty wind model (e.g. Wang et al., 2013). This is now possible by combing data from the SDSS spectroscopic and photometric surveys with infrared photometric surveys such as UKIDSS and WISE. At redshifts $2 \lesssim z \lesssim 3$, SDSS spectra reveal BH masses, accretion rates and diagnostics of the BLR dynamics. At the same time, the available photometric data provides full ultra-violet to infrared rest-frame coverage of the SED. In particular, the WISE photometry is sensitive to the 3 μm region of the SED which is dominated by hot dust.

In this chapter, we build a simple parametric SED model that is able to reproduce the median optical to infrared colours of tens of thousands of SDSS AGN at redshifts $1 \lesssim z \lesssim 3$ (Section 5.4). We use this model to measure the hot dust properties of a large sample of $2 < z < 2.7$ quasars for which we have already measured C IV emission properties, BH masses and Eddington ratios (Section 5.5).

5.2 DATA

5.2.1 *SDSS*

We use both spectroscopic and photometric data from the SDSS DR7 quasar catalogue. The SDSS photometric survey obtained images in five broad optical passbands: u, g, r, i and z (Table 5.1). We use point-spread function magnitudes from the catalogue.

5.2.2 *UKIDSS Large Area Survey*

We use the tenth data release of the UKIDSS Large Area Survey which has observed $\sim 3,200$ deg^2 in four near-infrared pass-

Survey	Passband	$\lambda_{\rm Eff}$ [μm]	AB offset	$A_{\rm filter}/E(B-V)$
SDSS	u	0.3543	0.913	4.875
	g	0.4770	−0.081	3.793
	r	0.6231	0.169	2.721
	i	0.7625	0.383	2.099
	z	0.9134	0.542	1.537
UKIDSS	Y	1.0305	0.641	1.194
	J	1.2483	0.941	0.880
	H	1.6313	1.378	0.569
	K	2.2010	1.897	0.352
WISE	W1	3.4	2.691	0.182
	W2	4.6	3.331	0.130
	W3	12.0	5.174	

Table 5.1: Available photometric data, effective wavelengths, $\lambda_{\rm Eff}$, of passbands, Vega to AB magnitude offsets and conversions from $E(B-V)$ to passband extinction.

bands: Y, J, H and K. We use 'apermag3' magnitudes, which are aperture corrected magnitudes in a 2″ diameter aperture.

5.2.3 *WISE All-WISE Survey*

WISE mapped the entire sky in four mid-IR passbands: *W*1, *W*2, *W*3 and *W*4. The WISE AllWISE Data Release ('AllWISE') combines data from the nine-month cryogenic phase of the mission that led to the 'AllSky' data release with data from the NEOWISE program (Mainzer et al., 2011). We use profile-fitting 'mpro' magnitudes. Only information from the first three WISE passbands are used in this work.

5.2.4 *Computing Vega-AB magnitude offsets*

Vega magnitudes are used throughout this chapter. This is the native magnitude system for UKIDSS[1] and WISE. SDSS uses an 'asinh' magnitude system (Lupton, Gunn, and Szalay, 1999) which is intended to be on the AB system (Oke and Gunn, 1983). However, the photometric zero-points are known to be slightly off the AB standard. The *z* passband is in error by 0.02

1 We find that adding 0.08 mag to the UKIDSS Y passband magnitudes brings the photometry into better agreement with the SDSS *z* and UKIDSS J photometry.

($z_{AB} = z_{SDSS} + 0.02$)[2]. The u passband was in error by 0.04 dex at the time of DR7. However, the u throughput function has subsequently been updated (Doi et al., 2010) and the zero-point is now consistent with the AB system.

We use synthetic photometry to calculate the AB magnitude of Vega in each passband. This can then be used to compute zero-point offsets between the Vega and AB magnitude systems. The mean flux density $f_\lambda(P)$ in a passband defined by a throughput function $P(\lambda)$ is given by:

$$f_\lambda(P) = \frac{\int P(\lambda) f_\lambda(\lambda) \lambda d\lambda}{\int P(\lambda) \lambda d\lambda} \tag{5.1}$$

where $f_\lambda(\lambda)$ is the flux density of the object. The passband magnitude is then given by:

$$m_\lambda(P) \quad = \quad -2.5\log(f_\lambda(P)) - m_0(P), \tag{5.2}$$

where $m_0(P)$ is the zero-point magnitude of passband P, given by evaluating Equation 5.1 for a reference spectrum. In the AB system this is a constant spectral flux density of 3631 Jy. In flux per unit wavelength this is:

$$\frac{f_\lambda(\lambda)}{\text{erg cm}^{-2}\ \text{s}^{-1}\text{Å}^{-1}} = 0.1087 \left(\frac{\lambda}{\text{Å}}\right)^{-2}. \tag{5.3}$$

In the Vega system, a spectrum of the A0V star Vega is used. Although the magnitude of Vega is by design zero in every passband, more recent measurements reveal the star to have a small positive magnitude. The Vega to AB zero-point conversions given in Table 5.1 assume Vega to have a magnitude 0.026.

5.2.5 *Galactic extinction correction*

$A(u)$, the Galactic extinction in the u passband, is given in the SDSS catalogue. It is computed using the maps of Schlegel, Finkbeiner, and Davis (1998). Schlegel, Finkbeiner, and Davis (1998) calculate the extinction assuming a $z = 0$ elliptical galaxy SED and find $A(u)/E(B-V) = 5.155$, where $E(B-V)$ is the relative extinction between the B and V passbands. Quasar and

2 http://classic.sdss.org/dr7/algorithms/fluxcal.html.

galaxy optical SEDs have very different shapes, and so we re-derived passband extinctions using a $z = 1.5$ quasar SED template[3]. Conversions from the selective extinction $E(B-V)$ to the total extinction $A(\lambda)$ in each passband are given in Table 5.1.

5.2.6 *Cross-matching SDSS to UKIDSS and WISE*

There are 105 783 objects in the SDSS DR7 quasar catalogue. While WISE mapped virtually the entire sky, the UKIDSS footprint covers approximately one third of the SDSS footprint. 36 607 objects are cross-matched to UKIDSS (with a $2''$ matching radius) and WISE (with a $3''$ matching radius).

5.2.7 *Quasar sample*

We include only the 20 637 quasars with i passband magnitudes brighter than 19.1, i.e. the quasars selected by the main $z < 3$ SDSS quasar selection algorithm (Richards et al., 2002). We verified that above the $i = 19.1$ limit the sample is 95 per cent complete in all passbands. BAL quasars are excluded using the Allen et al. (2011) catalogue. The C IV line parameters of these quasars can not be reliably measured. This leaves 19 837 objects in the sample.

We further limit our sample to the redshift range $1 < z < 3$. Imposing a $z = 1$ lower limit on the redshift of our sample ensures that contributions to the SED from quasar host galaxies are negligible. The completeness of the main SDSS DR7 quasar selection algorithm decreases at $z \sim 2.75$, and the limited numbers of quasars at higher redshifts sets the upper redshift limit. The redshift and luminosity distribution of the final sample, containing 12 934 quasars, is shown in Figure 5.1.

5.3 CONSTRUCTING AN AGN SED MODEL

Since the physical processes that power AGN are generally understood only qualitatively, almost all AGN SED templates are empirical. The empirical template of Elvis et al. (1994) is still the most commonly cited, despite many additions and updates (e.g. Polletta et al., 2000; Kuraszkiewicz et al., 2003; Risaliti and Elvis, 2004; Richards et al., 2006a; Polletta et al., 2007; Lusso et al., 2010; Shang et al., 2011; Marchese et al., 2012; Trichas

3 Extinction corrections were derived by Prof. Paul Hewett.

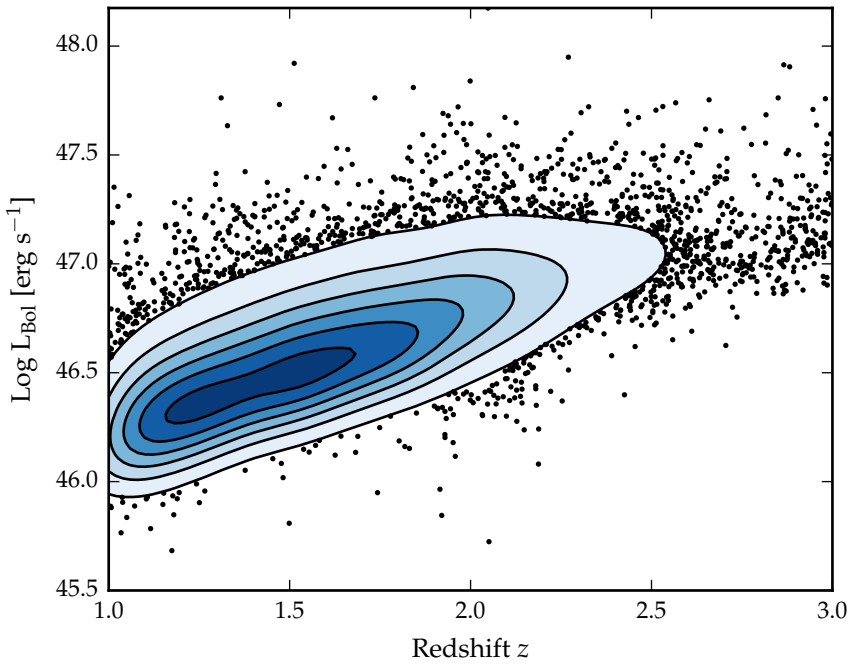

Figure 5.1: Distribution of our sample in the redshift-luminosity plane.

et al., 2012). However, these composite spectra are often constructed from quasars with a huge range in luminosity as a function of rest-frame wavelength. In addition, the host-galaxy contribution at optical wavelengths in low-redshift objects can be significant and is challenging to completely eliminate. There is therefore a strong rationale for taking a parametric approach to modelling quasar SEDs. This is the approach adopted in this work.

We construct an SED model that is valid between 1216 Å and 3 μm. In this region the SED is dominated by the accretion disc, broad ultra-violet/optical emission-lines and thermal emission from the hottest (T ~ 1200K) dust. In this section, we describe how each of these components are represented in our parametric SED model. The effect of dust extinction at the AGN redshift is also incorporated into the model. At high redshifts, Lyα forest absorption becomes significant. Because we do not attempt to include this effect, our model is valid only at wavelengths long-ward of 1216 Å. We model dust emission using a single temperature (T ~ 1200 K) blackbody, which peaks at ~ 2 μm. At longer wavelengths, emission from cooler dust further from the central engine becomes increasingly important. We do not include this emission in our model, which restricts its validity

to $\lesssim 3\,\mu$m. The model spectrum is shown in Figure 5.2, with each of the main components indicated.

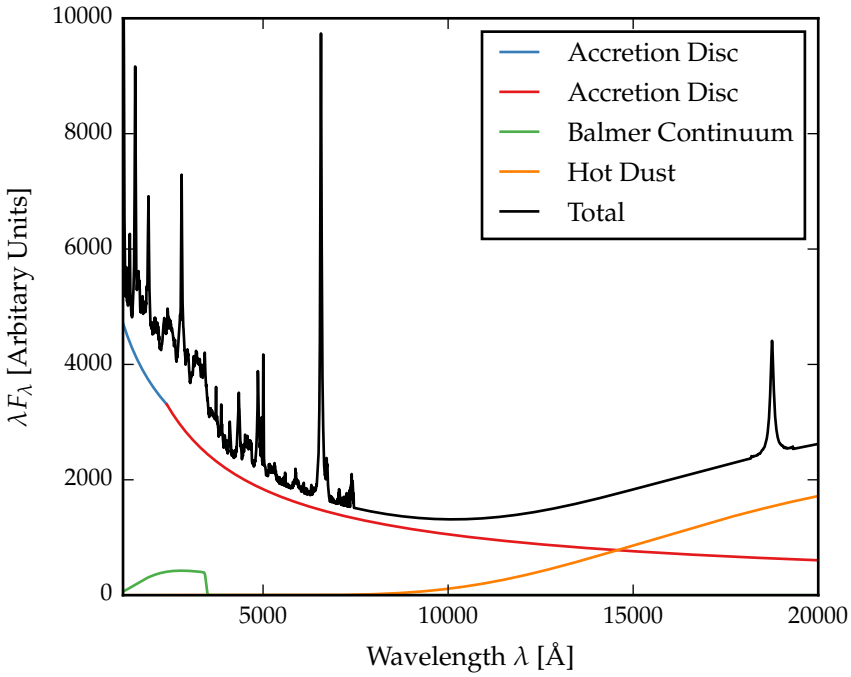

Figure 5.2: Model quasar spectrum at $z = 1$, showing the contributions to the total flux from the accretion disc, Balmer continuum, hot dust and emission-lines.

5.3.1 *Accretion disc*

Thermal accretion disc emission in the $0.1 - 1\,\mu$m region is characterised by a broken power-law with three free parameters: a break-wavelength, $\lambda_{\rm break}$, a blue power-law index, $\alpha_{\rm blue}$, for wavelengths shorter than the break wavelength, and a red power-law index, $\alpha_{\rm red}$, for wavelengths longer than the break wavelength.

5.3.2 *Balmer continuum*

High order Balmer lines, optically thin Balmer continuum emission, two-photon emission and Fe II emission blend together to form the 'Balmer' continuum at ~ 3000 Å. We simulate the

Balmer continuum using the empirical model given by Grandi (1982):

$$F(\lambda) = C_{BC} \times B_\lambda(T_e)(1 - e^{-\tau_\lambda}); \quad \lambda \leqslant \lambda_{BE} \tag{5.4}$$

where C_{BC} is a normalisation factor (and a free parameter in the model), $B_\lambda(T_e)$ is the Planck function, $T_e = 13150\,\mathrm{K}$ is the effective temperature, $\lambda_{BE} = 3460\,\text{Å}$ is the wavelength at the Balmer edge, and $\tau_\lambda = \tau_{BE}\,(\lambda_{BE}/\lambda)^{-3}$ is the optical depth with $\tau_{BE} = 45$ the optical depth at λ_{BE}. This function is convolved with a Gaussian with width $\sigma = 5000\,\mathrm{km\,s^{-1}}$ to simulate the effect of bulk velocity shifts comparable to those present in broad AGN emission-lines.

5.3.3 *Hot dust*

Thermal emission from hot dust, which dominates the SED at wavelengths longer than 1 μm, is modeled using a blackbody

$$F_\lambda = C_{BB} \times \frac{2hc^2}{\lambda^5} \frac{1}{e^{\frac{hc}{\lambda k_B T_{BB}}} - 1}, \tag{5.5}$$

with two free parameters: the temperature T_{BB} and normalisation C_{BB} relative to the power-law continuum.

5.3.4 *Emission-lines*

We use an emission-line template taken from Francis et al. (1991), which has been extended by Maddox and Hewett (2006) to include the Hα and Paα emission-lines[4]. All emission-lines, with the exception of Hα and Hβ, are scaled equally using a single free parameter C_{EL}, which preserves relative EQWs:

$$F_\lambda = C_{EL} \times \frac{F_{\lambda,el}}{F_{\lambda,cont}} \times F_\lambda \tag{5.6}$$

where $F_{\lambda,el}$ is the emission-line template, $F_{\lambda,cont}$ is the continuum flux in the template, and F_λ is the continuum flux in the SED model. The redshifts and luminosities of the quasars contributing to the emission-line template change as a function of

4 The spectrum is not significantly different from the Vanden Berk et al. (2001) SDSS composite.

wavelength. To account for possible variations in the strengths of the different lines, Hα and Hβ are scaled separately with parameter $C_{H\alpha}$:

$$F_\lambda = C_{EL} \times C_{H\alpha} \times \left(\frac{L(z)}{L(z_{nrm})}\right)^\beta \times \frac{F_{\lambda,el}}{F_{\lambda,cont}} \times F_\lambda. \tag{5.7}$$

The luminosity dependence of the Hα and Hβ EQW (i.e. the Baldwin effect) is parametrised with a power-law with slope $\beta = -0.04$. The dependence of the mean AGN luminosity on redshift, $L(z)$, is determined empirically from the SDSS quasar catalogue.

5.3.5 *Dust extinction*

We simulate the effect of dust extinction at the quasar redshift using a custom extinction curve that is appropriate for the quasar population[5]. To derive the quasar extinction curve, UKIDSS photometry was used to provide an $E(B-V)$ estimate, via the magnitude displacement of each quasar from the locus of un-reddened objects. At redshifts $2 < z < 3$ the reddening measure is made at rest-frame wavelengths $3500 - 7000$ Å, where Galaxy, LMC and SMC[6] extinction curves are very similar. The SDSS spectra of the same objects are then employed to generate an empirical extinction curve in the ultra-violet, down to 1200 Å. The resulting curve has no 2200 Å feature and rises rapidly with decreasing wavelength but is not as steep as the SMC curve. The extinction curve gives the colour excess $E(\lambda - V)$ relative to the colour excess $E(B-V)$ as a function of wavelength λ. The colour excess $E(B-V)$ is related to the extinction in the V passband, $A(V)$, via the ratio R_V:

$$R_V = \frac{A(V)}{E(B-V)} \tag{5.8}$$

where we assume $R_V = 3$. Hence the extinction at a wavelength lambda $A(\lambda)$ is

$$A(\lambda) = E(B-V) \times \left[\frac{E(\lambda - V)}{E(B-V)} + R_V\right] \tag{5.9}$$

5 The extinction curve has been derived by Prof. Paul Hewett.
6 LMC and SMC: Large and Small Magellanic Clouds.

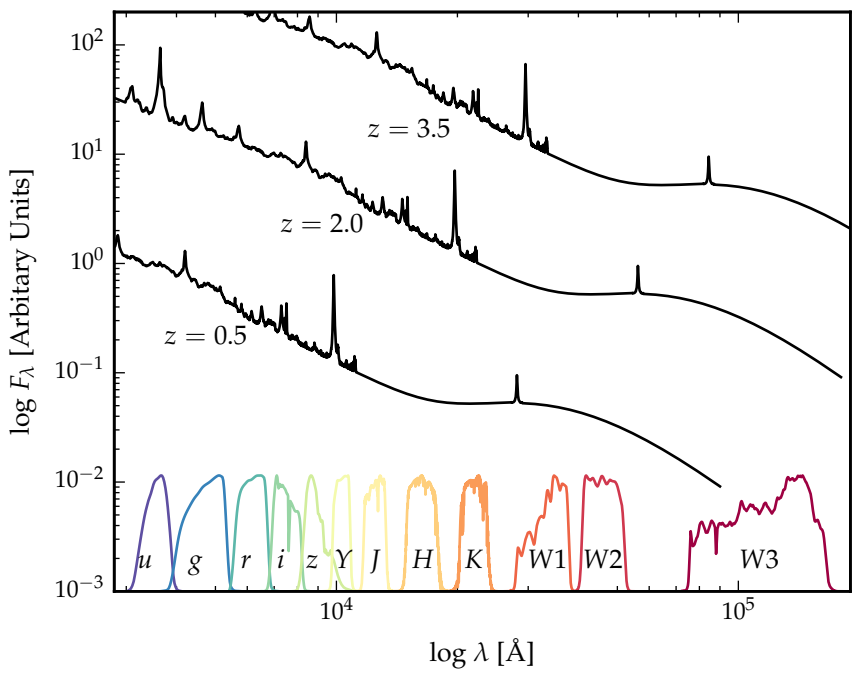

Figure 5.3: Model quasar spectra at three different redshifts and throughput functions for SDSS, UKIDSS and WISE passbands. The model spectra have been offset for clarity.

where the colour excess $E(B-V)$ is a free parameter in our model. The attenuation of the flux at a given wavelength is then:

$$F_\lambda = F_\lambda 10^{-A(\lambda)/2.5} \tag{5.10}$$

in the rest-frame of the quasar.

5.4 A PARAMETRIC SED TEMPLATE FOR THE QUASAR POPULATION

In this section we determine a single set of SED model parameters for all 19 853 quasars, encompassing a range of redshifts, luminosities, accretion rates and other properties.

5.4.1 *Fitting procedure*

The free parameters in our SED model are summarised in Table 5.2. The reddening $E(B-V)$ is fixed to zero, since a large

Parameter	Symbol	Value
Blue power-law index	α_{blue}	-0.478
Red power-law index	α_{red}	-0.199
Power-law break	λ_{break}	2402
Blackbody temperature	T_{BB}	1306 K
Blackbody normalisation	C_{BB}	2.673
Emission-line scaling	C_{EL}	1.240
Hα emission-line scaling	$C_{H\alpha}$	0.713
Balmer continuum scaling	C_{BC}	0.135

Table 5.2: Free parameters in SED model and best-fitting values from fit to the median colours of quasars at redshifts $1 < z < 3$.

fraction of SDSS quasars have very small amounts of dust reddening (Richards et al., 2003).

We divide the quasar sample into redshift bins from $z = 1$ to $z = 3$ in intervals of $\Delta z = 0.1$. In each redshift bin median passband magnitudes are calculated, and normalised such that $i = 18$. We use the $rizYJHKW1W2$ passbands to constrain the model, which covers $1550 - 23000$ Å in the rest-frame. Model SEDs are generated at redshifts corresponding to the centres of the redshift bins. The SED model is shown at three different redshifts in Figure 5.3. Model magnitudes are calculated using Equations 5.1 and 5.2 and are normalised such that $i = 18$. We find the best-fitting model parameters by minimising the χ^2 statistic for the $9 \times 21 = 189$ model and data magnitudes using the Nelder-Mead algorithm.

5.4.2 *Quality of fit*

The best-fitting parameters from the fit are given in Table 5.2. The colours ($r - i$, $i - z$, etc.) of the median SED and the best-fitting model are plotted as a function of redshift in Figure 5.4. Most of the large variations that can be seen in the median colours as a function of redshift are due to strong emission-lines being redshifted into and out of the passbands.

In Figure 5.5 we show the data minus model residuals as a function of the rest-frame wavelength. The residuals indicate that over a large redshift range the model is very effective at reproducing the median observed colours of the sample. Discrepancies are at the < 0.1 mag level. At a given rest-frame wavelength, there are no significant discrepancies between residuals in different passbands. This indicates that there is no signifi-

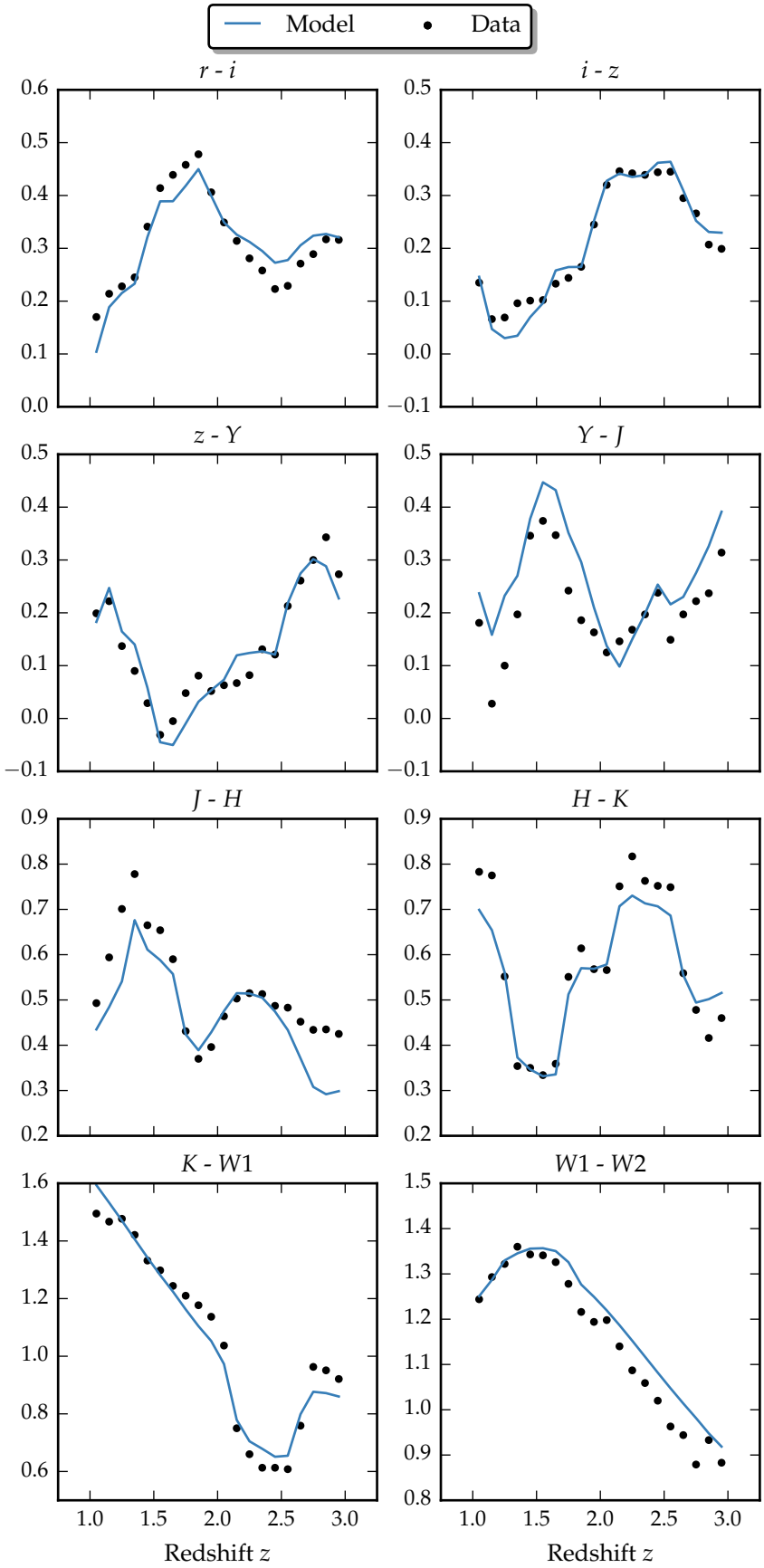

Figure 5.4: Median colours of quasars and best-fitting SED model as a function of redshift.

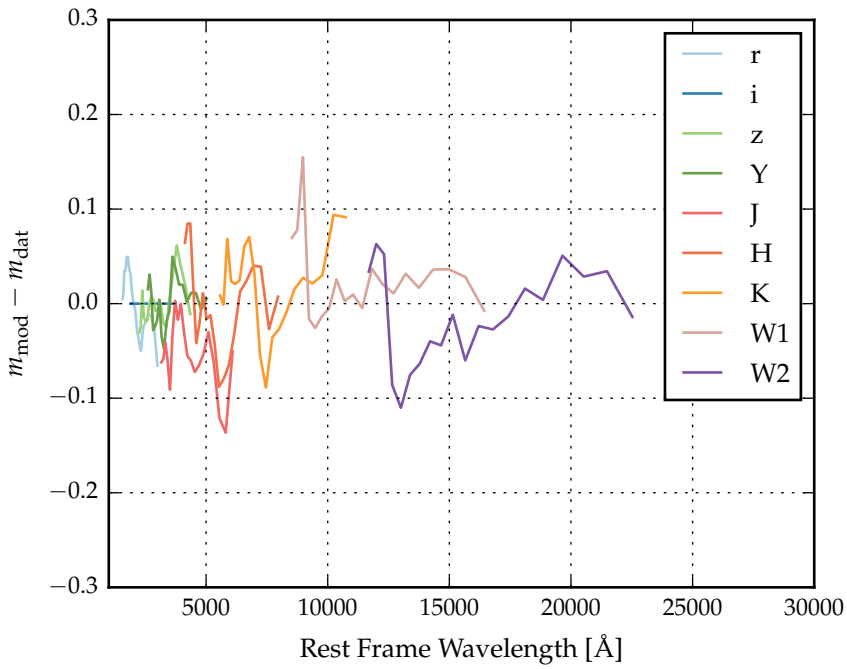

Figure 5.5: Residuals from fitting a single SED model to the colours of $1 < z < 3$ quasars as a function of rest-frame wavelength. Discrepancies are at the < 0.1 mag level, demonstrating that a simple parametric model is effective at reproducing the median colours of tens of thousands of AGN with a large dynamic range in redshift and luminosity.

cant evolution in the median SED as a function of redshift. We conclude that a single, fairly simple parametric model is effective at reproducing the median colours of tens of thousands of AGN with a large dynamic range in redshift and luminosity.

5.5 DIVERSITY OF HOT DUST PROPERTIES

In Figure 5.6 we plot the $W1 - W2$ colours of the sample as a function of redshift. At any given redshift we see a ~ 0.5 mag dispersion in the $W1 - W2$ colours. In this redshift range the $W1$ and $W2$ passbands are probing the $1.2 - 2.8\,\mu$m and $1.6 - 3.8\,\mu$m regions of the rest frame SED respectively. The peak wavelength for a blackbody radiating at 1200 K is $2.4\,\mu$m. Therefore, the large spread in $W1 - W2$ colours is highly suggestive of significant diversity in the hot dust properties in this sample.

We characterise the hot dust properties of our sample in terms of the temperature of the blackbody component and

the near-infrared to ultra-violet luminosity ratio, $R_{NIR/UV}$. The ultra-violet and near-infrared luminosities are calculated between 2000 and 9000 Å and 1 and 3 μm respectively in the SED. We show the $W1 - W2$ colours derived from our SED model with a fixed blackbody temperature (1306 K) and varying $R_{NIR/UV}$ in Figure 5.6. The $W1 - W2$ colours indicate that the hot dust luminosity in this sample varies by a factor of ~ 5.

The temperature is likely related to the distance of the dust from the central engine. Dust that is closer in will be hotter, with the sublimation temperature of the dust grains setting the minimum radius. The value of $R_{NIR/UV}$ may be related to the covering factor of the hot dust. However, this simple interpretation is somewhat complicated by the fact that at large inclinations sight-lines to the hot dust may be obscured by cooler dust in the putative torus.

In the remainder of this chapter, we will measure hot dust parameters for individual quasars via SED fitting. We will characterise the range of hot dust properties present in the sample, and test its relation to quasar properties such as luminosity, BH mass and normalised accretion rate, as well as outflow properties.

5.5.1 *Defining a sample with uniform UV/optical properties*

The shifting of passbands due to redshift limits the redshift range of the quasars for which hot dust properties can be reliably constrained. Constraining a $T \sim 1200$ K blackbody component in the SED model requires photometric data covering $\sim 1 - 3$ μm in the rest-frame of the quasar. At the limits of the redshift range $2 < z < 2.7$ $W1W2W3$ is probing the $1.1 - 4$ and $0.9 - 3.2$ μm regions of the SED. Therefore the available data is sensitive to the hot dust component across the entirety of this redshift interval. In general, care must be taken looking for trends with luminosity (and related properties including the BH mass and Eddington ratio) given the observed-frame passband information on the rest-frame SED can produce some strong systematics with redshift. However, the adopted redshift interval is narrow enough to prevent this from being a significant problem in this instance. In this redshift range, C IV emission is located within the wavelength coverage of the SDSS spectra. This will allow us to test the relationship between the hot dust and BLR outflow properties. There are 2329 quasars in the sample with redshifts $2 < z < 2.7$.

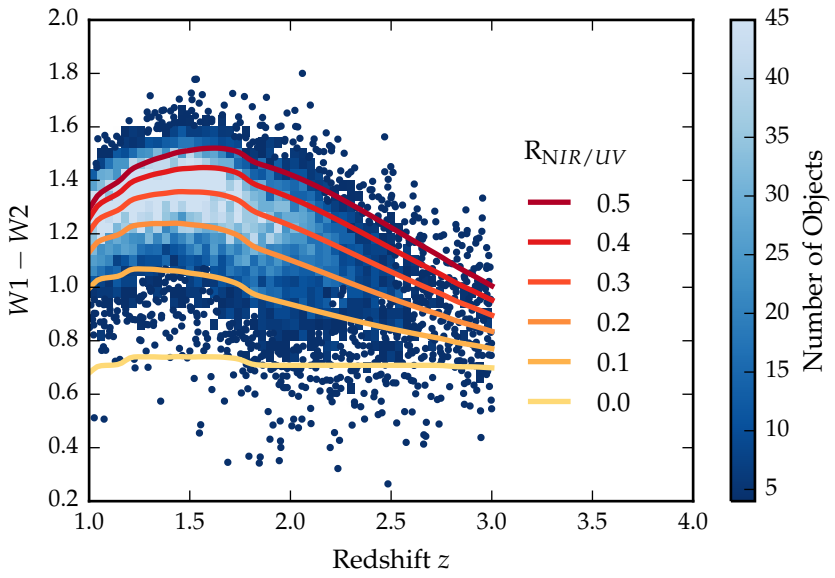

Figure 5.6: $W1 - W2$ colours of quasars as a function of redshift. Above a density threshold of four points per pixel points are represented by a two-dimensional histogram. Overlaid we plot the colours of our SED model, with a fixed blackbody temperature and a varying near-infrared ($1 - 3\,\mu$m) to ultra-violet ratio.

Holding the rest of the model parameters fixed, we will vary only the parameters of the blackbody. This requires the SED model to be a reasonable fit to the quasar SEDs in the ultraviolet/optical region. In practice, this means excluding objects with extreme emission-line EQWs and/or significant dust extinction. We use $i - K$ as a measure of the overall colour of the quasars as it provides the longest baseline in wavelength without being affected by absorption in the Lyα forest at high redshifts. $i - K$ colours are shown as a function of redshift in Figure 5.7. In the same plot we show the quasar SED model with $E(B - V) = -0.075, 0, 0.075$. A significant amount of the scatter in $i - K$ can be attributed to intrinsic variations in the ultraviolet power-law slopes of the individual quasars. Because this is degenerate with $E(B - V)$, we allow negative $E(B - V)$ values in the SED model.

The SDSS and UKIDSS photometry are separated by $3 - 4$ years in the source rest-frame. Therefore, some of the scatter in the $i - K$ colours could be due to temporal variations in the brightness of the targets. However, the red-asymmetry of the

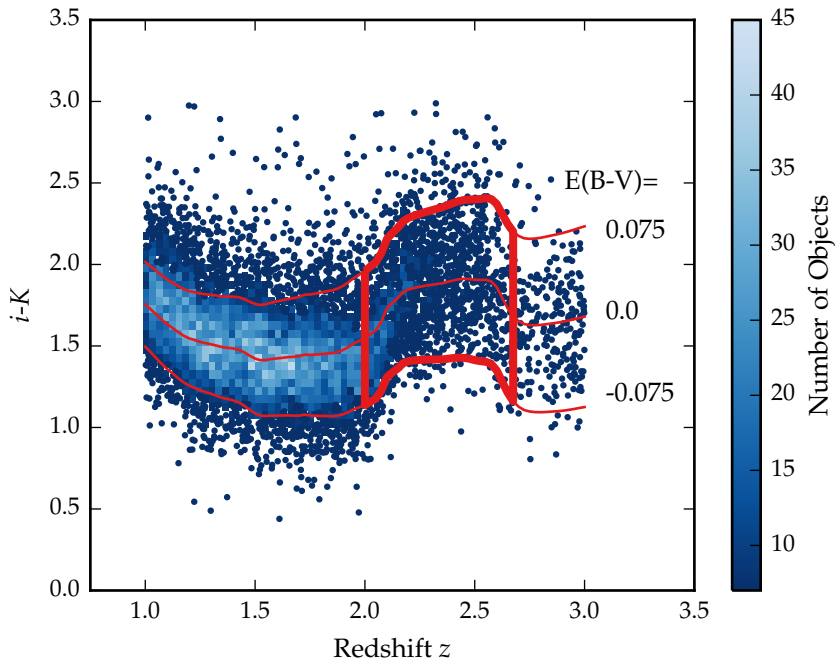

Figure 5.7: $i-K$ colours of quasars as a function of redshift. The lines show the colours of the SED model with varying amounts of dust extinction. Quasars with extinction $|E(B-V)| > 0.075$ are excluded from our $2 < z < 2.7$ sample.

$i-K$ colours about the un-reddened SED model suggests that this effect is sub-dominant to dust extinction.

We discarded from our sample quasars with $i-K$ colours redder than our standard model with dust reddening $E(B-V)= 0.075$ and bluer than $E(B-V)= -0.075$ (Figure 5.7). Following this cut we are left with 2030 quasars in the sample.

5.5.2 *Fitting procedure*

We fit the model to the individual quasar SEDs with the temperature and normalisation of the blackbody component as free parameters. The model spectrum is redshifted to the redshift of the quasar being fit and passband magnitudes are calculated using Equations 5.1 and 5.2. We minimise the inverse variance weighted χ^2 statistic using the Levenberg-Marquardt algorithm. We impose a minimum error of 0.1 mag on the quasar magnitudes, corresponding to the size of the residuals from the model fit to the median colours of the population (Figure 5.5). Data from $ugrizYJHKW1W2W3$ is used to constrain the model.

However, to avoid Lyα forest absorption, passbands are excluded if $\lambda_{\rm Eff}/(1+z) < 1400\,$Å.

5.5.3 *Distribution of hot dust parameters*

The best-fitting hot dust temperature (T_{BB}) and abundance ($R_{NIR/UV}$) for the individual quasars are shown in Figure 5.8. Even after restricting the sample to have a relative narrow range of ultra-violet/optical SED shapes, we see significant diversity in the hot dust abundance, with the near-infrared to ultra-violet luminosity ratio having a broad range from 0.1 to 0.6. The temperature takes on a relatively narrow range of values: $1177 \pm 136\,$K. This is consistent with the dust radius being set by the sublimation temperature of the dust grains.

We note a degeneracy between the temperature and $R_{NIR/UV}$. This is a result of the dependence of the blackbody peak on temperature and the fixed wavelength interval used to calculate the blackbody luminosity. However, this does not affect any of the results presented below.

5.5.4 *Relationship between hot dust and BLR outflows*

In this section, we measure the dependence of the hot dust parameters on the blueshift and EQW of the C IV emission. C IV measurements are described in Section 3.5 and the C IV blueshift is defined with respect to a systemic redshift measured by Allen & Hewett (2017, in preparation). This information is available for 98 per cent of the objects in our sample.

In Figure 5.9 we show that the near-infrared to ultra-violet luminosity ratio is correlated with the C IV blueshift and EQW. There is a clear enhancement in the hot dust emission for quasars in the large C IV blueshift, low EQW region of the parameter space: for quasars with C IV blueshifts $> 2000\,\mathrm{km\,s^{-1}}$, $R_{NIR/UV} = 0.43 \pm 0.13$, while for quasars with C IV blueshifts $< 1000\,\mathrm{km\,s^{-1}}$, $R_{NIR/UV} = 0.31 \pm 0.14$ (median $\pm$ intra-sample dispersion). A similar result was recently reported by Wang et al. (2013). The distribution of blackbody temperatures is relatively narrow ($\sigma \sim 200\,$K) and so, as expected, we do not observe any correlations between the hot dust temperature and the C IV emission parameters.

The profiles of the emission-lines with large C IV blueshifts suggest that the BLR dynamics in these objects are dominated by high-velocity outflows. As we discussed in the introduction

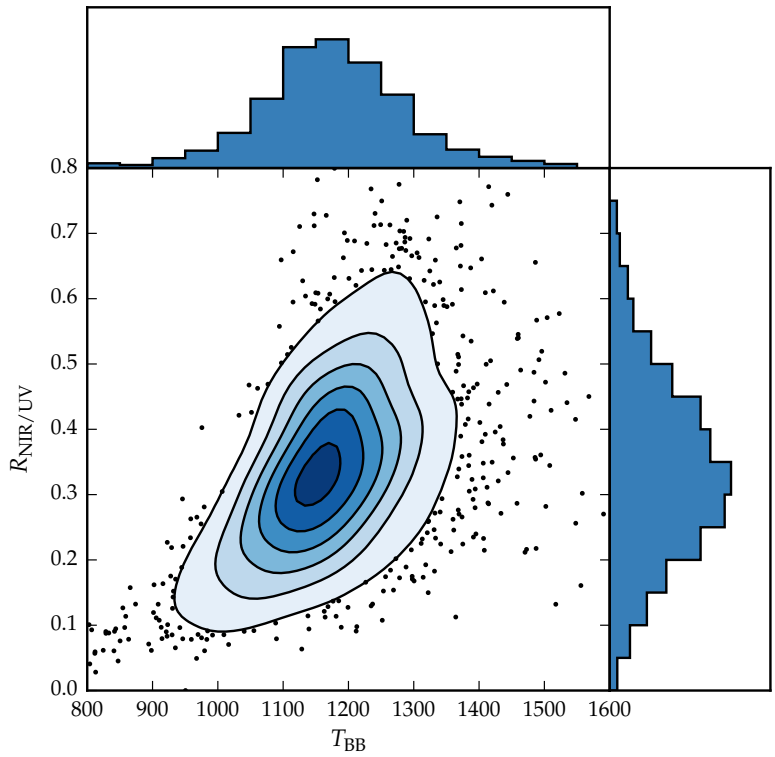

Figure 5.8: Histograms of the ratio of near-infrared to ultra-violet luminosity ($R_{NIR/UV}$) and blackbody temperature (T_{BB}) and the correlation between these two parameters.

to this chapter, outflows from the outer regions of the accretion disc could contain significant amounts of dust. As the dusty wind is lifted above the accretion disc, it is directly exposed to ultra-violet radiation from the inner accretion disc. Radiation pressure could then efficiently accelerate the wind owing to the high cross-section of the dust grains[7] (e.g. Fabian, 2012). This would flatten the geometry of the wind, which would expose more of the inner edge of the base of the wind to relatively face-on lines of sight. This is where the hot dust is located, and so the hot dust emission would be enhanced. The more the wind is accelerated, the flatter it's geometry will become, and the more hot dust will be exposed. This model therefore predicts the correlation we observe between the strength of BLR outflows (which is reflected in the C IV blueshift) and the hot dust abundance. The hot dust abundance in $z \lesssim 1$ SDSS AGN is also found to be higher when optical Fe II is strong (Shen and

7 Radiation line-driving and free electrons are also likely to play important roles in accelerating the wind.

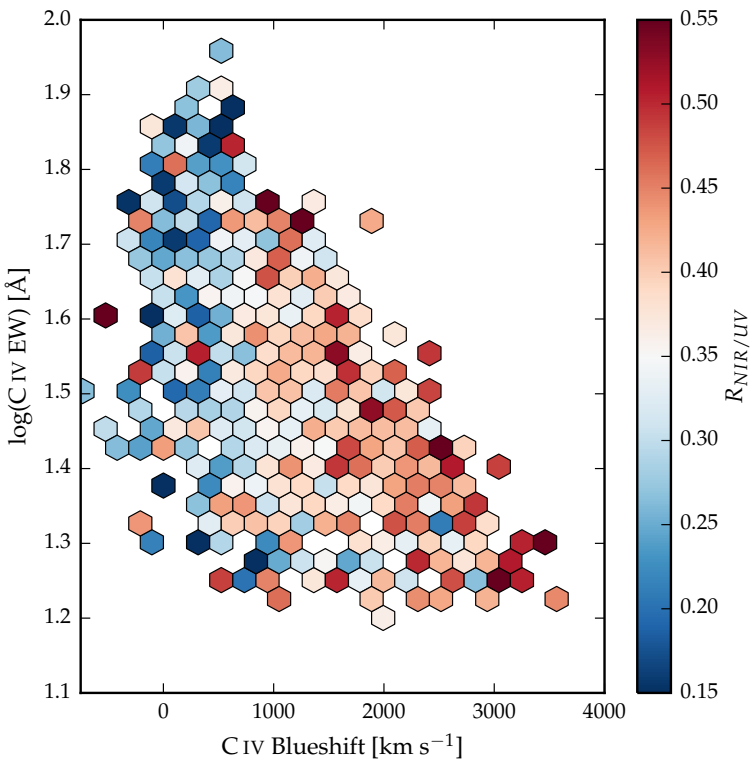

Figure 5.9: Rest-frame EQW and blueshift of the C IV line. The colours of the hexagons denote the median hot dust ($T \simeq 1200$ K) abundance for all quasars at a given EQW and blueshift. Quasars with the most extreme outflow signatures (in the bottom right) have enhanced hot dust emission.

Ho, 2014). Given the known correlations between the C IV emission properties and the Fe II strength (e.g. Figures 4.9 and 4.10), this is very likely to be a related result. Recent results from Roseboom et al. (2013) reporting an anti-correlation between the torus covering factor and the hot dust abundance are also naturally explained in this model. If the circum-nuclear obscuration is due to the dusty accretion disc wind, then flattening the geometry of the wind will decrease the torus covering factor and increase the surface area of hot dust that can be seen.

5.5.5 *Correlations with fundamental quasar properties*

In this section, we look for correlations between the hot dust abundance, $R_{NIR/UV}$, and the ultra-violet luminosity, BH mass and Eddington ratio.

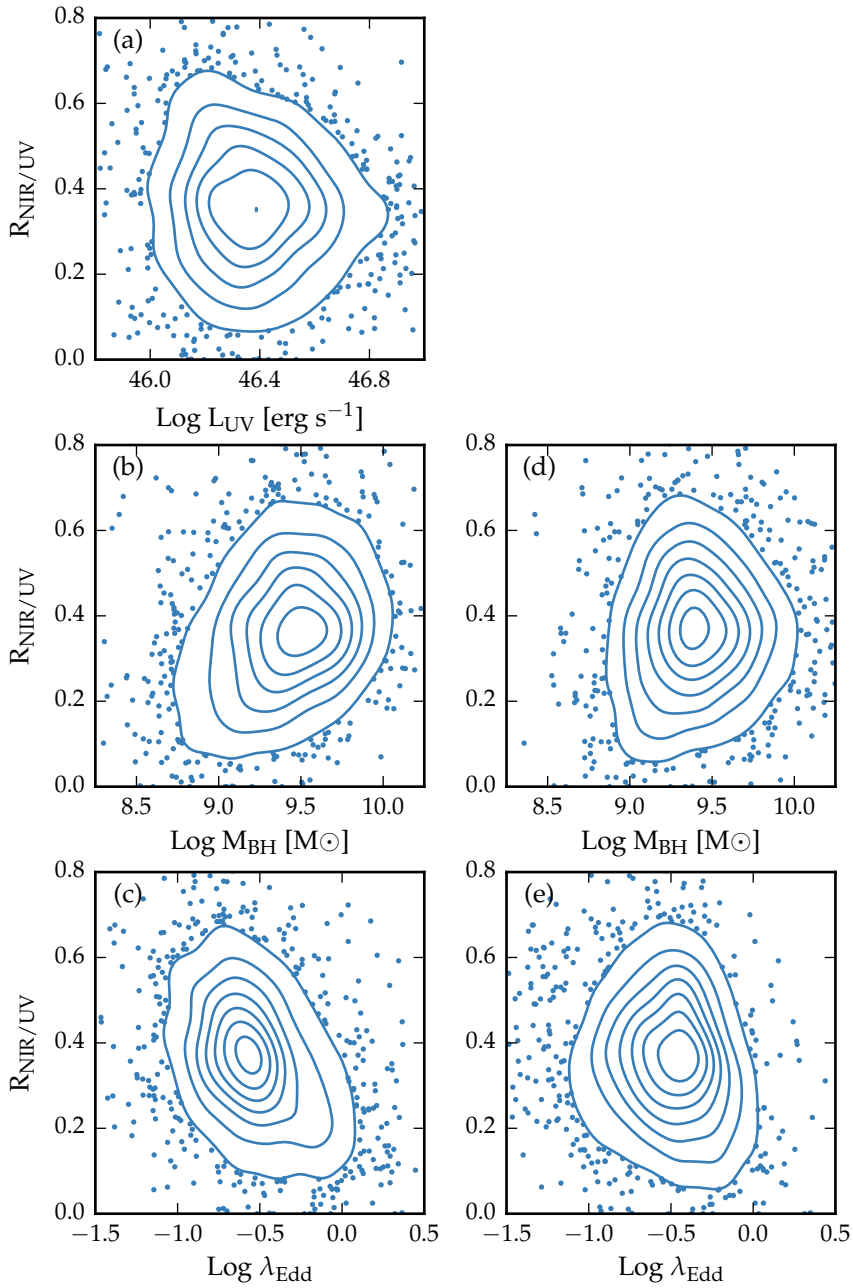

Figure 5.10: Best-fitting near-infrared to ultra-violet luminosity ($R_{NIR/UV}$) as a function of ultra-violet luminosity, BH mass and Eddington ratio. In (b) and (c) BH mass estimates are taken from Shen et al. (2011). In (d) and (e) BH mass estimates have been corrected using the procedure described in Chapter 3. Using the corrected masses the correlations between $R_{NIR/UV}$ and the BH mass and Eddington ratio are significantly reduced.

In Figure 5.10a we show $R_{NIR/UV}$ as a function of the ultra-violet luminosity. The ultra-violet luminosity, which is measured at 1350 Å, is reported in the catalogue of SDSS spectral properties from Shen et al. (2011). We do not observe any correlation between $R_{NIR/UV}$ and the ultra-violet luminosity (Figure 5.10a). However, the dynamic range in luminosity is small (~ 1 dex) because of the restricted redshift range.

In Figure 5.10b we show $R_{NIR/UV}$ as a function of the BH mass. Masses are C IV FWHM-based single-epoch virial estimates, as computed by Shen et al. (2011). $R_{NIR/UV}$ is positively correlated with the BH mass ($\rho_S = 0.26$; p-value $= 6 \times 10^{-26}$). However, in the previous section, we found $R_{NIR/UV}$ to be correlated with the C IV blueshift and, in Chapter 3, we demonstrated that BH masses are severely overestimated in quasars with large C IV blueshifts. We therefore predict that the apparent correlation between $R_{NIR/UV}$ and the BH mass is due to systematic biases in the C IV-based masses that are correlated with the C IV blueshift. We can test this by comparing $R_{NIR/UV}$ with BH mass estimates which have been corrected using the prescription described in Chapter 3 (Figure 5.10d). As predicted, the correlation vanishes ($\rho_S = 0.07$; p-value $= 2 \times 10^{-3}$) A similar result is found when $R_{NIR/UV}$ is compared to the Eddington ratio, which is inversely proportional to the BH mass. Using uncorrected masses from Shen et al. (2011) an anti-correlation is observed between $R_{NIR/UV}$ and the Eddington ratio ($\rho_S = -0.36$; p-value $= 4 \times 10^{-51}$; Figure 5.10c) but this disappears when unbiased masses are employed ($\rho_S = -0.12$; p-value $= 1 \times 10^{-10}$; Figure 5.10e). This demonstrates how using conventional BH mass estimates based on C IV can lead to spurious correlations with other quasar properties that are correlated with the C IV blueshift, but that this can be avoided using the un-biased mass estimates presented in Chapter 3.

5.6 SUMMARY

The main results for this chapter are as follows:

- Using data from a number of recent wide-field photometric surveys, we build a parametric SED model that is able to reproduce the median optical to infrared colours of tens of thousands of SDSS AGN at redshifts $1 < z < 3$.
- In individual objects, we find significant variation in the near-infrared SED dominated by emission from hot dust.

We find the hot dust abundance to be strongly correlated with the strength of outflows in the quasar BLR, suggesting that the hot dust may be in a wind emerging from the outer edges of the accretion disc.

6 SUMMARY AND FUTURE PROSPECTS

Supermassive BHs and their host-galaxies are thought to evolve in tandem, with the energy output from the rapidly-accreting BH regulating star formation and the growth of the BH itself. The goal of better understanding this process has led to much work focussing on the properties of quasars and AGN at relatively high redshifts, $z \gtrsim 2$, when cosmic star formation and BH accretion both peaked. At these redshifts, however, ground-based statistical studies of the quasar population generally have no access to the rest-frame optical spectral region, which is needed to measure Hβ-based BH masses and NLR outflow properties. The cornerstone of this thesis has been a new near-infrared spectroscopic catalogue providing rest-frame optical data on 434 luminous quasars at redshifts $1.5 \lesssim z \lesssim 4$. This chapter provides a summary of the key results, together with a discussion of future directions for this research.

6.1 CORRECTING C IV-BASED VIRIAL BLACK HOLE MASSES

At high redshift, $z \gtrsim 2$, quasar BH masses are derived using the velocity-width of the C IV broad emission-line, based on the assumption that the observed velocity-widths arise from virial-induced motions. However, C IV exhibits significant asymmetric structure which suggests that the associated gas is not tracing virial motions. We find the C IV emission-based BH masses to be systematically in error by a factor of more than five at $3000\,\mathrm{km\,s^{-1}}$ in C IV emission blueshift and the overestimate reaches a factor of 10 for quasars exhibiting the most extreme blueshifts, $\gtrsim 5000\,\mathrm{km\,s^{-1}}$. Using the monotonically increasing relationship between the C IV blueshift and the mass ratio BH(C IV)/BH(Hα) we derive an empirical correction to all C IV BH-masses. The correction depends only on the C IV line properties – i.e. the FWHM and blueshift – and allows unbiased single-epoch virial BH mass estimates to be made from optical spectra, such as those provided by the SDSS, out to redshifts exceeding $z \sim 5$.

6.2 QUASAR-DRIVEN GALAXY-WIDE OUTFLOWS IN IONISED GAS

Quasars driving powerful outflows over galactic scales is a central tenet of galaxy evolution models involving 'quasar feedback' and significant resources have been devoted to searching for observational evidence of this phenomenon. We have used [O III] emission to probe ionised gas extended over kilo-parsec scales in luminous $z \gtrsim 2$ quasars. Broad [O III] velocity-widths and large blueshifts indicate that strong outflows are prevalent in this population. We estimate the kinetic power of the outflows to be up to a few percent of the quasar bolometric luminosity, which is similar to the efficiencies required in recent quasar-feedback models. [O III] emission is very weak in quasars with large C IV blueshifts, suggesting that quasar-driven winds are capable of sweeping away gas extended over kilo-parsec scales in the host galaxies.

6.3 OUTFLOWS AND HOT DUST EMISSION

Using data from a number of recent wide-field photometric surveys, we have built a parametric SED model that is able to reproduce the median optical to infrared colours of tens of thousands of SDSS AGN at redshifts $1 < z < 3$. In individual objects, we find significant variation in the near-infrared SED dominated by emission from hot dust. We find the hot dust abundance to be strongly correlated with the strength of outflows in the quasar BLR, suggesting that the hot dust may be in a wind emerging from the outer edges of the accretion disc.

6.4 FUTURE PROSPECTS

6.4.1 *Further improvements to BH mass estimates*

With it's twelfth data release in 2016, the number of AGN and quasars in the SDSS spectroscopic catalogue alone reached almost 400 000. SDSS-IV eBOSS will take this number to 800 000 (Myers et al., 2015) and it will grow to several million in the near future with planned-surveys including 4MOST and DESI (de Jong et al., 2012; Levi et al., 2013). These enormous surveys will open up new possibilities in large-scale studies of AGN and quasar demographics using C IV-based single-epoch virial BH mass estimates.

Allen & Hewett (2017, in preparation) will soon publish improved redshifts for all quasars in the SDSS DR7 and DR12 catalogues. At the same time, we will publish catalogues of unbiased BH masses for both SDSS DR7 and DR12 based on the Allen & Hewett redshifts. The MFICA components used in the Allen & Hewett redshift algorithm will also be published. With these components, if a rest-frame ultra-violet spectrum is available, it will be straightforward to determine the systemic redshift, via a simple optimisation procedure, and hence calculate the C IV blueshift and BH mass.

While the large C IV blueshift-dependent systematic error in the C IV-based BH masses is removed using the method developed in Chapter 3, the remaining scatter between the C IV- and Balmer-based BH masses is significant, particularly for objects with small C IV blueshifts. It may be possible to reduce this scatter further by adding more features from the rest-frame ultra-violet spectrum to the model.

An efficient way to do this would be to adopt a data-driven approach. The MFICA components used in the Allen & Hewett redshift algorithm provide a compact representation of the rest-frame ultra-violet spectral properties of SDSS quasars. Taking the set of 230 objects with near-infrared spectra (and hence reliable Balmer-based BH masses), a model could be built that learns how these MFICA component weights depend on the BH mass. After the training step, the model could be used to predict a BH mass based only on the MFICA component weights for the ultra-violet spectrum. There are numerous algorithms available to tackle this class of supervised learning problem (e.g. random forests).

Taking this one step further, a data-driven model could be built to predict the unseen rest-frame optical spectrum from the rest-frame ultra-violet region probed by SDSS spectra at redshifts $z \gtrsim 2$. This approach is inspired by the data-driven model for deriving stellar labels from spectroscopic data developed by Ness et al. (2015). The MFICA component weights can be thought of as a set of 'labels' describing the rest-frame optical spectrum. A flexible generative model could be built that predicts the flux at each wavelength in the SDSS ultra-violet spectrum as a function of these weights. The coefficients in this model, which could be linear or a low-order polynomial, could be trained on the sub-sample of quasars with spectra covering the full rest-frame optical to ultra-violet region. Once the coefficients in the model have been determined, the model

can statistically infer the rest-frame optical MFICA component weights based only on the rest-frame ultra-violet spectrum. The rest-frame optical spectrum can then straightforwardly be reconstructed from the MFICA components and parameters of interest, including the BH mass, can be calculated, without the need for follow-up near-infrared spectroscopy.

It is important to recall that the sample of AGN with reverberation mapping measurements is strongly biased to low luminosity Seyfert 1 galaxies, and the maximum redshift is just $z \sim 0.3$. The reliability of single-epoch virial BH mass estimates for quasars at high-redshifts, even using low-ionisation lines like Hβ, is dependent on the (as of yet untested) extrapolation of relations calibrated for sub-Eddington BHs with $M_{BH} \sim 10^7\,M_\odot$ to BHs with masses up to $10^{10}\,M_\odot$ that are radiating near the Eddington luminosity. In the future, this situation will be improved with the results of large on-going statistical reverberation mapping projects for luminous quasars at high-redshifts (e.g. Shen et al., 2015; King et al., 2015).

6.4.2 *Studying feedback with IFU spectroscopy*

In Chapter 4, we made some order of magnitude calculations of the energetics of the outflows traced by the [O III] emission based on a number of assumptions about the properties of this gas. However, to study the morphology and energetics of the outflows in detail, we must turn to spatially-resolved integral field unit (IFU) spectroscopy.

Extended outflows have been detected at high redshifts ($z \gtrsim 2$) in a handful of objects using SINFONI on the VLT (e.g. Carniani et al., 2015). With the analysis presented in Chapter 4 we now have a much improved understanding of the distribution of [O III] emission properties in luminous quasars at high redshifts. Quasars with a range of [O III] emission properties could be selected from this sample as targets for IFU spectroscopy. The MFICA component weights, which are effective even at low S/N, could be used to isolate the systemic and outflowing components in the [O III] emission in the spatially resolved spectra. Measuring the extent of the outflowing gas traced by [O III] could reveal the nature of the correlation between the [O III] and C IV blueshifts.

Large optical spectroscopic surveys (e.g. SDSS) have provided constraints on the prevalence and drivers of ionised outflows in tens of thousands of quasars. A new generation of sur-

veys using multi-object IFU spectrographs (including KMOS, MaNGA and SAMI; Croom et al., 2012; Sharples et al., 2013; Bundy et al., 2015) are now providing spatially-resolved information on the physical properties of galaxies (such as gas kinematics and star formation histories) for statistically powerful samples at a range of redshifts. However, ionised gas accounts for only a small fraction of the total gas in galaxies. Submillimetre interferometers (including ALMA) provide complementary information by probing the cold, molecular gas from which stars are formed. Massive molecular outflows in quasar host galaxies are now being detected up to very high redshifts (e.g. Maiolino et al., 2012) and this will lead to great advances in our understanding of the AGN/host galaxy connection.

BIBLIOGRAPHY

Ahn, C. P. et al. (2012). "The Ninth Data Release of the Sloan Digital Sky Survey: First Spectroscopic Data from the SDSS-III Baryon Oscillation Spectroscopic Survey." In: *ApJS* 203, 21, p. 21. arXiv: 1207.7137.

Alatalo, K. et al. (2011). "Discovery of an Active Galactic Nucleus Driven Molecular Outflow in the Local Early-type Galaxy NGC 1266." In: *ApJ* 735, 88, p. 88. arXiv: 1104.2326.

Alexander, D. M. and R. C. Hickox (2012). "What drives the growth of black holes?" In: *New Astron. Rev.* 56, pp. 93–121. arXiv: 1112.1949.

Alexander, D. M., A. M. Swinbank, I. Smail, R. McDermid, and N. P. H. Nesvadba (2010). "Searching for evidence of energetic feedback in distant galaxies: a galaxy wide outflow in a $z \sim 2$ ultraluminous infrared galaxy." In: *MNRAS* 402, pp. 2211–2220. arXiv: 0911.0014.

Allen, J. T., P. C. Hewett, N. Maddox, G. T. Richards, and V. Belokurov (2011). "A strong redshift dependence of the broad absorption line quasar fraction." In: *MNRAS* 410, pp. 860–884. arXiv: 1007.3991.

Allen, J. T., P. C. Hewett, C. T. Richardson, G. J. Ferland, and J. A. Baldwin (2013). "Classification and analysis of emission-line galaxies using mean field independent component analysis." In: *MNRAS* 430, pp. 3510–3536. arXiv: 1301.5930.

Aller, M. C. and D. O. Richstone (2007). "Host Galaxy Bulge Predictors of Supermassive Black Hole Mass." In: *ApJ* 665, pp. 120–156. arXiv: 0705.1165.

Antonucci, R. (1993). "Unified models for active galactic nuclei and quasars." In: *ARA&A* 31, pp. 473–521.

Arav, N., M. Moe, E. Costantini, K. T. Korista, C. Benn, and S. Ellison (2008). "Measuring Column Densities in Quasar Outflows: VLT Observations of QSO 2359-1241." In: *ApJ* 681, 954-964, pp. 954–964. arXiv: 0807.0228.

Assef, R. J. et al. (2011). "Black Hole Mass Estimates Based on C IV are Consistent with Those Based on the Balmer Lines." In: *ApJ* 742, p. 93. arXiv: 1009.1145.

Baldwin, J. A. (1977). "Luminosity Indicators in the Spectra of Quasi-Stellar Objects." In: *ApJ* 214, pp. 679–684.

Barth, A. J. et al. (2011). "The Lick AGN Monitoring Project 2011: Reverberation Mapping of Markarian 50." In: *ApJ* 743, L4, p. L4. arXiv: 1111.0061.

Barvainis, R. (1987). "Hot dust and the near-infrared bump in the continuum spectra of quasars and active galactic nuclei." In: *ApJ* 320, pp. 537–544.

Baskin, A. and A. Laor (2005a). "What controls the CIV line profile in active galactic nuclei?" In: *MNRAS* 356, pp. 1029–1044. arXiv: astro-ph/0409196.

— (2005b). "What controls the [OIII]λ5007 line strength in active galactic nuclei?" In: *MNRAS* 358, pp. 1043–1054. arXiv: astro-ph/0501436.

Begelman, M. C. (1985). "Accretion disks in active galactic nuclei." In: *Astrophysics of Active Galaxies and Quasi-Stellar Objects*. Ed. by J. S. Miller, pp. 411–452.

Bennert, N., H. Falcke, H. Schulz, A. S. Wilson, and B. J. Wills (2002). "Size and Structure of the Narrow-Line Region of Quasars." In: *ApJ* 574, pp. L105–L109. arXiv: astro-ph/0206334.

Bennert, V. N., M. W. Auger, T. Treu, J.-H. Woo, and M. A. Malkan (2011). "The Relation between Black Hole Mass and Host Spheroid Stellar Mass Out to z ˜ 2." In: *ApJ* 742, 107, p. 107. arXiv: 1102.1975.

Bentz, M. C. et al. (2009). "The Lick AGN Monitoring Project: Broad-line Region Radii and Black Hole Masses from Reverberation Mapping of Hβ." In: *ApJ* 705, pp. 199–217. arXiv: 0908.0003.

Bischetti, M. et al. (2016). "The WISSH Quasars Project I. Powerful ionised outflows in hyper-luminous quasars." In: *ArXiv e-prints*. arXiv: 1612.03728.

Blandford, R. D. and C. F. McKee (1982). "Reverberation mapping of the emission line regions of Seyfert galaxies and quasars." In: *ApJ* 255, pp. 419–439.

Blandford, R. D. and D. G. Payne (1982). "Hydromagnetic flows from accretion discs and the production of radio jets." In: *MNRAS* 199, pp. 883–903.

Bonnet, H. et al. (2004). "First light of SINFONI at the VLT." In: *The Messenger* 117, pp. 17–24.

Boroson, T. A. and R. F. Green (1992). "The emission-line properties of low-redshift quasi-stellar objects." In: *ApJS* 80, pp. 109–135.

Boroson, T. (2005). "Blueshifted [O III] Emission: Indications of a Dynamic Narrow-Line Region." In: *AJ* 130, pp. 381–386. arXiv: astro-ph/0505127.

Bower, R. G., A. J. Benson, R. Malbon, J. C. Helly, C. S. Frenk, C. M. Baugh, S. Cole, and C. G. Lacey (2006). "Breaking the hierarchy of galaxy formation." In: *MNRAS* 370, pp. 645–655. arXiv: astro-ph/0511338.

Bowler, R. A. A., P. C. Hewett, J. T. Allen, and G. J. Ferland (2014). "Line-driven radiative outflows in luminous quasars." In: *MNRAS* 445, pp. 359–377. arXiv: 1408.5808.

Boyle, B. J. and R. J. Terlevich (1998). "The cosmological evolution of the QSO luminosity density and of the star formation rate." In: *MNRAS* 293, pp. L49–L51. arXiv: astro-ph/9710134.

Brandt, W. N. and G. Hasinger (2005). "Deep Extragalactic X-Ray Surveys." In: *ARA&A* 43, pp. 827–859. arXiv: astro-ph/0501058.

Brotherton, M. S. (1996). "The Profiles of H beta and [O iii] lambda 5007 in Radio-loud Quasars." In: *ApJS* 102, p. 1. arXiv: astro-ph/9507067.

Brotherton, M. S., J. C. Runnoe, Z. Shang, and M. A. DiPompeo (2015). "Bias in C IV-based quasar black hole mass scaling relationships from reverberation mapped samples." In: *MNRAS* 451, pp. 1290–1298. arXiv: 1504.03427.

Brusa, M. et al. (2015). "X-shooter reveals powerful outflows in z~1.5 X-ray selected obscured quasi-stellar objects." In: *MNRAS* 446, pp. 2394–2417. arXiv: 1409.1615.

Brusa, M. et al. (2016). "A fast ionised wind in a star-forming quasar system at z ˜ 1.5 resolved through adaptive optics assisted near-infrared data." In: *A&A* 588, A58, A58. arXiv: 1602.03181.

Bundy, K. et al. (2015). "Overview of the SDSS-IV MaNGA Survey: Mapping nearby Galaxies at Apache Point Observatory." In: *ApJ* 798, 7, p. 7. arXiv: 1412.1482.

Cano-Díaz, M., R. Maiolino, A. Marconi, H. Netzer, O. Shemmer, and G. Cresci (2012). "Observational evidence of quasar feedback quenching star formation at high redshift." In: *A&A* 537, L8, p. L8. arXiv: 1112.3071.

Cappellari, M., E. K. Verolme, R. P. van der Marel, G. A. Verdoes Kleijn, G. D. Illingworth, M. Franx, C. M. Carollo, and P. T. de Zeeuw (2002). "The Counterrotating Core and the Black Hole Mass of IC 1459." In: *ApJ* 578, pp. 787–805. arXiv: astro-ph/0202155.

Carniani, S. et al. (2015). "Ionised outflows in z ˜ 2.4 quasar host galaxies." In: *A&A* 580, A102, A102. arXiv: 1506.03096.

Cicone, C. et al. (2014). "Massive molecular outflows and evidence for AGN feedback from CO observations." In: *A&A* 562, A21, A21. arXiv: 1311.2595.

Cimatti, A., M. Brusa, M. Talia, M. Mignoli, G. Rodighiero, J. Kurk, P. Cassata, C. Halliday, A. Renzini, and E. Daddi (2013). "Active Galactic Nucleus Feedback at z ˜ 2 and the Mutual Evolution of Active and Inactive Galaxies." In: *ApJ* 779, L13, p. L13. arXiv: 1311.4401.

Coatman, L., P. C. Hewett, M. Banerji, and G. T. Richards (2016). "CIV emission-line properties and systematic trends in quasar black hole mass estimates." In: *MNRAS* 461, pp. 647–665. arXiv: 1606.02726.

Coatman, L., P. C. Hewett, M. Banerji, G. T. Richards, J. F. Hennawi, and J. X. Prochaska (2017). "Correcting C IV-based virial black hole masses." In: *MNRAS* 465, pp. 2120–2142. arXiv: 1610.08977.

Collin, S., T. Kawaguchi, B. M. Peterson, and M. Vestergaard (2006). "Systematic effects in measurement of black hole masses by emission-line reverberation of active galactic nuclei: Eddington ratio and inclination." In: *A&A* 456, pp. 75–90. arXiv: astro-ph/0603460.

Crenshaw, D. M., S. B. Kraemer, A. Boggess, S. P. Maran, R. F. Mushotzky, and C.-C. Wu (1999). "Intrinsic Absorption Lines in Seyfert 1 Galaxies. I. Ultraviolet Spectra from the Hubble Space Telescope." In: *ApJ* 516, pp. 750–768. arXiv: astro-ph/9812265.

Croom, S. M., R. J. Smith, B. J. Boyle, T. Shanks, L. Miller, P. J. Outram, and N. S. Loaring (2004). "The 2dF QSO Redshift Survey - XII. The spectroscopic catalogue and luminosity function." In: *MNRAS* 349, pp. 1397–1418. arXiv: astro-ph/0403040.

Croom, S. M. et al. (2012). "The Sydney-AAO Multi-object Integral field spectrograph." In: *MNRAS* 421, pp. 872–893. arXiv: 1112.3367.

Dall'Aglio, A., L. Wisotzki, and G. Worseck (2008). "An unbiased measurement of the UV background and its evolution via the proximity effect in quasar spectra." In: *A&A* 491, pp. 465–481. arXiv: 0807.5089.

Dawson, K. S. et al. (2013). "The Baryon Oscillation Spectroscopic Survey of SDSS-III." In: *AJ* 145, p. 10. arXiv: 1208.0022.

Dekker, H., S. D'Odorico, A. Kaufer, B. Delabre, and H. Kotzlowski (2000). "Design, construction, and performance of UVES, the echelle spectrograph for the UT2 Kueyen Telescope at the ESO Paranal Observatory." In: *Optical and IR Telescope Instrumentation and Detectors*. Ed. by M. Iye and A. F. Moorwood. Vol. 4008. Proc. SPIE, pp. 534–545.

Denney, K. D. (2012). "Are Outflows Biasing Single-epoch C IV Black Hole Mass Estimates?" In: *ApJ* 759, p. 44. arXiv: 1208.3465.

Denney, K. D. et al. (2010). "Reverberation Mapping Measurements of Black Hole Masses in Six Local Seyfert Galaxies." In: *ApJ* 721, pp. 715–737. arXiv: 1006.4160.

Denney, K. D., R. W. Pogge, R. J. Assef, C. S. Kochanek, B. M. Peterson, and M. Vestergaard (2013). "C IV Line-width Anomalies: The Perils of Low Signal-to-noise Spectra." In: *ApJ* 775, p. 60. arXiv: 1303.3889.

Deo, R. P., G. T. Richards, R. Nikutta, M. Elitzur, S. C. Gallagher, Ž. Ivezić, and D. Hines (2011). "Dusty Tori of Luminous Type 1 Quasars at z ˜ 2." In: *ApJ* 729, 108, p. 108. arXiv: 1101.2855.

Di Matteo, T., V. Springel, and L. Hernquist (2005). "Energy input from quasars regulates the growth and activity of black holes and their host galaxies." In: *Nature* 433, pp. 604–607. arXiv: astro-ph/0502199.

Doi, M. et al. (2010). "Photometric Response Functions of the Sloan Digital Sky Survey Imager." In: *AJ* 139, pp. 1628–1648. arXiv: 1002.3701.

Dunn, J. P., M. Bautista, N. Arav, M. Moe, K. Korista, E. Costantini, C. Benn, S. Ellison, and D. Edmonds (2010). "The Quasar Outflow Contribution to AGN Feedback: VLT Measurements of SDSS J0318-0600." In: *ApJ* 709, pp. 611–631. arXiv: 0911.3896.

Edelson, R. A. and M. A. Malkan (1986). "Spectral energy distributions of active galactic nuclei between 0.1 and 100 microns." In: *ApJ* 308, pp. 59–77.

Edge, A., W. Sutherland, K. Kuijken, S. Driver, R. McMahon, S. Eales, and J. P. Emerson (2013). "The VISTA Kilo-degree Infrared Galaxy (VIKING) Survey: Bridging the Gap between Low and High Redshift." In: *The Messenger* 154, pp. 32–34.

Eisenhauer, F. et al. (2003). "SINFONI - Integral field spectroscopy at 50 milli-arcsecond resolution with the ESO VLT." In: *Instrument Design and Performance for Optical/Infrared Ground-based Telescopes*. Ed. by M. Iye and A. F. M.

Moorwood. Vol. 4841. Proc. SPIE, pp. 1548–1561. arXiv: astro-ph/0306191.

Elias, J. H., R. R. Joyce, M. Liang, G. P. Muller, E. A. Hileman, and J. R. George (2006). "Design of the Gemini near-infrared spectrograph." In: *Society of Photo-Optical Instrumentation Engineers (SPIE) Conference Series*. Vol. 6269. Proc. SPIE, p. 62694C.

Elitzur, M. and I. Shlosman (2006). "The AGN-obscuring Torus: The End of the "Doughnut" Paradigm?" In: *ApJ* 648, pp. L101–L104. arXiv: astro-ph/0605686.

Elvis, M. (2000). "A Structure for Quasars." In: *ApJ* 545, pp. 63–76. arXiv: astro-ph/0008064.

Elvis, M., B. J. Wilkes, J. C. McDowell, R. F. Green, J. Bechtold, S. P. Willner, M. S. Oey, E. Polomski, and R. Cutri (1994). "Atlas of quasar energy distributions." In: *ApJS* 95, pp. 1–68.

Elvis, M. et al. (2012). "Spectral Energy Distributions of Type 1 Active Galactic Nuclei in the COSMOS Survey. I. The XMM-COSMOS Sample." In: *ApJ* 759, 6, p. 6. arXiv: 1209.1478.

Everett, J. E. (2005). "Radiative Transfer and Acceleration in Magnetocentrifugal Winds." In: *ApJ* 631, pp. 689–706. arXiv: astro-ph/0506321.

Everett, J., S. Gallagher, and S. Keating (2009). "Blowing Away the "Torus": Dusty Winds in AGN." In: *American Institute of Physics Conference Series*. Ed. by S. Heinz and E. Wilcots. Vol. 1201. American Institute of Physics Conference Series, pp. 56–59.

Fabian, A. C. (2012). "Observational Evidence of Active Galactic Nuclei Feedback." In: *ARA&A* 50, pp. 455–489. arXiv: 1204.4114.

Fanidakis, N., C. M. Baugh, A. J. Benson, R. G. Bower, S. Cole, C. Done, C. S. Frenk, R. C. Hickox, C. Lacey, and C. Del P. Lagos (2012). "The evolution of active galactic nuclei across cosmic time: what is downsizing?" In: *MNRAS* 419, pp. 2797–2820. arXiv: 1011.5222.

Faucher-Giguère, C.-A. and E. Quataert (2012). "The physics of galactic winds driven by active galactic nuclei." In: *MNRAS* 425, pp. 605–622. arXiv: 1204.2547.

Feldman, F. R., D. W. Weedman, V. A. Balzano, and L. W. Ramsey (1982). "Emission-line widths in galactic nuclei." In: *ApJ* 256, pp. 427–434.

Ferrarese, L. and H. Ford (2005). "Supermassive Black Holes in Galactic Nuclei: Past, Present and Future Research." In: *Space Sci. Rev.* 116, pp. 523–624. arXiv: astro-ph/0411247.

Ferrarese, L. and D. Merritt (2000). "A Fundamental Relation between Supermassive Black Holes and Their Host Galaxies." In: *ApJ* 539, pp. L9–L12. arXiv: astro-ph/0006053.

Feruglio, C., R. Maiolino, E. Piconcelli, N. Menci, H. Aussel, A. Lamastra, and F. Fiore (2010). "Quasar feedback revealed by giant molecular outflows." In: *A&A* 518, L155, p. L155. arXiv: 1006.1655.

Font-Ribera, A. et al. (2013). "The large-scale quasar-Lyman α forest cross-correlation from BOSS." In: *J. Cosmology Astropart. Phys.* 5, 018, p. 018. arXiv: 1303.1937.

Foreman-Mackey, D., D. W. Hogg, D. Lang, and J. Goodman (2013). "emcee: The MCMC Hammer." In: *PASP* 125, pp. 306–312. arXiv: 1202.3665.

Francis, P. J., P. C. Hewett, C. B. Foltz, F. H. Chaffee, R. J. Weymann, and S. L. Morris (1991). "A high signal-to-noise ratio composite quasar spectrum." In: *ApJ* 373, pp. 465–470.

Francis, P. J., P. C. Hewett, C. B. Foltz, and F. H. Chaffee (1992). "An objective classification scheme for QSO spectra." In: *ApJ* 398, pp. 476–490.

Gallagher, S. C., J. E. Everett, S. K. Keating, A. R. Hill, and R. P. Deo (2012). "Looking for the Wind in the Dust." In: *AGN Winds in Charleston*. Ed. by G. Chartas, F. Hamann, and K. M. Leighly. Vol. 460. Astronomical Society of the Pacific Conference Series, p. 199. arXiv: 1201.5018.

Gallagher, S. C., J. E. Everett, M. M. Abado, and S. K. Keating (2015). "Investigating the structure of the windy torus in quasars." In: *MNRAS* 451, pp. 2991–3000. arXiv: 1505.04219.

Gaskell, C. M. (1982). "A redshift difference between high and low ionization emission-line regions in QSOs - Evidence for radial motions." In: *ApJ* 263, pp. 79–86.

Gaskell, C. M. and R. W. Goosmann (2016). "The case for inflow of the broad-line region of active galactic nuclei." In: *Ap&SS* 361, 67, p. 67. arXiv: 1512.08900.

Gavignaud, I. et al. (2008). "Eddington ratios of faint AGN at intermediate redshift: evidence for a population of half-starved black holes." In: *A&A* 492, pp. 637–650. arXiv: 0810.2172.

Gebhardt, K. et al. (2000). "A Relationship between Nuclear Black Hole Mass and Galaxy Velocity Dispersion." In: *ApJ* 539, pp. L13–L16. arXiv: astro-ph/0006289.

Graham, A. W., P. Erwin, N. Caon, and I. Trujillo (2001). "A Correlation between Galaxy Light Concentration and Supermassive Black Hole Mass." In: *ApJ* 563, pp. L11–L14. arXiv: astro-ph/0111152.

Grandi, S. A. (1982). "The 3000 A bump in quasars." In: *ApJ* 255, pp. 25–38.

Greene, J. E. and L. C. Ho (2005a). "A Comparison of Stellar and Gaseous Kinematics in the Nuclei of Active Galaxies." In: *ApJ* 627, pp. 721–732. arXiv: astro-ph/0503675.

— (2005b). "Estimating Black Hole Masses in Active Galaxies Using the Hα Emission Line." In: *ApJ* 630, pp. 122–129. arXiv: astro-ph/0508335.

Greene, J. E., N. L. Zakamska, X. Liu, A. J. Barth, and L. C. Ho (2009). "The Growth of Black Holes: Insights from Obscured Active Galaxies." In: *ApJ* 702, pp. 441–459. arXiv: 0907.1086.

Greene, J. E., N. L. Zakamska, L. C. Ho, and A. J. Barth (2011). "Feedback in Luminous Obscured Quasars." In: *ApJ* 732, 9, p. 9. arXiv: 1102.2913.

Grier, C. J. et al. (2012). "Reverberation Mapping Results for Five Seyfert 1 Galaxies." In: *ApJ* 755, 60, p. 60. arXiv: 1206.6523.

Gültekin, K. et al. (2009). "The M-σ and M-L Relations in Galactic Bulges, and Determinations of Their Intrinsic Scatter." In: *ApJ* 698, pp. 198–221. arXiv: 0903.4897.

Hainline, K. N., R. Hickox, J. E. Greene, A. D. Myers, and N. L. Zakamska (2013). "SALT Long-slit Spectroscopy of Luminous Obscured Quasars: An Upper Limit on the Size of the Narrow-line Region?" In: *ApJ* 774, 145, p. 145. arXiv: 1307.5852.

Hainline, K. N., R. C. Hickox, J. E. Greene, A. D. Myers, N. L. Zakamska, G. Liu, and X. Liu (2014). "Gemini Long-slit Observations of Luminous Obscured Quasars: Further Evidence for an Upper Limit on the Size of the Narrow-line Region." In: *ApJ* 787, 65, p. 65. arXiv: 1404.1921.

Hall, P. B. et al. (2013). "Broad absorption line quasars with redshifted troughs: high-velocity infall or rotationally dominated outflows?" In: *MNRAS* 434, pp. 222–256. arXiv: 1306.2680.

Hamann, F., T. A. Barlow, V. Junkkarinen, and E. M. Burbidge (1997). "High-Resolution Spectra of Intrinsic Absorption

Lines in the Quasi-stellar Object UM 675." In: *ApJ* 478, pp. 80–86.

Hao, H. et al. (2010). "Hot-dust-poor Type 1 Active Galactic Nuclei in the COSMOS Survey." In: *ApJ* 724, pp. L59–L63. arXiv: 1009.3276.

Hao, H., M. Elvis, F. Civano, and A. Lawrence (2011). "Hot-dust-poor Quasars in Mid-infrared and Optically Selected Samples." In: *ApJ* 733, 108, p. 108. arXiv: 1011.0429.

Hao, H. et al. (2013). "A quasar-galaxy mixing diagram: quasar spectral energy distribution shapes in the optical to near-infrared." In: *MNRAS* 434, pp. 3104–3121. arXiv: 1210.3044.

Harrison, C. M. et al. (2012). "Energetic galaxy-wide outflows in high-redshift ultraluminous infrared galaxies hosting AGN activity." In: *MNRAS* 426, pp. 1073–1096. arXiv: 1205.1801.

Harrison, C. M., D. M. Alexander, J. R. Mullaney, and A. M. Swinbank (2014). "Kiloparsec-scale outflows are prevalent among luminous AGN: outflows and feedback in the context of the overall AGN population." In: *MNRAS* 441, pp. 3306–3347. arXiv: 1403.3086.

Harrison, C. M., D. M. Alexander, J. R. Mullaney, J. P. Stott, A. M. Swinbank, V. Arumugam, F. E. Bauer, R. G. Bower, A. J. Bunker, and R. M. Sharples (2016). "The KMOS AGN Survey at High redshift (KASHz): the prevalence and drivers of ionized outflows in the host galaxies of X-ray AGN." In: *MNRAS* 456, pp. 1195–1220. arXiv: 1511.00008.

Heckman, T. M. and P. N. Best (2014). "The Coevolution of Galaxies and Supermassive Black Holes: Insights from Surveys of the Contemporary Universe." In: *ARA&A* 52, pp. 589–660. arXiv: 1403.4620.

Heckman, T. M., G. K. Miley, and R. F. Green (1984). "The kinematics of the narrow-line region in active galaxies and quasars. III - Correlations with the broad-line region and radio emission." In: *ApJ* 281, pp. 525–534.

Heckman, T. M., G. K. Miley, W. J. M. van Breugel, and H. R. Butcher (1981). "Emission-line profiles and kinematics of the narrow-line region in Seyfert and radio galaxies." In: *ApJ* 247, pp. 403–418.

Hennawi, J. F. et al. (2006a). "Binary Quasars in the Sloan Digital Sky Survey: Evidence for Excess Clustering on Small Scales." In: *AJ* 131, pp. 1–23. arXiv: astro-ph/0504535.

Hennawi, J. F. et al. (2006b). "Quasars Probing Quasars. I. Optically Thick Absorbers near Luminous Quasars." In: *ApJ* 651, pp. 61–83. arXiv: astro-ph/0603742.

Hennawi, J. F. et al. (2010). "Binary Quasars at High Redshift. I. 24 New Quasar Pairs at z ˜ 3-4." In: *ApJ* 719, pp. 1672–1692. arXiv: 0908.3907.

Hennawi, J. F., J. X. Prochaska, S. Cantalupo, and F. Arrigoni-Battaia (2015). "Quasar quartet embedded in giant nebula reveals rare massive structure in distant universe." In: *Science* 348, pp. 779–783. arXiv: 1505.03786.

Herter, T. L. et al. (2008). "The performance of TripleSpec at Palomar." In: *Ground-based and Airborne Instrumentation for Astronomy II*. Vol. 7014. Proc. SPIE, p. 70140X.

Hewett, P. C. and C. B. Foltz (2003). "The Frequency and Radio Properties of Broad Absorption Line Quasars." In: *AJ* 125, pp. 1784–1794. arXiv: astro-ph/0301191.

Hewett, P. C. and V. Wild (2010). "Improved redshifts for SDSS quasar spectra." In: *MNRAS* 405, pp. 2302–2316. arXiv: 1003.3017.

Higginbottom, N. and D. Proga (2015). "Coronae and Winds from Irradiated Disks in X-Ray Binaries." In: *ApJ* 807, p. 107. arXiv: 1504.03328.

Hodapp, K. W. et al. (2003). "The Gemini Near-Infrared Imager (NIRI)." In: *PASP* 115, pp. 1388–1406.

Hogg, D. W., J. Bovy, and D. Lang (2010). "Data analysis recipes: Fitting a model to data." In: *ArXiv e-prints*. arXiv: 1008.4686.

Hönig, S. F., M. Kishimoto, R. Antonucci, A. Marconi, M. A. Prieto, K. Tristram, and G. Weigelt (2012). "Parsec-scale Dust Emission from the Polar Region in the Type 2 Nucleus of NGC 424." In: *ApJ* 755, 149, p. 149. arXiv: 1206.4307.

Hönig, S. F., M. Kishimoto, K. R. W. Tristram, M. A. Prieto, P. Gandhi, D. Asmus, R. Antonucci, L. Burtscher, W. J. Duschl, and G. Weigelt (2013). "Dust in the Polar Region as a Major Contributor to the Infrared Emission of Active Galactic Nuclei." In: *ApJ* 771, 87, p. 87. arXiv: 1306.4312.

Hopkins, P. F., L. Hernquist, T. J. Cox, T. Di Matteo, B. Robertson, and V. Springel (2006). "A Unified, Merger-driven Model of the Origin of Starbursts, Quasars, the Cosmic X-Ray Background, Supermassive Black Holes, and Galaxy Spheroids." In: *ApJS* 163, pp. 1–49. arXiv: astro-ph/0506398.

Hoyle, F. and W. A. Fowler (1963). "On the nature of strong radio sources." In: *MNRAS* 125, p. 169.

Jackson, N. and I. W. A. Browne (1991). "Optical Properties of Quasars - Part Two - Emission Line Geometry and Radio Properties." In: *MNRAS* 250, p. 422.

Jiang, L. et al. (2010). "Dust-free quasars in the early Universe." In: *Nature* 464, pp. 380–383. arXiv: 1003.3432.

Kakkad, D. et al. (2016). "Tracing outflows in the AGN forbidden region with SINFONI." In: *A&A* 592, A148, A148. arXiv: 1605.08631.

Kaspi, S., P. S. Smith, H. Netzer, D. Maoz, B. T. Jannuzi, and U. Giveon (2000). "Reverberation Measurements for 17 Quasars and the Size-Mass-Luminosity Relations in Active Galactic Nuclei." In: *ApJ* 533, pp. 631–649. arXiv: astro-ph/9911476.

Kaspi, S., W. N. Brandt, D. Maoz, H. Netzer, D. P. Schneider, and O. Shemmer (2007). "Reverberation Mapping of High-Luminosity Quasars: First Results." In: *ApJ* 659, pp. 997–1007. arXiv: astro-ph/0612722.

Kauffmann, G. and M. Haehnelt (2000). "A unified model for the evolution of galaxies and quasars." In: *MNRAS* 311, pp. 576–588. arXiv: astro-ph/9906493.

Keating, S. K., J. E. Everett, S. C. Gallagher, and R. P. Deo (2012). "Sweeping Away the Mysteries of Dusty Continuous Winds in Active Galactic Nuclei." In: *ApJ* 749, 32, p. 32. arXiv: 1202.4681.

Kelly, B. C. and Y. Shen (2013). "The Demographics of Broad-line Quasars in the Mass-Luminosity Plane. II. Black Hole Mass and Eddington Ratio Functions." In: *ApJ* 764, p. 45. arXiv: 1209.0477.

Kelly, B. C., M. Vestergaard, X. Fan, P. Hopkins, L. Hernquist, and A. Siemiginowska (2010). "Constraints on Black Hole Growth, Quasar Lifetimes, and Eddington Ratio Distributions from the SDSS Broad-line Quasar Black Hole Mass Function." In: *ApJ* 719, pp. 1315–1334. arXiv: 1006.3561.

Kim, M., L. C. Ho, C. J. Lonsdale, M. Lacy, A. W. Blain, and A. E. Kimball (2013). "Evidence for Active Galactic Nucleus Driven Outflows in Young Radio Quasars." In: *ApJ* 768, L9, p. L9. arXiv: 1303.7194.

King, A. L. et al. (2015). "Simulations of the OzDES AGN reverberation mapping project." In: *MNRAS* 453, pp. 1701–1726. arXiv: 1504.03031.

King, A. R., K. Zubovas, and C. Power (2011). "Large-scale outflows in galaxies." In: *MNRAS* 415, pp. L6–L10. arXiv: 1104.3682.

King, A. (2003). "Black Holes, Galaxy Formation, and the M_{BH}-σ Relation." In: *ApJ* 596, pp. L27–L29. arXiv: astro-ph/0308342.

King, A. and K. Pounds (2015). "Powerful Outflows and Feedback from Active Galactic Nuclei." In: *ARA&A* 53, pp. 115–154. arXiv: 1503.05206.

Kishimoto, M., S. F. Hönig, T. Beckert, and G. Weigelt (2007). "The innermost region of AGN tori: implications from the HST/NICMOS type 1 point sources and near-IR reverberation." In: *A&A* 476, pp. 713–721. arXiv: 0709.0431.

Kollatschny, W. and M. Zetzl (2011). "Broad-line active galactic nuclei rotate faster than narrow-line ones." In: *Nature* 470, pp. 366–368.

— (2013). "The shape of broad-line profiles in active galactic nuclei." In: *A&A* 549, A100, A100. arXiv: 1211.3065.

Kollmeier, J. A. et al. (2006). "Black Hole Masses and Eddington Ratios at $0.3 < z < 4$." In: *ApJ* 648, pp. 128–139. arXiv: astro-ph/0508657.

Konigl, A. and J. F. Kartje (1994). "Disk-driven hydromagnetic winds as a key ingredient of active galactic nuclei unification schemes." In: *ApJ* 434, pp. 446–467.

Kormendy, J. and L. C. Ho (2013). "Coevolution (Or Not) of Supermassive Black Holes and Host Galaxies." In: *ARA&A* 51, pp. 511–653. arXiv: 1304.7762.

Kormendy, J. and D. Richstone (1995). "Inward Bound—The Search For Supermassive Black Holes In Galactic Nuclei." In: *ARA&A* 33, p. 581.

Kratzer, R. M. and G. T. Richards (2015). "Mean and Extreme Radio Properties of Quasars and the Origin of Radio Emission." In: *AJ* 149, p. 61.

Krawczyk, C. M., G. T. Richards, S. S. Mehta, M. S. Vogeley, S. C. Gallagher, K. M. Leighly, N. P. Ross, and D. P. Schneider (2013). "Mean Spectral Energy Distributions and Bolometric Corrections for Luminous Quasars." In: *ApJS* 206, p. 4. arXiv: 1304.5573.

Krolik, J. H. and M. C. Begelman (1988). "Molecular tori in Seyfert galaxies - Feeding the monster and hiding it." In: *ApJ* 329, pp. 702–711.

Kuraszkiewicz, J. K. et al. (2003). "The Far-Infrared Spectral Energy Distributions of X-Ray-selected Active Galaxies." In: *ApJ* 590, pp. 128–148. arXiv: astro-ph/0302572.

Landt, H., M. Elvis, M. J. Ward, M. C. Bentz, K. T. Korista, and M. Karovska (2011). "The near-infrared broad emission line

region of active galactic nuclei - II. The 1-μm continuum." In: *MNRAS* 414, pp. 218–240. arXiv: 1101.3342.

Lau, M. W., J. X. Prochaska, and J. F. Hennawi (2016). "Quasars Probing Quasars. VIII. The Physical Properties of the Cool Circumgalactic Medium Surrounding z ˜ 2-3 Massive Galaxies Hosting Quasars." In: *ApJS* 226, 25, p. 25. arXiv: 1510.06018.

Lawrence, A. et al. (2007). "The UKIRT Infrared Deep Sky Survey (UKIDSS)." In: *MNRAS* 379, pp. 1599–1617. arXiv: astro-ph/0604426.

Lee, K.-G. et al. (2013). "The BOSS Lyα Forest Sample from SDSS Data Release 9." In: *AJ* 145, 69, p. 69. arXiv: 1211.5146.

Leighly, K. M. (2004). "Hubble Space Telescope STIS Ultraviolet Spectral Evidence of Outflow in Extreme Narrow-Line Seyfert 1 Galaxies. II. Modeling and Interpretation." In: *ApJ* 611, pp. 125–152. arXiv: astro-ph/0402452.

Levi, M. et al. (2013). "The DESI Experiment, a whitepaper for Snowmass 2013." In: *ArXiv e-prints*. arXiv: 1308.0847.

Liu, G., N. L. Zakamska, J. E. Greene, N. P. H. Nesvadba, and X. Liu (2013). "Observations of feedback from radio-quiet quasars - II. Kinematics of ionized gas nebulae." In: *MNRAS* 436, pp. 2576–2597. arXiv: 1305.6922.

López-Gonzaga, N., L. Burtscher, K. R. W. Tristram, K. Meisenheimer, and M. Schartmann (2016). "Mid-infrared interferometry of 23 AGN tori: On the significance of polar-elongated emission." In: *A&A* 591, A47, A47. arXiv: 1602.05592.

Luo, B. et al. (2015). "X-ray Insights into the Nature of PHL 1811 Analogs and Weak Emission-line Quasars: Unification with a Geometrically Thick Accretion Disk?" In: *ApJ* 805, p. 122. arXiv: 1503.02085.

Lupton, R. H., J. E. Gunn, and A. S. Szalay (1999). "A Modified Magnitude System that Produces Well-Behaved Magnitudes, Colors, and Errors Even for Low Signal-to-Noise Ratio Measurements." In: *AJ* 118, pp. 1406–1410. arXiv: astro-ph/9903081.

Lusso, E. et al. (2010). "The X-ray to optical-UV luminosity ratio of X-ray selected type 1 AGN in XMM-COSMOS." In: *A&A* 512, A34, A34. arXiv: 0912.4166.

Lynden-Bell, D. (1969). "Galactic Nuclei as Collapsed Old Quasars." In: *Nature* 223, pp. 690–694.

Lynden-Bell, D. and M. J. Rees (1971). "On quasars, dust and the galactic centre." In: *MNRAS* 152, p. 461.

MacLeod, C. L. et al. (2010). "Modeling the Time Variability of SDSS Stripe 82 Quasars as a Damped Random Walk." In: *ApJ* 721, pp. 1014–1033. arXiv: 1004.0276.

MacLeod, C. L. et al. (2016). "A systematic search for changing-look quasars in SDSS." In: *MNRAS* 457, pp. 389–404. arXiv: 1509.08393.

Maddox, N. and P. C. Hewett (2006). "Simulating wide-field quasar surveys from the optical to near-infrared." In: *MNRAS* 367, pp. 717–731. arXiv: astro-ph/0512325.

Magorrian, J. et al. (1998). "The Demography of Massive Dark Objects in Galaxy Centers." In: *AJ* 115, pp. 2285–2305. arXiv: astro-ph/9708072.

Mainzer, A. et al. (2011). "Preliminary Results from NEOWISE: An Enhancement to the Wide-field Infrared Survey Explorer for Solar System Science." In: *ApJ* 731, 53, p. 53. arXiv: 1102.1996.

Maiolino, R. et al. (2012). "Evidence of strong quasar feedback in the early Universe." In: *MNRAS* 425, pp. L66–L70. arXiv: 1204.2904.

Manchado, A. et al. (1998). "LIRIS: a long-slit intermediate-resolution infrared spectrograph for the WHT." In: *Infrared Astronomical Instrumentation*. Ed. by A. M. Fowler. Vol. 3354. Proc. SPIE, pp. 448–455.

Marchese, E., R. Della Ceca, A. Caccianiga, P. Severgnini, A. Corral, and R. Fanali (2012). "The optical-UV spectral energy distribution of the unabsorbed AGN population in the XMM-Newton Bright Serendipitous Survey." In: *A&A* 539, A48, A48. arXiv: 1111.4409.

Marconi, A. and L. K. Hunt (2003). "The Relation between Black Hole Mass, Bulge Mass, and Near-Infrared Luminosity." In: *ApJ* 589, pp. L21–L24. arXiv: astro-ph/0304274.

Martini, P. and D. H. Weinberg (2001). "Quasar Clustering and the Lifetime of Quasars." In: *ApJ* 547, pp. 12–26. arXiv: astro-ph/0002384.

Marziani, P. and J. W. Sulentic (2012). "Estimating black hole masses in quasars using broad optical and UV emission lines." In: *New Astron. Rev.* 56, pp. 49–63. arXiv: 1108.5102.

Marziani, P., J. W. Sulentic, G. M. Stirpe, S. Zamfir, and M. Calvani (2009). "VLT/ISAAC spectra of the Hβ region in intermediate-redshift quasars. III. Hβ broad-line profile analysis and inferences about BLR structure." In: *A&A* 495, pp. 83–112. arXiv: 0812.0251.

Marziani, P., J. W. Sulentic, I. Plauchu-Frayn, and A. del Olmo (2013). "Is MgIIλ2800 a reliable virial broadening estimator for quasars?" In: *A&A* 555, A89, A89. arXiv: 1305.1096.

McGill, K. L., J.-H. Woo, T. Treu, and M. A. Malkan (2008). "Comparing and Calibrating Black Hole Mass Estimators for Distant Active Galactic Nuclei." In: *ApJ* 673, pp. 703–714. arXiv: 0710.1839.

McLure, R. J. and M. J. Jarvis (2002). "Measuring the black hole masses of high-redshift quasars." In: *MNRAS* 337, pp. 109–116. arXiv: astro-ph/0204473.

McMahon, R. G., M. Banerji, E. Gonzalez, S. E. Koposov, V. J. Bejar, N. Lodieu, R. Rebolo, and VHS Collaboration (2013). "First Scientific Results from the VISTA Hemisphere Survey (VHS)." In: *The Messenger* 154, pp. 35–37.

Mejía-Restrepo, J. E., B. Trakhtenbrot, P. Lira, H. Netzer, and D. M. Capellupo (2016). "Active galactic nuclei at z~1.5 - II. Black hole mass estimation by means of broad emission lines." In: *MNRAS* 460, pp. 187–211. arXiv: 1603.03437.

Minezaki, T., Y. Yoshii, Y. Kobayashi, K. Enya, M. Suganuma, H. Tomita, T. Aoki, and B. A. Peterson (2004). "Inner Size of a Dust Torus in the Seyfert 1 Galaxy NGC 4151." In: *ApJ* 600, pp. L35–L38. arXiv: astro-ph/0311338.

Mittaz, J. P. D., M. V. Penston, and M. A. J. Snijders (1990). "Ultraviolet variability of NGC 4151 - A study using principal component analysis." In: *MNRAS* 242, pp. 370–378.

Moe, M., N. Arav, M. A. Bautista, and K. T. Korista (2009). "Quasar Outflow Contribution to AGN Feedback: Observations of QSO SDSS J0838+2955." In: *ApJ* 706, pp. 525–534. arXiv: 0911.3332.

Moorwood, A., J.-G. Cuby, and C. Lidman (1998). "SOFI sees first light at the NTT." In: *The Messenger* 91, pp. 9–13.

Moorwood, A. et al. (1998). "ISAAC sees first light at the VLT." In: *The Messenger* 94, pp. 7–9.

Mor, R., H. Netzer, and M. Elitzur (2009). "Dusty Structure Around Type-I Active Galactic Nuclei: Clumpy Torus Narrow-line Region and Near-nucleus Hot Dust." In: *ApJ* 705, pp. 298–313. arXiv: 0907.1654.

Mor, R. and B. Trakhtenbrot (2011). "Hot-dust Clouds with Pure-graphite Composition around type-I Active Galactic Nuclei." In: *ApJ* 737, L36, p. L36. arXiv: 1105.3198.

Mortlock, D. J. et al. (2011). "A luminous quasar at a redshift of z = 7.085." In: *Nature* 474, pp. 616–619. arXiv: 1106.6088.

Mullaney, J. R., D. M. Alexander, S. Fine, A. D. Goulding, C. M. Harrison, and R. C. Hickox (2013). "Narrow-line region gas kinematics of 24 264 optically selected AGN: the radio connection." In: *MNRAS* 433, pp. 622–638. arXiv: 1305.0263.

Murray, N., J. Chiang, S. A. Grossman, and G. M. Voit (1995). "Accretion Disk Winds from Active Galactic Nuclei." In: *ApJ* 451, p. 498.

Myers, A. D. et al. (2015). "The SDSS-IV Extended Baryon Oscillation Spectroscopic Survey: Quasar Target Selection." In: *ApJS* 221, 27, p. 27. arXiv: 1508.04472.

Nardini, E. et al. (2015). "Black hole feedback in the luminous quasar PDS 456." In: *Science* 347, pp. 860–863. arXiv: 1502.06636.

Ness, M., D. W. Hogg, H.-W. Rix, A. Y. Q. Ho, and G. Zasowski (2015). "The Cannon: A data-driven approach to Stellar Label Determination." In: *ApJ* 808, 16, p. 16. arXiv: 1501.07604.

Nesvadba, N. P. H., M. D. Lehnert, F. Eisenhauer, A. Gilbert, M. Tecza, and R. Abuter (2006). "Extreme Gas Kinematics in the z=2.2 Powerful Radio Galaxy MRC 1138-262: Evidence for Efficient Active Galactic Nucleus Feedback in the Early Universe?" In: *ApJ* 650, pp. 693–705. arXiv: astro-ph/0606530.

Nesvadba, N. P. H., M. D. Lehnert, C. De Breuck, A. M. Gilbert, and W. van Breugel (2008). "Evidence for powerful AGN winds at high redshift: dynamics of galactic outflows in radio galaxies during the "Quasar Era"." In: *A&A* 491, pp. 407–424. arXiv: 0809.5171.

Nesvadba, N. P. H., F. Boulanger, P. Salomé, P. Guillard, M. D. Lehnert, P. Ogle, P. Appleton, E. Falgarone, and G. Pineau Des Forets (2010). "Energetics of the molecular gas in the H_2 luminous radio galaxy 3C 326: Evidence for negative AGN feedback." In: *A&A* 521, A65, A65. arXiv: 1003.3449.

Netzer, H. (1990). "AGN emission lines." In: *Active Galactic Nuclei*. Ed. by R. D. Blandford, H. Netzer, L. Woltjer, T. J.-L. Courvoisier, and M. Mayor, pp. 57–160.

— (2015). "Revisiting the Unified Model of Active Galactic Nuclei." In: *ARA&A* 53, pp. 365–408. arXiv: 1505.00811.

Netzer, H. and B. M. Peterson (1997). "Reverberation Mapping and the Physics of Active Galactic Nuclei." In: *Astronomical Time Series*. Ed. by D. Maoz, A. Sternberg, and E. M. Leibowitz. Vol. 218. Astrophysics and Space Science Library, p. 85. arXiv: astro-ph/9706039.

Netzer, H., O. Shemmer, R. Maiolino, E. Oliva, S. Croom, E. Corbett, and L. di Fabrizio (2004). "Near-Infrared Spectroscopy of High-Redshift Active Galactic Nuclei. II. Disappearing Narrow-Line Regions and the Role of Accretion." In: *ApJ* 614, pp. 558–567. arXiv: astro-ph/0406560.

Oke, J. B. and J. E. Gunn (1983). "Secondary standard stars for absolute spectrophotometry." In: *ApJ* 266, pp. 713–717.

Onken, C. A. and J. A. Kollmeier (2008). "An Improved Method for Using Mg II to Estimate Black Hole Masses in Active Galactic Nuclei." In: *ApJ* 689, p. L13. arXiv: 0810.1950.

Onken, C. A. and B. M. Peterson (2002). "The Mass of the Central Black Hole in the Seyfert Galaxy NGC 3783." In: *ApJ* 572, pp. 746–752. arXiv: astro-ph/0202382.

Osterbrock, D. E. (1989). *Astrophysics of gaseous nebulae and active galactic nuclei*.

Pâris, I. et al. (2012). "The Sloan Digital Sky Survey quasar catalog: ninth data release." In: *A&A* 548, A66, A66. arXiv: 1210.5166.

Pâris, I. et al. (2014). "The Sloan Digital Sky Survey quasar catalog: tenth data release." In: *A&A* 563, A54. arXiv: 1311.4870.

Pâris, I. et al. (2017). "The Sloan Digital Sky Survey Quasar Catalog: Twelfth data release." In: *A&A* 597, A79. arXiv: 1608.06483.

Park, D., J.-H. Woo, K. D. Denney, and J. Shin (2013). "Calibrating C-IV-based Black Hole Mass Estimators." In: *ApJ* 770, p. 87. arXiv: 1304.7281.

Perna, M. et al. (2015). "Galaxy-wide outflows in z ˜ 1.5 luminous obscured quasars revealed through near-IR slit-resolved spectroscopy." In: *A&A* 574, A82, A82. arXiv: 1410.5468.

Peterson, B. M. (1993). "Reverberation mapping of active galactic nuclei." In: *PASP* 105, pp. 247–268.

— (1997). *An Introduction to Active Galactic Nuclei*.

— (2010). "Toward Precision Measurement of Central Black Hole Masses." In: *Co-Evolution of Central Black Holes and Galaxies*. Ed. by B. M. Peterson, R. S. Somerville, and T. Storchi-Bergmann. Vol. 267. IAU Symposium, pp. 151–160. arXiv: 1001.3675.

— (2014). "Measuring the Masses of Supermassive Black Holes." In: *Space Sci. Rev.* 183, pp. 253–275.

Peterson, B. M. et al. (2004). "Central Masses and Broad-Line Region Sizes of Active Galactic Nuclei. II. A Homogeneous

Analysis of a Large Reverberation-Mapping Database." In: *ApJ* 613, pp. 682–699. arXiv: astro-ph/0407299.

Plotkin, R. M. et al. (2015). "Detection of Rest-frame Optical Lines from X-shooter Spectroscopy of Weak Emission Line Quasars." In: *ApJ* 805, p. 123. arXiv: 1503.07523.

Polletta, M., T. J.-L. Courvoisier, E. J. Hooper, and B. J. Wilkes (2000). "The far-infrared emission of radio loud and radio quiet quasars." In: *A&A* 362, pp. 75–96. arXiv: astro-ph/0006315.

Polletta, M. et al. (2007). "Spectral Energy Distributions of Hard X-Ray Selected Active Galactic Nuclei in the XMM-Newton Medium Deep Survey." In: *ApJ* 663, pp. 81–102. arXiv: astro-ph/0703255.

Pringle, J. E. (1981). "Accretion discs in astrophysics." In: *ARA&A* 19, pp. 137–162.

Prochaska, J. X. and J. F. Hennawi (2009). "Quasars Probing Quasars. III. New Clues to Feedback, Quenching, and the Physics of Massive Galaxy Formation." In: *ApJ* 690, pp. 1558–1584. arXiv: 0806.0862.

Proga, D., J. M. Stone, and T. R. Kallman (2000). "Dynamics of Line-driven Disk Winds in Active Galactic Nuclei." In: *ApJ* 543, pp. 686–696. arXiv: astro-ph/0005315.

Raban, D., W. Jaffe, H. Röttgering, K. Meisenheimer, and K. R. W. Tristram (2009). "Resolving the obscuring torus in NGC 1068 with the power of infrared interferometry: revealing the inner funnel of dust." In: *MNRAS* 394, pp. 1325–1337. arXiv: 0901.1306.

Rafiee, A. and P. B. Hall (2011). "Supermassive Black Hole Mass Estimates Using Sloan Digital Sky Survey Quasar Spectra at $0.7 < z < 2$." In: *ApJS* 194, 42, p. 42. arXiv: 1104.1828.

Reichard, T. A., G. T. Richards, P. B. Hall, D. P. Schneider, D. E. Vanden Berk, X. Fan, D. G. York, G. R. Knapp, and J. Brinkmann (2003). "Continuum and Emission-Line Properties of Broad Absorption Line Quasars." In: *AJ* 126, pp. 2594–2607. arXiv: astro-ph/0308508.

Richards, G. T. (2006). "AGN Outflows in Emission and Absorption: The SDSS Perspective." In: *AGN Winds in the Caribbean*. arXiv: astro-ph/0603827.

Richards, G. T., D. E. Vanden Berk, T. A. Reichard, P. B. Hall, D. P. Schneider, M. SubbaRao, A. R. Thakar, and D. G. York (2002). "Broad Emission-Line Shifts in Quasars: An Orientation Measure for Radio-Quiet Quasars?" In: *AJ* 124, pp. 1–17. arXiv: astro-ph/0204162.

Richards, G. T. et al. (2003). "Red and Reddened Quasars in the Sloan Digital Sky Survey." In: *AJ* 126, pp. 1131–1147. arXiv: astro-ph/0305305.

Richards, G. T. et al. (2006a). "Spectral Energy Distributions and Multiwavelength Selection of Type 1 Quasars." In: *ApJS* 166, pp. 470–497. arXiv: astro-ph/0601558.

Richards, G. T. et al. (2006b). "The Sloan Digital Sky Survey Quasar Survey: Quasar Luminosity Function from Data Release 3." In: *AJ* 131, pp. 2766–2787. arXiv: astro-ph/0601434.

Richards, G. T., N. E. Kruczek, S. C. Gallagher, P. B. Hall, P. C. Hewett, K. M. Leighly, R. P. Deo, R. M. Kratzer, and Y. Shen (2011). "Unification of Luminous Type 1 Quasars through CIV Emission." In: *AJ* 141, p. 167. arXiv: 1011.2282.

Riffel, R. A., T. Storchi-Bergmann, and P. J. McGregor (2009). "The Dusty Nuclear Torus in NGC 4151: Constraints from Gemini Near-Infrared Integral Field Spectrograph Observations." In: *ApJ* 698, pp. 1767–1770. arXiv: 0903.2798.

Risaliti, G. and M. Elvis (2004). "A Panchromatic View of AGN." In: *Supermassive Black Holes in the Distant Universe*. Ed. by A. J. Barger. Vol. 308. Astrophysics and Space Science Library, p. 187. arXiv: 1011.2282.

Roseboom, I. G., A. Lawrence, M. Elvis, S. Petty, Y. Shen, and H. Hao (2013). "IR-derived covering factors for a large sample of quasars from WISE-UKIDSS-SDSS." In: *MNRAS* 429, pp. 1494–1501. arXiv: 1205.4543.

Ross, N. P. et al. (2013). "The SDSS-III Baryon Oscillation Spectroscopic Survey: The Quasar Luminosity Function from Data Release Nine." In: *ApJ* 773, p. 14. arXiv: 1210.6389.

Runnoe, J. C., M. S. Brotherton, Z. Shang, and M. A. DiPompeo (2013). "Rehabilitating C IV-based black hole mass estimates in quasars." In: *MNRAS* 434, pp. 848–861. arXiv: 1306.3521.

Runnoe, J. C., M. S. Brotherton, M. A. DiPompeo, and Z. Shang (2014). "The behaviour of quasar C IV emission-line properties with orientation." In: *MNRAS* 438, pp. 3263–3274. arXiv: 1312.7500.

Rupke, D. S. N. and S. Veilleux (2013). "Breaking the Obscuring Screen: A Resolved Molecular Outflow in a Buried QSO." In: *ApJ* 775, L15, p. L15. arXiv: 1308.4988.

Salpeter, E. E. (1964). "Accretion of Interstellar Matter by Massive Objects." In: *ApJ* 140, pp. 796–800.

Sanders, D. B., B. T. Soifer, J. H. Elias, B. F. Madore, K. Matthews, G. Neugebauer, and N. Z. Scoville (1988). "Ultraluminous infrared galaxies and the origin of quasars." In: *ApJ* 325, pp. 74–91.

Schlegel, D. J., D. P. Finkbeiner, and M. Davis (1998). "Maps of Dust Infrared Emission for Use in Estimation of Reddening and Cosmic Microwave Background Radiation Foregrounds." In: *ApJ* 500, pp. 525–553. arXiv: astro-ph/9710327.

Schmidt, M. (1963). "3C 273 : A Star-Like Object with Large Red-Shift." In: *Nature* 197, p. 1040.

Schmidt, M. and R. F. Green (1983). "Quasar evolution derived from the Palomar bright quasar survey and other complete quasar surveys." In: *ApJ* 269, pp. 352–374.

Schneider, D. P. et al. (2010). "The Sloan Digital Sky Survey Quasar Catalog. V. Seventh Data Release." In: *AJ* 139, p. 2360. arXiv: 1004.1167.

Shang, Z. et al. (2011). "The Next Generation Atlas of Quasar Spectral Energy Distributions from Radio to X-Rays." In: *ApJS* 196, 2, p. 2. arXiv: 1107.1855.

Sharples, R. et al. (2013). "First Light for the KMOS Multi-Object Integral-Field Spectrometer." In: *The Messenger* 151, pp. 21–23.

Shen, Y. (2013). "The mass of quasars." In: *Bulletin of the Astronomical Society of India* 41, pp. 61–115. arXiv: 1302.2643.

— (2016). "Rest-Frame Optical Properties of Luminous $1.5 < z < 3.5$ Quasars: The Hβ-[O III] Region." In: *ApJ* in press. arXiv: 1512.00005.

Shen, Y. and L. C. Ho (2014). "The diversity of quasars unified by accretion and orientation." In: *Nature* 513, pp. 210–213. arXiv: 1409.2887.

Shen, Y. and X. Liu (2012). "Comparing Single-epoch Virial Black Hole Mass Estimators for Luminous Quasars." In: *ApJ* 753, p. 125. arXiv: 1203.0601.

Shen, Y., J. E. Greene, M. A. Strauss, G. T. Richards, and D. P. Schneider (2008). "Biases in Virial Black Hole Masses: An SDSS Perspective." In: *ApJ* 680, pp. 169–190. arXiv: 0709.3098.

Shen, Y. et al. (2011). "A Catalog of Quasar Properties from Sloan Digital Sky Survey Data Release 7." In: *ApJS* 194, p. 45. arXiv: 1006.5178.

Shen, Y. et al. (2015). "The Sloan Digital Sky Survey Reverberation Mapping Project: Technical Overview." In: *ApJS* 216, p. 4. arXiv: 1408.5970.

Shen, Y. et al. (2016). "The Sloan Digital Sky Survey Reverberation Mapping Project: Velocity Shifts of Quasar Emission Lines." In: *ArXiv e-prints*. arXiv: 1602.03894.

Silk, J. and M. J. Rees (1998). "Quasars and galaxy formation." In: *A&A* 331, pp. L1–L4. arXiv: astro-ph/9801013.

Simcoe, R. A. et al. (2010). "The FIRE infrared spectrometer at Magellan: construction and commissioning." In: *Ground-based and Airborne Instrumentation for Astronomy III*. Vol. 7735. Proc. SPIE, p. 773514.

Skrutskie, M. F. et al. (2006). "The Two Micron All Sky Survey (2MASS)." In: *AJ* 131, pp. 1163–1183.

Springel, V. et al. (2005). "Simulations of the formation, evolution and clustering of galaxies and quasars." In: *Nature* 435, pp. 629–636. arXiv: astro-ph/0504097.

Stern, J. and A. Laor (2012). "Type 1 AGN at low z - II. The relative strength of narrow lines and the nature of intermediate type AGN." In: *MNRAS* 426, pp. 2703–2718. arXiv: 1207.5543.

Stockton, A. (1976). "The Structure and Spectrum of Nebulosity Associated with the QSO 4c 37.43." In: *ApJ* 205, p. L113.

Suganuma, M., Y. Yoshii, Y. Kobayashi, T. Minezaki, K. Enya, H. Tomita, T. Aoki, S. Koshida, and B. A. Peterson (2006). "Reverberation Measurements of the Inner Radius of the Dust Torus in Nearby Seyfert 1 Galaxies." In: *ApJ* 639, pp. 46–63. arXiv: astro-ph/0511697.

Sulentic, J. W., P. Marziani, and D. Dultzin-Hacyan (2000). "Phenomenology of Broad Emission Lines in Active Galactic Nuclei." In: *ARA&A* 38, pp. 521–571.

Sulentic, J. W., T. Zwitter, P. Marziani, and D. Dultzin-Hacyan (2000). "Eigenvector 1: An Optimal Correlation Space for Active Galactic Nuclei." In: *ApJ* 536, pp. L5–L9. arXiv: astro-ph/0005177.

Sulentic, J. W., G. M. Stirpe, P. Marziani, R. Zamanov, M. Calvani, and V. Braito (2004). "VLT/ISAAC spectra of the Hβ region in intermediate redshift quasars." In: *A&A* 423, pp. 121–132. arXiv: astro-ph/0405279.

Sulentic, J. W., P. Repetto, G. M. Stirpe, P. Marziani, D. Dultzin-Hacyan, and M. Calvani (2006). "VLT/ISAAC spectra of the Hβ region in intermediate-redshift quasars. II. Black hole

mass and Eddington ratio." In: *A&A* 456, pp. 929–939. arXiv: astro-ph/0606309.

Sulentic, J. W., R. Bachev, P. Marziani, C. A. Negrete, and D. Dultzin (2007). "C IV λ1549 as an Eigenvector 1 Parameter for Active Galactic Nuclei." In: *ApJ* 666, pp. 757–777. arXiv: 0705.1895.

Sunyaev, R. A. and L. G. Titarchuk (1980). "Comptonization of X-rays in plasma clouds - Typical radiation spectra." In: *A&A* 86, pp. 121–138.

Tilton, E. M. and J. M. Shull (2013). "Ultraviolet Emission-line Correlations in HST/COS Spectra of Active Galactic Nuclei: Single-epoch Black Hole Masses." In: *ApJ* 774, p. 67. arXiv: 1307.6560.

Trakhtenbrot, B. and H. Netzer (2012). "Black hole growth to z = 2 - I. Improved virial methods for measuring M_{BH} and L/L_{Edd}." In: *MNRAS* 427, pp. 3081–3102. arXiv: 1209.1096.

Tremaine, S. et al. (2002). "The Slope of the Black Hole Mass versus Velocity Dispersion Correlation." In: *ApJ* 574, pp. 740–753. arXiv: astro-ph/0203468.

Trichas, M. et al. (2012). "The Chandra Multi-wavelength Project: Optical Spectroscopy and the Broadband Spectral Energy Distributions of X-Ray-selected AGNs." In: *ApJS* 200, 17, p. 17. arXiv: 1204.5148.

Tristram, K. R. W., L. Burtscher, W. Jaffe, K. Meisenheimer, S. F. Hönig, M. Kishimoto, M. Schartmann, and G. Weigelt (2014). "The dusty torus in the Circinus galaxy: a dense disk and the torus funnel." In: *A&A* 563, A82, A82. arXiv: 1312.4534.

Turnshek, D. A. (1988). "BAL QSOs: Observations, Models and Implications for Narrow Absorption Line Systems." In: *QSO Absorption Lines: Probing the Universe*. Ed. by J. C. Blades, D. A. Turnshek, and C. A. Norman, p. 17.

Urry, C. M. and P. Padovani (1995). "Unified Schemes for Radio-Loud Active Galactic Nuclei." In: *PASP* 107, p. 803. arXiv: astro-ph/9506063.

Vanden Berk, D. E. et al. (2001). "Composite Quasar Spectra from the Sloan Digital Sky Survey." In: *AJ* 122, pp. 549–564. arXiv: astro-ph/0105231.

Veilleux, S. et al. (2013). "Fast Molecular Outflows in Luminous Galaxy Mergers: Evidence for Quasar Feedback from Herschel." In: *ApJ* 776, 27, p. 27. arXiv: 1308.3139.

Venemans, B. P., F. Walter, L. Zschaechner, R. Decarli, G. De Rosa, J. R. Findlay, R. G. McMahon, and W. J. Sutherland

(2016). "Bright [C ii] and Dust Emission in Three z > 6.6 Quasar Host Galaxies Observed by ALMA." In: *ApJ* 816, 37, p. 37. arXiv: 1511.07432.

Vernet, J. et al. (2011). "X-shooter, the new wide band intermediate resolution spectrograph at the ESO Very Large Telescope." In: *A&A* 536, A105, A105. arXiv: 1110.1944.

Veron, M. P. (1981). "On the width and profile of nuclear emission lines in galaxies." In: *A&A* 100, pp. 12–19.

Véron, P., A. C. Gonçalves, and M.-P. Véron-Cetty (2002). "The "red shelf" of the Hβ line in the Seyfert 1 galaxies RXS J01177+3637 and HS 0328+05." In: *A&A* 384. arXiv: astro-ph/0201240.

Vestergaard, M. (2002). "Determining Central Black Hole Masses in Distant Active Galaxies." In: *ApJ* 571, pp. 733–752. arXiv: astro-ph/0204106.

— (2004). "Early Growth and Efficient Accretion of Massive Black Holes at High Redshift." In: *ApJ* 601, pp. 676–691. arXiv: astro-ph/0309521.

Vestergaard, M. and P. S. Osmer (2009). "Mass Functions of the Active Black Holes in Distant Quasars from the Large Bright Quasar Survey, the Bright Quasar Survey, and the Color-selected Sample of the SDSS Fall Equatorial Stripe." In: *ApJ* 699, pp. 800–816. arXiv: 0904.3348.

Vestergaard, M. and B. M. Peterson (2006). "Determining Central Black Hole Masses in Distant Active Galaxies and Quasars. II. Improved Optical and UV Scaling Relationships." In: *ApJ* 641, pp. 689–709. arXiv: astro-ph/0601303.

Vestergaard, M., X. Fan, C. A. Tremonti, P. S. Osmer, and G. T. Richards (2008). "Mass Functions of the Active Black Holes in Distant Quasars from the Sloan Digital Sky Survey Data Release 3." In: *ApJ* 674, pp. L1–L4. arXiv: 0801.0243.

Vestergaard, M., K. Denney, X. Fan, J. J. Jensen, B. C. Kelly, P. S. Osmer, B. M. Peterson, and C. A. Tremonti (2011). "Black hole mass estimations: limitations and uncertainties." In: *Narrow-Line Seyfert 1 Galaxies and their Place in the Universe*, p. 38.

Vogt, S. S. et al. (1994). "HIRES: the high-resolution echelle spectrometer on the Keck 10-m Telescope." In: *Instrumentation in Astronomy VIII*. Ed. by D. L. Crawford and E. R. Craine. Vol. 2198. Proc. SPIE, p. 362.

Vrtilek, J. M. (1985). "Seyfert galaxy narrow-line regions. II - Kinematic models." In: *ApJ* 294, pp. 121–133.

Wang, H., F. Xing, K. Zhang, T. Wang, H. Zhou, and S. Zhang (2013). "Outflow and Hot Dust Emission in High-redshift Quasars." In: *ApJ* 776, p. L15. arXiv: 1309.4465.

Wang, J.-G., X.-B. Dong, T.-G. Wang, L. C. Ho, W. Yuan, H. Wang, K. Zhang, S. Zhang, and H. Zhou (2009). "Estimating Black Hole Masses in Active Galactic Nuclei Using the Mg II λ2800 Emission Line." In: *ApJ* 707, pp. 1334–1346. arXiv: 0910.2848.

Weedman, D. W. (1970). "High-Velocity Gas Motions in Galactic Nuclei." In: *ApJ* 159, p. 405.

Weymann, R. J., S. L. Morris, C. B. Foltz, and P. C. Hewett (1991). "Comparisons of the emission-line and continuum properties of broad absorption line and normal quasi-stellar objects." In: *ApJ* 373, pp. 23–53.

White, R. L., R. H. Becker, D. J. Helfand, and M. D. Gregg (1997). "A Catalog of 1.4 GHz Radio Sources from the FIRST Survey." In: *ApJ* 475, pp. 479–493.

Whittle, M. (1985). "The narrow line region of active galaxies. I - Nuclear forbidden line profiles. II - Relations between forbidden line profile shape and other properties." In: *MNRAS* 213, pp. 1–31.

Williams, R. J., R. Maiolino, Y. Krongold, S. Carniani, G. Cresci, F. Mannucci, and A. Marconi (2016). "An ultra-dense fast outflow in a quasar at z=2.4." In: *ArXiv e-prints*. arXiv: 1605.08046.

Willott, C. J., R. J. McLure, and M. J. Jarvis (2003). "A 3×10^9 $M_\odot$ Black Hole in the Quasar SDSS J1148+5251 at z=6.41." In: *ApJ* 587, pp. L15–L18. arXiv: astro-ph/0303062.

Wilson, J. C. et al. (2004). "Mass producing an efficient NIR spectrograph." In: *Ground-based Instrumentation for Astronomy*. Ed. by A. F. M. Moorwood and M. Iye. Vol. 5492. Proc. SPIE, pp. 1295–1305.

Wisotzki, L., N. Christlieb, N. Bade, V. Beckmann, T. Köhler, C. Vanelle, and D. Reimers (2000). "The Hamburg/ESO survey for bright QSOs. III. A large flux-limited sample of QSOs." In: *A&A* 358, pp. 77–87. arXiv: astro-ph/0004162.

Wright, E. L. et al. (2010). "The Wide-field Infrared Survey Explorer (WISE): Mission Description and Initial On-orbit Performance." In: *AJ* 140, 1868, pp. 1868–1881. arXiv: 1008.0031.

Wu, X.-B., R. Wang, M. Z. Kong, F. K. Liu, and J. L. Han (2004). "Black hole mass estimation using a relation between the

BLR size and emission line luminosity of AGN." In: *A&A* 424, pp. 793–798. arXiv: astro-ph/0403243.

Wu, X.-B. et al. (2015). "An ultraluminous quasar with a twelve-billion-solar-mass black hole at redshift 6.30." In: *Nature* 518, pp. 512–515. arXiv: 1502.07418.

Yip, C. W. et al. (2004). "Spectral Classification of Quasars in the Sloan Digital Sky Survey: Eigenspectra, Redshift, and Luminosity Effects." In: *AJ* 128, pp. 2603–2630. arXiv: astro-ph/0408578.

York, D. G. et al. (2000). "The Sloan Digital Sky Survey: Technical Summary." In: *AJ* 120, pp. 1579–1587. arXiv: astro-ph/0006396.

Yuan, M. J. and B. J. Wills (2003). "Eddington Accretion and QSO Emission Lines at z˜2." In: *ApJ* 593, pp. L11–L14. arXiv: astro-ph/0306518.

Zakamska, N. L. and J. E. Greene (2014). "Quasar feedback and the origin of radio emission in radio-quiet quasars." In: *MNRAS* 442, pp. 784–804. arXiv: 1402.6736.

Zakamska, N. L., F. Hamann, I. Pâris, W. N. Brandt, J. E. Greene, M. A. Strauss, C. Villforth, D. Wylezalek, R. M. Alexandroff, and N. P. Ross (2016). "Discovery of extreme [O III] λ5007 Å outflows in high-redshift red quasars." In: *MNRAS* 459, pp. 3144–3160. arXiv: 1512.02642.

Zamfir, S., J. W. Sulentic, P. Marziani, and D. Dultzin (2010). "Detailed characterization of Hβ emission line profile in low-z SDSS quasars." In: *MNRAS* 403, pp. 1759–1786. arXiv: 0912.4306.

Zhang, K., X.-B. Dong, T.-G. Wang, and C. M. Gaskell (2011). "The Blueshifting and Baldwin Effects for the [O III] λ5007 Emission Line in Type 1 Active Galactic Nuclei." In: *ApJ* 737, 71, p. 71. arXiv: 1105.1094.

Zhang, S., H. Wang, T. Wang, F. Xing, K. Zhang, H. Zhou, and P. Jiang (2014). "Outflow and Hot Dust Emission in Broad Absorption Line Quasars." In: *ApJ* 786, p. 42. arXiv: 1403.3166.

Zubovas, K. and A. King (2012). "Clearing Out a Galaxy." In: *ApJ* 745, L34, p. L34. arXiv: 1201.0866.

de Jong, R. S. et al. (2012). "4MOST: 4-metre multi-object spectroscopic telescope." In: *Ground-based and Airborne Instrumentation for Astronomy IV*. Vol. 8446. Proc. SPIE, 84460T. arXiv: 1206.6885.

van der Marel, R. P. and M. Franx (1993). "A new method for the identification of non-Gaussian line profiles in elliptical galaxies." In: *ApJ* 407, pp. 525–539.